Constructing Correlated Spin States with Neutral Atoms in Optical Lattices

Dissertation

zur Erlangung des Grades

"Doktor

der Naturwissenschaften"

am Fachbereich Physik

der Johannes Gutenberg-Universität

in Mainz

Artur Widera

geboren in Fulda

Mainz, den 10. September 2007

D77

Datum der mündlichen Prüfung: 10. September 2007

Abstract

This thesis reports on the experimental investigation of controlled spin dependent interactions in a sample of ultracold ^{87}Rb atoms trapped in a periodic optical potential. In such a situation, the most basic interaction between only two atoms at one common potential well, forming a micro laboratory for this atom pair, can be investigated. Spin dependent interactions between the atoms can lead to an intriguing time evolution of the system. In this work, we present two examples of such spin interaction induced dynamics. First, we have been able to observe and control a coherent spin changing interaction. Second, we have achieved to examine and manipulate an interaction induced time evolution of the relative phase of a spin 1/2-system, both in the case of particle pairs and in the more general case of N interacting particles.

The first part of this thesis elucidates the spin-changing interaction mechanism underlying many fascinating effects resulting from interacting spins at ultracold temperatures. This process changes the spin states of two colliding particles, while preserving total magnetization. If initial and final states have almost equal energy, this process is resonant and leads to large amplitude oscillations between different spin states. The measured coupling parameters of such a process allow to precisely infer atomic scattering length differences, that e.g. determine the nature of the magnetic ground state of the hyperfine states in ^{87}Rb.

Moreover, a method to tune the spin oscillations at will based on the AC-Zeeman effect has been implemented. This allowed us to use resonant spin changing collisions as a quantitative and non-destructive particle pair probe in the optical lattice. This led to a series of experiments shedding light on the Bosonic superfluid to Mott insulator transition.

In a second series of experiments we have been able to coherently manipulate the interaction induced time evolution of the relative phase in an ensemble of spin 1/2-systems. For two particles, interactions can lead to an entanglement oscillation of the particle pair. For the general case of N interacting particles, the ideal time evolution leads to the creation of spin squeezed states and even Schrödinger cat states. In the experiment we have been able to control the underlying interactions by a Feshbach resonance. For particle pairs we could directly observe the entanglement oscillations. For the many particle case we have been able to observe and reverse the interaction induced dispersion of the relative phase.

The presented results demonstrate how correlated spin states can be engineered through control of atomic interactions. Moreover, the results point towards the possibility to simulate quantum magnetism phenomena with ultracold atoms in optical traps, and to realize and analyze many novel quantum spin states which have not been experimentally realized so far.

Zusammenfassung

In dieser Arbeit werden Experimente vorgestellt, die den Einfluß von spinabhängiger Wechselwirkung auf das Verhalten von ultrakalten ^{87}Rb Atomen in einem 3D periodischen optischen Potential untersuchen. In solch einem Potential kann die grundlegende Wechselwirkung zwischen nur zwei Atomen, gefangen in einem gemeinsamen Potentialminimum, wie in einem Mikrolabor untersucht werden. Hängt die Wechselwirkung zwischen den Atomen vom jeweiligen Spinzustand der Teilchen ab, so kann das zu einer faszinierenden Zeitentwicklung des Systems führen. In der vorliegenden Arbeit werden zwei Beispiele einer solchen Zeitentwicklung vorgestellt, die durch spinabhängige Stöße induziert sind. Zum einen konnten wir in unseren Experimenten eine kohärente, spinändernde Wechselwirkung beobachten und kontrollieren. Zum anderen waren wir in der Lage, die wechselwirkungsinduzierte Zeitentwicklung der relativen Phase eines Spin-1/2 Systems zu beobachten und zu manipulieren, sowohl für zwei als auch für N wechselwirkende Teilchen.

Der erste Teil der Arbeit behandelt die spin-ändernde Wechselwirkung, die vielen beobachteten Effekten mit wechselwirkenden Spins zugrunde liegt. Diese Wechselwirkung ändert die Spinzustände der beiden stoßenden Teilchen, während die Gesamtmagnetisierung erhalten bleibt. Wenn Anfangs- und Endzustände fast gleiche Energien haben, kann dieser Prozeß resonant ablaufen und zu deutlichen Oszillationen zwischen den Besetzungen verschiedener Spinzustände führen. Aus den gemessenen Kopplungsparametern dieses Prozesses können fundamentale Differenzen von Streulängen, die zum Beispiel den magnetischen Grundzustand der beiden Hyperfeinzustände des ^{87}Rb Grundzustandes definieren, sehr genau abgeleitet werden.

Zudem konnten wir basierend auf dem AC-Zeemaneffekt eine Methode entwickeln, um die Spinoszillationen nach Belieben zu kontrollieren. Diese Kontrolle erlaubte es uns, die spinändernden Stöße als quantitatives Maß für Teilchenpaare im optischen Gitter zu verwenden. Diese Methode ermöglichte eine Reihe von Experimenten, die sehr genaue Einblicke in den bosonischen Superfluid nach Mott-Isolator Übergang gewährt haben.

In einer zweiten Serie von Experimenten konnten wir die wechselwirkungsinduzierte Zeitentwicklung der relativen Phase in einem Spin-1/2 System kohärent manipulieren. Für ein Atompaar kann die Wechselwirkung zu einer zeitlichen Oszillation zwischen einem separablen und einem verschränkten Zustand führen. Für den allgemeineren Fall von N wechselwirkenden Teilchen kann die Dynamik korrelierte Zustände erzeugen, wie zum Beispiel Spin-gequetschte oder maximal verschränkte Schrödinger-Katzen Zustände. In den Experimenten konnten wir die zugrunde liegenden Wechselwirkungen mit Hilfe einer Feshbach Resonanz einstellen. Im Fall zweier wechselwirkender Atome waren die Verschränkungsoszillationen direkt zu beobachten. Für das Vielteilchensystem konnten wir die Dispersion

der relativen Phase detektieren und zeitlich umkehren.

Die dargestellten Experimente demonstrieren, daß korrelierte Spinzustände allein durch Kontrolle der Wechselwirkungseigenschaften in optischen Potentialen konstruiert werden können. Darüber hinaus zeigen die Ergebnisse die Möglichkeit auf, Quantenmagnetismus mit ultrakalten Atomen in optischen Gittern zu simulieren, und viele neue Quantenzustände zu erzeugen und zu analysieren, die dem Experiment bisher nicht zugänglich waren.

Contents

Contents

1 Introduction

Recent experimental progress in the preparation and manipulation of ultracold atomic samples has allowed to access an intriguing regime where strong adjustable interactions dominate the properties of the system. In this regime, fascinating, however still unresolved questions of condensed matter physics or quantum information processing could be experimentally addressed in a very controlled atomic physics system. Prominent examples for such experiments are the realization of the superfluid to Mott-insulator transition of Bosons in optical lattices [1, 2, 3] or the creation of condensed systems in degenerate Fermi gases consisting of molecules [4, 5, 6, 7] or correlated fermion pairs [8, 9, 10]. The strong interatomic interactions present in such experiments build up quantum correlations between particles. These inter-particle correlations are responsible for the remarkable properties of the novel quantum states. For example, atom number correlations between lattice sites in the case of a Mott-insulator imply the absence of inter-site coherence [5], but reflect the existence of number squeezed states at each lattice site [11, 12]. Atom-pair correlations in the case of degenerate Fermi gases enable the condensation to a molecular Bose-Einstein condensate or a condensate of loosely bound Fermion pairs [13, 14], despite the Pauli principle which tends to hinder interactions between particles.

The class of the so-called *correlated states* comprises a much larger manifold of quantum states, including the pair condensates and insulating states mentioned above, but also highly entangled few and many-body states as well as squeezed states. Moreover, many novel quantum states, such as Luttinger liquids (see e.g. Ref. [15]), have been predicted, and partly been realized. One example for such a low-dimensional correlated system is the Tonks-Girardeau gas in a one-dimensional system [16, 17] which shows an interesting Fermionized behavior of Bosons, for example in the two-body correlation function [18]. All these correlated states have unique properties markedly different from classical states that make them ideal candidates for a large number of applications in quantum physics experiments. For example, spin squeezed states have reduced quantum fluctuations below the standard quantum limit along one observable [19]. Therefore they have been proposed to enhance the performance of interferometers and precision measurements [20]. Entangled states exhibit non-local information, i.e. information that cannot be inferred from just independent measurements of the single-particle properties of the entangled states [21]. These states are an important prerequisite in quantum computing schemes [21]. Moreover, understanding the interplay between interactions and correlations might offer a better insight into how the quantum world connects to the classical world, in particular for increasing number of particles involved. The creation, controlled manipulation and analysis of strongly correlated quantum states is therefore an important aim of both experimental and theoretical effort in quantum physics.

This thesis

This thesis focuses on experimental *spin dependent* quantum state engineering and analysis in an ultracold sample of neutral atoms trapped in a periodic optical potential. In optical potentials the spin degree of freedom is liberated because all spin states can be trapped. Such multi-spin superpositions are usually referred to as spinor systems. The realization of these systems adds a novel degree of freedom in experiments with ultracold atoms that can be used to simulate quantum magnetism phenomena in a very controlled way, or to encode quantum information in the spin degree of freedom, for which e.g. entangled spin states are desirable. As will be outlined below, spin dependent interactions between atoms are usually substantially weaker than the spin independent interactions in the experiments mentioned above. Therefore it is crucial to enhance the ratio of spin dependent to spin independent interactions in experiments. In the cases presented in the following, an interaction dominated regime is entered by loading a Rubidium Bose-Einstein condensate into an optical lattice. Thus an array of strongly interacting particle pairs can be realized, where each pair can be considered a well isolated "micro laboratory", perfectly suited to study interaction effects on a fundamental level. In order to enhance the spin dependent interaction compared to the spin independent, certain resonance phenomena are used. Thereby, two remarkable effects could be experimentally observed and will be discussed in this thesis. The first effect results in an interaction driven coherent spin-population oscillation of particle pairs. The second effect affects the relative phase between two spin states and results in an intriguing time evolution of the relative two- or even many-body phase from an initially classical, coherent spin state into a correlated spin state.

Coherent spin changing collisions If the initial spin state of two colliding atoms is energetically degenerate with another combination of spin states of the two atoms, a resonant spin changing dynamics can be observed, assuming conservation laws are obeyed (see e.g. Ref. [22]). In our experiments we have been able to observe such a coherent spin changing dynamics in a 3D optical lattice filled with a ^{87}Rb Bose-Einstein condensate, which almost perfectly realizes the ideal case of an array of strongly interacting atom pairs, where each pair is well isolated from the environment. The two hyperfine ground states with total atomic spin[1] $f = 1$ and $f = 2$ constitute a perfect example for spin dynamics in a spin-1 and spin-2 manifold, respectively (see Fig. 1.1). As will be outlined, the dynamics can be related to fundamental scattering properties of the atomic species, that also determine the magnetic ground state of the system. Our results allow to make quantitative statements on the magnetic ground state of the $f = 1$ and $f = 2$ hyperfine manifold at zero magnetic field, which we find to be ferromagnetic and antiferromagnetic, respectively.

Moreover we have been able to develop a method to control the observed dynamics by means of an external electromagnetic field due to the AC-Zeeman effect, which allows for an efficient quantum state preparation. As a consequence, the number of atom pairs is

[1] Throughout this thesis we will use lower size letters to denote properties for single atoms, whereas capital letters are used for combined, coupled quantities of two atoms.

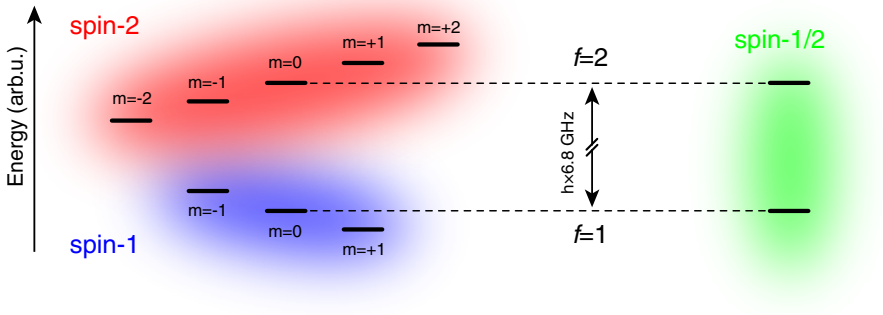

Figure 1.1: Encoding spins in hyperfine states of the ^{87}Rb $5S_{1/2}$ ground state, here depicted at small magnetic field. The Zeeman levels within the $f = 1$ and $f = 2$ hyperfine manifolds represent examples of spin-1 (blue) and spin-2 (red) systems, respectively. Choosing one Zeeman level in each of the two hyperfine states can be considered a quasi spin-1/2 system (green), provided the other Zeeman level are decoupled.

directly related to the amplitude of the spin population oscillations. This amplitude has therefore been used as a sensitive probe for pairs in our optical lattice, leading to the observation of number squeezing across the superfluid to Mott-insulator transition, and to the detection of Mott-insulator shells in the inhomogeneous system.

Coherent time evolution of the relative many-body phase Even if in a collision no change in the spin state populations occurs, a time evolution of the relative phase between the spin states is present. For the spin-1/2 system this phase evolution can cause an initially coherent (classical) state to evolve into an entangled state in the two-particle case. In a many-body system the phase evolution is more intricate (see e.g. Ref. [23] for a review), including the evolution to a spin squeezed state and possibly to a maximally entangled Schrödinger cat state. This evolution is in fact is not limited to the experimental situation presented in this thesis. It is intrinsic to many quantum systems like Josephson junctions, interacting Bose-Einstein condensates in double wells, or in experiments with single atoms coupled to a microwave cavity field.

We have been able to control the coherent phase evolution of spin-1/2 systems by tuning the relative interaction strength of certain spin-combinations. Here the spin-1/2 system has been realized in two Zeeman levels, one in the $f = 1$ and the other in the $f = 2$ hyperfine state (see Fig. 1.1). The tuning has been achieved via a so-called Feshbach resonance [24], i.e. by bringing the state of the initially unbound particles energetically close to a molecular bound state coupled to the initial state of the unbound particles, which enhances the corresponding interaction energy.

For the two-particle case the resulting entanglement dynamics could be observed by monitoring the interaction induced collapse and revival of coherence through a Ramsey-

type atom interferometer sequence. This allows to extract precise information about the scattering properties of the system. For the many body case, the coherent revival of the initial state could be tracked after a time reversal sequence. Thereby the coherent nature of this interaction could be demonstrated.

Overview

This thesis is organized as follows. Chapter 2 will introduce the description of scattering at ultralow temperatures by the *s*-wave scattering length in the spin independent case. The modifications due to the spin degree of freedom will be discussed. The experimental situation of a Bose-Einstein condensate in optical lattices and the relevant energy scales are described in Chapter 3. The technical tools for the creation, manipulation and detection of a spinor Bose-gas in an optical lattice will be introduced. In particular Ramsey interferometry will be explained. Chapter 4 presents the first series of experiments investigating the coherent spin changing interaction, leading to an oscillatory population transfer between spin states. The theoretical description suggests a Rabi-type model which is applicable for a wide parameter range; from this, fundamental scattering parameters can be extracted. A method to tune the dynamics by means of an "AC-Zeeman effect" is introduced. The implications of the presented results on the magnetic properties of the system will be discussed. Exemplary applications of spin changing collisions as a particle pair probe in a 3D optical lattice are outlined. This chapter is mainly based on Refs. [25, 26, 27]. An experimental demonstration of a coherent phase evolution under a non-linear spin interaction in a spin-1/2 system is considered in Chapter 5. The basic idea is given for two interacting particles, and the time evolution is outlined. Then the situation is generalized to a system of N interacting spin 1/2 particles, and the corresponding time evolution is sketched. The concept of magnetic Feshbach resonances is briefly discussed. This type of resonance is used in order to enhance the spin dependent interaction strength in the experimental realization. Finally experimental results for such an intriguing phase evolution are presented, demonstrating the possibility to create a huge array of entangled particle pairs in a 3D optical periodic potential. Moreover, the coherent nature of the interaction driven phase dynamics in the many-body case is demonstrated. This chapter is partly based on Ref. [28, 29]. Chapter 6 outlines the potential of the experiments performed and points towards possible further experiments and applications.

Publications in the context of this PhD thesis

In the following list of results published during the last few years, the most relevant for this thesis have been marked.

⇒ **Entanglement Interferometry for Precision Measurement of Atomic Scattering Properties**
A. Widera, O. Mandel, M. Greiner, S. Kreim, T.W. Hänsch and I. Bloch
Phys. Rev. Lett. **92**, *160406* (2004)

- **Tonks-Girardeau gas of ultracold atoms in an optical lattice**
  B. Paredes, A. Widera, V. Murg, O. Mandel, S. Fölling, I. Cirac, G.V. Shlyapnikov, T.W. Hänsch and I. Bloch
  Nature **429**, *277* (2004)

- **State Selective Production of Molecules in Optical Lattices**
  T. Rom, T. Best, O. Mandel, A. Widera, M. Greiner, T.W. Hänsch and I. Bloch
  Phys. Rev. Lett. **93**, *073002* (2004)

- **Spatial quantum noise interferometry in expanding ultracold atom clouds**
  S. Fölling, F. Gerbier, A. Widera, O. Mandel, T. Gericke and I. Bloch
  Nature **434**, *481* (2005)

- **Phase coherence of an atomic Mott insulator**
  F. Gerbier, A. Widera, S. Fölling, O. Mandel, T. Gericke and I. Bloch
  Phys. Rev. Lett. **95**, *050404* (2005)

⇒ **Coherent collisional spin dynamics in optical lattices**
  A. Widera, F. Gerbier, S. Fölling, T. Gericke, O. Mandel and I. Bloch
  Phys. Rev. Lett. **95**, *190405* (2005)

- **Interference pattern and visibility of a Mott insulator**
  F. Gerbier, A. Widera, S. Fölling, O. Mandel, T. Gericke and I. Bloch
  Phys. Rev. A **72**, *053606* (2005)

- **Probing Number squeezing of Ultracold Atoms across the Superfluid-Mott Insulator Transition**
  F. Gerbier, S. Fölling, A. Widera, O. Mandel, T. Gericke and I. Bloch
  Phys. Rev. Lett. **96**, *090401* (2006)

⇒ **Resonant control of spin dynamics in ultracold quantum gases by microwave dressing**
  F. Gerbier, A. Widera, S. Fölling, O. Mandel and I. Bloch
  Phys. Rev. A **73**, *041602(R)* (2006)

- **Adiabatic loading of a Bose-Einstein condensate in a 3D optical lattice**
  T. Gericke, F. Gerbier, A. Widera, S. Fölling, O. Mandel and I. Bloch
  arXiv:cond-mat/0603590 (2006)

⇒ **Precision measurement of spin-dependent interaction strengths for spin-1 and spin-2 ^{87}Rb atoms**
  A. Widera, F. Gerbier, S. Fölling, T. Gericke, O. Mandel and I. Bloch
  New J. Phys. **8**, *152* (2006)

- **Formation of spatial shell structures in the superfluid to Mott insulator transition**

S. Fölling, A. Widera, T. Müller, F. Gerbier and I. Bloch
Phys. Rev. Lett. **96**, *090401* (2006)

- **State preparation and dynamics of ultracold atoms in higher lattice orbitals**
  T. Müller, S. Fölling, A. Widera and I. Bloch
  to be published, (2007)

⇒ **Quantum spin dynamics of squeezed Luttinger liquids in two-components atomic gases**
A. Widera, S. Trotzky, P. Cheinet, S. Fölling, F. Gerbier, I. Bloch, V. Gritsev, M.D. Lukin and E. Demler
to be published.

2 Interactions at ultracold temperatures

Interactions play a central role in experiments with ultracold atoms. The most basic process that can occur is the collision between only two particles. Understanding this mechanism yields insight into more complex interaction driven phenomena. Therefore in this chapter, the elementary scattering theory at ultralow temperatures between two spinless atoms will be briefly recalled. In particular, the description of a scattering event by a single parameter only, the *s*-wave scattering length, will be introduced. Further, the effects resulting from the spin-degree of freedom will be discussed. These spin-dependent interactions are the key ingredient leading to the spin dynamics presented in following chapters.

2.1 Scattering in the *s*-wave regime

Partial wave decomposition

Scattering of two identical, neutral, and spinless particles with mass m can be reduced to the problem of one particle with effective mass $\mu_{\text{red}} = m/2$ in a spherically symmetric scattering potential $V(r)$. The problem is described by a Schödinger equation for the wave function $\psi(r)$

$$\left(-\frac{\hbar^2 \nabla^2}{2\mu_{\text{red}}} + V(r)\right)\psi_{\mathbf{k}}(r) = E_{\mathbf{k}}\psi_{\mathbf{k}}(r), \tag{2.1}$$

where $E_{\mathbf{k}} = \frac{\hbar^2\mathbf{k}^2}{2\mu_{\text{red}}}$ with $\mathbf{k}$ being the wave vector at large particle separation. This problem is solved in many text books [30]. Therefore we will only briefly outline the relevant case for the further treatment in this thesis. For a spherically symmetric potential, it is convenient to express the amplitudes of the various outgoing modes, i.e. the scattering amplitudes, in terms of eigenfunctions of the angular momentum operator, which are called *partial waves*. This results in an effective one-dimensional potential

$$V_{\text{eff}}(r) = \frac{\hbar^2 l(l+1)}{2\mu_{\text{red}} r^2} + V(r), \tag{2.2}$$

where l labels the partial wave. The total scattering cross section – usually calculated as the sum over all scattering amplitudes – is the sum of all partial wave contributions

$$\sigma_{\text{tot}} = \sum_{l=0}^{\infty} \sigma_l = \sum_{l=0}^{\infty} \frac{4\pi}{k^2}(2l+1)\sin^2\delta_l, \tag{2.3}$$

where δ_l is the phase shift of the partial wave with respect to the incoming wave due to the scattering potential. This phase shift can be calculated in the case of low energy to be

$$\delta_l(k) \approx n\pi - a_l\, k^{2l+1}. \tag{2.4}$$

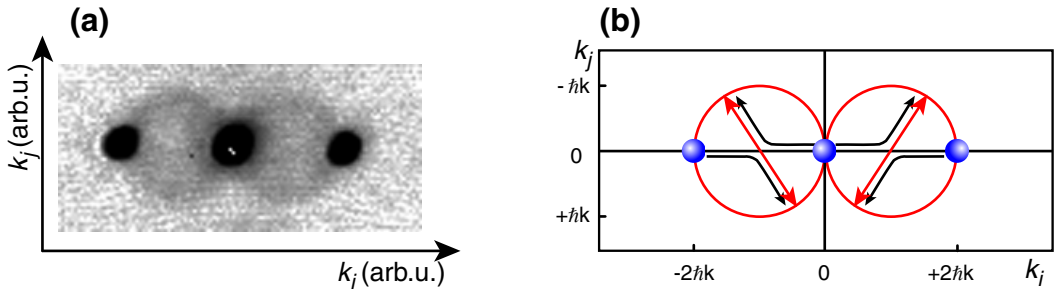

Figure 2.1: Demonstration of *s*-wave scattering in ultracold collisions. **(a)** A pulsed optical lattice creates higher momentum components $\pm 2\hbar k$ in an initially $k = 0$ Bose-Einstein condensate in trap, where $k = 2\pi/\lambda$, with $\lambda/2$ the lattice spacing. When the atoms are allowed to expand in free fall, in-trap momentum is mapped onto spatial position after free flight. During the first period of free fall, atoms from the central order $k = 0$ can collide with atoms having higher order momentum $k = \pm 2\hbar k$. **(b)** Due to the *s*-wave character, the final states are isotropically distributed over a sphere with the relative momentum difference $2\hbar k$ as diameter and the center at the mean momentum $\hbar k$.

Here, n is an integer, and the coefficients a_l are proportionality constants for the l^{th} partial wave, depending on the form of the potential $V(r)$. Substituting this into Eq. (2.3) and expanding around $k = 0$ shows that for extremely low energies the contribution of the l^{th} partial wave vanishes as $\lim_{k\to 0} \sigma_l = k^{4l}$. In particular, for typical experiments with Bose-Einstein condensates, only the $l = 0$ partial wave has to be taken into account, because all higher partial waves are reflected by the centrifugal barrier in Eq. (2.2) before they experience an influence of the scattering potential $V(r)$. In this regime, the scattered wave function can be written as

$$\psi_k \sim e^{i\mathbf{kr}} + f_k \frac{e^{ikr}}{r}, \tag{2.5}$$

where f_k is the corresponding scattering amplitude of the spherical outgoing wave. Here, no angular dependence is left over. This regime is referred to as *s*-wave scattering regime. For ^{87}Rb – the atomic species under investigation in this work – this regime is reached below some $100\,\mu$K [31], whereas typical temperatures of the atomic sample used throughout this thesis is below $1\,\mu$K. Therefore we can treat all further interaction effects between ultracold bosonic atoms safely in the framework of *s*-wave scattering only. The discussion of the free-particle collision can be equivalently used for the situation of a trapped ultracold gas, because in the approximately harmonic trapping potential, the center of mass motion can be separated from the relative dynamics; then the arguments given above hold in the same way for the relative wave functions in the trap. An experimental demonstration of the *s*-wave scattering is shown in Fig. 2.1.

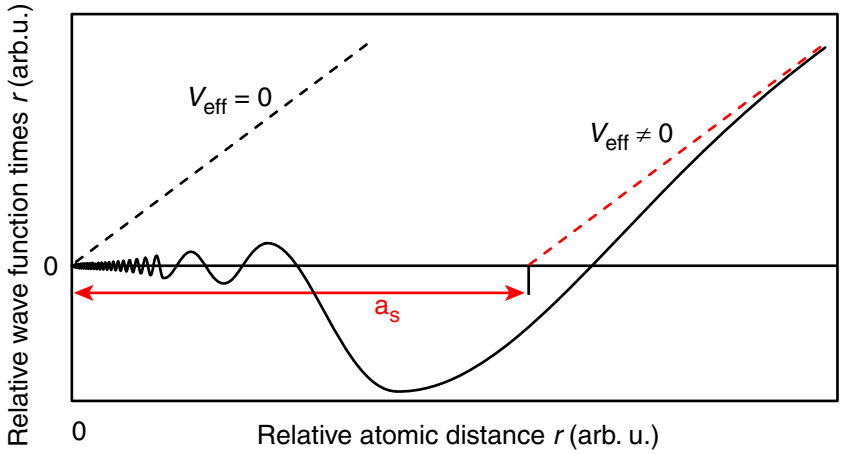

Figure 2.2: Effect of the scattering potential on a relative wave function. The asymptotic part of the wave function for long distances r shows a zero-crossing at the value of the scattering length when extended to small distances, reflecting the repulsive interaction for the case presented $a_s > 0$. This zero crossing goes to $a_s = 0$ for $V_{\text{eff}} \to 0$.

The s-wave scattering length

For s-wave collisions the phase shift δ_0 between the outgoing and incoming wave can be characterized by a single parameter $a_s \equiv a_{l=0}$, which is called the s-wave scattering length given by

$$a_s = -\lim_{k\to 0} \frac{\tan \delta_0}{k}. \tag{2.6}$$

Here the notation for the s-wave scattering length should not be confused with the notation for the singlet scattering length, which is widely used in the literature. The physical meaning of the s-wave scattering length is given by the asymptotic behavior of the radial part of the wave function, see Fig. 2.2. This asymptote has a zero crossing at a_s. Therefore, the effect of the scattering potential is to shift the asymptotic wave function by a_s. The sign of the scattering length determines the kind of interaction: For a negative scattering length the interaction is attractive, whereas a positive scattering length corresponds to a repulsive interaction. The latter situation can be visualized as scattering of hard spheres with radius a_s. For ^{87}Rb the s-wave scattering length is on the order of $a_s \approx 100\, a_B$, where $a_B \approx 0.53$ Å.

The s-wave scattering length plays a central role for the description of interatomic collisions at ultracold temperatures, as it is the only parameter characterizing the fundamental strength of the interaction.

Crossections

So far we have considered the case of two-particle collisions, where both particles are distinguishable. In this case the total scattering cross section for s-wave scattering is

$$\sigma_{\text{tot}} = 4\pi a_s^2. \tag{2.7}$$

Here, the scattering cross section again resembles the geometric cross section of hard spheres with size a_s.

For identical, i.e. indistinguishable particles the amplitudes of forward and backward scattering (see Fig. 2.1(b)) have to be summed which alters the cross section by a factor of two:

$$\sigma_{\text{tot}}^{\text{identical}} = 8\pi a_s^2. \tag{2.8}$$

2.2 The Fermi-contact potential

The s-wave interaction induced above can conveniently be expressed by an effective contact potential

$$V(\mathbf{r}) = g\,\delta(\mathbf{r}), \tag{2.9}$$

where $\mathbf{r}$ is the relative distance between the two interacting particles, and g is the coupling constant of the interaction. The coupling constant has to be chosen such that both potentials, the complicated "real" potential and the effective contact potential lead to the same phase shift, i.e. scattering length. This implies

$$g = \frac{4\pi\hbar^2}{m}\, a_s, \tag{2.10}$$

where $\hbar$ is Planck's constant divided by 2π, and a_s is the corresponding scattering length. With this the interaction energy for two ^{87}Rb atoms in state ψ becomes

$$U = |\langle\psi|V(\mathbf{r})|\psi\rangle|^2 = \frac{4\pi\hbar^2}{m_{Rb}}\, a_s \times \int |\phi_0(\mathbf{r})|^4 d\mathbf{r}, \tag{2.11}$$

where ϕ_0 is the identical spatial wave function of each particle, m_{Rb} is the mass of a rubidium atom, and a_s is the s-wave scattering length corresponding to the internal state of the two particles. If the two particles do not share the same spatial wave function, the term in Eq. (2.11) is replaced by an integral over the corresponding single particle densities: $\int |\phi_1|^2\, |\phi_2|^2\, d^3r$.

2.3 Interactions between particles with spin-degree of freedom

So far we considered two interacting particles that had no further degree of freedom, similar to the case of colliding hard spheres. This assumption greatly simplified the description by an s-wave scattering length characterizing the interaction strength irrespective of the

detailed form of the potential. In general, the situation is more complicated, as both atoms might have a spin degree of freedom which changes the problem in two important respects. First, the additional degree of freedom can interact with external fields, e.g. magnetic fields. Second, in the collision of two particles, the spins can interact with each other. Hence, depending on the relative orientation of the two interacting spins the interaction strength can vary and thus the s-wave scattering length might depend on the spin quantum numbers. The knowledge of the precise form of the interaction potential is crucial in order to determine proper values of the s-wave scattering lengths. As this will be of central importance in this thesis, the section will expand in more detail on this issue.

2.3.1 Single particle effects

An atom with electron spin $\mathbf{s}$ and nuclear spin $\mathbf{i}$ will experience an energy shift in a magnetic field $\mathbf{B}$ due to the Zeeman interaction

$$\hat{H}_Z = (\gamma_e \mathbf{s} + \gamma_n \mathbf{i}) \cdot \mathbf{B}, \tag{2.12}$$

where γ_e and γ_n are the gyromagnetic ratios, i.e. ratio between angular momentum and corresponding magnetic moments, for the electron and nucleus, respectively. In addition, both spins couple to the total atomic spin $\mathbf{f} = \mathbf{s}+\mathbf{i}$. This coupling gives rise to the hyperfine interaction

$$\hat{H}_{\mathrm{hf}} = a_{\mathrm{hf}}\, \mathbf{s} \cdot \mathbf{i}, \tag{2.13}$$

where a_{hf} is the hyperfine coupling constant; for ^{87}Rb in the electronic ground state $s = 1/2$ and $i = 3/2$, and this energy amounts to a splitting of $h \times 6.8\,\mathrm{GHz}$ between the $f = 1$ and $f = 2$ hyperfine ground states.

2.3.2 Spin dependent interactions

For the ground state collision of two interacting spin-1/2 particles, each particle experiences a central potential V_C originating from the other atom. Depending on the relative distance, different mechanisms dominate the character of this potential. For extremely small internuclear distances, the Coulomb repulsion of the atomic cores dominates V_C, see Fig. 2.3. For larger internuclear separation, the quantum mechanical exchange interaction for the overlapping electron clouds is dominating. This interaction depends on the total spin $\mathbf{S} = \mathbf{s}_1 + \mathbf{s}_2$ and leads to a splitting of V_C into a singlet ($S = 0$) potential V_S and a triplet ($S = 1$) potential V_T. These potentials differ by twice the exchange energy, which essentially is an exponentially decreasing function of the relative distance r

$$V_{\mathrm{ex}} \propto e^{-2r/r_0}, \tag{2.14}$$

where r_0 is some constant. The common course of both potentials is approximately given by a dispersive energy

$$V_{\mathrm{disp}} = -\frac{C_6}{r^6} - \frac{C_8}{r^8} - \frac{C_{10}}{r^{10}} + \ldots. \tag{2.15}$$

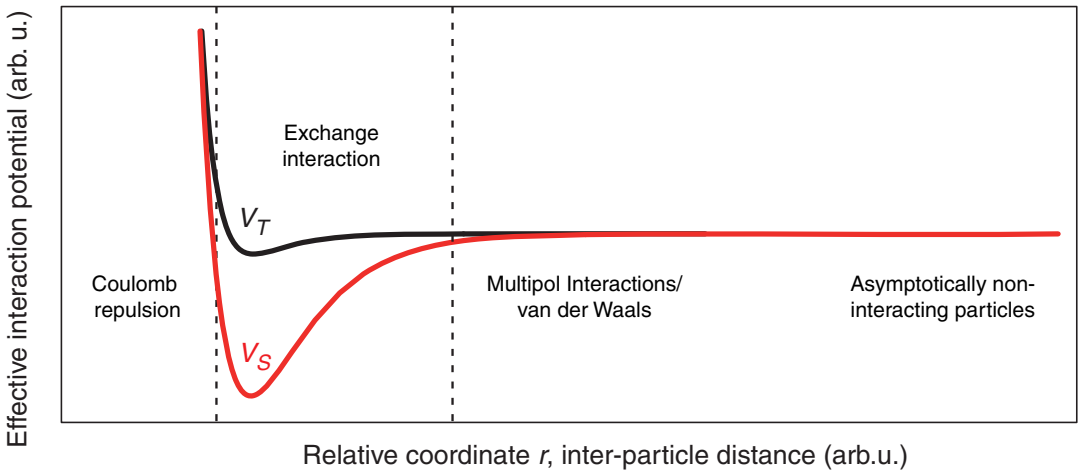

Figure 2.3: Molecular potentials for the scattering of two particles with spin 1/2. For very small inter-nuclear distance the Coulomb repulsion is dominating. In an intermediate regime the quantum mechanical exchange interaction dominates. For even larger separation, when the hyperfine energy becomes larger than the exchange energy, multipole interactions, e.g. van der Waals type, are the most relevant, before the problem asymptotically connects to two independent particles.

Here exact knowledge of the coefficients C_i is crucial for a precise determination of the respective scattering length. For extremely large separation of the two particles, the problem asymptotically turns into the case of two independent particles.

2.3.3 Combined potentials

Combining the results of the two parts above, one finds the total Hamiltonian for the interaction of two particles with spin degree of freedom for the relative coordinate r as

$$\hat{H} = \hat{H}_{\text{kin}} + \sum_{j=1,2} \hat{H}_{Z,j} + \hat{H}_{\text{hf},j} + V_C(r), \tag{2.16}$$

where $\hat{H}_{\text{kin}} = \mathbf{p}^2/(2\mu_{\text{red}})$, with $\mathbf{p}$ the relative momentum and μ_{red} the reduced mass.

For very large inter-nuclear separation the interaction potential V_C can be neglected. In this situation the atoms are well described by their respective total atomic spin f_i and its projection onto the quantization axis m_i, where $i = 1, 2$ labels the atom. Strictly, f is a good quantum number only for $|\mathbf{B}| = 0$, but for all cases considered in the following, the magnetic field values are small enough to justify the use of f.

As the atoms approach each other, however, the exchange energy in V_C, i.e. the splitting between singlet and triplet potentials, can become comparable to the individual Zeeman- and hyperfine energies. Therefore the individual total spin $\mathbf{f}$ and its projection m are not good quantum numbers any more. However, the interaction (2.16) is invariant under

rotation of the coupled total angular momentum $\mathbf{F} = \mathbf{f}_1 + \mathbf{f}_2$. Consequently $\mathbf{F}$ and its projection M onto the quantization axis are still conserved. Therefore collisions can be treated in the basis of total coupled spin $\mathbf{F}$. Each value F of total spin corresponds to the collision in a certain scattering channel, that imposes a certain phase shift onto the asymptotic atomic wave function in this channel. According to the previous section, the effect of this phase shift can be summarized in an s-wave scattering length a_F, labeled by the particular scattering channel. For different values of the coupled spin F, the corresponding scattering length a_F is in general also different. In ultracold collisions for the case of two interacting $f = 1$ ($f = 2$) bosons, the coupled spin F can take the values 0 and 2 (0, 2 and 4), since for bosons due to symmetry reasons only even combinations of the total coupled spin are possible in s-wave collisions.

In practice, and in particular in the cases discussed throughout this thesis, the initial states of atoms entering a collisional event are experimentally prepared in a certain hyperfine state. Therefore the initial basis is conveniently expressed in terms of the individual atomic total spin quantum numbers $|f, m_f\rangle$. In order to describe the effect of an interaction for two atoms, these initial, asymptotic quantum states $|\psi_i\rangle$ have to be decomposed into the basis of total coupled angular momentum

$$|\psi_i\rangle = |f_1, m_1\rangle \otimes |f_2, m_2\rangle = \sum_{F=0}^{f_1+f_2} \sum_{M=-F}^{F} |F, M\rangle\langle F, M|f_1, m_1; f_2, m_2\rangle\,, \quad F \text{ even}. \tag{2.17}$$

Each state $|F, M\rangle$ evolves according to the interaction strength a_F, and the outgoing wave $|\psi_f\rangle$ can be re-expressed in the original basis of individual total atomic spin f and m

$$|\psi_f\rangle = \sum_{f_3,f_4} \sum_{m_3+m_4=M} C_F\, |f_3, m_3; f_4, m_4\rangle\langle F, M|f_3, m_3; f_4, m_4\rangle, \quad F \text{ even}, \tag{2.18}$$

where C_F is a complex amplitude depending on the scattering length a_F. It is important to note that in general the outgoing wave in one asymptotic channel[1] $|f_3, m_3; f_4, m_4\rangle$ is the coherent superposition of various waves coming from different channels with coupled spin F. The complex amplitudes C_F in these channels give rise to interference effects in the final state. In particular, even if a state has been polarized in $|f_1, m_1; f_2, m_2\rangle$, interactions can transfer amplitude to different hyperfine states $|f_3, m_3; f_4, m_4\rangle$. This interference effect will be important for the dynamics presented in chapter 4.

In some cases, however, only atoms which leave the collision region in the same state as they entered in are considered. In this case, population transfer to other states is summarized as loss, because part of the outgoing wave function in the relevant state is missing. Effectively, this situation can then be described in terms of a complex effective scattering length labeled by the asymptotic hyperfine state of interest. The real part of this scattering length describes the phase shift of the relevant asymptotic state, and the imaginary part accounts for losses due to the interaction.

[1] The streched state, i.e. with extremal quantum number m for one given angular momentum f, maps directly onto a single interaction channel.

In the discussion of interaction driven spin dynamics it is important to note the following distinction. The *bare scattering length* is responsible for the overall phase shift of the asymptotic outgoing wave. In contrast, for spin effects the *difference* between the various interaction channels is important. This translates into a difference of phases for the different channels. Therefore, the dynamical effects discussed in Chapters 4 and 5 relate to certain differences of s-wave scattering lengths for the various coupling channels that the initially prepared states can access. In fact, measuring the time scales of the spin dynamics allows to extract exact knowledge of the difference of scattering lengths, which unambiguously determine spin properties such as the magnetic ground state of the system.

2.3.4 Additional interactions

The types of interaction discussed above are the dominating ones for the discussion of the experiments presented in the following. On a much smaller energy scale there exist additional interaction mechanisms. First, the dipole-dipole interaction of two atoms via their electron spin's magnetic moments; and second the spin-orbit interaction of the electrons coupling angular momentum and spin degree of freedom leads in second order to a spin-spin coupling of the two electron spins [32]. As a consequence of these coupling mechanisms, the total coupled angular momentum $\mathbf{F}$ is not independently conserved any more. However, the energy scales of these two interactions are several orders of magnitude smaller than the typical energy of spin dependent interactions. Therefore they are neglected for most cases considered here. They do play a role, however, as a mechanism leading to a loss of atoms from the trap.

2.4 Loss processes and inelastic collisions

For trapped atomic samples, collisions between atoms can lead to an unwanted loss of atoms. This is the case if either internal energy is converted into kinetic energy, which can be sufficient for particles to leave the trap, or if the new internal state of the particles cannot be detected any more. For experiments with degenerate gases, there are two important processes. First, two interacting particles can form a weakly bound molecule while a third carries the excess energy and momentum. This process is referred to as *three-body recombination*. And second, in a collision between two particles the internal states can change, leading to a loss of atoms from the trap, called *two-body decay*. In addition, collisions with untrapped particles from the background can lead to loss. The decay of atoms over time from a sample can be calculated as

$$\frac{dN}{dt} = \sum_{p=1}^{3} -K_p \int n^p(\mathbf{r}, t)\, d\mathbf{r}, \tag{2.19}$$

where $p = 1, 2, 3$ denotes background collisions, two-body decay and three-body recombination, respectively. This leads for each process to a decay according to [33]

$$N(t) = N(0)\,\exp\left\{-K_p \int_0^{t'} dt' \int_V \frac{n^p(\mathbf{r}, t)}{N(t')} d\mathbf{r}\right\}. \tag{2.20}$$

For experiments with ultracold clouds it is important to know the contributions of the three different processes, as loss usually implies heating of the sample and a reduction of measured signal.

Background collisions The number of collisions with hot, untrapped particles depends on the vacuum conditions in the experimental situation. For the experiments presented here, the decay time resulting from (2.20) is well above one minute. Therefore this contribution can be neglected for the experiments discussed in the following as they take much less time.

Two-body decay This process is due to two different physical mechanisms [34]. First, the spin exchange interaction can transfer population to other hyperfine states according to the corresponding scattering lengths. If the final scattering states are not magnetically trapped, this process leads to loss from the trap. This was originally discussed in the context of experiments with two-component ^{87}Rb gases in magnetic traps. There, a mixture of the two states $|f = 1, m = -1\rangle$ and $|f = 2, m = +1\rangle$ was prepared in a magnetic trap [35, 36]. A surprising long lifetime of the overlapping system could be measured. This could be explained by relating the absolute value of the corresponding loss rate K_2^{exch} to the difference of singlet and triplet scattering lengths [37, 38, 39]. For ^{87}Rb the difference is small, therefore this loss process is suppressed. In our case, an optical trap is used, such that all final spin states could be trapped and detected. In fact, this process is exactly the one that causes the coherent time evolution of two-particle spin states, in our case *within* one hyperfine state as presented in Chapter 4.

The second mechanism contributing to two-body decay is dipolar relaxation. This mechanism is caused by the weak dipole-dipole interaction mentioned in Section 2.3.4. Here, the total angular momentum $\mathbf{F}$ is not independently conserved in a collision. As a consequence, an individual atom can change its hyperfine state, and release the hyperfine energy of $h\times 6.8\,\text{GHz}$, exceeding the typical optical trap depth around $h\times 100\,\text{kHz}$ by far. Therefore one, possibly both atoms are lost.

For the experiments presented here, strong losses due to two-body decay occur for atoms is the $f = 2$ hyperfine state[2] of ^{87}Rb, and for mixtures of $f = 1$ and $f = 2$. The corresponding loss rates have been measured to be $K_2 \approx 8.8 \times 10^{-14}\,\text{cm}^3/\text{s}$, see Ref. [25].

Three-body recombination In a recombination process usually all particles are lost from the trap. The molecule cannot be detected by the standard imaging procedure, and the kinetic energy of the third particle is usually much larger than the trap depth. This process

[2] Not in the stretched spin states with $m = \pm 2$.

depends strongly on the atomic density, as the probability for three particles to collide scales as $n(\mathbf{r})^3$. In current experiments with Bose-Einstein condensates this mechanism limits the maximal achievable number of atoms in the condensate. It has been shown that the decay rate K_3 shows a strong dependence on the s-wave scattering length [40]. In particular, for large values $|a_s|$ of the scattering length, the decay rate grows as $K_3 \propto a^4$ [41, 42]. The corresponding decay rates for ^{87}Rb have been experimentally determined to be for the $f = 1$ hyperfine state $K_3 = 5.8 \times 10^{-30}\,\mathrm{cm}^6/\mathrm{s}$ [33], and for the $f = 2$ hyperfine state $K_3 = 1.8 \times 10^{-29}\,\mathrm{cm}^6/\mathrm{s}$ [43].

2.5 Quantitative theoretical predictions

In the experiments presented in this thesis, the interesting dynamics is driven by a spin dependent interaction energy. The value of this energy can be experimentally determined on a sub-percent level compared to other energy scales. In order to compare these results with theory, the values for the s-wave scattering lengths have to be known to a similar degree.

For precise, quantitative predictions in inter-atomic collisions, in principle the exact form of the interaction potential has to be known. From this, the eigenenergies of the bound states can be calculated, which permits the prediction of transition frequencies in e.g. photo-association experiments, and moreover the translation into scattering lengths. However, especially the innermost part of the interaction potential is extremely hard to model, as the energy scales of many different interaction mechanisms become comparable. This allows neither to solve the problem analytically, nor to simplify the problem by proper approximations. Therefore, the "real" potential is assembled by a series of effective potentials, each for a certain region of the internuclear distance. They are chosen such that they connect smoothly to each other and describe the experimental findings as good as possible.

An ongoing interplay between theoretical and experimental effort led to successively refined interaction potentials. For ^{87}Rb, improving the accuracy of the scattering potentials could be achieved by adding information on loss rates to the initial photo-association data. Reducing thereby the error bars on the scattering length values from a $\gtrsim 5\%$ level [44, 38, 45] to $\approx 1\%$ [46] already allowed first predictions on magnetic properties of the system. Further improvement could be achieved by precisely locating the positions of magnetic Feshbach resonances in addition with more accurate photo-association data [47]. Finally, the measurement of several rather high-field Feshbach resonances in ^{87}Rb led to an extremely good knowledge of the interaction potentials and predictions for the scattering lengths with errors on a level of $\lesssim 1‰$ [48]. One of the current models for the precise calculation of the molecular potential is the *accumulated phase method* [49, 32]. As the innermost part of the potential is very hard to model, the effect of this part for distances $r < r_0$ is effectively captured by an accumulated phase ϕ_S, ϕ_T for singlet and triplet potentials, respectively, at a certain relative distance r_0. The potential itself is modeled for internuclear distances $r > r_0$ such that the boundary condition for the phase in each channel is met at $r = r_0$. The advantage of this model compared to other approaches is that only three

parameters r_0, ϕ_S and ϕ_T are involved. With this model and the experimental results outlined above, scattering lengths can be calculated with unprecedented accuracy. These values [47, 32, 50] will be given in the corresponding context and compared with the experimentally determined data presented in this work.

3 Multi-component Bose-Einstein condensates in optical lattices

Trapping Bose-Einstein condensates (BEC) in periodic optical potentials has been shown to allow for entering an interaction dominated regime. Moreover, since in optical traps the spin degree of freedom is not frozen as in magnetic traps, these systems offer the possibility to create and investigate interactions between atoms possessing different internal degrees of freedom, which lead to novel physical effects. This chapter aims at describing the basic properties of BEC and periodic dipole potentials as traps for ultracold bosonic samples. We will briefly sketch the description of such a system by the Bose-Hubbard Hamiltonian and how in such an environment interactions can be studied in detail. We will describe how the spin degree of freedom can be coherently manipulated and used for a precise state preparation in the system. Finally we will outline the experimental realization of a degenerate spinor gas in an optical lattice potential in our experimental setup.

3.1 Bose-Einstein condensation in magnetic traps

Since the first realization of BEC in 1995 [51, 52], the creation of coherent macroscopic matter waves has become a standard tool in many laboratories world wide. We will therefore only briefly describe the most important steps on the way to a BEC and refer to literature for a more detailed description of BEC in general (see Refs. [23, 53, 54] and references therein) or our specific experimental apparatus used in the cases presented here [55, 56, 57, 58].

3.1.1 Theoretical description of BEC

The first approach in creating a BEC was to use a magnetic trap as container for the atomic sample [59, 60]. Originally, the so-called Earnshaw theorem states, that in any static electric field there does not exist a stable configuration of charged particles [1] [61]. If, however, the internal degree of freedom can interact with the external field, this can lead to a position- and level-dependent interaction energy, and hence to a force trapping the atom. For magnetic fields, no field maximum can be created in free space. Therefore only states that minimize their Zeeman energy $E_z = g_f \mu_B m B$ with decreasing magnetic field B can be trapped in a magnetic field minimum. Here μ_B is the Bohr magneton ($\mu_B/h \approx 1.4\,\mathrm{MHz/G}$) and g_f is the Landé factor. For ^{87}Rb which is the element used throughout this thesis, the Zeeman energy of the two ground state manifolds is shown in Fig. 3.1.

[1] This can be extended to other static fields, e.g. gravitational or magnetic potentials.

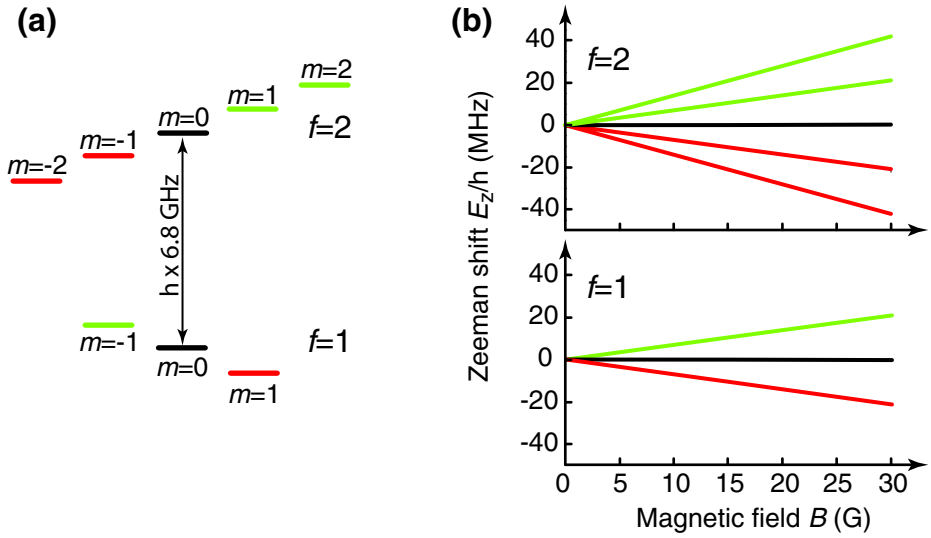

Figure 3.1: **(a)** Ground state manifold of the electronic $5\,^2S_{1/2}$ state of ^{87}Rb for a finite magnetic field. **(b)** Zeeman splitting due to an external magnetic field in the low field regime. Only states that lower their energy with decreasing magnetic field (green) can be trapped in magnetic traps. The others are either untrapped (black) or repelled from the trap (red).

By application of additional cooling through forced radio frequency evaporation [60, 62, 63] in these traps, the phase space density of the system can be compressed to above a critical value on the order

$$n\,\lambda_{\mathrm{dB}}^3 \approx 1, \tag{3.1}$$

where n is the particle density and $\lambda_{\mathrm{dB}} = 2\pi/k$ is the deBroglie wavelength with $\hbar k$ the momentum of the atomic matter wave. When the critical phase space density is reached, a macroscopic number of particles occupies the ground state of the trapping potential; this part of the atoms is called Bose-Einstein condensate (BEC). For zero temperature in the non-interacting case, all atoms occupy this state as predicted originally by Einstein [64].

The zero-momentum population can be described by a macroscopic condensate wave function $\Phi(\mathbf{r}, t)$ which obeys a non-linear Schrödinger equation, the so-called Gross-Pitaevskii equation

$$i\hbar\frac{\partial}{\partial t}\Phi(\mathbf{r}, t) = \left(-\frac{\hbar^2\,\nabla_{\mathbf{r}}^2}{2m_{Rb}} + V_{\mathrm{trap}} + g|\Phi(\mathbf{r}, t)|^2\right)\Phi(\mathbf{r}, t), \tag{3.2}$$

where V_{trap} is the magnetic trapping potential, and g is the interaction coupling constant introduced in Section 2.2. For the ground state, the condensate wave function can be written as

$$\Phi(\mathbf{r}, t) = \phi(\mathbf{r}) \times e^{-i\mu\,t/\hbar} \equiv \sqrt{n(\mathbf{r})} \times e^{-i\,\varphi}, \tag{3.3}$$

with μ the constant chemical potential of the condensate in the trap. In the last step in Eq. (3.3) we have introduced the normalization of the spatial wave function to the total number of atoms $\int d\mathbf{r}\,|\phi(\mathbf{r})|^2 = N$, and the global phase $\varphi = \mu \times t/\hbar$.

Due to the interaction term in Eq. (3.2), part of the atoms, however, do not occupy the zero-momentum state. This is usually referred to as *quantum depletion*. The ratio of atoms with non-zero momentum N_{depl} to the total atom number N can be calculated to be [53, 65]

$$\frac{N_{\text{depl}}}{N} = \frac{5\sqrt{\pi}}{8}\sqrt{a_s^3\, n(0)}, \tag{3.4}$$

where $n(0)$ is the atomic density in the center. For typical BECs this depletion amounts to roughly one percent of the total atom number [53]. In case interactions are enhanced, e.g. by an optical lattice, the depletion can grow up to several ten percent [66]. In the extreme case of a Mott-insulating state (see below), the quantum depletion can cause the zero momentum component to vanish.

Substituting Eq. (3.3) into Eq. (3.2) leads to a stationary non-linear Schrödinger equation

$$\left(-\frac{\hbar^2\,\nabla_{\mathbf{r}}^2}{2m_{Rb}} + V_{\text{trap}} + g\phi^2(\mathbf{r})\right)\phi(\mathbf{r}) = \mu\phi(\mathbf{r}). \tag{3.5}$$

Neglecting the kinetic term, one finds the density profile of the BEC to be

$$n(\mathbf{r}) = |\phi(\mathbf{r})|^2 = \frac{\mu - V_{\text{trap}}}{g}. \tag{3.6}$$

Since the chemical potential is constant over the system, a harmonic trap leads to a harmonic density profile as shown in Fig. 3.2.

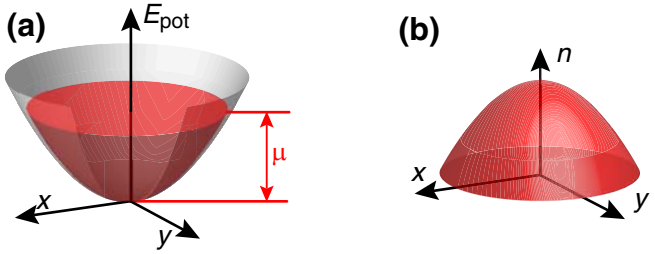

Figure 3.2: **(a)** Bose-Einstein condensate in a harmonic trap. The chemical potential in the trap is flat over the system. This leads to a harmonic density profile **(b)**.

The normalization condition on the total number of atoms for a harmonic trap yields the chemical potential

$$\mu = \frac{\hbar\bar{\omega}}{2}\left(\frac{15N\,a_s}{a_{\text{ho}}}\right)^{2/5}, \tag{3.7}$$

where a_s is the s-wave scattering length of the coupling constant g, N is the total number of atoms, $\bar{\omega} = \sqrt[3]{\prod_i^3 \omega_i}$ is the geometric average of trapping frequencies along the different axes, and $a_{\text{ho}} = \sqrt{\frac{\hbar}{m_{Rb}\bar{\omega}}}$ is the mean ground state harmonic oscillator length.

At this point it can already be seen from Eq. (3.7) and (3.3) that in the ground state the mean field interaction, represented by the s-wave scattering length a_s, leads to a coherent evolution of the global phase of the BEC.

It should be noted that the description of a BEC introduced above so far assumed a 3D system. Some experiments described in this thesis have been carried out in a 1D regime. There, due to the particular geometry, a degenerate gas strictly cannot form a BEC. In addition, interactions in such a gas lead to a slightly different value of e.g. the chemical potential. A more quantitative treatment describing the specific situation of our experimental realization can be found in Appendix B.3. For related work on 1D gases see Refs. [67, 68, 69].

3.2 Dipole traps

Magnetic traps that have been introduced as containers for BEC so far have the serious constraint that only few of the ground state Zeeman levels can be trapped. In case of ^{87}Rb these are $|f = 2, m = +2\rangle$, $|f = 2, m = +1\rangle$, and $|f = 1, m = -1\rangle$. The other states are either untrapped ($|f = 1, m = 0\rangle$, $|f = 2, m = 0\rangle$), or repelled. Although spin-1/2 phenomena have been studied with BEC in magnetic traps for certain internal states in a series of experiments [35, 36, 70, 71, 72], the restrictions of a magnetic trap make it difficult to study arbitrary multi-spin systems and their dynamics. This problem can be overcome by the use of far detuned dipole traps. In contrast to the magnetic traps they can exhibit an attractive force on all quantum states in the ground state manifold of a particle, which can even be a molecule. For a proper choice of parameters, the trap depth can be approximately the same for different hyperfine or Zeeman levels of one atom.

3.2.1 Dipole potential

The mechanism of optical traps can be understood in the following simple picture. A more thorough treatment can be found in Refs. [73, 61]. Placing a two-level atom with an atomic transition of frequency ω_0 into a laser field with amplitude E and frequency ω of the electric field will induce a dipole $\mathbf{d}$ in the atom. The magnitude of the induced dipole is related to the amplitude of the electric field $\mathbf{E}$ through the atomic polarizability $\alpha(\omega)$

$$\mathbf{d} = \alpha(\omega)\,\mathbf{E}. \tag{3.8}$$

This induced dipole has a certain potential energy in the external electric field. The time averaged potential energy can be calculated to be

$$U_{\text{dip}} = -\text{Re}\,(\alpha(\omega))\;|\mathbf{E}|^2, \tag{3.9}$$

which is proportional to the intensity of the light field $I = 1/2\,\varepsilon_0 c|E|^2$, with ε_0 the electric constant and c the speed of light. The polarizability can be calculated in a semiclassical model, i.e. considering the atom as quantum mechanical two-level system interacting with

a classical radiation field. With the resulting value for the polarizability $\alpha(\omega)$ Eq. (3.9) can be re-written in the rotating wave approximation as [73]

$$U_{\text{dip}} = \frac{3\pi c^2}{2\omega_0^3} \frac{\Gamma}{\Delta} I(r), \tag{3.10}$$

with Γ being the natural line width of the atomic transition, and $\Delta \equiv \omega - \omega_0$ the detuning from the atomic transition. The sign of the detuning determines the nature of the corresponding conservative force $-\nabla_{\mathbf{r}} U_{\text{dip}}$ that the light field exerts on the atom. For $\Delta > 0$ (blue detuning) the potential is positive, and the force $\nabla U_{\text{dip}} \sim \nabla I(\mathbf{r})$ is repulsive. For $\Delta < 0$ (red detuning), the potential is negative, and the corresponding force attractive. The dipole potential (3.10) is identical to the AC-Stark shift which a detuned laser induces

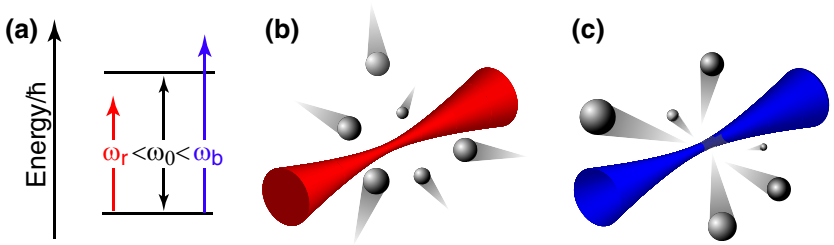

Figure 3.3: Far detuned dipole trap. **(a)** A laser beam that is detuned to lower (higher) frequencies than the atomic transition, i.e. $\omega < \omega_0$ ($\omega > \omega_0$) causes atoms to be attracted (repelled) from intensity maxima **(b,c)**.

in a two-level atom [73].

In reality, atoms cannot be described as simple two-level systems, as they show further substructure due to fine- and hyperfine energy splitting. However, in the case where the detuning Δ becomes much larger than the excited or ground state hyperfine energy, or even the fine structure splitting, those substructures are not resolved and the approximation by a two-level system yields reasonable results. For our experiment, typically a dipole laser wavelength of $\lambda_{\text{dip}} = 845\,\text{nm}$ is used, whereas the atomic transitions are found at $\lambda_{\text{D1}} \approx 795\,\text{nm}$ and $\lambda_{\text{D2}} \approx 780\,\text{nm}$. Therefore the detunings to the two fine structure multiplets are considered individually and their contributions are summed.

3.2.2 Spontaneous scattering in dipole traps

Another important quantity in the discussion of optical traps is the photon scattering rate Γ_{sc}. Due to the imaginary part of the polarizability, the atom can absorb energy from the radiation field and re-emit it as dipole radiation. This process corresponds to the absorption and spontaneous emission of a photon from the light field. For experiments with BEC, spontaneous photon scattering events are usually unwanted as they introduce heating in the system and can create excitations. Therefore the experimental parameters

are chosen as to minimize the scattering rate. For large detuning, the scattering rate can be calculated from the model described above to be [73]

$$\Gamma_{\mathrm{sc}} = \frac{3\pi c^2}{2\hbar\omega_0^3}\left(\frac{\Gamma}{\Delta}\right)^2 I(\mathbf{r}). \tag{3.11}$$

Comparison of Eq. (3.10) with Eq. (3.11) shows that for the same dipole potential the scattering rate can be minimized by increasing the detuning Δ and correspondingly the intensity I. For a typical experiment described in this thesis, the dipole potential amounts to $U_{\mathrm{dip}} \approx h \times 10^3\,\mathrm{Hz}$, while the scattering rate is on the order of $\Gamma_{\mathrm{sc}} \approx 1\,\mathrm{s}^{-1}$.

3.3 Periodic dipole potentials

In this section we will investigate the case where a dipole trap is not formed by a single laser beam but by the interference pattern of two counter propagating laser beams. This changes the situation drastically, as it creates a periodic potential resembling the crystalline potential structure of an idealized, simple-cubic solid. For a review and further information than can be given in this section see Ref. [74] and references therein.

For a Gaussian laser beam with wave vector $\mathbf{k}$ traveling along the $\hat{e}_x$ direction, the electric field amplitude, i.e. neglecting polarization effects, can be described by

$$E(\rho, z) = E_0\, e^{-\rho^2/w^2} \times \mathrm{Re}\left[e^{i\mathbf{k}\,\mathbf{x}}\, e^{i\omega t}\right], \tag{3.12}$$

where ρ denotes the radial coordinate in the plane perpendicular to the propagation axis, and we consider a focused beam with waist w ($1/e^2$ radius). For two counter propagating beams with wave vectors $\mathbf{k}_1 = \mathbf{k}$ and $\mathbf{k}_2 = -\mathbf{k}$, respectively, the resulting time independent intensity pattern can be calculated to be

$$I(\rho, z) = |E_k(\rho, x) + E_{-k}(\rho, x)|^2 = 4E_0\, e^{-2\frac{\rho^2}{w^2}}\, \cos^2(kx). \tag{3.13}$$

In the following we will assume the laser frequency to be red detuned with respect to the atomic transition ($\omega < \omega_0$), because this is the case in the experiments described below. Following the arguments in Section 3.2, atoms are attracted by the anti-nodes of the standing wave (3.13) leading to a potential

$$V(\rho, z) = -V_0\, e^{-2\frac{\rho^2}{w^2}}\, \sin^2(kx), \tag{3.14}$$

where V_0 is the maximally achievable potential depth given by $4\,U_{\mathrm{dip}}$. This potential is periodic along the axis of propagation with periodicity $\lambda/2$, where λ is the laser wavelength. Along the propagation axis of the laser beams, we can therefore identify several periodically spaced potential minima (see Fig. 3.4) that we will call from now on *lattice sites*. Radially the potential has a Gaussian profile in the plane perpendicular to the propagation axis which leads to a transversal confinement of the atoms. This will be important

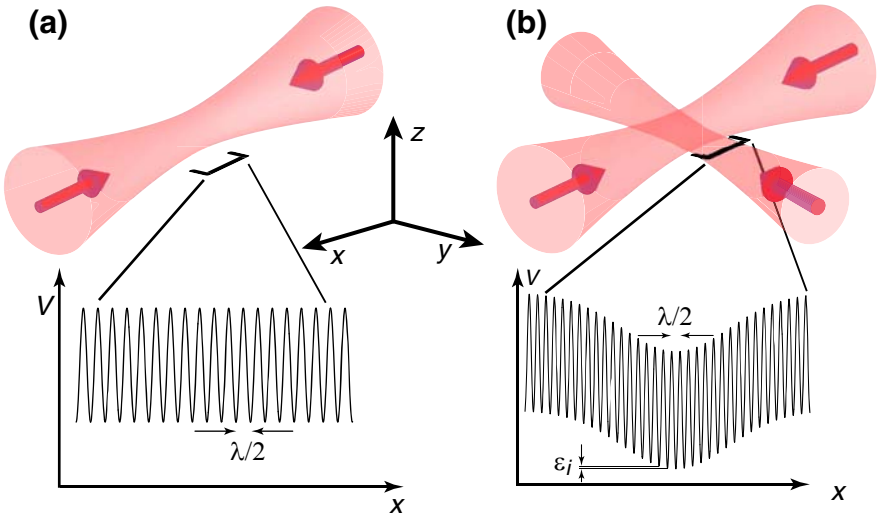

Figure 3.4: Periodic dipole Potential. **(a)** Two counter propagating laser beams create a periodic interference pattern. **(b)** In case of an additional inhomogeneity, such as the harmonic magnetic trap potential or the Gaussian profile of perpendicularly aligned dipole lasers, the periodic potential is varying on a large length scale due to this smooth overall confinement.

when discussing effects arising from the inhomogeneity of the trapping potential. While Eq. (3.14) describes a one-dimensional periodic potential, which is often referred to as a one-dimensional *optical lattice*, this can be extended to higher dimensions by adding additional standing waves. The resulting potential landscapes for the various configuration is shown in Fig. 3.5.

3.3.1 Bose-Hubbard Hamiltonian

The situation of Bosonic matter waves trapped in a periodic potential as given in Eq. (3.14) can be described by the Bose-Hubbard Hamiltonian [75, 76, 77]

$$\hat{H} = -J \sum_{\langle i,j \rangle} \hat{a}_j^\dagger \hat{a}_i + \frac{U}{2} \sum_i \hat{n}_i (\hat{n}_i - 1) + \sum_i \epsilon_i n_i, \tag{3.15}$$

where $\hat{a}_i$ is the bosonic annihilation operator on site i and $\hat{n}_i \equiv \hat{a}_i^\dagger \hat{a}_i$ is the corresponding atom number operator. The three terms in this Hamiltonian stand for three different physical mechanisms:
The first term in Eq. 3.15 describes *tunneling* between adjacent lattice wells (see Fig. 3.6(a)), denoted by the angled brackets in the sum. By tunneling from site i to site j an atom can lower its energy by the amount

$$J = \int \phi^*(x - x_i) \left(-\frac{\hbar^2 \nabla^2}{2m_{Rb}} + V_{\text{lat}} \right) \phi(x - x_j)\, d^3x \tag{3.16}$$

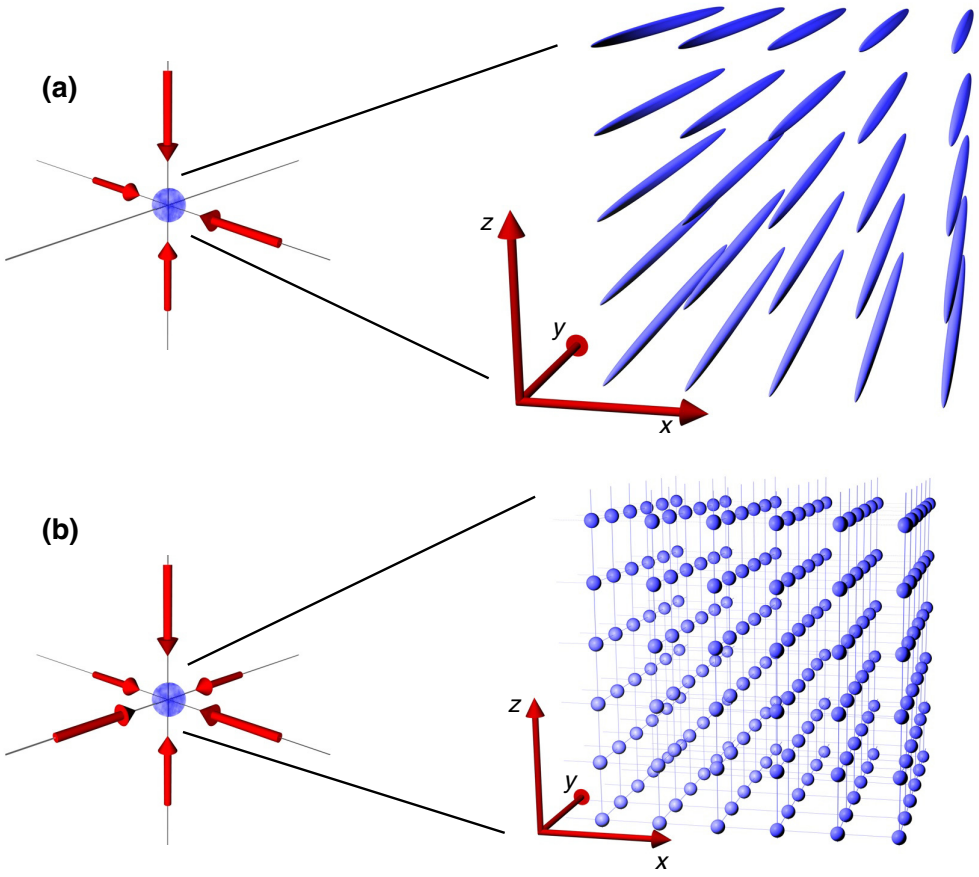

Figure 3.5: **(a)** Two dimensional optical lattice. The superposition of two mutually orthogonal pairs of counter propagating laser beams results in a 2D array of cigar shaped traps. **(b)** If three orthogonal pairs of laser beams are superimposed, the resulting pattern resembles the structure of a simple cubic crystal.

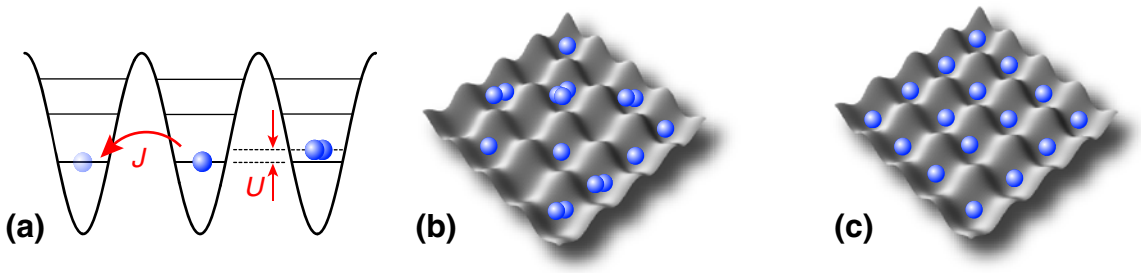

Figure 3.6: **(a)** Sketch of tunnel matrix element J and interaction energy U in a periodic potential. **(b)** Sketch of a possible lattice site occupation in a measurement for the superfluid ground state ($U/J \ll 1$) and averaged filling $\bar{n} = 1$ in the homogeneous system. Site occupation numbers follow Poissonian statistics. **(c)** Same for the Mott-insulating ground state ($U/J \gg 1$). Other parameters as in (b).

where $\phi(x_i)$ is a localized wave function at lattice site i; a convenient set of localized wave functions are Wannier functions, which can be approximated by Gaussian wave packets for large values of the optical potential.

The second term in Eq. (3.15) describes the *on-site interaction* (see Fig. 3.6(a)). If there are n_i atoms trapped at lattice site i, each of the n_i atoms interacts with $n_i - 1$ others. In each such interaction, the total energy is raised because of the repulsive interaction energy (2.11) by the amount

$$U = \frac{4\pi\hbar^2 a_s}{m_{Rb}} \int |\phi(x - x_i)|^4 \, d^3x. \tag{3.17}$$

The last term in Eq. (3.15) accounts for an *energy offset* ϵ_i at lattice site i due to the inhomogeneous trapping potential, which is essentially given by the transversal confinement given in Eq. (3.14) (see Fig. 3.4(b)).

Interaction and tunneling are competing terms, as the one lowers the total energy while the other increases it. Depending on the relative strength of these two terms, the system can be in two different ground states which will be described here only briefly. For further discussion of the superfluid to Mott-insulator transition, see Refs. [57, 78].

Superfluid ground state For $U/J \to 0$ the atomic waves are delocalized over the entire lattice, thereby minimizing the total energy and preserving phase coherence throughout the system. At each lattice site one finds a coherent state where the atom number follows a Poissonian distribution. This state is referred to as *superfluid state* (SF). A possible realization of such a ground state is depicted in Fig. 3.6(b) for an average filling of $\bar{\nu} = 1$, where the average filling is defined as ratio of atom number divided by the number of lattice sites.

Mott-insulating ground state For $U/J \to \infty$, on the other hand, delocalization cannot compensate for the on-site repulsion. Therefore the system arranges in a way as to minimize the interaction energy. This can be achieved by forming localized states at each lattice site with a well defined number of particles, so-called Fock or number states. As a consequence, phase coherence between lattice sites is lost. This many-body state of the system is known as *Mott-insulating state* (MI). In the homogeneous system for an average filling of $\bar{\nu} = 1$ the state is a uniform array of sites with exactly one atom per lattice well as shown in Fig. 3.6(c).
The depth of a periodic optical potential can be precisely controlled by the intensity of the laser beams forming the optical lattice. This allows to vary the ratio of U/J over a wide range of parameters in an experiment. This offered the opportunity to adiabatically transfer an initially delocalized BEC at very shallow potential depths in a three-dimensional optical lattice into the Mott-insulating state of the system, where tunneling is suppressed at very deep potential depths. Thereby, the quantum phase transition from a SF to a MI state could be systematically studied for the first time [1, 57]. For the further discussion it is important to note that in the MI, each lattice well can be prepared with a well defined number of particles that is perfectly isolated from all the other lattice wells. This situation can be seen as a micro-laboratory, where for example the interaction of exactly two atoms can be studied.

3.3.2 Energy scales in the Bose-Hubbard model

For the experimental realization it is often crucial to compare relevant energy scales in the system in order to estimate time scales on which different physical mechanisms – such as interaction driven phase evolution or tunneling – take place. Therefore a precise knowledge of the parameters appearing in the Bose-Hubbard Hamiltonian (3.15) is indispensable. In particular we will present calculations on the tunneling matrix element J (3.16), the interaction matrix element U (3.17) and give an estimate on the inhomogeneity ϵ_i in our system.

Calculating tunneling rates

A periodic potential, i.e. a potential where sites are coupled by tunneling, is in general described in terms of a band structure. This can be obtained by diagonalizing the Hamiltonian

$$\hat{H}_{\text{lat}} = \frac{\hbar \nabla^2}{2m_{Rb}} + V_{\text{lat}}, \tag{3.18}$$

assuming Bloch waves as single particle wave functions, i.e. combinations of plane waves and functions $u_q^{(n)}$ that have the same periodicity as the lattice

$$\phi_q^{(n)}(x) = e^{iqx/\hbar}\, u_q^{(n)}. \tag{3.19}$$

Here, q is the quasi momentum of the particle, and n is the band index. The eigenenergies of the Hamiltonian (3.18) are the allowed energy values $E_q^{(n)}$ that a Bloch wave with certain

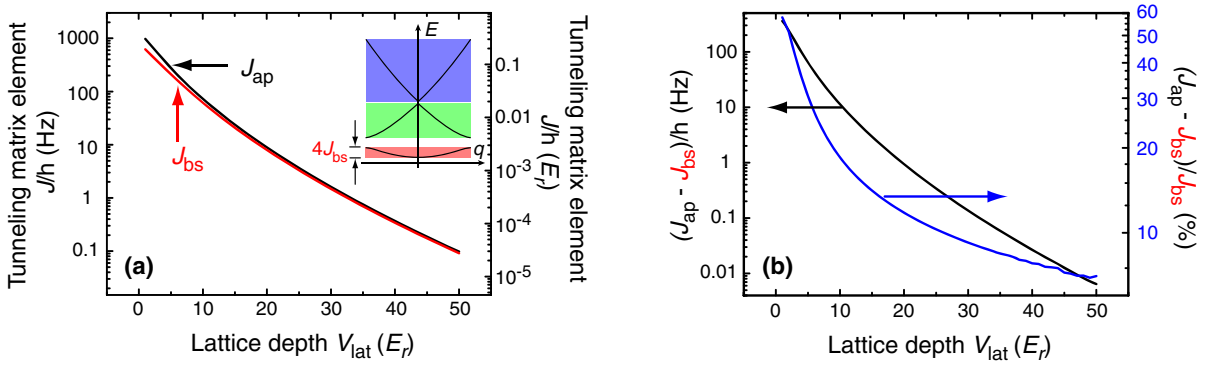

Figure 3.7: **(a)** Calculated tunneling matrix element J in single photon recoil units E_r and frequency assuming $\lambda_{\mathrm{lat}} = 840\,\mathrm{nm}$. The red line has been calculated as one fourth the width of the lowest band (see inset for a band structure for $V_{\mathrm{lat}} = 1\,E_r$). The black line represents the analytical approximation given in Eq. (3.21). **(b)** Absolute (black line) and relative (blue line) difference between the two calculations in part (a).

quasi-momentum q can have such that

$$\hat{H}_{\mathrm{lat}}\,\phi_q^{(n)} = E_q^{(n)}\phi_q^{(n)}. \tag{3.20}$$

From such a band structure calculation one finds the tunneling energy in the lowest band J as one fourth the width of the lowest band [78], i.e. the energy difference between $q = 0$ and $q = \hbar k$ (see inset in Fig.3.7(a)).

An analytical expression for the tunneling energy in deep potentials $V_{\mathrm{lat}} \gg E_r$ has been derived [77]

$$J \approx \frac{4}{\sqrt{\pi}}\,E_r \left(\frac{V_{\mathrm{lat}}}{E_r}\right)^{3/4} \exp\left[-2\sqrt{\frac{V_{\mathrm{lat}}}{E_r}}\right], \tag{3.21}$$

where E_r is the single photon recoil energy, which is given by

$$E_r = \frac{\hbar^2 k^2}{2m_{Rb}}. \tag{3.22}$$

For most cases in our experiment, the analytical formula (3.21) is a good approximation for depths $V_{\mathrm{lat}} \geq 20\,E_r$, although the relative difference is still on the order of 10%. The abolute tunneling energy, however, is already rather small compared to other energy scales, so that this error is usually not important.

Calculating interaction energies

As this work closely investigates the interaction of ultracold atoms, calculation of the interaction matrix element (3.17) is a central point in the discussion of the Bose Hubbard Hamiltonian. Besides the precise knowledge of the s-wave scattering lengths a_s, which will

be the focus in later chapters, the essential quantity is the wave function overlap between two particles trapped at a common lattice site

$$\int |\phi_1(x)|^2 \, |\phi_2(x)|^2 d^3x. \tag{3.23}$$

The problem in calculating the wave function overlap is to find the correct single particle wave functions. In the following we will introduce two approximations and discuss their limitations.

A first approximation, which is in particular valid for $V_0 \gg E_r$, expands the periodic lattice potential up to second order around the potential minimum

$$V_{\text{lat}}(z) = -V_0 \, \sin^2(kz) \approx -V_0 \, k^2 z^2 + O(z^4). \tag{3.24}$$

This harmonic oscillator has a trapping frequency ω_{trap} and harmonic oscillator length a_{ho} of

$$\omega_{\text{trap}} = \sqrt{\frac{2V_0 k^2}{m_{Rb}}} \quad \text{and} \quad a_{\text{ho}} = \sqrt{\frac{\hbar}{m_{Rb} \, \omega_{\text{trap}}}}. \tag{3.25}$$

The harmonic oscillator ground state function can therefore be taken as a first approximation of the real on-site wave function

$$\phi_0(x) = \frac{1}{\sqrt{\pi a_{\text{ho}}^2}} \exp\left[-\frac{1}{2}\left(\frac{x}{a_{\text{ho}}}\right)^2\right]. \tag{3.26}$$

Using this approximation, the on-site interaction energy (3.17) becomes

$$U \approx \sqrt{\frac{8}{\pi}} k \, a_s \, E_r \left(\frac{V_0}{E_r}\right)^{3/4}. \tag{3.27}$$

The course of the interaction energy with changing lattice depth according to Eq. (3.27) is shown in Fig. 3.8(a).

For many purposes, however, this approximation is not accurate enough. In this case, one has to find a better approximation of the on-site wave function. The next step would be to take the higher order terms into account in Eq. (3.24). Ultimately, this corresponds to finding the localized eigenfunctions of the full sinusoidal potential. A convenient set of such localized functions are Wannier functions which can be written as

$$w(x - x_i) = \sum_q e^{iqx_i/\hbar} \, \phi_q(x), \tag{3.28}$$

and are constructed from the eigenfunctions ϕ_q of Eq. (3.20). Wannier functions differ from Gaussian wave packets for small lattice potentials especially in side-lobes at adjacent sites which increase the tunneling probability compared to Gaussian wave packets. The interaction energy U_{bs} calculated with Wannier functions is displayed in Fig. 3.8(a).

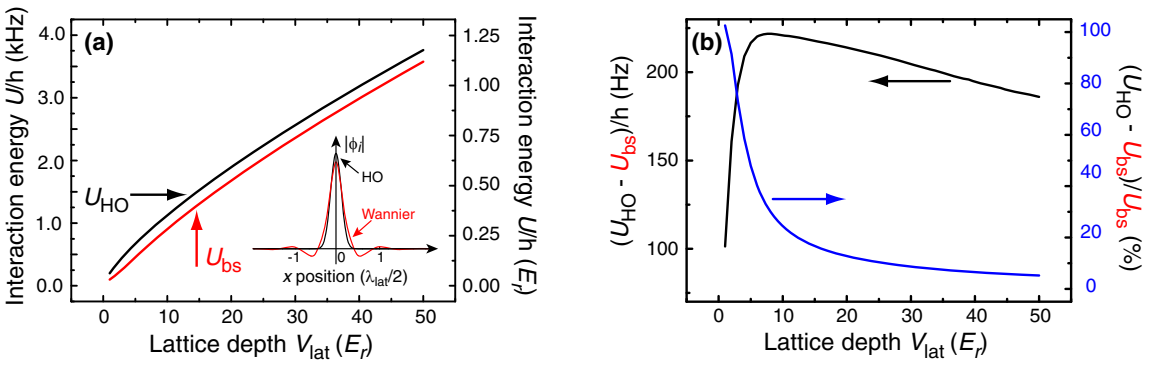

Figure 3.8: **(a)** Calculated interaction energy U in single photon recoil units E_r and frequency assuming $\lambda_{\mathrm{lat}} = 840\,\mathrm{nm}$. The black line shows an approximation of the wave function by a harmonic oscillator ground state, the red line uses Wannier functions from a band structure calculation. The inset shows the sketch of a harmonic oscillator wave function (black) and a Wannier function (red) in a $1\,E_r$ deep lattice. **(b)** Absolute (black line) and relative (blue line) differences of the two approximations shown in (a)

The on-site interaction energy changes for small lattice potentials by several tens of percent when comparing Gaussian wave packets with Wannier functions. The absolute difference in Fig. 3.8(b) shows that for larger lattice depth the band structure calculation predicts a more and more Gaussian-like on-site wave function. For typical lattice depths around $40\,E_r$ where the experiments described below have been prepared, the relative difference between harmonic approximation and band structure calculation is about $\approx 5\%$ of U_{bs}, which is the value obtained in the band structure calculation.

Recently, several approximations to the relative wave function of two particles in a trap have been compared. In particular, the non-interacting Gaussian ansatz is compared with two other approximations. First, a variational method including dipolar interaction has been presented, where the width of the on-site wave packet has been used as variational parameter. Second, a "mean field" approach was applied to the problem of two atoms in a trap, including the conventional spin-independent interaction [79]. A comparison of the three approaches shows a difference for a typical depth of $40\,E_r$ again on the order of 5% [80]. More recently, a model has been presented that calculates the wave function of interacting particles while taking into account the correct optical lattice potential [81]. The results indicate a difference to the band structure calculation displayed in Fig. 3.8 on the order of $+3\%$ of U_{bs} for a depth of $40\,E_r$.

Inhomogeneities in the trapping potential

The Gaussian shape of the laser beam profile on the one hand leads to an additional overall confinement of the atoms. On the other hand the spatially changing intensity leads to a varying lattice depth in 2D and 3D optical lattices that results for example in a spatially

varying on-site interaction strength U and tunneling energy J. In order to quantify these effects, we expand the radial term in Eq. (3.14) to quadratic order in ρ around the point of maximal intensity

$$V(\rho) = -V_0\, e^{-2\frac{\rho^2}{w^2}} \approx -V_0\left(1 - \frac{2\rho^2}{w^2} + \mathcal{O}(\rho^4)\right). \tag{3.29}$$

This harmonic oscillator has a trapping frequency Ω and oscillator length a_Ω of

$$\Omega = \sqrt{\frac{4V_0}{m_{Rb}w^2}} \quad \text{and} \quad a_\Omega = \sqrt{\frac{\hbar}{m_{Rb}\Omega}}. \tag{3.30}$$

This leads to an anharmonicity parameter ϵ_i in Eq. (3.15) of

$$\epsilon_i = \frac{1}{2}\, m_{Rb}\Omega^2\, \rho_i^2, \tag{3.31}$$

where ρ_i is the distance from lattice site i to the center of the trap.

For typical experimental parameters ($w \approx 130\,\mu$m, $V_0 \approx 40\,E_r$), one can calculate the ratio of axial to radial trapping frequencies in a single standing wave trap to be on the order of 10^{-3}. Therefore atoms in such a one dimensional optical lattice take the form of a stack of pancakes. Similarly, the differential change of on-site interaction energy between the center and the border of the cloud due to the overall harmonic confinement can be calculated for these parameters to be on the order of $\lesssim 5\%$ of U_{bs}.

3.4 Coherent control of the spin-degree of freedom

One of the great advantages of optical traps, as opposed to magnetic traps, is the possibility to trap all magnetic sublevels of the ground state manifolds. Since our experiment starts from a spin polarized sample in a magnetic trap, additional tools have to be used to bring the atoms into a desired spin state. In particular, for many applications it is necessary to have not only control over the different spin populations, but also over the relative phases between different spin states. This allows the controlled creation of coherent superpositions of spin states. We next introduce the experimental methods which allow us to create any desired polarized spin state in the ^{87}Rb $f = 1$ and $f = 2$ hyperfine manifolds starting from the initially prepared $|f = 1, m = -1\rangle$ BEC, together with the Bloch-sphere representation for single particle operations in a spin 1/2 system.

3.4.1 The Bloch-sphere

For most cases considered in this thesis, any individual transition between two spin states can be seen as a transition in a two-level system $\{|g\rangle, |e\rangle\}$, as long as all other transitions are sufficiently far detuned (see Fig. 3.9(a)). This problem is well known, and the following standard treatment can be found for instance in Refs. [82, 61].

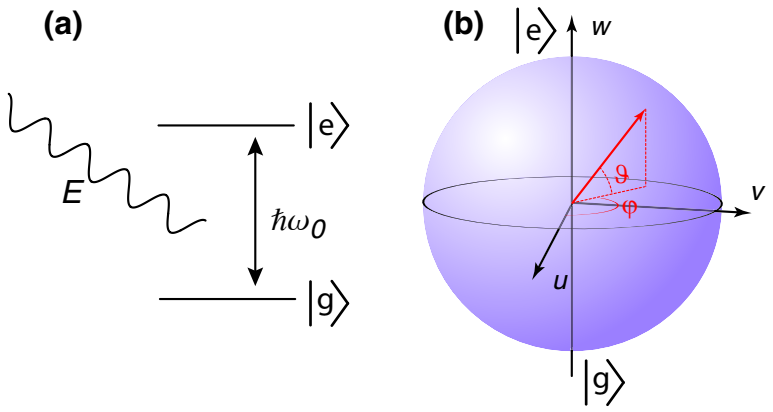

Figure 3.9: **(a)** Two level system driven by an external electro-magnetic field. **(b)** Bloch sphere representation of the two-level system depicted in (a).

A convenient way of visualizing the state of such a two-level system is the Bloch sphere as depicted in Fig. 3.9(b). Here, the surface of the sphere is the manifold of all possible pure quantum states that a single two-level system can be prepared in. In particular, the two poles represent the two polarized states $|g\rangle$ and $|e\rangle$. The position of the tip of the so-called Bloch vector characterizes the actual state of the system. Here, the projection of the Bloch vector onto the axis through the two poles, the w-axis, gives the population difference $N_e - N_g$. Thus, any vector within the equatorial plane describes an equal superposition of both states. Additionally, the phase in the equatorial plane reflects the relative quantum phase ϕ between the two states.

If the system is manipulated by a radiation field with energy $\hbar\omega$, the Hamiltonian describing the time dynamics of the system is given by

$$\hat{H} = \frac{\hbar}{2}\begin{pmatrix} \delta & \Omega \\ \Omega & -\delta \end{pmatrix}, \tag{3.32}$$

where $\Omega = dE/\hbar$ is the coupling strength with d the dipole matrix element and E the electric field amplitude of the driving field; $\delta = \omega - \omega_0$ is the detuning from the two-level resonance, and $\hbar\omega_0$ is the energy difference between the two levels $|g\rangle$ and $|e\rangle$. In the following we will consider two ways to transfer population from an initially prepared system in state $|g\rangle$ to $|e\rangle$, depending on the specific choice of the values for Ω and δ.

3.4.2 Transitions with variable detuning: Rapid adiabatic passage

The first possibility in transferring population from $|g\rangle$ to $|e\rangle$ is to apply a radiation field with time varying detuning $\delta(t)$. The basic mechanism can be understood in the so-called dressed state picture, i.e. in a picture of eigenstates of the Hamiltonian (3.32), which are combined states of atom and radiation field; for further information see Refs. [61, 83, 84].

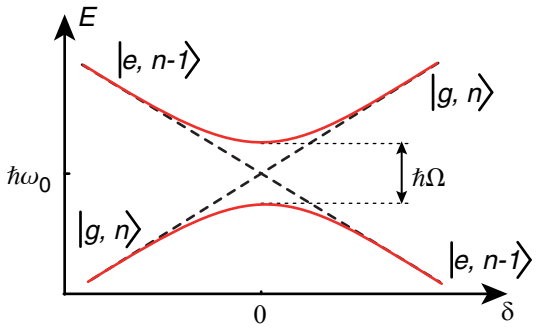

Figure 3.10: Energy diagram for a two-level system and a light field in the dressed state picture. The energy of $(n-1)$ photons has been subtracted on the energy axis. For no atom-field coupling, the energy of the dressed states is given by the dashed lines according to Eq. (3.34). For a coupling of strength Ω, an avoided crossing opens up, where the energy gap is given by Eq. (3.35).

The eigenenergies of the two eigenstates of Eq. (3.32) are given by

$$E = \pm\frac{\hbar}{2}\sqrt{\Omega^2 + \delta^2}. \tag{3.33}$$

The initial dressed state is $|g, n\rangle$, where the first entry in the state vector denotes the state of the atom, the second denotes the number of photons in the radiation field. If the atom absorbs a photon, it is transferred into the excited state, while one photon is missing in the radiation field. The corresponding dressed state is $|e, n-1\rangle$. In the absence of coupling $\Omega = 0$, the energy shift for the two dressed states is according to Eq. (3.33)

$$\Delta E_{g,e} = \pm\frac{\hbar\delta}{2}, \tag{3.34}$$

where the upper (lower) sign is for $|g, n\rangle$ ($|e, n-1\rangle$), see Fig. 3.10. If a coupling between these two dressed states is present (cf. Fig. 3.10), it leads to an avoided crossing, where the energy separation for $\delta = 0$ is according to (3.33) given by

$$\Delta E = \hbar\Omega. \tag{3.35}$$

As a consequence, starting from $|g, n\rangle$ with $\delta \ll -\Omega$ and increasing the detuning sufficiently slow to $\delta \gg \Omega$ results in an adiabatic following of the actual state of the system into the state $|e, n-1\rangle$ due to the avoided crossing (see Fig. 3.10). "Sufficiently slow" here means to be slow enough so that the system cannot intersect the avoided crossing. This adiabaticity condition can be written as

$$\frac{d}{dt}|\delta| \ll \Omega^2. \tag{3.36}$$

On the other hand, the passage must be fast enough so that no population can decay while the sweep is still in progress. But as the life-time of the hyperfine states in ^{87}Rb is much

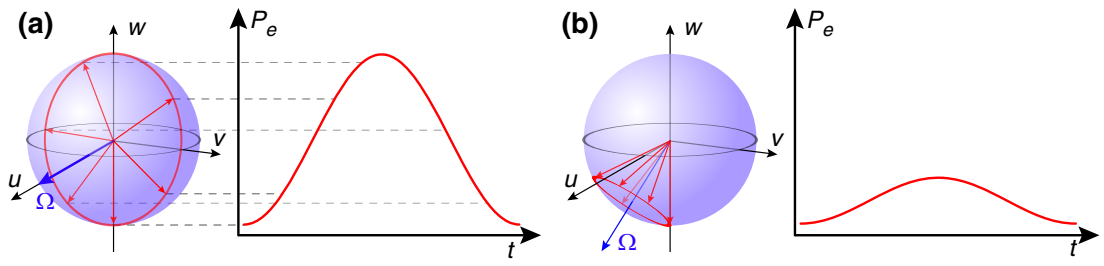

Figure 3.11: Rabi oscillations on the Bloch sphere and the correspondingly measured population of the excited state for the case of resonant excitation **(a)** or strongly detuned excitation **(b)**. The power has been adapted such that the oscillation frequency is the same for both cases.

longer than any other experimentally relevant time scale, this is in practice not a limiting factor. The combination of both requirements leads to the name *Rapid Adiabatic Passage* for this method. Also, in the literature it is often referred to as *Landau Zener transition* from the underlying theoretical model that describes this situation [83, 84].

3.4.3 Transitions on resonance: Rabi flopping

The second possibility to transfer population from $|g\rangle$ to $|e\rangle$ is by applying near-resonant radiation, i.e. $\delta \ll \Omega$ as introduced by I. Rabi [85]; in contrast to the previous situation, δ is constant in time. From Eq. (3.32), one can calculate the probability of exciting the two-level system from its ground state to the excited state to be

$$P_{|e\rangle}(t) = \left(\frac{\Omega}{\Omega'}\right)^2 \frac{1}{2} \left(1 - \cos(\Omega' t)\right), \tag{3.37}$$

where $\Omega' = \sqrt{\Omega^2 + \delta^2}$ is the effective Rabi frequency. The periodic population transfer which is described by Eq. (3.37) is called Rabi oscillation.

In the experiment, the coupling strength Ω can be adjusted by controlling the power of the radiation field. Transitions within the hyperfine manifold, as in our case, are highly electric dipole forbidden. Instead they are magnetic dipole transitions, which leads to a coupling strength Ω that is several orders of magnitude smaller than the coupling strength for dipole transitions. Typical values of the Rabi frequency for transitions $|f = 1, m = -1\rangle \rightarrow |f = 2, m = -1 + \Delta m\rangle$, $\Delta m = 0, \pm 1$ are $\Omega \approx 2\pi \times 5 \ldots 50\,\mathrm{kHz}$.

Controlling the time during which the microwave field is applied, enables us to perform pulses with well defined pulse area. In particular, for a general pulse area $\vartheta = \Omega' t$ and phase φ, the transformation matrix is given by

$$M[\vartheta, \varphi] = \begin{pmatrix} \cos\left(\frac{\vartheta}{2}\right) & e^{i\varphi} \sin\left(\frac{\vartheta}{2}\right) \\ -e^{-i\varphi} \sin\left(\frac{\vartheta}{2}\right) & \cos\left(\frac{\vartheta}{2}\right) \end{pmatrix}. \tag{3.38}$$

This transformation acts on the two-particle states

$$\begin{pmatrix} g \\ e \end{pmatrix} \equiv g\,|g\rangle + e\,|e\rangle. \tag{3.39}$$

In the literature there is often a difference between a $\pi/2$-pulse and a so-called Hadamard gate, which differ by a phase $\varphi = \pi/2$. For simplicity, we omit writing this phase of $\pi/2$ and assume pulses with $\varphi = 0$ if not otherwise noted. With this, the transformation matrices for a $\pi/2$-pulse and a π-pulse are represented by the matrices $M[\pi/2, 0]$ and $M[\pi, 0]$, respectively. It should be noted that Eq. (3.38) shows the correct behaviour for a rotation of $\vartheta = 2\pi$, reflecting the underlying symmetry group of $SU(2)$ rather than the group for spatial rotations, $SO(3)$.

Applied to a usual experimental situation, starting from a spin-polarized sample in $|f = 1, m = -1\rangle$, a $\pi/2$-pulse with the correct frequency will prepare the system in a coherent superposition of for example $1/\sqrt{2}\,(|f = 1, m = -1\rangle - |f = 2, m = 0\rangle)$, whereas a π-pulse will transfer all atoms into the $f = 2$ state. The pulse area can be controlled on a percent level. Additionally, the phase φ of the microwave radiation can be controlled to a high degree. That enables us to perform Ramsey type interferometer sequences.

3.4.4 Ramsey interferometry

An important tool to exploit the coherence of atomic systems for precision measurements, e.g. to measure acceleration and rotation or to construct precise frequency standards, is atom interferometry (for a review see Ref. [86] and references therein). The backbone of atom interferometry is the Ramsey method of separated oscillatory fields [87]. Before the invention of this method, precision measurements on atomic beams were done by making use of the Rabi method [85]. Thereby, an atomic beam was sent through a region of well defined homogeneous magnetic field, and on a certain atomic transition Rabi flopping was driven. The measured frequency was used for example as a signal to determine the precise transition frequency. In order to increase precision, the interaction region had to be extended, as more oscillation periods correspond to a better frequency resolution. However, it became technically increasingly difficult to control the homogeneity of the magnetic fields sufficiently well in order to obtain a higher resolution. This problem could be overcome by Ramsey's famous method of two separated oscillatory fields, where a very homogeneous field had only to be present in two small interaction zones, whereas the space between those two regions could be field free.

In our case, we use an adopted method as our sample is stationary in space. The experiments presented in the following start with a polarized sample to which a $\pi/2$-pulse is applied, i.e. a radiation field is switched such that the atoms are prepared in a coherent superposition of two internal states. The atomic state after this pulse according to (3.38) reads

$$|\psi\rangle_{\text{initial}} = |g\rangle \xrightarrow{\pi/2} |\psi'\rangle(0) = \frac{1}{\sqrt{2}}\,(|g\rangle - |e\rangle)\,, \tag{3.40}$$

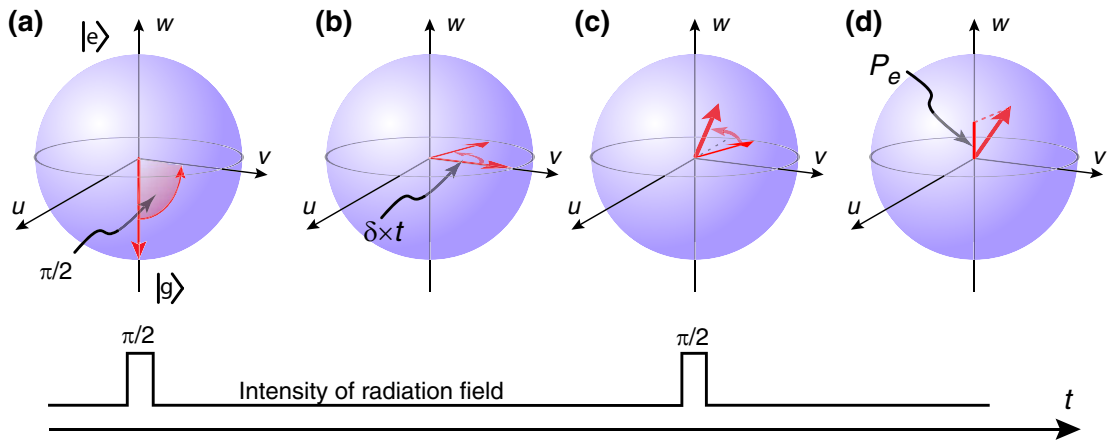

Figure 3.12: Ramsey method:**(a)** Starting from a spin polarized sample in the internal state $|g\rangle$, a first $\pi/2$ pulse prepares a coherent superposition where the Bloch vector lies in the equatorial plane **(b)**. During a wait time t the relative phase evolves, for example due to a detuning δ between the external radiation field and the transition frequency of the atom, **(c)**. A final $\pi/2$-pulse is used to read out this phase evolution by mapping the phase onto the population of the two internal states **(d)**.

where we have set the phase of the first pulse $\varphi = 0$ without loss of generality, as this only determines an arbitrary orientation of the Bloch sphere itself. This first pulse rotates the Bloch vector of each atom into the equatorial plane, see Fig. 3.12(a). Subsequently the system evolves for a time t. This corresponds[2] to a precession of the Bloch vector in the equatorial plane with the rotation frequency δ. During the wait time, the atomic Bloch vector has thus collected a phase $\phi = \delta t$ compared to the microwave field (Fig. 3.12(b)) and the state after the evolution reads

$$|\psi'\rangle(t) = \frac{1}{\sqrt{2}}\left(|g\rangle - e^{-i\delta t}|e\rangle\right). \tag{3.41}$$

The relative phase can finally be read out by a second $\pi/2$-pulse with phase α, mapping the relative phase between the spin states onto the populations of the internal states, see Fig. 3.12(c). Depending on the relative phase between the atomic Bloch vector and the radiation field, the Bloch vector is rotated to different positions on the Bloch sphere. The final state $|\psi_{\text{final}}\rangle$ created by the last $\pi/2$-pulse reads

$$|\psi_{\text{final}}\rangle = \frac{1}{2}\left(\left[1 - e^{-i\delta t + i\alpha}\right]|g\rangle - \left[e^{-i\alpha} + e^{-i\delta t}\right]|e\rangle\right), \tag{3.42}$$

where the microwave phase α cannot be neglected anymore. A subsequent measurement of the population in one of the two internal states (Fig. 3.12(d)) therefore yields a relative

[2]In this Bloch-sphere picture a rotating frame has been adopted.

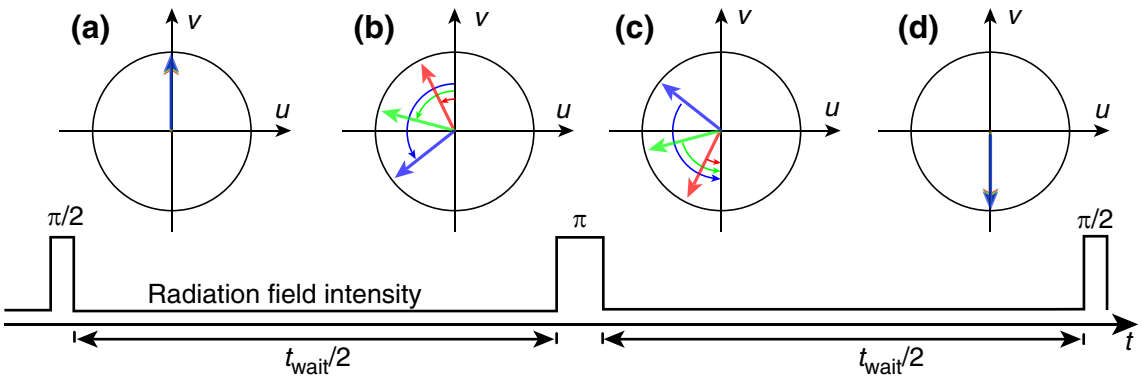

Figure 3.13: Spin echo sequence in an ensemble where individual particles (with red, green and blue Bloch vectors) experience different detunings. **(a)** Directly after a first $\pi/2$-pulse, all Bloch vectors point in the equatorial plane along the v-direction. **(b)** Different detunings cause the Bloch vectors to acquire different phases during the wait time $t_{\mathrm{wait}}/2$. **(c)** A π-pulse causes each Bloch vector to perform one half rotation around the u-axis of the Bloch sphere until it ends again in the equatorial plane, effectively mirroring each vector on the u-axis. **(d)** The subsequent time evolution with different detuning leads to a re-phasing of all Bloch vectors after another time interval $t_{\mathrm{wait}}/2$. The final $\pi/2$-pulse therefore rotates all vectors to one common position on the sphere.

population in the excited state

$$P_e = |\langle e|\psi_{\mathrm{final}}\rangle|^2 = \frac{1}{2}\Big(1 + \cos(\alpha - \delta\, t)\Big). \tag{3.43}$$

This gives the form of a so called Ramsey fringe, where the measured population is an oscillating function of (i) the detuning, (ii) the time for a given non-zero detuning, and (iii) the phase of the last microwave pulse. In the experiments presented here, the time separation t often is the interaction time which must be varied independently in order to control the atom-atom interaction. Instead, the detuning δ is set to zero and Ramsey fringes are obtained by scanning the phase α of the final $\pi/2$-pulse.

The recorded fringe can be affected by several mechanisms. First, spatial inhomogeneities might lead to a spatially varying detuning. In an ensemble measurement Ramsey fringes with different phases are therefore added which leads to decreased contrast of the signal. Second, a fringe is recorded by performing a number of measurements with different phases α. If for different measurements the detuning changes over time, for example due to varying magnetic fields, the phase of the Ramsey fringe acquires a random contribution which leads to noise in the final signal.

The effect of spatial inhomogeneities can be canceled by a single particle spin-echo technique. Here, the sequence is split into two parts, where after the first $\pi/2$-pulse a waiting time $t_{\mathrm{wait}}/2$ is introduced. During this time, at different positions of the system, local phases $\delta(r)\,t$ have been acquired as shown in Fig. 3.13(b). Subsequently a π-pulse is applied that

exchanges the roles of the two internal states $|g\rangle \leftrightarrow |e\rangle$. In the Bloch sphere picture the π-pulse effectively mirrors each Bloch vector with respect to the u axis and transforms each phase $\delta\, t_{\mathrm{wait}}/2 \rightarrow \pi - \delta\, t_{\mathrm{wait}}/2$. During a second waiting time $t_{\mathrm{wait}}/2$ the same phase $\delta(r)\, t$ is acquired. The Bloch vectors thus re-phase after this second wait time at the common phase $\phi = \pi$ in the equatorial plane (see Fig. 3.13(d)). A final $\pi/2$-pulse can therefore rotate the Bloch vectors of all particles onto a common final position on the Bloch sphere. This method allows to compensate for time constant inhomogeneities in the experimental realization of Ramsey spectroscopy, which can play an important role due to the overall confinement of the optical potential or magnetic field gradients.

3.4.5 Two-photon transitions

Although in principle any polarized spin state can be prepared by the two methods introduced above, sometimes it is necessary to create coherent superpositions between two internal states that cannot be coupled by a single photon transition due to conservation of angular momentum. This is for example the case for the two states $|\psi_i\rangle \equiv |f = 1, m = +1\rangle$ and $|\psi_f\rangle \equiv |f = 2, m = -1\rangle$. Here the transition requires $\Delta m = -2$, while a photon can only carry a single quantum of angular momentum. Therefore this transition can only be driven by a two-photon transition, where two radiation photons together fulfill the condition for the transition. In particular, energy conservation requires

$$\hbar(\omega_1 + \omega_2) = \hbar\omega_0, \tag{3.44}$$

where ω_0 is the transition frequency between the two states of interest, and ω_i is the frequency of the radiation field i. Those two frequencies cannot be chosen arbitrarily, as for very large detuning from any atomic transition the effect on the atom will be negligible. Therefore the frequencies have to be chosen close to a transition to some intermediate state $|\mathrm{aux}\rangle$. In order not to drive the single photon transition to $|\mathrm{aux}\rangle$, the detuning from the intermediate state Δ has to be chosen sufficiently large. Then, the system can again be considered as a coupled two-level system with an effective coupling strength, i.e. two-photon Rabi frequency, of

$$\Omega_{2\mathrm{photon}} \propto \frac{\Omega_1\, \Omega_2}{4\Delta}, \tag{3.45}$$

where Ω_i denotes the single-photon Rabi frequency of radiation field i for the single photon transition.

3.5 Experimental sequence for spinor quantum gases in optical lattices

The apparatus used for BEC creation and subsequent loading into a periodic potential has been described in detail elsewhere [57, 58, 88]. Therefore this section will only briefly summarize the main steps on the way to a degenerate spinor gas in optical lattices. It is interesting to note that a single realization in total takes about 55 s, from the beginning of

the first laser cooling stage to the final, destructive image of the ultracold atom cloud. For each change of parameters, a new sample has to be prepared.

3.5.1 Bose-Einstein condensate

The present apparatus consists of a two-chamber vacuum system, separated by a differential pumping stage. In the first chamber with a gas pressure of $\approx 10^{-10}$ mbar, about 10^9 ^{87}Rb atoms are captured in a standard six-beam magneto optical trap (MOT) from the background gas in 15 s. The atoms are optically pumped into the $|f = 1, m = -1\rangle$ hyperfine state, which is magnetically trappable, and subsequently loaded into a pure magnetic quadrupole trap. By making use of a magnetic conveyor belt setup [88], the magnetic trap minimum is shifted into the second part of the vacuum chamber within ≈ 3 s. This second chamber has a pressure roughly one order of magnitude smaller than the MOT chamber. After transport, the atoms are transferred into a quadrupole-Ioffe configuration (QUIC) magnetic trap [55] which leads to a cigar shaped trap geometry with trapping frequencies of axially $\omega_{\mathrm{ax}} = 2\pi \times 15$ Hz and radially $\omega_{\perp} = 2\pi \times 120$ Hz.

There, radio-frequency (rf) forced evaporation cooling [60, 62, 63] provides the last step on the way to BEC, taking about 30 s. This cooling stage results in an atomic sample of up to 5×10^5 atoms in a quasi-pure BEC in the magnetic trap. As for further experiments the anisotropy of the QUIC trap is unfavorable, a homogeneous magnetic offset field of ≈ 150 G is ramped up within $0.7 \ldots 1$ s along the weak axis of the QUIC trap, thereby releasing the confinement along the radial axes without exciting sloshing motions of the BEC. The resulting combined potential is an almost isotropic trap with trapping frequencies around $\omega_{\mathrm{mag}} \approx 2\pi \times 12$ Hz.

3.5.2 3D optical lattice potential

In order to adiabatically load the sample into a periodic lattice potential, up to three pairs of counter propagating laser beams are superimposed onto the BEC. The beams are all derived from a common laser source[3] which has a tunable wavelength around 840 nm. The resulting standing waves are mutually orthogonal and have orthogonal polarizations to avoid cross interference between the standing waves. In addition, the orthogonal standing waves are artificially detuned by several tens of MHz in order to average any residual interference pattern on a time scale of a few tens of nano seconds.

The intensity of the laser beams is slowly increased by an active stabilization in order to avoid any excitation in the system, especially population of higher vibrational bands. The ramps have either an exponentially rising form [1, 57], or an s-shape, specifically calculated in order to minimize residual perturbations [89]. The ramps typically last between 160 ms and 320 ms; the time constant of the exponential rise is usually $\tau \approx 40 \ldots 80$ ms; cf. Ref. [90]. For most experiments, the final light intensity can be on the order of a few hundred

[3] Coherent MBR Ti:Sa laser pumped by a Coherent Verdi V18, or Coherent 899 Ti:Sa ring laser pumped by Coherent Verdi V10

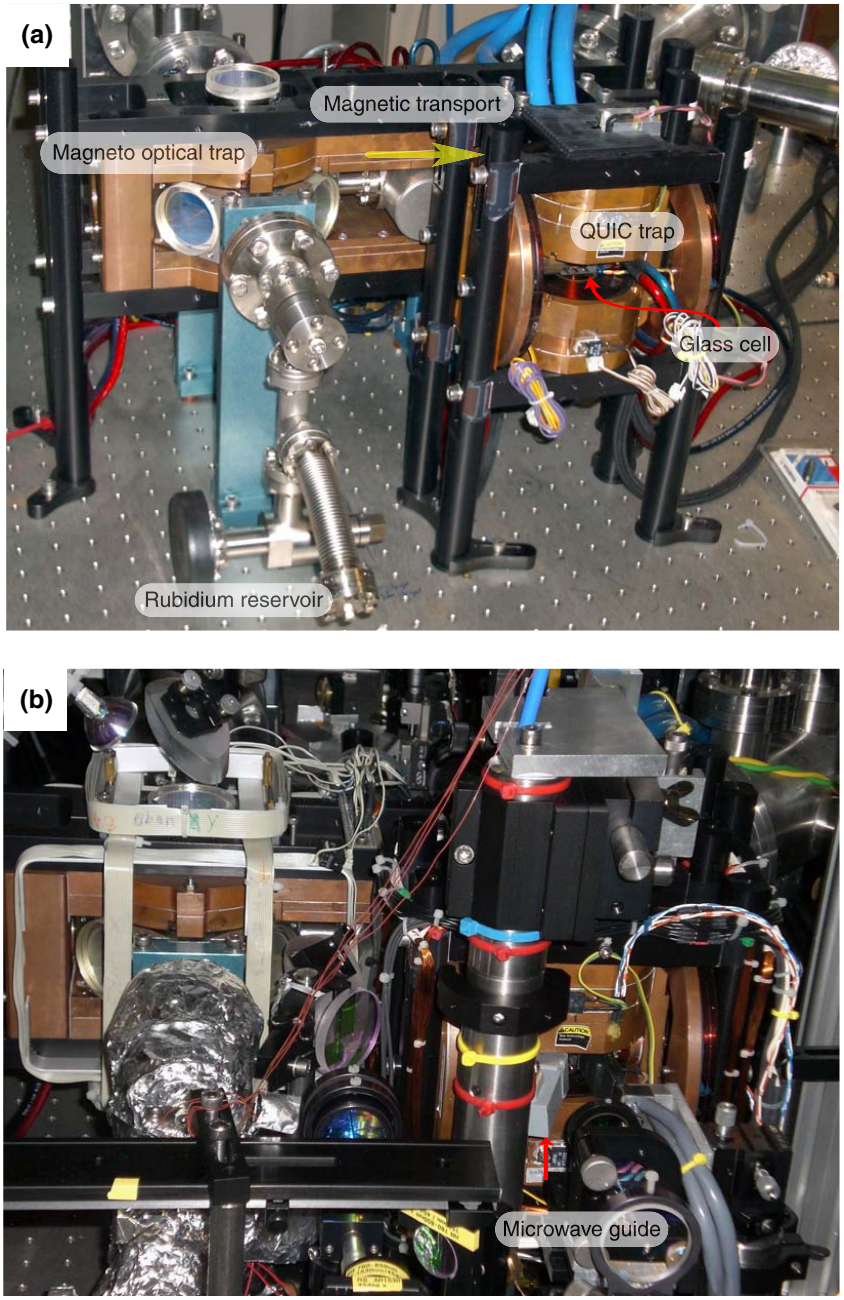

Figure 3.14: Experimental setup, **(a)** with optics removed and **(b)** with optics and further electronics. Atoms from a Rubidium reservoir diffuse into the magneto optical trap (left), where they are cooled by laser colling and subsequently transfered into a pure magnetic trap. A "magnetic conveyor belt" [88] transports them into a glass cell (right), where they are loaded into a QUIC trap [55]. There rf-forced evaporation creates a BEC. Laser beams can be applied from three perpendicular directions onto the BEC. In addition, a wave guide is installed to drive microwave transitions between different hyperfine states.

Milliwatts per axis, which for our beam waists of $\bar{w} \approx 130\,\mu$m corresponds to a maximum lattice potential depth of up to $60\,E_r$, deep within the MI regime.

For these parameters, in particular for total atom numbers between 2×10^5 and 3×10^5, the MI system is expected to exhibit a shell structure [76, 91, 92, 93], where approximately half of the atoms are trapped in a central core at lattice sites with double occupancy. They are surrounded by a shell of isolated atoms (see Refs. [94, 12] and references therein for the numerical model). Due to the deep lattice, tunneling is well suppressed. For a $40\,E_r$ lattice the tunneling matrix element is on the order of $J/\hbar \approx 2\pi\times30\cdot10^{-3}$ Hz, whereas typical spin-dependent interaction energies investigated below are well above $U_{\mathrm{spin}}/\hbar \approx 2\pi\times10$ Hz. Moreover, the spatial degree of freedom in the trap is also frozen, because the next higher lying vibrational level has a frequency of $\omega_{v=1} \approx 2\pi\times40$ kHz; therefore the typical interaction energy ($U/\hbar \approx 2\pi\times3$ kHz) cannot excite atoms to higher vibrational states. This is a convenient situation to study interaction phenomena in a very controlled situation.

3.5.3 Spin sensitive detection

After the system has been manipulated and possibly has interacted for a certain time, the quantum state of the ultracold atomic sample has to be detected. This is done by standard absorption imaging, see e.g. Ref. [95]. For that, all traps are switched off, and the atomic cloud can fall due to gravity and expand for a certain time-of-flight (TOF), usually between 10 ms and 16 ms. Subsequently, a light pulse resonant to the D_2 transition between the hyperfine states $f = 2 \rightarrow f' = 3$ is applied for approximately $70\,\mu$s, and the shadow of the atomic cloud is imaged by a CCD camera[4] as indicated in Fig. 3.15(a). Typical images are displayed in Fig. 3.15(b-d). The imaging involves scattering of many resonant photons, which heats the sample and destroys the quantum state. Therefore, each specific realization can be imaged only once; for another set of parameters the experimental cycle of approximately 55 s has to be repeated.

As the imaging pulse is only seen by the $f = 2$ hyperfine state, for the detection of the $f = 1$ state, an additional laser beam has to be applied, resonant to the D_2 $f = 1 \rightarrow f' = 2$ transition. Turning this additional laser beam on or not allows to discriminate detection of either only atoms in $f = 2$ or all atoms, respectively. In order to detect the relative atom number in $f = 2$ of one atomic sample, both the atom number in $f = 2$ and the total atom number have to be measured shortly after each other. This is done on two different cameras along two different spatial axes, one for the $f = 2$ atom number and the other for the total atom number. As for each imaging axis the projection of the light polarization onto the magnetic field axis is different, the same "real" atom number leads to two slightly different measured numbers of the two cameras. This results in relative atom numbers slightly different from unity. This can be compensated for by taking images of atom clouds with the same atom number. From the statistics of the atom numbers measured on the two cameras the correction factor can be inferred. For the cases presented here, the factor between the atom number in $f = 2$ $N_{f=2}$ and the total atom number N_{tot}

[4] The camera types used are Andor IXON and Apogee AP1E

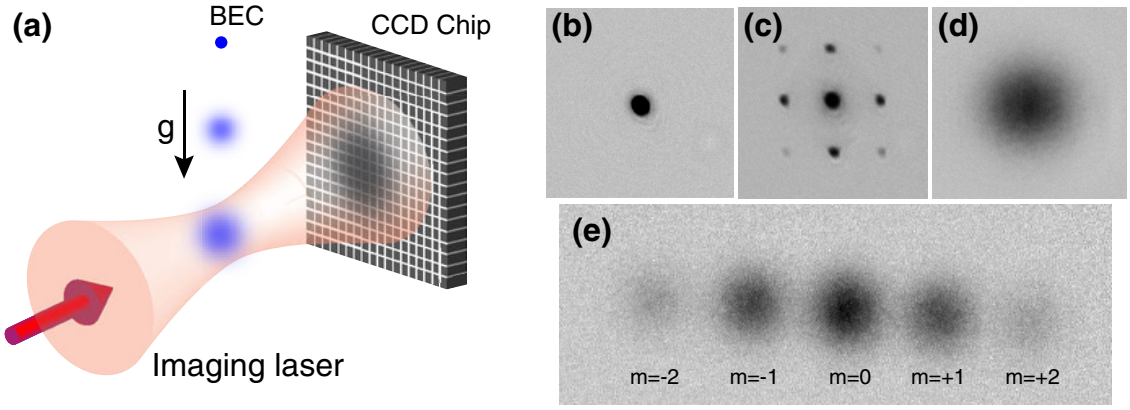

Figure 3.15: **(a)** Sketch of imaging procedure by absorption in the experiment and typical images of **(b)** a BEC, **(c)** a SF 3D lattice at $6\,E_r$, and **(d)** a MI at $25\,E_r$. If a magnetic field gradient is applied during TOF, clouds with different magnetic moments can be spatially separated **(e)**, as shown here for the $f = 2$ hyperfine state. The field gradient is slightly tilted with respect to the horizontal plane.

measured on another camera is 1.06(3). This factor has been included in the images of the Rabi oscillations shown in Figs. 3.16 or 3.17.

In order to distinguish different Zeeman sublevels, during the first 3 ms of TOF a magnetic field gradient is applied which exerts a force onto the atoms that depends on the magnetic sublevel, similar to the historical Stern-Gerlach experiment [96]. Thereby clouds of different magnetic moments are separated after TOF and can be imaged independently. A typical camera picture with all Zeeman sublevels in $f = 2$ populated is depicted in Fig. 3.15(e). This allows for the quantitative detection of any internal state in the hyperfine ground states of ^{87}Rb.

3.5.4 Addressing the spin

Due to the magnetic trap, only the $|f = 1, m = -1\rangle$ state is present in the combined optical and magnetic potential. Therefore all magnetic fields are switched off after the lattice ramp has reached the final potential depth. Only a small ≈ 1 G magnetic offset field is preserved in order to maintain spin polarization of the atomic sample. The magnetic field is switched within a few milliseconds, but it needs several 10 ms until residual transients have decayed to below ≈ 10 mG. In practice, homogeneous magnetic fields are created by currents running through coils that are approximately in Helmholtz configuration. The absolute value of the magnetic field is measured by driving single photon transitions between $f = 1$ and $f = 2$ at low power ($\Omega_{\mu W} \leq 2\pi \times 100$ Hz) and calculating from the measured transition frequency the magnetic field value via the Breit-Rabi formula [97].

In order to drive transitions between the hyperfine ground states, a microwave field with a frequency close to 6.8 GHz – the hyperfine splitting of the ^{87}Rb ground state – is radiated from a hollow wave guide. As this wave guide is not matched to the impedance of free space,

just a fraction of the initially injected 10 W is in fact radiated upon the atom cloud; the rest is reflected from the wave guide. Additionally, the contributions of the various polarizations in the field are not well known, as the wave guide is placed at a distance to the atoms that is neither clearly in the near field nor in the far field. Moreover, when the magnetic field value changes between different realizations of the experiment, the magnetic field axis can also change direction. Hence the projection of the different polarization components onto the magnetic field axis can change. Therefore the coupling strength of the microwave transitions is calibrated for one specific experimental realization by driving single-particle Rabi oscillations on the various transitions and the Rabi frequency is determined according to Eq. (3.37).

Single photon Rabi oscillations

Typical Rabi oscillations used in order to calibrate the microwave pulse duration are shown in Fig. 3.16. This enables for example the state preparation of all atoms in $|f = 1, m = 0\rangle$

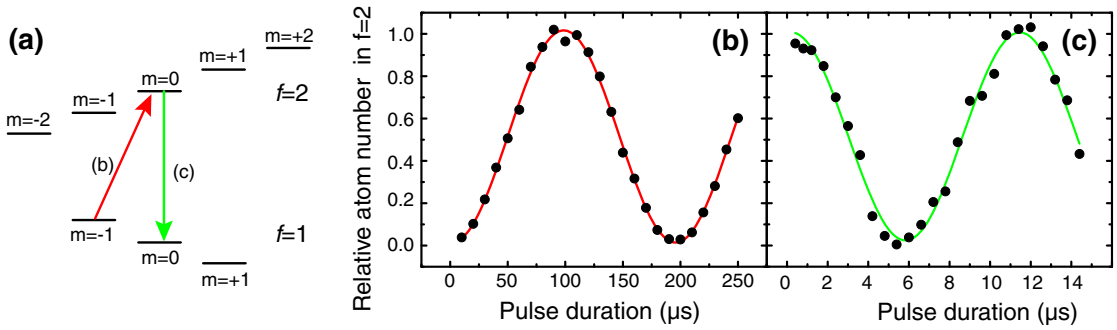

Figure 3.16: Rabi oscillations for two transitions in the hyperfine ground states of ^{87}Rb indicated in the scheme **(a)** at a magnetic field of 1.2 G. The σ^--transition $|f = 1, m = -1\rangle \rightarrow |2, 0\rangle$ **(b)** has a transition frequency of 6.833832(3) GHz and a coupling strength of $\Omega \approx 2\pi \times 5.1$ kHz. The π-transition $|f = 2, m = 0\rangle \rightarrow |1, 0\rangle$ **(c)** is resonant for a frequency of 6.834683(1) GHz and has a Rabi frequency of $\Omega \approx 2\pi \times 89$ kHz for maximum micro wave powers.

starting from $|1, -1\rangle$ by application of a microwave pulse on the first transition (Fig.3.16(b)) for $\approx 97\,\mu$s and a subsequent pulse on the second transition (Fig. 3.16(c)) for $5.7\,\mu$s.

Two-photon Rabi oscillations

As pointed out before, for some experiments it is necessary to coherently couple two internal states that differ by two quanta of angular momentum. This can be done by a two-photon transition. Such a transition coupling the two states $|f = 1, m = +1\rangle$ and $|2, -1\rangle$ is shown in Fig. 3.17(b). Here, the microwave field is detuned from the single-photon transition to $|2, 0\rangle$ by 130 kHz and an additional radio frequency (rf) field is applied at a frequency

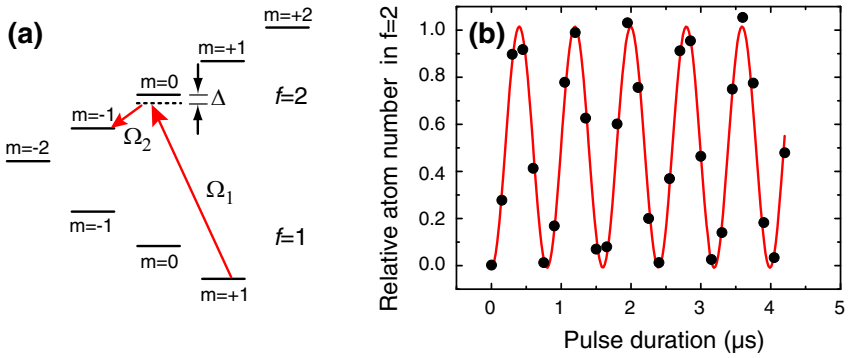

Figure 3.17: Two photon Rabi oscillations between the hyperfine ground states as indicated in **(a)** at a magnetic field of $B = 9.13\,G$. The oscillations are driven by a combined microwave and rf-field with frequencies of 6.841020 GHz and 6.275 MHz, respectively, which corresponds to a detuning of $\Delta = -130\,\mathrm{kHz}$ from the intermediate state. The effective two-photon Rabi frequency is $\Omega_{2\mathrm{photon}} \approx 2\pi \times 1.25\,\mathrm{kHz}$ for full powers of the microwave and rf-radiation field.

around 6 MHz, corresponding to the linear Zeeman splitting between the $|2,0\rangle$ and $|2,-1\rangle$ states. Thereby we reach effective coupling strengths of $\Omega_{2\mathrm{photon}} = 2\pi \times 1.25\,\mathrm{kHz}$.

Rapid adiabatic passage

In order to populate the initial state $|1,+1\rangle$ starting from $|1,-1\rangle$, a rapid adiabatic passage is performed, similar to the scheme explained in Section 3.4.2. In the case presented here, however, there are three levels present. This situation can be considered as a combination of two two-level systems that are nearly degenerate for low magnetic fields. Therefore, a single sweep allows to transfer population from $|1,-1\rangle$ via $|1,0\rangle$ to $|1,+1\rangle$ at a magnetic field of $B \approx 1\,\mathrm{G}$ by sweeping the rf frequency linearly within 10 ms from 380 kHz to 1.08 MHz. The resulting population transfer efficiency is typically above 95% .

4 Coherent spin changing collisions

After degenerate quantum gases had been loaded into optical traps, one of the first observations was that an initially spin polarized sodium BEC loaded into a dipole trap could show the formation of domains when the trapped sample could evolve freely over time [98]. Since then many fascinating spin changing phenomena have been observed and proposed. In particular, ultracold atomic samples with liberated spin degree of freedom have been seen to exhibit a rather intricate spin dynamics [99, 100, 101] and can lead to spin mixing [102, 103], spin-segregation [70] and spin waves [71, 104].

The underlying mechanism of these phenomena is a coherent interaction between two atoms which changes the individual spins of the colliding particles while preserving the total magnetization [22, 46, 105, 106, 107], see Fig. 4.1. This interaction is described by a unitary Hamiltonian. Despite this fact, the coherent nature of the interaction driven time evolution has for a long time eluded direct observation. The reason for this is that in many BEC experiments, dynamics and excitations of the spatial degree of freedom can perturb the spin dynamics signature. In the interpretation of many spin dynamics experiments with BECs, a single-mode approximation is proposed, which assumes a time-independent common wave function for all spin-components. However, the spin dependent interaction energy is rather small compared to the usual mean field energy (a few percent, as will be explained later). Therefore the time scale on which the spin mixing signal occurs is rather long compared to typical time scales on which mean field driven effects evolve. These effects can lead to a breakdown of the single mode approximation and make an interpretation therefore ambiguous. Independently from the work presented in this chapter, other groups have recently observed the coherent nature of the spin changing interaction in a BEC by exploiting the Bosonic-enhancement factor when working with a macroscopic sample of atoms [108, 109].

The experiments described in the following pursue a different approach. In an optical lattice, atom pairs can be trapped in the vibrational ground state of individual lattice sites. Due to the tight confinement, they are isolated from the environment as the tunnel energy can be suppressed to a small value compared to the spin-dependent interaction strength. Moreover, the next vibrational level on a lattice site is energetically so high that no interaction energy can vibrationally excite the system. Consequently, at each lattice site only the spin-dependent interaction causes the ensuing time evolution and can be studied in a very controlled way, thus forming a micro-laboratory for a single atomic pair.

This chapter focuses on the fundamental spin changing mechanism, which we observe through coherent spin population oscillations. Moreover many promising applications have come into reach due to the high level of control over the spin changing interaction. Section

4.1 introduces the fundamental mechanism of spin changing collisions and the resulting collisionally induced Rabi-oscillations between spin population states in an optical lattice. A detailed description of the experimental sequence is presented in Section 4.2. In Section 4.3 the main experimental results are discussed for both ^{87}Rb hyperfine states, and the relevant parameters characterizing the spin-dependent interaction are deduced. Those parameters are derived from differences of fundamental s-wave scattering lengths, which can be inferred from the spin oscillation frequency with high precision[1]. Moreover, a method to tune and switch the interaction in a convenient way based on the *AC-Zeeman effect* is presented in Section 4.4[2].

Furthermore, the differences of scattering lengths also have wide reaching implications on the magnetic state of the system. In a many-particle system, the spin dependence of the scattering potential leads to a spin-dependent interaction energy. The spin configuration which minimizes this energy at zero magnetic field is energetically favoured and is called the magnetic ground state of the system. Section 4.5 describes how the precise determination of the collisional coupling constants can identify the magnetic ground states of spin-1 and spin-2 ^{87}Rb ground state atoms. Finally, two applications that have been realized based on the spin-changing interaction mechanism are outlined in Section 4.6, namely the observation of number squeezing in the SF to MI transition and the observation of spatial shell structures in the inhomogeneous MI.

4.1 Theory of coherent collisional spin dynamics

4.1.1 Spin changing collisions in optical lattices

Let us consider two colliding ^{87}Rb atoms of spin-f, initially in the single-particle Zeeman states with magnetic quantum numbers m_1 and m_2. The particles can undergo a spin changing collision and be tranferred into a final state characterized by the quantum numbers m_3 and m_4 (see Fig. 4.1a). In binary collisions between alkali atoms the total spin projection on the quantization axis is conserved [22, 102, 103, 105], which implies $m_1 + m_2 = m_3 + m_4$. This limits the number of accessible final scattering states after a collision to those that have the same total magnetization as the initial one. For two colliding spin-f particles, the interaction strength is characterized by $2f$ independent scattering lengths a_F, labeled by the total coupled spin F of the two particles. For bosons (fermions) the total spin F takes even (odd) values between 0 and $2f$. Following the discussion in Section 2.3 the interaction

[1] The first three sections are mainly based on two publications:
A. Widera, F. Gerbier, S. Fölling, T. Gericke, O. Mandel and I. Bloch. Coherent collisional spin dynamics in optical lattices. *Phys. Rev. Lett.* 95, 190405 (2005).
A. Widera, F. Gerbier, S. Fölling, T. Gericke, O. Mandel and I. Bloch. Precision measurements of spin-dependent interaction strengths for spin-1 and spin-2 ^{87}Rb atoms. *New J. Phys.* 8, 152 (2006).

[2] This section is based on
F. Gerbier, A. Widera, S. Fölling, O. Mandel and I. Bloch. Resonant control of spin dynamics in ultracold quantum gases by microwave dressing. *Phys. Rev. A* 73, 041602(R) (2006).

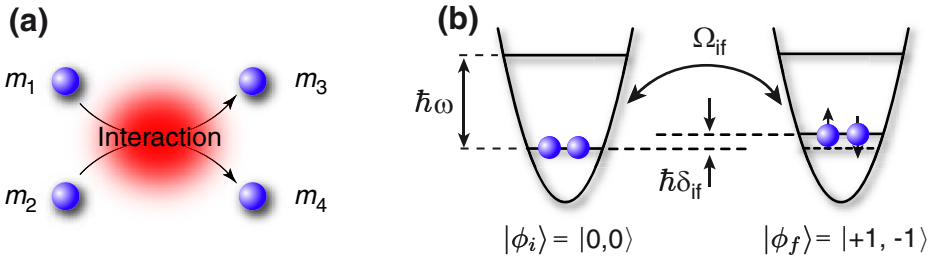

Figure 4.1: Sketch of a spin-changing collisional event. **(a)** Two atoms with magnetic quantum numbers m_1 and m_2 undergo a collisional event which they leave with quantum numbers m_3 and m_4, respectively. **(b)** An atom pair trapped in the vibrational ground state of a deep potential well oscillates between the two-particle states $|f = 1, m = 0; f = 1, m = 0\rangle$ and $|f = 1, m = +1; f = 1, m = -1\rangle$ due to the spin-changing interaction. As the spatial wave function is frozen due to the tight confinement, the interaction only affects the spin wave function.

can be described by a potential of the form [22]

$$V(\mathbf{r}_1 - \mathbf{r}_2) = V_s\,\delta(\mathbf{r}_1 - \mathbf{r}_2) = \sum_{F=0}^{2f} g_F\,\mathcal{P}_F\,\delta(\mathbf{r}_1 - \mathbf{r}_2)\,, \tag{4.1}$$

where $g_F = (4\pi\hbar^2/M)\,a_F$, M is the mass of one atom, $\mathcal{P}_F$ is the projection operator onto the subspace of total spin F, a_F is the s-wave scattering length for two atoms colliding in such a channel with total spin F, and $\hbar = h/2\pi$, with h Planck's constant. For more details, see Appendix A.

In a deep three-dimensional periodic potential as in the case presented here (see Section 4.2), the situation can be adjusted such that at many ($\sim 10^5$) lattice sites there are two atoms trapped in the vibrational ground state of the potential. Throughout the following discussion we assume a sufficiently deep potential such that the atoms can neither leave the trap nor be excited via interactions into a higher vibrational state. Consequently, the atoms remain in the lowest vibrational state at all times. Because the spatial dynamics is frozen, the ensuing dynamics caused by spin-dependent interactions only affects the spin component of the two-particle wavefunction. To describe this collisional dynamics, we write two-particle atomic wavefunctions in the form

$$|\Phi\rangle \equiv |\phi_0\rangle_1 |\phi_0\rangle_2 \otimes \mathcal{S}|f, m; f, m'\rangle. \tag{4.2}$$

Here $1, 2$ labels the two atoms in the pair, $\mathcal{S}$ is the symmetrization operator, $|\phi_0\rangle$ is the spatial wavefunction corresponding to the vibrational ground state in each well. Also $|f, m; f, m'\rangle$ denotes the (unsymmetrized) two-particle spin wavefunction. In the following we describe the atom pair by its spin wavefunction only. With this notation, the interaction potential (4.1) connecting an initial two-particle state $|f, m_1; f, m_2\rangle$ with a final two-particle state $|f, m_3; f, m_4\rangle$ can be written as (see Appendix A)

$$\langle f, m_3; f, m_4|V|f, m_1; f, m_2\rangle = \tilde{U} \times \Delta a^{m_3,m_4}_{m_1,m_2}, \tag{4.3}$$

where the "specific interaction strength" $\tilde{U}$ and the effective scattering length difference Δa are given by

$$\Delta a_{m_1,m_2}^{m_3,m_4} = \sum_{F=0}^{2f} \sum_{m=-F}^{F} \langle f, m_3; f, m_4 | F\ M\rangle \langle F\ M | f, m_1; f, m_2\rangle\, a_F \tag{4.4}$$

$$\tilde{U} = \frac{4\pi\hbar^2}{M} \times \int d^3r\, |\phi_0|^4. \tag{4.5}$$

Here, $\Delta a_{m_1,m_2}^{m_3,m_4}$ is given by a difference of the scattering lengths a_F weighted by the relevant Clebsch-Gordan coefficients $\langle f, m_3; f, m_4 | F\,, m\rangle$ connecting the initial and final spin states through an intermediate, coupled spin state $|F\,, m\rangle$. The prefactor $\tilde{U}$ contains all constants and the spatial wavefunction overlap. As explained in Section 3.3, it can be calculated as

$$\tilde{U} = \tilde{U}_{\mathrm{HO}} + \tilde{U}_{\mathrm{anharm}} + \tilde{U}_{\mathrm{int}}, \tag{4.6}$$

where $\tilde{U}_{\mathrm{HO}}$ is calculated by approximating the lattice potential by a harmonic well around each potential minimum, and by using the lowest harmonic oscillator eigenfunction as ϕ_0. For our case there are two possibly relevant corrections. First, using Wannier functions from a band structure calculation for the wave function ϕ_0 instead of a Gaussian yields a negative correction term $\tilde{U}_{\mathrm{anharm}}$ which is on the order of 5% of $\tilde{U}_{\mathrm{HO}}$. Second, at short distances the spatial wave function of the colliding particles is expected to deviate from the product form in (4.5). A recent theoretical investigation indicates that this deviation introduces a positive correction $\tilde{U}_{\mathrm{int}}$ amounting to $\sim 3\%$ of $\tilde{U}_{\mathrm{HO}}$ [81]. We have experimentally measured a value for the prefactor $\tilde{U}$ by observing the collapse and revival of the coherent matter-wave field [110][3]. We measure values of $\tilde{U}$ consistent with calculated values including only the correction due to the anharmonicity $\tilde{U}_{\mathrm{anharm}}$. Hence, the actual values we use in the following include the first correction term $\tilde{U}_{\mathrm{anharm}}$, but not the second $\tilde{U}_{\mathrm{int}}$. The values are $\tilde{U} = 2\pi \times (30.4 \pm 1.1)\,\mathrm{Hz}/a_{\mathrm{B}}$ for a lattice depth of $40\,E_r$, and $\tilde{U} = 2\pi \times (33.0 \pm 1.4)\,\mathrm{Hz}/a_{\mathrm{B}}$ for $45\,E_r$. Here a_{B} is the Bohr-radius and E_r is again the single photon recoil energy. The error is given by our uncertainty in optical potential depth, for which we assumed an upper bound of 10%, but a possible additional systematic error of $\tilde{U}$ due to the correction $\tilde{U}_{\mathrm{int}}$ is not explicitely given.

4.1.2 Two level system

In the experiments described below (see cases a-c in Figure 4.2), we prepare all atom pairs in the lattice in a specific spin state $|\psi_i\rangle$. This initial state is in general coupled to one or several final states $|\psi_f\rangle$ by the spin-changing interaction. In the simplest cases, where the atom pair is initially prepared in $|1, 0; 1, 0\rangle$ (Figure 4.2a) or in $|2, -1; 2, -1\rangle$ (Figure 4.2b), the system can access only one final state, $|1, +1; 1, -1\rangle$ or $|2, 0; 2, -2\rangle$, respectively,

[3] It should be noted that the collapse and revival experiment has been performed at a magnetic field of $B = 150\,\mathrm{G}$, whereas the dynamics driven by the spin-dependent interaction occurs at low magnetic fields around 1 G.

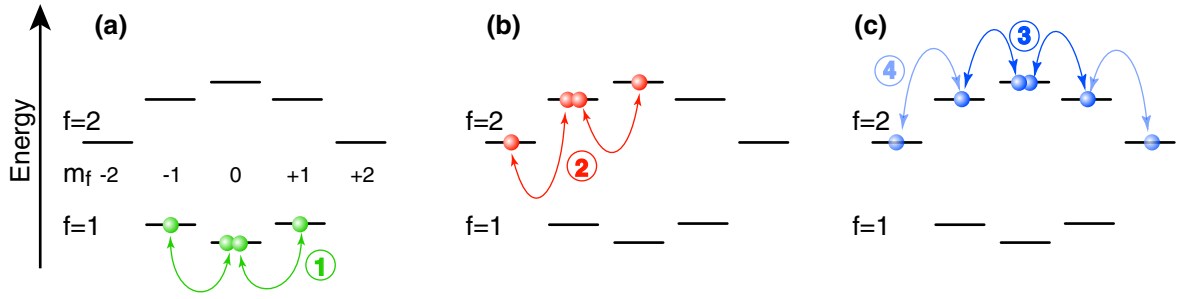

Figure 4.2: Different processes of spin changing collisions with linear Zeeman shift subtracted. While conserving total angular momentum, three different processes are possible in the ^{87}Rb hyperfine structure. **(a)** For the $f = 1$ ground state, two atoms can be coupled between $|1,0;1,0\rangle \leftrightarrow |1,+1;1,-1\rangle$. **(b)** In $f = 2$ the simplest process coupling only two states is $|2,-1;2,-1\rangle \leftrightarrow |2,0;2,-2\rangle$. **(c)** Due to the increased number of magnetic sublevels, also more complicated processes are possible coupling three states $|2,0;2,0\rangle \leftrightarrow |2,+1;2,-1\rangle \leftrightarrow |2,+2;2,-2\rangle$. The numbers refer to Fig. 4.3(b).

while conserving total magnetization. Thereby the initially large transfer matrix $\langle\psi_i|\hat{V}_S|\psi_f\rangle$ yielding the coupling strength between two arbitrary initial and final states, reduces to a 2×2 sub-matrix of non-zero entries. This sub matrix can be written in the form of a Rabi-model

$$H = \frac{\hbar}{2}\begin{pmatrix} 0 & \Omega_{if} \\ \Omega_{if} & 2\delta_{if} \end{pmatrix}, \tag{4.7}$$

where the coupling strength Ω_{if} is determined by the matrix element $\langle\psi_f|\hat{V}_S|\psi_i\rangle$ of the spin-changing interaction via $\hbar\,\Omega_{if}/2 = \langle\psi_f|\hat{V}_S|\psi_i\rangle$, and where the detuning δ_{if} can be decomposed into two parts:

$$\delta_{if} = \delta_{\text{int}} + \delta_B. \tag{4.8}$$

The first detuning δ_{int} arises from the difference of interaction energies in the initial and final states $\hbar\,\delta_{\text{int}} = \langle\psi_i|\hat{V}_S|\psi_i\rangle - \langle\psi_f|\hat{V}_S|\psi_f\rangle$ (see Fig. 4.3(a)). The second detuning δ_B is due to the energy shift of initial and final states in a non-zero magnetic field (see Fig. 4.3(b)). Since the total magnetization is conserved, the system is not sensitive to linear Zeeman shifts, because the initial and the final states experience the same linear Zeeman effect. Consequently the detuning is to leading order determined by the quadratic Zeeman shift. Therefore the second detuning in Equation (4.8) is given by the quadratic Zeeman-effect $\delta_B \propto \frac{(\mu_B B)^2}{2\hbar\omega_{\text{hfs}}}$, where ω_{hfs} denotes the hyperfine splitting. For the two-level systems considered in the following, the corresponding detuning δ_{B} is shown versus magnetic field in Fig. 4.3(c).

As for any two-level system interacting with a near resonant radiation field, the probability to find the atom pair initially prepared in $|\psi_i\rangle$ after a time t in the final state $|\psi_f\rangle$ is given by the Rabi formula

$$P_f = \frac{\Omega^2}{2\Omega_{if}'^2}\left[1-\cos(\Omega_{if}'\,t)\right], \tag{4.9}$$

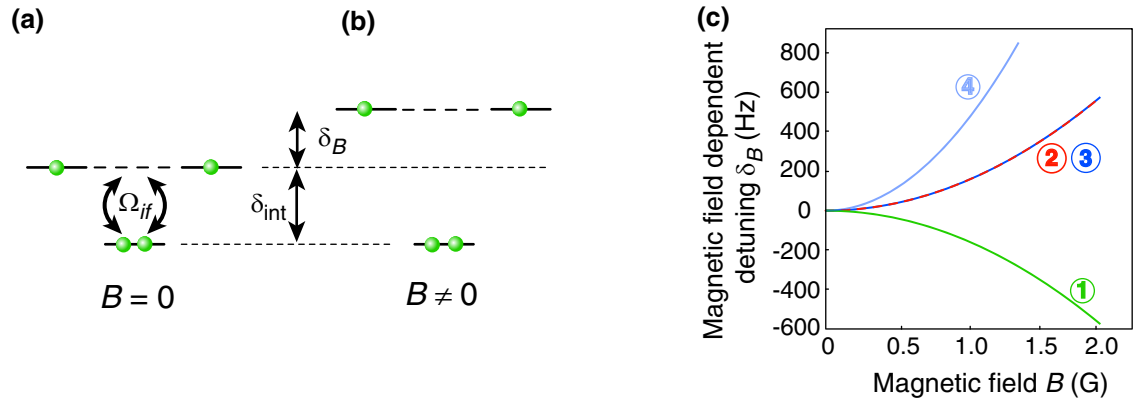

Figure 4.3: **(a)** Energy of the two-particle states (i. e. linear Zeeman shift is canceled) in the Rabi-model for spin-changing collisions. The only detuning for $B = 0$ is the difference in interaction energy between initial and final states, δ_{int}. **(b)** For a non-zero magnetic field a detuning δ_B due to the quadratic Zeeman effect additionally splits the two energy levels. **(c)** Detuning δ_B for the various cases depicted in Fig. 4.2(a-c).

with the effective Rabi frequency Ω'_{if} given by

$$\Omega'_{if} = \sqrt{\Omega_{if}^2 + \delta_{if}^2}. \tag{4.10}$$

As indicated in the previous section, the two parameters of the Rabi model can be written in the form $\Delta a \times \tilde{U}$, where the value of Δa, different for Ω_{if} and δ_{if}, can be calculated for each specific case (see Table A.1). It should be noted that for ^{87}Rb the bare scattering lengths a_F are almost equal; recently calculated values [47] are $a_0 = (101.78 \pm 0.2)\, a_{\text{B}}$ and $a_2 = (100.40 \pm 0.1)\, a_{\text{B}}$ for spin-1. Predicted values for spin-2 [111] are $a_0 = (87.93 \pm 0.2)\, a_{\text{B}}$, $a_2 = (91.28 \pm 0.2)\, a_{\text{B}}$ and $a_4 = (98.98 \pm 0.2)\, a_{\text{B}}$, where the Bohr-radius $a_{\text{B}} = 5.29 \times 10^{-11}$ m. The differences in scattering length describing the spin-dependent coupling give values of Δa on the order of a few percent of the bare scattering lengths a_F.

Since the course of the detuning δ_B with external magnetic field is known, a measurement of the effective Rabi frequency Ω'_{if} for different magnetic field values allows to extract the absolute value of the coupling strength Ω_{if}. In addition, both the absolute value of the constant detuning δ_{int} and its sign compared to the sign of the second order Zeeman shift can be inferred. The form of Equation (4.10) implies that even at zero external magnetic field, Rabi oscillations do not show unity contrast if δ_{int} and δ_B have the same sign, because the constant detuning δ_{int} is present for all magnetic field values.

An important point in the discussion of the spin-dependent interaction strength is that, for the case of more than two atoms, the interaction energy of the system increases with occupation number, similarly to the case of the Bose-Hubbard Hamiltonian (3.15). For example, the interaction strength of the process $|1,0;1,0\rangle \leftrightarrow |1,-1;1,+1\rangle$ is for three particles trapped in a common well larger by a factor $\sqrt{3}$ than for an atom pair: $\Omega_{if,3b} =$

$\sqrt{3}\Omega_{if}$. In most parts of the chapter we restrict the discussion to the case of only singly or doubly occupied lattice sites, thereby neglecting the occupation number dependency of the interaction strength.

4.1.3 Three-level system

The processes introduced in the previous section involved only two coupled states, so that the description by the Rabi model could be applied. Another possibility (case (c) in Figure 4.2) is that two final states ψ_{f_1} and ψ_{f_2} fulfill the condition of a conserved total magnetization. The dynamics can then be modeled by a coupled three-level system, as has been calculated in detail in Ref. [112]. Assuming that the direct coupling between $|\psi_i\rangle$ and $|\psi_{f_2}\rangle$ is negligible, as is the case in our experiment, the corresponding interaction Hamiltonian reads

$$\hat{H} = \frac{\hbar}{2}\begin{pmatrix} 0 & \Omega_1 & 0 \\ \Omega_1 & 2\,\delta_1 & \Omega_2 \\ 0 & \Omega_2 & 2\,\delta_2 \end{pmatrix}, \tag{4.11}$$

where Ω_i and δ_i describe the coupling strengths and total detunings, respectively, and $i = 1, 2$ labels the process $|\psi_i\rangle \leftrightarrow |\psi_{f_1}\rangle$ ($|\psi_{f_1}\rangle \leftrightarrow |\psi_{f_2}\rangle$). Similar to the treatment in [113] we find the eigenfrequencies ω as solutions to the secular equation

$$\omega^3 - \omega^2(\delta_1 + \delta_2) + \omega\left(\delta_1\delta_2 - \frac{\Omega_1^2}{4} - \frac{\Omega_2^2}{4} + \frac{\Omega_1^2}{4}\,\delta_2\right) = 0. \tag{4.12}$$

The eigenfrequencies then read

$$\begin{aligned} \omega^0 &= \frac{1}{3}\left(\delta_1 + \delta_2 + \tilde{\Omega}\,\cos\frac{\zeta}{3}\right) \\ \omega^+ &= \frac{1}{3}\left(\delta_1 + \delta_2 + \tilde{\Omega}\,\cos\frac{2\pi + \zeta}{3}\right) \\ \omega^- &= \frac{1}{3}\left(\delta_1 + \delta_2 + \tilde{\Omega}\,\cos\frac{2\pi - \zeta}{3}\right), \end{aligned} \tag{4.13}$$

where

$$\begin{aligned} \tilde{\Omega} &= \sqrt{3(\Omega_1^2 + \Omega_2^2) + 4(\delta_1^2 - \delta_1\delta_2 + \delta_2^2)} \\ \zeta &= 2\pi - \arccos\left\{\frac{[9(\Omega_1^2 + \Omega_2^2) - 4(2\delta_1 - \delta_2)(2\delta_2 - \delta_1)](\delta_1 + \delta_2) - 27\Omega_1^2\delta_2}{\tilde{\Omega}^3}\right\}. \end{aligned} \tag{4.14}$$

In the case where $|\psi_{f_2}\rangle$ is separated by a very large energy difference from the other two states, $\delta_2 \gg \delta_1$, the system effectively reduces to a two-level system oscillating between ψ_i and ψ_{f_1}. The relevant oscillation frequency then becomes $\lim_{\delta_2\to\infty}(\omega^0 - \omega^+) = \sqrt{\Omega_1^2 + \delta_1^2}$. In this limit, a description as a two-level system $|\psi_i\rangle \leftrightarrow |\psi_{f_1}\rangle$ is valid.

Comparing to the situation depicted in Figure 4.2c this means that for low magnetic fields a model including all three states has to be used in order to describe the dynamics.

For increasing magnetic fields, the quadratic Zeeman shift detunes the final state $|\psi_{f_2}\rangle = |2,+2;2,-2\rangle$ faster than the other final state $|\psi_{f_1}\rangle = |2,+1;2,-1\rangle$ (see Figure 4.2d), such that for magnetic fields large enough a two-level model including only the states $|2,0;2,0\rangle$ and $|2,+1;2,-1\rangle$ is sufficient.

4.2 Experimental sequence

In order to realize the different situations of spin dynamics in an optical lattice as depicted in Figure 4.2(a-c), we start from a BEC of around $2{\times}10^5$ atoms in a combined magnetic trap and optical lattice potential prepared as described in Section 3.5. The depth of the optical lattice during preparation of the sample is either $40\,E_r$ or $45\,E_r$, suppressing tunneling on the time scales of the experiment. We assume an uncertainty in the potential depth of $\sim 10\%$ for this particular experiment, which should be understood as an upper bound. The particular form of the lattice-intensity ramp has been taken from [114], minimizing excitations in the system. It has a total duration of 160 ms (see Fig. 4.4).

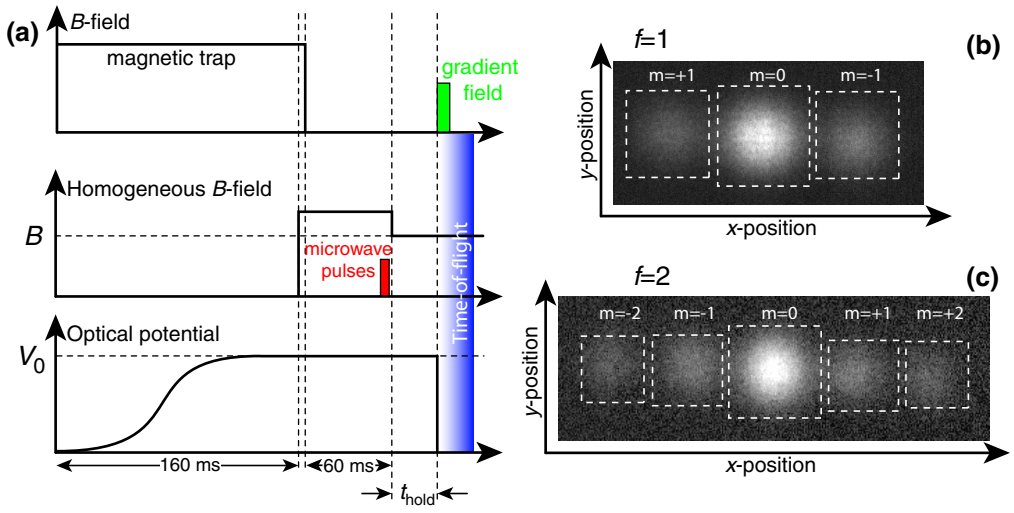

Figure 4.4: **(a)** Sketch of the experimental sequence. **(b)** Typical camera image for atoms in $f = 1$ and **(c)** $f = 2$. The dashed boxes illustrate areas in which the atom number for each magnetic sublevel is counted. The magnetic field gradient separating the different Zeeman levels has a small tilt compared to the horizontal plane. Therefore the clouds are not aligned perfectly horizontal.

In order to observe spin oscillations, the magnetic trap is switched off, leaving the sample in a pure optical trap. The spin-polarization of the atoms is preserved by a small homogeneous offset-field of ~ 1.2 G which is switched on 5 ms before switching off the magnetic trap (see Fig.4.4). After a hold time of 60 ms during which the bias field of the magnetic trap decays to below 1 mG, the atoms are prepared in their initial state for spin dynamics

by application of microwave pulses with a frequency around 6.8 GHz and a pulse duration between 6 μs and 150 μs, depending on the specific transition.

Directly after the last pulse, the homogeneous magnetic field is ramped to its final value. The time constant of the magnetic field change is on the order of a few hundred μs; this magnetic field has been calibrated by microwave spectroscopy and is known to a value better than ~ 10 mG, which in the following we consider as an upper bound of the systematic error in the magnetic field. After a variable hold time t the optical trapping potential is switched off and the atoms can expand during 7 ms of time-of-flight (TOF), while the homogeneous magnetic field is still present. During the first 3 ms of TOF a gradient field is switched on in order to spatially separate the different magnetic sublevels. The population N_m of each magnetic sublevel m is recorded after TOF with standard absorption imaging by counting the atom number around the corresponding atom cloud (see dashed boxes in Figure 4.4 (b,c)). The total atom number N_{tot} is counted in a large region including all magnetic sublevels. However, the different atom clouds corresponding to different magnetic sublevels are not well enough separated. In order to avoid double counting of atoms, we chose counting regions that do not overlap, and therefore slightly underestimate the population N_m of each cloud. Moreover, an additional background signal on the order of a few percent is counted in the global region used to find the total atom number N_{tot}. As a consequence, the relative atom numbers in the various spin states add up to a value slightly smaller than unity.

A time evolution obtained by this experimental sequence is shown in Fig. 4.5(a) for the spin dynamics starting from $|2,0;2,0\rangle$. The relative spin populations are determined from counting the number of atoms in the particular Zeeman sublevel as shown in Fig. 4.5(b). In the following we will use this representation of the population oscillation measurements.

For the analysis of the spin dynamics, it is important to note that the amplitude of the oscillations is affected by the initially prepared state of the system. Due to the Gaussian shape of the lattice laser beams, the atoms in the optical lattice experience an additional smooth confinement and the system therefore favours the formation of Mott shells with distinct, integer number of atoms per site [12, 76, 92, 115] (see also Section 4.6). For our trap parameters we calculate that a central core of atom pairs contains approximately half of the atoms. This core is surrounded by a shell with isolated atoms, whereas the number of sites with more than two atoms is negligible. Due to this shell structure, not all atoms contribute to the spin oscillations. Consequently the measured amplitude of the spin oscillation – normalized to the signal from *all* atoms – is decreased compared to the value predicted by the Rabi model. The measured relative amplitude is expected to be

$$\frac{N_{+1}+N_{-1}}{N_{\mathrm{tot}}} = n\,P_f, \tag{4.15}$$

where n is the fraction of atoms in sites with double filling.

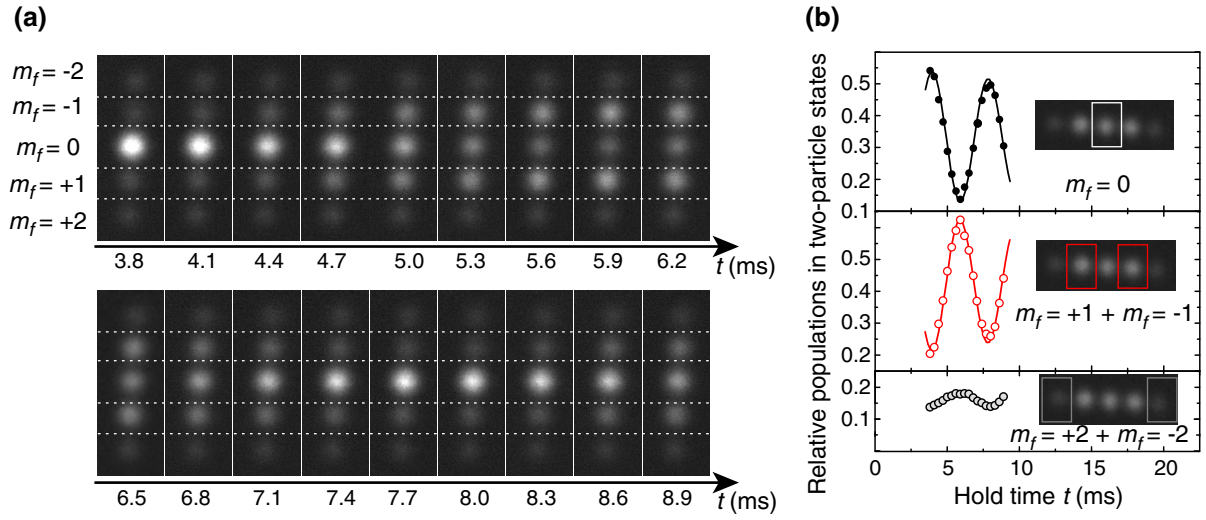

Figure 4.5: **(a)** Part of a time evolution for spin dynamics in the $f = 2$ hyperfine manifold. The spin populations show an oscillatory behaviour that becomes evident, when the relative population dynamics is extracted in **(b)**. For more details on this data set, see Fig. 4.10.

4.3 Experimental results

We have experimentally investigated the spin dynamics in the three situations depicted in Figure 4.2(a-c), where the system is initialized in different internal atomic states. The initial states for those cases are (i) $|f = 1, m_f = 0\rangle$, (ii) $|f = 2, m_f = -1\rangle$, and (iii) $|f = 2, m_f = 0\rangle$. In most cases, the assumption that for an initial state only one final state is accessible after a spin changing collision is valid. In the lower $f = 1$ hyperfine manifold, this is naturally fulfilled, because only one combination of two-particle states conserves total magnetization. For the upper $f = 2$ hyperfine state, there are in general more initial and final states accessible. For case (ii) the description as a two-level system is valid at all parameters used in our experiments. For case (iii) a sufficiently large external magnetic field can be used to tune the system via the quadratic Zeeman-shift into a regime where the approximation by a two-level system is sufficient. For small magnetic fields, however, a three-level system must be considered.

Another difference between the $f = 1$ and $f = 2$ cases is the role of losses. Due to our preparation in the optical lattice, three-body recombination processes are suppressed, because most atoms are either in singly or doubly occupied lattice sites. In the $f = 1$ state, two-body loss rates are very low, so that atom losses are negligible. This is not the case in $f = 2$ where hyperfine changing collisions have been seen to be significant [99, 116]. We still observe several coherent spin-oscillations in the upper hyperfine state, because of the relatively large spin-dependent coupling strengths in $f = 2$.

In each case, the frequency of the coherent spin oscillations can be changed by the magnetic field dependent detuning δ_B. We record the population in each Zeeman sublevel

as a function of time for the three initial states introduced above for different values of the external magnetic field. From these measurements we extract the corresponding oscillation frequency. From the theoretical analysis in Section 4.1 and Appendix A it is apparent that the strength of the spin dependent interaction is determined by only one (two) scattering length differences for $f = 1$ ($f = 2$). The strength of the interaction is then determining the oscillation frequency. In turn, from the measured oscillation frequencies, the important scattering length differences can be inferred.

In the following we will first show the main results of population oscillations in $f = 1$ (Section 4.3.1) and $f = 2$ (Section 4.3.2), while we describe the determination of the oscillation frequencies and the scattering length differences in Section 4.3.3. For simplicity, the notation of two-particle states in the following sections will omit the total spin f; for ambiguous cases the total angular momentum will be explicitly written.

4.3.1 Dynamics in the $f = 1$ hyperfine state

The collisional coupling between two $f = 1$ atoms is an almost ideal example of the Rabi model introduced above. The only possible process conserving total magnetization is $|0;0\rangle \leftrightarrow |+1;-1\rangle$, where the two-particle states in this section assume $f = 1$. In order to observe spin dynamics, the atomic sample is prepared by a first microwave pulse in the $|f = 2, m_f = 0\rangle$ state, immediately followed by a second pulse, transferring the atoms into $|f = 1, m_f = 0\rangle$. A typical oscillation for a lattice depth of $45\,E_r$ at a magnetic field of $B = 0.28\,\mathrm{G}$ is shown in Fig. 4.6a. A fit to the population oscillation reveals a slight damping with a rate of $\gamma \approx 3(2)\,\mathrm{s}^{-1}$ to be discussed below (see 4.3.6). Spin oscillations have been observed for various magnetic fields between approximately 170 mG and 600 mG. For larger magnetic field, the amplitude is strongly suppressed, because the magnetic field dependent detuning δ_B becomes large compared to the coupling strength. In this limit, spin oscillations become difficult to resolve. Technical limitations prevent the observation of spin oscillations for magnetic fields even smaller than 170 mG. The measured oscillation frequency (Fig. 4.6(b)) is well described by the effective Rabi frequency (4.10), when the detuning is changed via the external magnetic field. Instead of extracting the Rabi frequency and detuning separately, we perform a fit with only one parameter as will be explained in Section 4.3.3.

Further evidence for the validity of the Rabi model comes from the behavior of oscillation amplitude for varying magnetic field. The data set shown in Fig. 4.7 is well described by the Rabi formula. In order to fit the data, we employ the expected form of the amplitude for Rabi oscillations, equation (4.9) with (4.15), and fix the spin dependent interaction strength via the interaction detuning $\delta_1 = 11.8\,\mathrm{Hz}$. This value has been determined from the oscillation frequency measurement (cf. Section 4.3.3 and Table A.1). Hence the only free parameter in the fit is the relative number of doubly occupied sites n, defined in (4.15). We find as best fit parameter $n = 0.54(2)$ in good agreement with the expected value around 0.5 and previous measurements [25]. Because this scaling factor enters in the amplitude of the spin population oscillations and leads to additional statistical and systematic errors, we extract all relevant values concerning the s-wave scattering length differences only from the

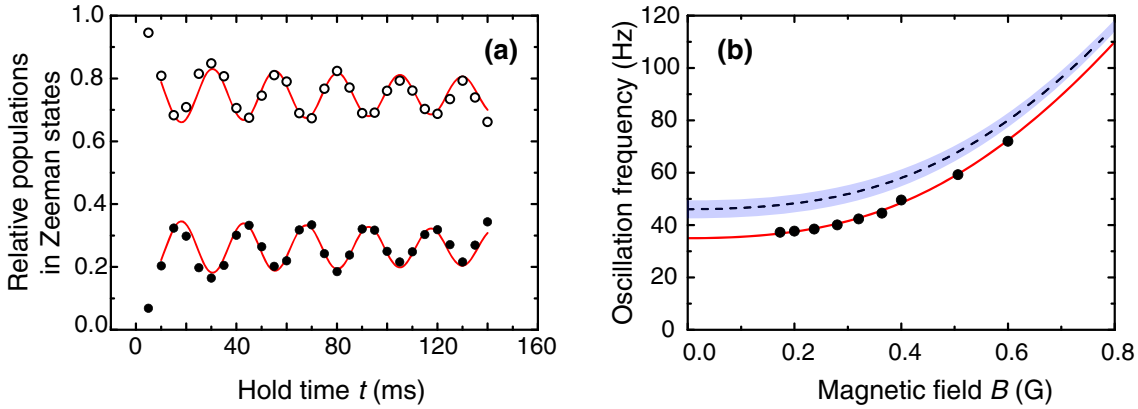

Figure 4.6: (a) Spin population oscillations in $f = 1$ between $|0;0\rangle$ (○) and $|+1;-1\rangle$ (●) at a magnetic field of 0.28 G and a lattice depth of $45\,E_r$. A fit to a damped sine (solid lines) yields an oscillation frequency of 40.2(3) Hz and a damping rate of $\gamma = 3(2)\,\mathrm{s}^{-1}$. For a discussion of the offset see Section 4.3.6. (b) Measured oscillation frequency of the $|0;0\rangle \leftrightarrow |+1;-1\rangle$ collision process versus external magnetic field B. The solid line is a fit to the expected behaviour according to the effective Rabi-frequency Ω'_{if}. The dashed line is the calculated curve based on the predicted scattering lengths [47]. The shaded region reflects our uncertainty in magnetic field of ±10 mG and the uncertainty in potential depth (upper bound of 10%).

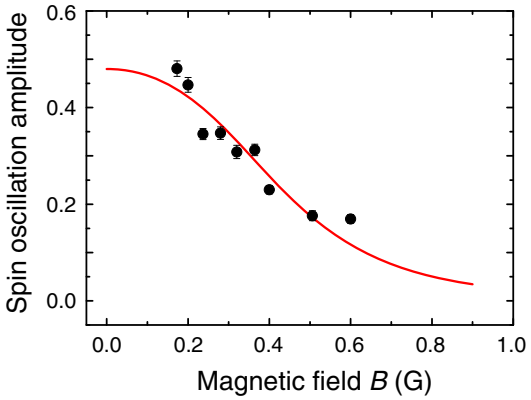

Figure 4.7: Amplitude of the interaction induced population oscillations in $f = 1$. The solid line is a fit assuming the coupled two-level model, where only the relative number of doubly occupied sites n is used as free parameter.

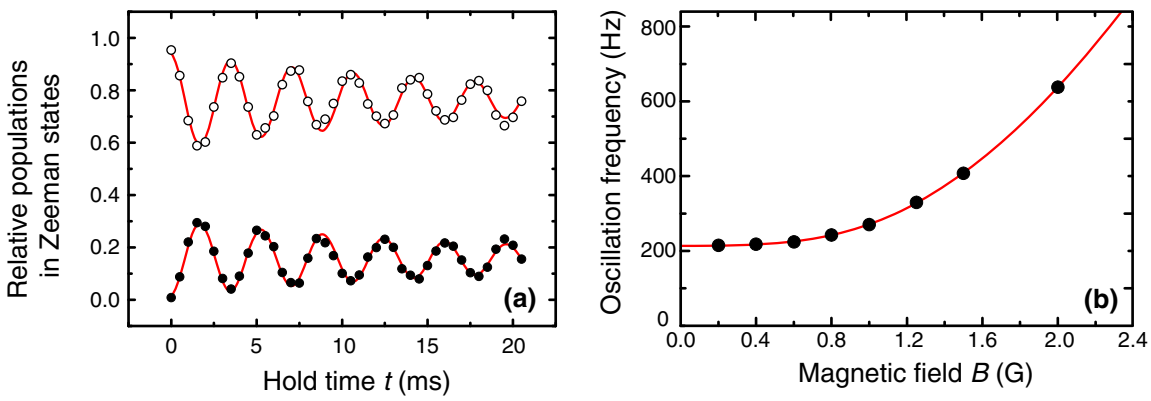

Figure 4.8: **(a)**Spin population oscillations of the process $|-1;-1\rangle \leftrightarrow |0;-2\rangle$ for a magnetic field of $B = 0.8\,\mathrm{G}$. The atoms are initially prepared in $|-1;-1\rangle$ (○) and can evolve to $|0;-2\rangle$ (●). **(b)** Oscillation frequency of the same process for varying magnetic field. The red line is a fit to the Rabi model.

oscillation frequency measurements. In fact, the oscillation frequencies can be measured independently of the value of n as long as the signal is strong enough to be detected.

In Fig. 4.6(b) the predicted curve for the spin oscillation frequency versus magnetic field is shown, based on the Rabi model presented in Section 4.1 and predicted scattering lengths [47]. The difference between experimentally measured values and the theoretical prediction will be discussed in more detail below.

4.3.2 Dynamics in the $f = 2$ hyperfine state

Two-level system. As mentioned above, the coherent coupling due to spin changing collisions in the upper hyperfine ground state $f = 2$ is more complicated than in the $f = 1$ case. For the case where the dynamics starts from[4] $|-1;-1\rangle$, the only possible interconversion process that preserves total magnetization is $|-1;-1\rangle \leftrightarrow |0;-2\rangle$. Thus this situation can also be described as a two-level system. The interaction induced spin population dynamics is shown in Fig. 4.8; the population oscillations (Fig. 4.8(a)) show a clearly sinusoidal behavior, and the oscillation frequency (Fig. 4.8(b)) is again well described by the Rabi model. Compared to the dynamics in the $f = 1$ hyperfine state, the presented dynamics in $f = 2$ takes place on a faster time scale. This is due to the corresponding effective scattering length differences Δa, which are larger for the $f = 2$ case. Also, in Fig. 4.8(a) the oscillation shows a damping with a rate $\gamma \approx 35(4)\,\mathrm{s}^{-1}$ that was strongly suppressed in the $f = 1$ case. This damping will be investigated below.

Three-level system. For the case where the system is initialized in $|0;0\rangle$, there are, however, the two final states $|+1;-1\rangle$ and $|+2;-2\rangle$ accessible. The direct process $|0;0\rangle \leftrightarrow$

[4] In the following, the notation of two-particle states implies $f = 2$.

$|+2;-2\rangle$ is strongly suppressed as the coupling matrix element is several orders of magnitude smaller than the other relevant matrix elements. However, this final state can be populated through a two-step process $|0;0\rangle \leftrightarrow |+1;-1\rangle \leftrightarrow |+2;-2\rangle$. For sufficiently large magnetic field, the state $|+2;-2\rangle$ is far detuned so that the situation is effectively described by a two-level system [25].

For lower magnetic fields, a three-level description as in Section 4.1.3 must be used in order to describe the population oscillation. In Figure 4.9(a) we show a population oscillation for a lattice depth of $40\,E_r$ and a magnetic field of $B = 0.24\,\mathrm{G}$ which clearly differs from the simple sinusoidal case. Here, the solid lines are a calculation from a three-level model which shows good agreement with the measured data.

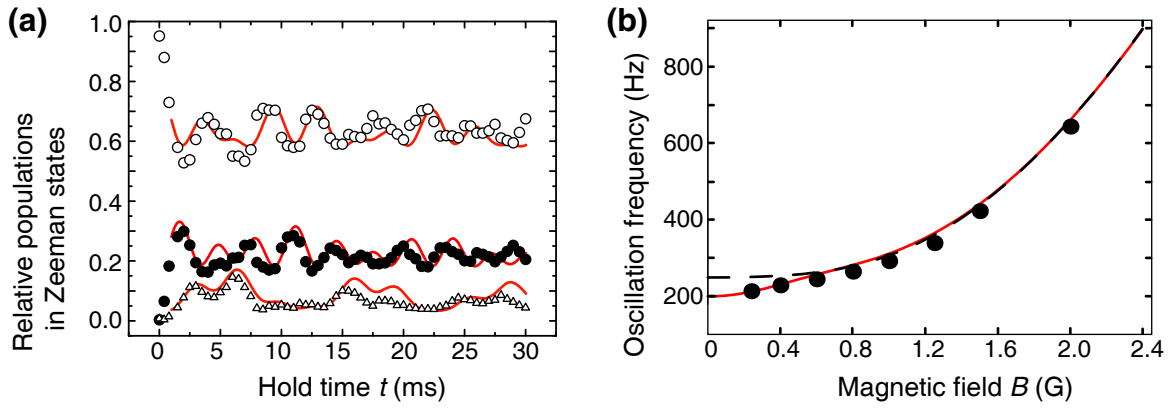

Figure 4.9: (a) Measured population dynamics for the coupled three-level system $|0;0\rangle(\bigcirc) \leftrightarrow |+1;-1\rangle(\bullet) \leftrightarrow |+2;-2\rangle(\triangle)$ at a magnetic field of $B = 0.24\,\mathrm{G}$ and a lattice depth of $40\,E_r$. One clearly sees the deviation from the pure sinusoidal two-level oscillations and the rather large population of $|+2;-2\rangle$. The solid lines are calculations based on a coupled three-level system (4.11) with parameters corresponding to the experimental realization. For a discussion of the offset see Section 4.3.6. (b) Oscillation frequency vs magnetic field for spin dynamics starting from $|0;0\rangle$. The red line is a fit to the analytical solution of the three-level model (4.13)and the dashed black line shows the result of a two-level model (see [25]).

For this calculation we use the fitted values of the two detunings $\delta_{2,1}$ and $\delta_{2,2}$ (see 4.3.3) together with the form of the Rabi parameters given in Table A.1. With this we calculate the values of the three-level model (4.11) $\Omega_1 = 2\pi\times 265\,\mathrm{Hz}$, $\delta_1 = 2\pi\times 33\,\mathrm{Hz}$ for the coupling of $|0;0\rangle$ with $|+1;-1\rangle$, and $\Omega_2 = 2\pi\times 134\,\mathrm{Hz}$, $\delta_2 = 2\pi\times 100\,\mathrm{Hz}$ for the coupling between $|+1;-1\rangle$ and $|+1,-2\rangle$. The phenomenological damping rates for both processes have been set to the experimentally determined value $\gamma \approx 30\,\mathrm{s}^{-1}$ and the decay from $|+2;-2\rangle$ has been neglected. The amplitude has been set to account for $\sim 50\%$ of the atoms contributing to the spin-dynamics, and the offset for each population (see Section 4.3.6) has been set in order to match the data.

Unfortunately, a fit to the coupled three-level system defined by (4.11) yields very unreliable results, because of the large number of parameters involved. Instead, we fit the

$m_f = 0$ population with the same sinusoidal form as used in the previous cases to approximate the predominant oscillation frequency. The observed oscillation frequency versus magnetic field is shown in Figure 4.9(b). In order to include the three-level character, we fit the measured oscillations frequency versus magnetic field (Fig. 4.9b) with the analytical solution of the three-level model (4.14). The fit is shown as solid line in Figure 4.9(b). The small deviations between experimentally measured data points and the fit in Fig. 4.9 come from the fact, that the fit is not independent, but related to the result of the fit for the process $|-1;-1\rangle \leftrightarrow |0,-2\rangle$ (Fig. 4.8) as will be explained in the next paragraph. The theoretical prediction from a two-level system (see [25]) is shown as dashed black line and does not describe the dynamics well for small magnetic fields.

4.3.3 Determining scattering length differences

From the population oscillations presented in the previous section, the scattering length differences driving the dynamics can be inferred. We briefly recall the results and give the extracted scattering length differences. For the analysis one has to keep in mind that in a spin dependent collision of two spin-1 atoms the dynamics is determined by only one scattering length difference, respectively two in the spin-2 case. It can be calculated from Eqs. (4.3)–(4.5) (cf. Table A.1) that the parameters Ω_{if} and δ_{int} are directly related to those scattering length differences. For example, in the spin-1 case one finds $\Omega_{if} = 2\sqrt{2}\,\delta_{\mathrm{int}}$, with $\delta_{\mathrm{int}} = \frac{(a_2-a_0)}{3}$.

For $f = 1$ the difference $(a_2 - a_0)$ directly relates to the interaction detuning δ_{int} and results from a fit of the form (4.10) to the measured data. We perform this fit with one free parameter δ_1 defined as the interaction detuning for the process. The fit yields a value of $\delta_1 = 2\pi \times (-11.8^{\pm 0.04}_{\pm 0.2})\,\mathrm{Hz}$, where here and in the following the errors in the upper and lower row denote the statistical and systematic error due to magnetic fields, respectively. The sign of this detuning reflects the fact that the $f = 1$ ground state is ferromagnetic, as will be explained in Section 4.5. We stress, that this parameter is still free from systematic effects due to our uncertainty in optical potential depth, but has a statistical error, as well as a systematic error due to magnetic field uncertainty.

For $f = 2$, the process $|2,-1;2,-1\rangle \leftrightarrow |2,0;2,-2\rangle$ depends only on the scattering length difference $(a_4 - a_2)$, whereas the dynamics starting from $|2,0;2,0\rangle$ depends on both differences, $(a_4 - a_2)$ and $(a_2 - a_0)$. We first fit the data set for oscillation frequency versus magnetic field of the process $|2,-1;2,-1\rangle \leftrightarrow |2,0;2,-2\rangle$ with only one parameter $\delta_{2,2}$, reflecting the scattering length difference $(a_4 - a_2)$. The resulting best fit parameter is $\delta_{2,2} = 2\pi \times (30.2^{\pm 0.1}_{\pm 0.3})\,\mathrm{Hz}$. Then we fit the data set for the dynamics starting from $|2,0;2,0\rangle$ with $\delta_{2,2}$ fixed to this value, and leave the second relevant interaction detuning $\delta_{2,1}$ – reflecting the influence of the scattering length difference $(a_2 - a_0)$ – as free parameter. For this fit, which is shown in Figure 4.9(b), we employ the analytical solution of the three level system, Equations (4.14). The best fit is achieved for $\delta_{2,1} = 2\pi \times (33.4^{\pm 1.4}_{\pm 1.1})\,\mathrm{Hz}$. Due to the small uncertainty in each data point of the first data set compared to the uncertainty of the second data set, this treatment is equivalent to one combined fit of both data sets with two parameters.

In order to extract the scattering length differences, we use the relations from Table A.1 and the values for $\tilde{U}$ given in Section 4.1.1. Those scattering length differences are summarized in Table 4.1. The values now have an uncertainty due to the optical potential, entering via the constant $\tilde{U}$.

f	Δa	Measured (a_B)	Predicted (a_B)
$f = 1$	$a_2 - a_0$	$-1.07^{\pm 0.01}_{\pm 0.02\,\pm 0.06}$	-1.38
$f = 2$	$a_2 - a_0$	$3.51^{\pm 0.2}_{\pm 0.18\,\pm 0.16}$	3.35
	$a_4 - a_2$	$6.95^{\pm 0.02}_{\pm 0.07\,\pm 0.26}$	7.70

Table 4.1: Scattering length differences inferred from the spin population oscillation measurement. The errors in the upper row give the statistical uncertainty from the fit, whereas the first and second value in the lower row give the systematic error due to the uncertainty in magnetic field and optical potential depth, respectively. The theoretical predictions are calculations based on values from [47, 111].

4.3.4 Comparison with theory

As indicated in Fig. 4.6 and Table 4.1, the experimentally obtained values differ from the theoretically predictions by significantly more than explained by the statistical and systematic errors. For the spin oscillation frequencies, the difference is largest in $f = 1$, indicated in Fig. 4.6. There the difference is on the order of 20% and slightly smaller for $f = 2$ [26]. As already stated in the discussion of Eq. (4.6), a correction of the wave function overlap due to interaction increases the difference by approximately 3%. Although experiment and theory agree if also the errors of the theoretically predicted scattering lengths are taken into account, in the following we will briefly discuss the possible origins for the remaining difference.

Possible sources for the deviations might be e.g. magnetic field gradients, causing the wave function overlap of the $|+1;-1\rangle$ two-particle state to decrease. The reason is that in a magnetic gradient field B' a magnetic sublevel with quantum number $m \neq 0$ tries to reduce the Zeeman energy $m\, g_F\, \mu_B\, B'\, \Delta x$ by moving a distance Δx at the expense of an increased potential energy in the trap. As the Zeeman energies in states $m = \pm 1$ shift opposite in a gradient, the corresponding wave functions tend to separate. However, a simple estimate using a harmonic oscillator approximation shows that in order to decrease the wave function overlap by 10%, each wave function has to move on the order of 15% of the harmonic oscillator length in the lattice well. For the trap parameters presented here, this corresponds to $\approx 0.15 \times 100\,\mathrm{nm}$. Thereby the potential energy is raised by $0.02 \times \hbar\omega_{\mathrm{trap}}$, where ω_{trap} is the trap frequency. Comparing this with the Zeeman energy in a gradient field, one finds that the magnetic gradient must be on the order of $\approx 100\,\mathrm{G/cm}$, which would be a large gradient in experiments with ultracold atoms. As a comparison, this gradient is on the order of typical gradients in quadrupole traps. This underlines the fact

that the tight confinement by the optical lattice essentially freezes out the spatial degree of freedom. Estimating the gradient fields in the present setup, the atomic sample could be displaced from the optimal position between the coils producing the homogeneous magnetic field. This can lead, however, to gradients on the order of 10 mG/cm, orders of magnitude smaller than the gradient needed to explain the difference between measured and calculated spin oscillation frequencies.

Second, the measured absolute value of the magnetic fields could be systematically shifted. All values of the magnetic fields are based on a measurement of a transition frequency difference between two Zeeman states, one in $f = 1$ and the other in $f = 2$. These frequencies around 6.8 GHz can be measured to a kHz level, corresponding to a magnetic field uncertainty of approximately 3 to 6 mG. A systematic shift of the transition line due to the AC-Stark shift is avoided by using long microwave pulses with very small microwave powers. From the measured frequency for one transition the magnetic field can be calculated by making use of the Breit-Rabi formula. The results for two independent measurements on two different transitions can be compared. They differ by approximately the same magnetic field as the uncertainty of a single measurement, i.e. 3 to 6 mG.

Another possible reason could result from imprecisely measured optical potential depths. However, independent measurements from vibrational band spectroscopy [117, 118] compared to direct measurements of the on-site interaction energy U through the collapse and revival of the coherent matter wave field [110] yield agreement to better than 10%.

A finally possible reason might origin from the errors of the predicted values for scattering lengths. Although they are known to a very high precision, for the scattering length differences considered here, even small deviations in the individual scattering lengths can lead to a large change in the scattering length difference, because they are rather small compared to the bare scattering lengths. This remaining difference still needs clarification by further theoretical as well as experimental investigation.

4.3.5 Contrast enhancement by filtering a Mott-insulator

As explained in Section 4.2, the harmonic confinement of the lattice laser beams leads to a Mott insulating state with both, singly and doubly occupied lattice sites. Only the atom pairs contribute to the spin population oscillations as they can interact in their lattice well. Because the spin populations are normalized to the total number of atoms, i.e. including the singly occupied sites, the contrast is reduced due to the isolated atoms. This artificial decrease can be removed by a contrast enhancement sequence. In Fig. 4.10(a) a typical signal of spin oscillations is shown for the process $|2,0;2,0\rangle \leftrightarrow |2,+1;2,-1\rangle$. Due to isolated atoms not contributing to the total signal (Fig. 4.10(b)), the amplitude is low ($\approx 31(3)\%$). After half an oscillation period, however, doubly occupied sites are in a different magnetic sublevel ($m = \pm 1$) compared to singly occupied sites ($m = 0$). A microwave pulse can therefore selectively transfer the atoms into the $f = 1$ hyperfine state. Since the imaging light is resonant to the optical transition $f = 2 \rightarrow f' = 3$ only, the isolated atoms become transparent for the imaging light pulse (see Fig. 4.10(c)) and remain undetected during the imaging. This enhances the observed amplitude in the subsequent spin oscillations

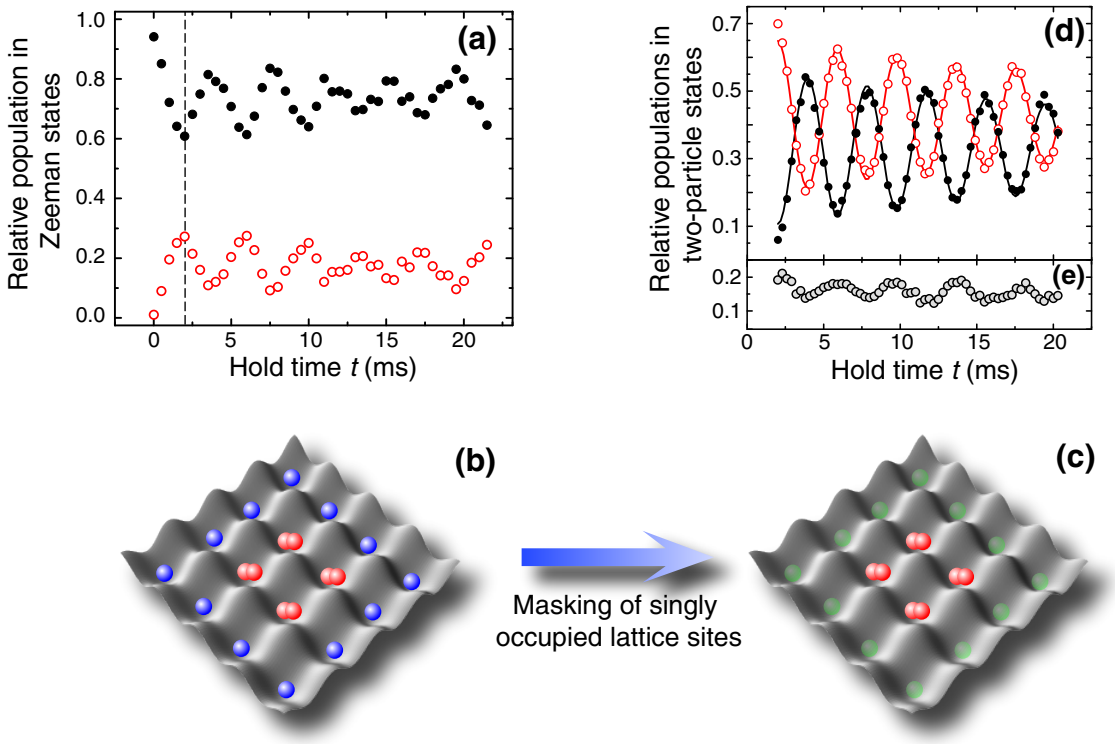

Figure 4.10: Contrast enhancement sequence. **(a)** Spin oscillation signal for the process $|2,0;2,0\rangle \leftrightarrow |2,+1;2,-1\rangle$ at a magnetic field $B = 0.6\,\mathrm{G}$. All atoms, isolated atoms and atom pairs as sketched in **(b)**, are detected in the signal. After the first half oscillations period the isolated atoms can be selectively transfered into a hyperfine state which is transparent to the imaging light as shown in the sketch **(c)**. Therefore these atoms remain undetected, and the contrast of the observed spin oscillations is enhanced as shown in **(d)**. The missing fraction of atoms is due to a population in the $m = \pm 2$ state **(e)**.

to $\approx$ 56(4)% (Fig. 4.10(d)). The difference to the expected value of 80% can be partly explained by a $\approx$ 17% fraction of atoms in $m = \pm 2$, see Fig. 4.10(e).

4.3.6 Damping mechanisms

An experimentally observed feature of the coherent spin dynamics in both hyperfine states is the damping which is not expected from the models describing the coherent dynamics. The strongest damping of the spin oscillations is present in the $f = 2$ hyperfine state (see Fig. 4.8(a) or Fig. 4.10(d)). In order to investigate this damping, we record spin population oscillations at different lattice depths and extract the damping rate for each depth (Fig. 4.11(a)). The damping shows an exponential increase for lower optical potentials, and levels at a constant, non-zero value for deep lattices. The exponential increase is well fitted by the behavior of the tunneling matrix element J, i.e. proportional to the tunneling rate between neighboring sites in the lattice. This can be understood in a simple picture. When two atoms undergo the Rabi-like spin oscillations and one atom tunnels to a neighboring site, the coherent oscillation stops. As the tunneling occurs randomly, and we detect the ensemble average of many thousand particle pairs, the increased tunneling probability leads to a damping of the coherent evolution. For large lattice depth the tunneling is well suppressed. However, a non-zero damping rate is still present in Fig. 4.11(a). The origin of this offset can be attributed to loss processes in $f = 2$. There, losses have been seen to be significant [25, 116], partly due to dipolar relaxation, where in the collision of two $f = 2$ atoms the spin of a single atom can flip, and the hyperfine energy is released as kinetic energy. This energy $\sim h \times 6.8\,\mathrm{GHz}$ is large compared to the trap depth and leads to a loss of at least one particle. If during the coherent spin evolution of an atom pair, one of the atoms is lost by such a process, the evolution stops and the total signal will exhibit a damping as in the case of tunneling.

Such large loss rates are absent for $f = 1$, and the observed damping is much smaller. Still, a finite damping on the order of $\gamma \approx 3\,\mathrm{s}^{-1}$ is observed even in the spin-1 data for large lattice depth. One source for this damping could be the inhomogeneity of our system, cf. Eq. (3.31). Due to the Gaussian intensity profile of the lattice laser beams, the wavefunction overlap $\int d^3r|\phi_0|^4$ is slightly higher in the center than in the outer regions of the system. Therefore the coupling strength Ω_{if} and the constant detuning δ_{int} are slightly position dependent. This leads to a small dephasing in the system, with a rate that we estimate to be on the order of $0.3\,\mathrm{s}^{-1}$. Therefore its influence on the observed damping is rather small. Another possible explanation for the observed damping at high lattice depths in the spin-1 case are off-resonant Raman transitions introduced by the lattice laser beams. The expected rate of those events has been estimated to be similar to the observed damping rate. However, this effect has not been experimentally investigated. Also, heating to higher vibrational bands and subsequent tunneling to neighboring sites is a possible damping mechanism.

Another feature of the coherent spin dynamics in $f = 1$ that has also been observed in $f = 2$ is an initial rise of the population in the final two-particle state, which is faster than predicted by the simple Rabi-model. This fast initial rise at the beginning of the

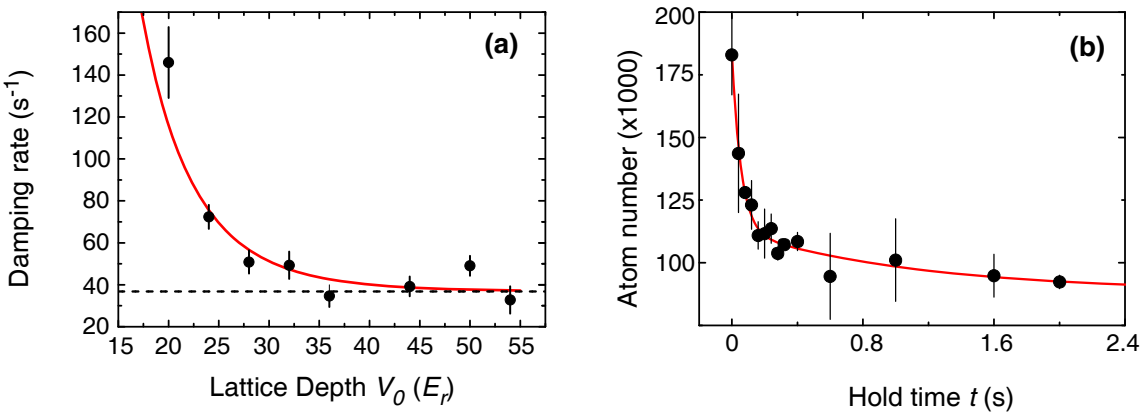

Figure 4.11: **(a)** Damping rate of the spin changing collisions in $f = 2$ versus depth of the confining optical lattice. The increased damping at low lattice depths can be attributed to increased tunneling; the solid line is a fit to a function of the form $c_J\, J/h + \gamma_0$ with the tunneling element J (cf. Eq. (3.21)) and yields an amplitude $c_J = 9(1)$ and an offset $\gamma_0 = 37(3)\,\mathrm{s}^{-1}$. **(b)** Loss of atoms in a 3D optical lattice in the $f = 2$ state. The fast loss in the beginning shows a decay rate of $\gamma_1 \approx 35(5)\,\mathrm{s}^{-1}$, coinciding with the damping offset in (a). After all sites with double occupancy have been depleted, only residual tunneling can induce additional loss, or collisions with background particles. Both processes occur with much smaller rate; therefore the losses slow down for longer hold times.

spin dynamics together with the offset of the oscillations can partially be explained by the magnetic field ramp after the last microwave pulse. Here, the sample experiences a changing detuning, and the state from which the spin dynamics start from can be changed.

4.4 Tuning spin-changing collisions via AC-Zeeman shift

As demonstrated in the previous section, control over the spin changing interaction can be gained by changing the external magnetic field. Thereby the energy detuning δ_{if} is adjusted and consequently also the effective Rabi frequency. Usually, full control over the detuning allows to either tune the system into resonance ($\delta = 0$), or completely suppress the dynamics ($\delta \gg \Omega$). For the case of ^{87}Rb, however, it turns out that the two terms δ_{int} and δ_B determining the total detuning δ_{if} in Eq. (4.8) have the same sign. As the magnetic field dependent detuning can take only positive values, even for $B = 0$ the second term due to different interaction strengths in the initial and final two-particle states, δ_{int}, persists. This so far prevented the observation of fully resonant interaction induced Rabi oscillations. In order to circumvent this problem, one has to introduce a selective energy shift which compensates the sum of detuning due to magnetic field δ_B and interaction induced detuning δ_{int}. In this section we present a method to gain full control over the energy difference of the two-particle states during the spin changing collisions and to tune it to a desired value (see Fig. 4.12a-c). This allows not only to observe fully resonant spin

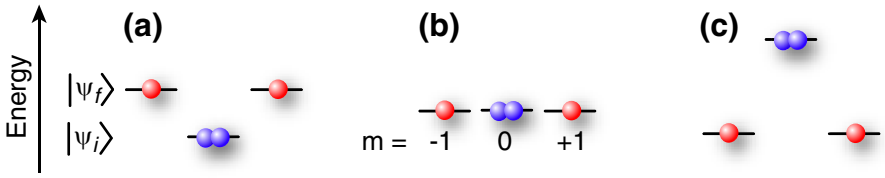

Figure 4.12: Selective control over the two-particle energy difference during the spin changing collisions. In a usual situation **(a)**, the energy difference between initial $|\psi_i\rangle$ and final $|\psi_f\rangle$ two-particle states (here in $f = 1$) are given by the sum of interaction detuning δ_{int} and the quadratic Zeeman shift δ_B, where the first persists even for zero external magnetic field. The aim is to introduce an additional energy shift, which can exactly compensate for the original detuning, bringing the two states into degeneracy **(b)**, or increasing the detuning to a large value **(c)**, thereby suppressing the spin changing collisional process.

dynamics, but also to switch the dynamics off by increasing the detuning to a large value, independent of the actual magnetic field value.

AC-Stark shift

In atomic systems, energy shifts can be exerted through the interaction with a light field detuned by a frequency Δ from an atomic transition. This energy shift, known as AC-Stark shift, is essentially the same as the dipole potential introduced in Eq. (3.10) [73], and can be written for a two-level system as

$$\Delta E = \pm \frac{\hbar \tilde{\Omega}^2}{4\Delta}, \tag{4.16}$$

where the lower (upper) sign holds for the ground (excited) state. Here $\tilde{\Omega} = -\mathbf{d}_{\text{el}}\mathbf{E}/\hbar$ is the coupling strength between electric field $\mathbf{E}$ and the atomic system, and $\mathbf{d}_{\text{el}}$ is the electric dipole. In order to distinguish this radiation induced coupling strength from the interaction induced coupling used before, we denote it by a tilde above in the following. A convenient theoretical treatment describes this shift in terms of the so-called "dressed states" which consider combined states of the atom and photon field (see also discussion is Section 3.4). Therefore we call the coupling strength in the following "dressing Rabi frequency". The energy shift (4.16) can be conveniently adjusted in the experiment by the detuning Δ and by the coupling strength $\tilde{\Omega}$ through the light field intensity I, because $\tilde{\Omega}^2 \sim \mathbf{E}^2 \sim I$. In a more realistic situation, there are more than two atomic levels involved. In addition, different polarizations will couple with different strengths. In this case the total energy shift is the sum of all individual contributions.

AC-Zeeman shift

In our case, we focus in the following on spin oscillations in $f = 1$ and again omit writing the total angular momentum in the two-particle states, but the method presented is not limited

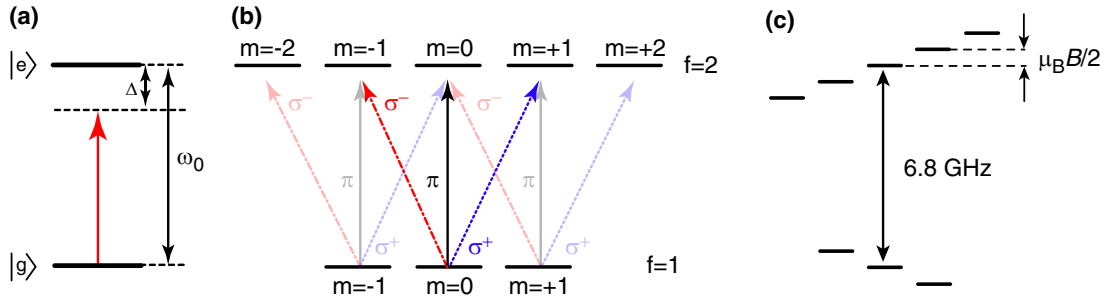

Figure 4.13: Scheme of energy shift due to a detuned radiation field. **(a)** In the two level system, a radiation field that is detuned from the transition frequency causes an energy shift according to Eq. (4.16) of both states. **(b)** For ^{87}Rb at zero magnetic field there are for each magnetic sublevel in $f = 1$ in general three contributions to the energy shift due to the possible transitions with π and $\sigma^{\pm}$ polarized light. **(c)** For a small magnetic field on the order of a few Gauss, each magnetic sublevel is shifted in energy by the linear Zeeman shift. This additionally changes the coupling to the microwave field as now the detuning changes.

to this case. Consequently, the detuning between the two particle states $|m = 0; m = 0\rangle$ and $|+1; -1\rangle$ (see Fig. 4.12a-c) has to be compensated by an external field. Instead of an optical transition, we use a microwave radiation field coupling the $f = 1$ hyperfine manifold to the $f = 2$ states. In this case, the coupling strength $\tilde{\Omega}$ is not determined by the electric dipole moment $\mathbf{d}_{\mathrm{el}}$, but by the magnetic moment μ of the atom. Therefore we call the resulting energy shift an *AC-Zeeman shift*. The detuning is defined as $\Delta = \omega_{\mu\mathrm{W}} - \omega_{\mathrm{hf}}$, where $\omega_{\mu\mathrm{W}}$ is the frequency of the microwave field applied, and ω_{hf} is the hyperfine splitting frequency between the $f = 1$ and the $f = 2$ state at zero magnetic field.

In contrast to the two-level system, the energy shift in the hyperfine structure will differ from the value given in Eq. (4.16) in two respects. First, because of selection rules, each $f = 1$ ground state can couple to the $f = 2$ manifold via three transitions with different polarizations denoted by the parameter q ($q = 0, \pm 1$ for π and $\sigma^{\pm}$ transitions, respectively) as depicted in Fig. 4.13(b). Each transition contributes with different strength due to the different geometrical wave function overlap. This is accounted for by the corresponding Clebsch-Gordan coefficient $\langle f = 1, m; 1, q | f = 2, m + q\rangle$, connecting the state $|f = 1, m\rangle$ to the state $|f = 2, m + q\rangle$ by a photon of polarization q. Additionally, in general different polarizations will have different intensities I_q in the experiment.

Second, a small magnetic field ($\sim 1\,\mathrm{G}$) will shift the magnetic sublevels due to the linear Zeeman effect (see Fig. 4.13(c)) by an amount

$$\Delta E_B \approx g_F \mu_B m B, \tag{4.17}$$

where μ_B is the Bohr magneton, $g_F = \pm\frac{1}{2}$ is the Landé factor, where the upper (lower) sign is for $f = 1$ ($f = 2$). This effectively changes the detuning Δ of the transition, as now the levels coupled by the microwave field might be shifted closer to resonance or further away. In particular, for π-transitions the differential shift is given by $m\,\mu_B\,B$, whereas for

circular polarized light the shift will be increased or decreased by $\frac{1}{2}\mu_B B$. Therefore the total detuning is given by $\hbar\Delta - (m + q/2)\mu_B B$.

Accounting for these effects and for sufficiently large detuning, the energy shift of the atomic state $|f = 1, m\rangle$ can be calculated as

$$\begin{aligned} \Delta E_m &\approx \frac{\hbar\tilde{\Omega}_\pi^2}{4\Delta} \times f_m\left(\frac{\mu_B B}{\hbar\Delta}\right), \\ f_m(x) &= \sum_{q=0,\pm1} \frac{3C_{m,q}}{4}\frac{I_q}{I_\pi}\frac{1}{1-(m+q/2)x}. \end{aligned} \tag{4.18}$$

Here the $C_{m,q} = |\langle f = 1, m; 1, q | f = 2, m + q\rangle|^2$ are square moduli of Clebsch-Gordan coefficients for the relevant transition. Furthermore we have defined the coupling strength of the π-transition $\tilde{\Omega}_\pi$ as the second free parameter in addition to the detuning Δ. This reflects the experimental situation, where the two adjustable parameters varied in the experiment are the frequency $\nu_{\mu\mathrm{W}}$ and the intensity $I_{\mu\mathrm{W}} \sim I_\pi$ of the microwave field. Therefore the different intensities of the other polarization components I_q enter relative to the π component. The I_q can be calibrated by fast Rabi flopping on different transitions in the experiment. Finally we have introduced $x = \frac{\mu_B B}{\hbar\delta}$.

In the absence of the microwave field, the detuning of the spin population oscillations are given by Eq. (4.8) as $\delta_{if} = \delta_{\mathrm{int}} + \frac{(\mu_B B)^2}{2\hbar\omega_{\mathrm{hf}}}$. In the presence of such a radiation field, the energy shift due to the AC-Zeeman shift adds, and the effective detuning between the two-particle states becomes

$$\hbar\delta_{\mathrm{eff}} = \hbar\alpha(\tilde{\Omega}_\pi^2 - \tilde{\Omega}_{\mathrm{res}}^2), \tag{4.19}$$

where the factor

$$\alpha = \frac{f_{+1}(x) + f_{-1}(x) - 2f_0(x)}{4\Delta} \tag{4.20}$$

accounts for the specific process $|0;0\rangle \leftrightarrow |+1;-1\rangle$ which we consider here. Moreover, the resonant Rabi frequency $\tilde{\Omega}_{\mathrm{res}}$ which we introduced in Eq. (4.19) describes the case where

$$\hbar\alpha\tilde{\Omega}_{\mathrm{res}}^2 = -(\delta_{\mathrm{int}} + \delta_B). \tag{4.21}$$

In this situation, the two-particle states $|0;0\rangle$ and $|+1;-1\rangle$ are degenerate and the interaction driven spin oscillations should occur with maximum amplitude.

AC-Zeeman shift in the experiment

Before implementing the AC-Zeeman shift in the experiment, one has to estimate the effect of a radiation field on the level structure in the ^{87}Rb hyperfine states. First, as mentioned already in Section 3.4, the microwave field radiated upon the atoms comprises all three polarizations with unknown ratio. In addition, due to the experimental setup, a change of magnetic field value can also be accompanied by a change in the direction of the magnetic field, which also changes the direction of the quantization axis. Therefore, even for constant ratios of polarization components in the microwave field, the relevant

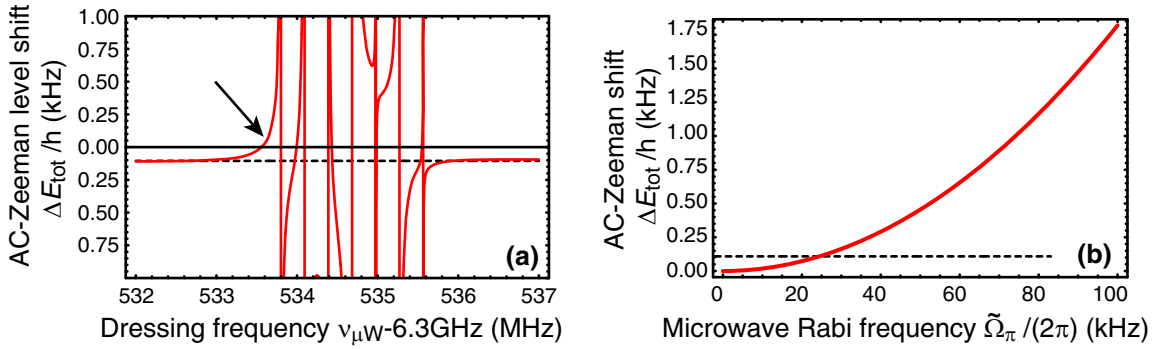

Figure 4.14: **(a)** Expected level energy shift due to AC-Zeeman effect for a microwave coupling of $\tilde{\Omega}_\pi = 2\pi \times 2.5\,\mathrm{kHz}$ at a magnetic field of $B = 0.4\,\mathrm{G}$ (solid line). The dashed line indicates the energy of the detuning $\delta_{if} \approx -105\,\mathrm{Hz}$ for the spin oscillations at this magnetic field. For the experiments and part (b), we choose the dressing frequency $\nu_{\mu\mathrm{W}} \approx 533.545\,\mathrm{MHz}$, marked by the arrow. **(b)** AC-Zeeman level shift as a function of the coupling strength $\tilde{\Omega}_\pi$ at the same conditions as in (a) and the microwave field tuned to the arrow position. From the graph we find that for a microwave Rabi frequency around $\tilde{\Omega}_\pi \approx 2\pi \times 23\,\mathrm{kHz}$ the spinor detuning can be compensated for by the AC-Zeeman shift.

projections onto the quantization axis can change with magnetic field. In order to work under controlled conditions, we fix in the following the magnetic field value at which the spin-changing collisions can occur to $B \approx 0.42\,\mathrm{G}$ and calibrate the different polarization components I_q by driving fast single-particle Rabi oscillations starting from $|f = 1, m = -1\rangle$ and ending in $|f = 2, m = -1 + q\rangle$. Thereby we obtain $\frac{I_{\sigma^-}}{I_\pi} \approx 0.33(2)$, and $\frac{I_{\sigma^+}}{I_\pi} \approx 0.02(1)$.

With this we can calculate the energy shift on the relevant quantity for the spin oscillation process as

$$\Delta E_{\mathrm{f=1}} = 2\,\Delta E_0 - (\Delta E_{+1} + \Delta E_{-1}). \tag{4.22}$$

Assuming a moderate coupling strength of $\tilde{\Omega}_\pi = 2\pi \times 2.5\,\mathrm{kHz}$, we plot the change of $\Delta E_{\mathrm{f=1}}$ when changing the microwave frequency $\nu_{\mu\mathrm{W}}$ in Fig. 4.14(a). The positions of the seven resonances coincide with the possible transition frequencies calculated at the given magnetic field with the Breit-Rabi formula. We observe only seven instead of nine as there are two degenerate pairs ($|f = 1, m = \pm 1\rangle \rightarrow |f = 2, m = 0\rangle$ is quasi-degenerate with $|f = 1, m = 0\rangle \rightarrow |f = 2, m = \pm 1\rangle$ at these low magnetic field values and for our frequency resolution). These degeneracies are lifted by higher order contributions of the Zeeman shift for larger magnetic field values. In order to choose the correct dressing frequency $\nu_{\mu\mathrm{W}}$, one has to consider two constraints. First, as the difference energy $\hbar(\delta_{\mathrm{int}} + \delta_B)$ is negative at any magnetic field, i.e. the two-particle state $|1, 0; 1, 0\rangle$ has a lower energy than $|1, -1; 1, +1\rangle$, the AC-Zeeman shift has to be positive. As depicted in Fig. 4.14(a) there are several regions where the AC-Zeeman energy shift can counteract this detuning. However in an experiment, any transition to the $f = 2$ hyperfine manifold is unwanted as this will destroy the coherent spin changing collisions. Therefore the detuning Δ between the atomic transitions and

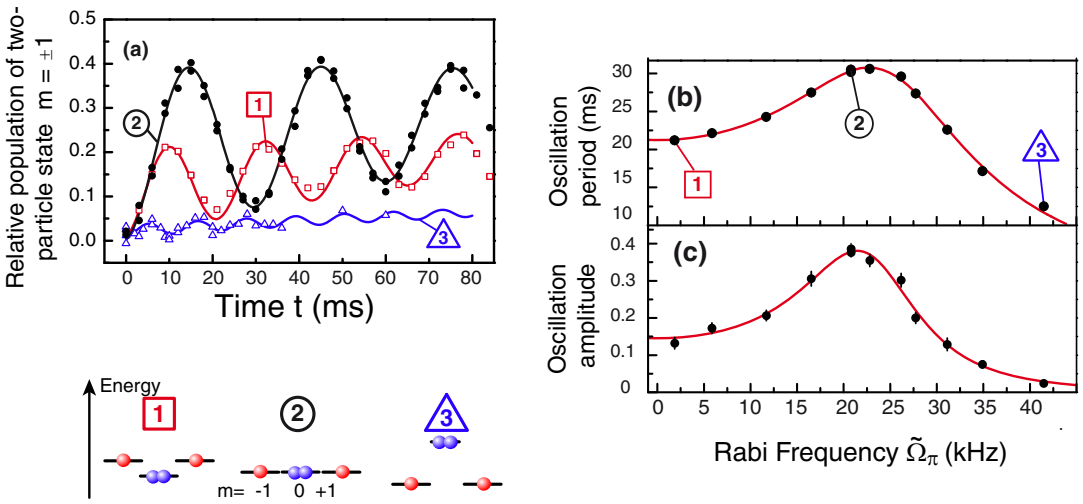

Figure 4.15: **(a)** Measured spin population oscillations for the process $|0;0\rangle \leftrightarrow |-1;+1\rangle$ at $B = 0.4\,\mathrm{G}$ and various intensities of the dressing microwave radiations: (1) $\tilde{\Omega}_\pi = 0$; (2) $\tilde{\Omega}_\pi = -\delta_{if}$; (3) $\tilde{\Omega}_\pi > \delta_{if}$. The microwave frequency is set to $\nu_{\mu\mathrm{W}} = 533.545\,\mathrm{MHz}{+}6.3\,\mathrm{GHz}$. From this type of curves we extract oscillation period **(b)** and amplitude **(c)** versus the microwave coupling strength $\tilde{\Omega}_\pi$. Both curves show a maximum, indicating resonant coupling. The solid lines are fits to the Rabi model including the AC-Zeeman energy shift.

the microwave field should be as large as possible. We choose a frequency which is red detuned from any hyperfine transition at $\nu_{\mu\mathrm{W}} = 533.545\,\mathrm{MHz}{+}6.3\,\mathrm{GHz}$, which is still in the region of positive energy shift ΔE_{tot}. This is marked by an arrow in Fig. 4.14(a). Using this frequency, we calculate the energy shift that can be achieved versus the microwave coupling strength $\tilde{\Omega}_\pi$ in Fig. 4.14(b). Apparently, the AC-Zeeman shift can easily compensate the spin oscillation detuning (i.e. for a dressing Rabi frequency of $\tilde{\Omega}_\pi \approx 2\pi \times 23\,\mathrm{kHz}$), and even overcompensate it, which is important in case the interaction shall be completely switched off.

The experimental sequence to observe the effect of the detuned microwave field on the atoms is similar to the one introduced above for $f = 1$. In addition, after the second pulse preparing the atoms in $|f = 1, m = 0\rangle$, we add a microwave dressing field which introduces an AC-Zeeman shift. For different values of the microwave intensity, i.e. different values of $\tilde{\Omega}_\pi$, we study the behavior of the spin population oscillations. We present a result of such an experimental sequence in Fig. 4.15(a). The data shows that the Rabi oscillations can indeed be tuned into resonance, when amplitude and oscillation period are maximal. This can be seen when the oscillation period and amplitude are plotted versus the microwave coupling strength $\tilde{\Omega}_\pi$ in Fig. 4.15(b) and (c), respectively. The values for the resonant coupling strength extracted from the period ($\tilde{\Omega}_{\mathrm{res}} = 2\pi \times 22.8(2)\,\mathrm{kHz}$) and amplitude ($\tilde{\Omega}_{\mathrm{res}} = 2\pi \times 21.7(3)\,\mathrm{kHz}$) are in good agreement with the calculated value given above.

A non-destructive probe for atom pairs

This method thus offers a convenient tool to control the spin changing collisional interaction, independent of the external magnetic field. Resonant spin changing collisions have also been observed for different magnetic fields by choosing the dressing frequency properly [27]. Since the microwave field can be switched fast ($\approx 100\,\mathrm{ns}$) compared to all relevant time scales in the experiment, the interaction can be literally switched on and off. This is in particular important when the spin changing interaction is supposed to be applied in a pulsed-like manner for a well defined time.

Moreover, on resonance, the Rabi model predicts unity transfer efficiency from the initial to the final state. Therefore, dressed spin changing collisions constitute a quantitative probe of particle pairs in the optical lattice. After half an oscillation period t_π, the populations of the different Zeeman sublevels directly reflect the atom number distribution throughout the lattice. In the case of $f = 1$, after an interaction time t_π the isolated atoms will all be in $|f = 1, m = 0\rangle$, whereas the number of atoms in doubly occupied sites corresponds to the population of the $m = \pm 1$ Zeeman levels. Even more appealing, this pair probe is non-destructive, as the dynamics can be reversed in the resonant case, and the initial state can be restored. As will be demostrated in Section 4.6, this probe for particle pairs gives rise to many intriguing applications.

In addition, based on this atom pair probe, we could propose a method to transform an inhomogeneous Mott-insulator with shells including singly and doubly occupied sites into a system with only singly occupied sites. For this, only an alternating sequence of π-pulses for spin changing population oscillations on the one hand and single particle microwave pulses on the other hand has to be applied [27].

4.5 Nature of the magnetic ground state

The experimentally determined values of the coupling parameters for the spin-changing interaction presented in Section 4.3 have wide reaching consequences on interactions in the two hyperfine ground states of ^{87}Rb. In particular, their knowledge contains all information about the spin dependent part of the interaction potential. The value of the inferred scattering length differences e.g. determines the particular relative spin orientation which has the smallest spin dependent interaction energy. The many-body state minimizing the spin-dependent interaction energy is called magnetic ground state.

For interacting spin-1 gases this magnetic ground state can be either ferromagnetic or antiferromagnetic in nature, i.e. spin dependent interactions favour the relative orientation of two atomic spins to be either parallel or antiparallel. In the spin-2 case an additional cyclic phase can also arise (see e.g. Refs. [106, 107]). Here spin-spin correlations are revealed for three particles, whose spin orientations tend to form an equilateral triangle in a plane. The phase diagram for both spin states is depicted in Fig. 4.16 as a function of one (two) interaction parameters for $f = 1$ ($f = 2$), which will be defined below. These systems are promising in order to study quantum magnetism phenomena [22, 105, 106, 46], and to create strongly correlated magnetic quantum states in optical traps [107, 119, 120, 121, 122]

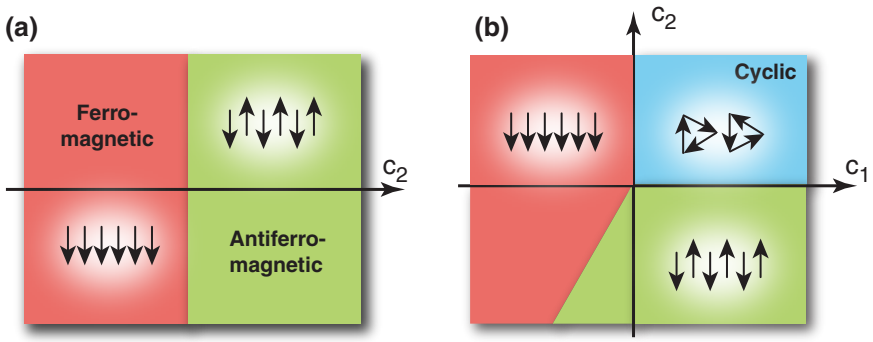

Figure 4.16: Phase diagram of the magnetic ground state for ^{87}Rb in **(a)** $f = 1$ and **(b)** $f = 2$. The diagram is shown as a function of specific parameters defined below in Eq. (4.23) and (4.24).

and optical lattices [123, 124, 125, 126, 127, 15, 128, 129, 130, 131].

The magnetic ground state of the hyperfine ground states in ^{87}Rb has been addressed in many experiments on multi-component quantum gases [99, 100, 101, 108]. In order to identify the magnetic ground state of spin-1 ^{87}Rb BECs the dynamics of such systems has been experimentally investigated [99, 100]. There, a slow spin dynamics has been observed on a second timescale leading to a final state close to the predicted ferromagnetic ground state at zero external magnetic field. Recently, an experiment observing coherent spin dynamics in a BEC [108] has shown the spin-1 magnetic ground state of ^{87}Rb to be ferromagnetic. For spin-2 ^{87}Rb atoms, the magnetic ground state has been predicted to be antiferromagnetic, but close to the phase boundary of the cyclic phase. Recent experiments [99, 101], again observing the spin dynamics for various population of the Zeeman sublevels, seem to agree with this prediction. One problem, however, arises from the fact that even small magnetic fields can perturb the system and pin it to some configuration which is not the ground state at zero external field. Another difficulty in precisely determining the ground state stems from the fact that the differences of the scattering lengths driving the spin dynamics is very small (typically only a few percent of the bare scattering lengths), so that the time scale on which the system relaxes to its ground state is very long. More recently, a novel method has been proposed theoretically to identify the magnetic ground state of ^{87}Rb spin-2 atoms [132] circumventing many of the problems described above. By preparing an initial state with controlled population and phases of the Zeeman sublevels, the initial dynamics of the system would reveal the nature of the spin singlet term.

Here, we present a different approach and introduce a method based on the coherence of the spin evolution. The absolute value and sign of the various spin-dependent interaction terms in the Hamiltonian can be directly deduced from the observed coherent Rabi-type oscillations in an optical lattice driven by spin changing collisions [25]. From the measured oscillation frequencies we are able to infer the coefficients in the interaction Hamiltonian and the value of the differences in scattering lengths. The knowledge of these allow in

turn to determine the magnetic ground state. There are several advantages of this method compared to similar experiments in the mean field regime. First, in our system the spatial degree of freedom is frozen, so that any dynamics observed can be attributed to the spin interaction only. Second, the optical lattice leads to a significant enhancement of the coupling strength determining the time scale of the spin-changing dynamics. Therefore, even for the spin-2 case where strong losses are present, coherent spin-changing collisions can be observed.

As explained in the introduction, the relative orientation of two spins in a collisional event changes the actual interaction strength. In order to determine the particular orientation that minimizes the mean field energy at zero magnetic field, i.e. the magnetic ground state, it is convenient to express the interaction potential in terms of spin-independent and spin dependent parts (see e.g. [22, 133]).

For the spin-1 case this yields the potential

$$V_S = c_0 + c_2 \mathbf{f}_1 \cdot \mathbf{f}_2, \tag{4.23}$$

where $c_0 \equiv (4\pi\hbar^2/M) \times (a_0 + 2a_2)/3$ is the spin-independent part, and $c_2 \equiv (4\pi\hbar^2/M) \times (a_2 - a_0)/3$ describes spin-spin interactions. For the antiferromagnetic or polar phase, the mean field energy according to (4.1) is minimized by aligning the spins of two interacting atoms anti-parallel, and it emerges for $c_2 > 0$, i.e. $a_2 > a_0$ [22], whereas the mean field energy in the ferromagnetic case is minimized by aligning the spins parallel, implying $c_2 < 0$ (see Fig. 4.16(a)).

In a similar way, the interaction potential for the spin-2 case can be written as [133]

$$V_S = c_0 + c_1 \mathbf{f}_1 \cdot \mathbf{f}_2 + 5c_2 \mathcal{P}_0. \tag{4.24}$$

Here, $\mathcal{P}_0$ is a projector onto the singlet subspace, $c_0 \equiv (4\pi\hbar^2/M) \times (4a_2 + 3a_4)/7$ describes the spin-independent part, $c_1 \equiv (4\pi\hbar^2/M) \times (a_4 - a_2)/7$ determines the spin-spin interaction and $c_2 \equiv (4\pi\hbar^2/M) \times (7a_0 - 10a_2 + 3a_4)/7$ accounts for the interaction between spin-singlet pairs. Differently from the spin-1 case, there exist three possible phases for a spin-2 Bose-gas at zero magnetic field. In addition to the ferromagnetic and antiferromagnetic phases the system can have a cyclic phase. In this phase the spin orientation of three interacting particles tend to form an equilateral triangle in a plane. The phase diagram is now two dimensional, depending on the spin-dependent coefficients c_1 and c_2 as shown in Fig. 4.16(b). The ground state is ferromagnetic for $c_1 < 0$ and $c_1 - c_2/20 < 0$, antiferromagnetic for $c_2 < 0$ and $c_1 - c_2/20 > 0$, and cyclic for $c_1 > 0$ and $c_2 > 0$.

A summary of the values for the spin-dependent coefficients in $f = 1$ and $f = 2$ determined from the frequency measurement of the coherent spin dynamics is given in Table 4.2 together with the theoretically predicted values that show in general good agreement. For the spin-1 case the inferred coefficient c_2 clearly shows a ferromagnetic ground state at zero magnetic field. For the spin-2 case the coefficients point towards the antiferromagnetic ground state within our error bars. The coefficient c_1 clearly excludes a ferromagnetic ground state. For the coefficient c_2,however, slight changes in, e.g., the fit procedure can imply large changes of the resulting fit value and strongly increases the uncertainty on this

f	$c_i/(4\pi\hbar^2/M)$	Measured $\Delta a/a_B$	Predicted $\Delta a/a_B$
$f = 1$	c_2	$-0.36^{\pm 0.01}_{\pm 0.01 \pm 0.02}$	-0.46
$f = 2$	c_1	$+0.99^{\pm 0.01}_{\pm 0.01 \pm 0.04}$	$+1.1$
	c_2	$-0.53^{\pm 0.2}_{\pm 0.18 \pm 0.2}$	-0.05

Table 4.2: Summary of the measured coefficients of the spin-dependent interaction (4.23,4.24). The errors are the statistical errors (upper row) and the systematic errors (lower row, first number due to magnetic field, second due to lattice potential). The calculated values are based on recently predicted scattering lengths [47, 111].

value. The theoretically predicted coefficient is so small that for most practical situations the expected interaction energy arising from this term will be also small. This implies that other terms in energy are easily dominant and that the time scales to reach the magnetic ground state are extremely long.

It should be noted that the statements about the magnetic ground state of the system made above hold equally for the measured interaction detunings δ_i. These quantities, however, are still free from systematic errors due to the optical potential.

4.6 Applications

In summary, we have shown that both hyperfine states of ^{87}Rb show collisionally driven spin oscillations between two-particle states in a deep optical lattice. The oscillations can be described by a Rabi-model for a broad range of parameters. In the case where two final states are accessible, the observed spin dynamics can be explained by a coupled three-level system.

The parameters of the Rabi model are directly related to differences of the scattering lengths in the ^{87}Rb hyperfine states $f = 1$ and $f = 2$. The measured values can be compared to calculations based on recent theoretical predictions of the scattering lengths, and show good agreement. The residual deviation from the predicted values may be due to a systematically different value of the parameter $\tilde{U}$ as mentioned in Section 4.1.1, connecting the fundamental scattering length differences with the actual experimentally observed interaction energy. Another possibility might be small deviations of the scattering lengths from the theoretically calculated values. A resolution of the observed deviations requires further experimental and theoretical investigation.

The possibility to control resonant spin oscillations enabled a series of experiments yielding deeper insight about the SF to MI transition [11, 12] which will be presented in the following.

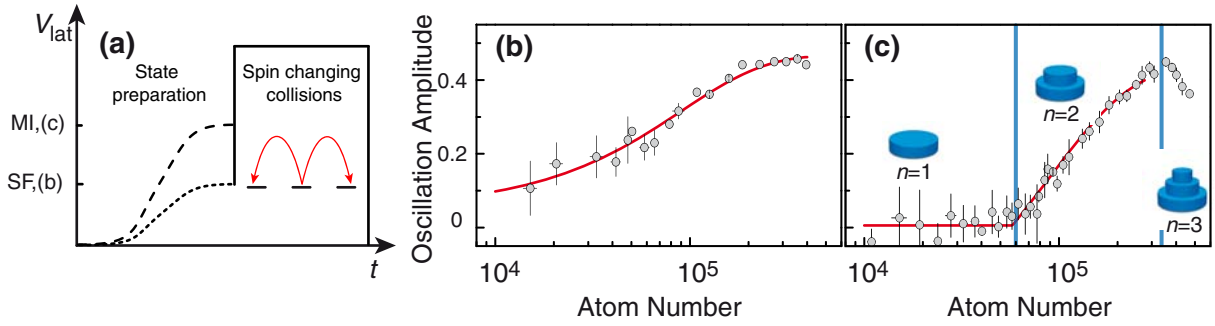

Figure 4.17: Number squeezing in the SF to MI transition. **(a)** The system is prepared either in a SF or in a MI situation in the optical lattice. The actual atom number distribution is frozen by a fast increase of the optical potential. Subsequently, the amplitude of resonance spin changing collisions is measured. **(b)** In case of shallow lattices in the SF regime, atom number fluctuations lead to a non-zero signal, i.e. atom pairs are present at some lattice sites, even for very low total atom number $\bar{\nu} < 1$. The signal increases with increasing total atom number as the Poissonian distribution predicts a larger probability for double occupancy. **(c)** In case of a deep lattice potential, i.e. in the MI regime, the atom number fluctuations are suppressed, and for low total atom number only sites with unity filling are occupied. Starting from $\sim 6 \times 10^4$ atoms, a shell with $\bar{\nu} = 2$ starts to form. Consequently, the atom pairs can undergo a spin changing collisional event, and the detected signal becomes non-zero. The solid lines are guides to the eye.

4.6.1 Number squeezing in the superfluid to Mott-insulator transition

The superfluid (SF) to Mott-insulator (MI) quantum phase transition in a 3D optical lattice [1] was one of the first examples of a strongly correlated quantum phase, experimentally realized in an ultracold atomic system. Since then it has attracted a lot of attention and initiated large theoretical and experimental effort to further understand the system and exploit its properties for quantum information processing or solid state simulations. In the first experiments, the quantum phase transition was observed through the signature of a loss of phase coherence and an opening gap for excitations on the order of the interaction energy U in the MI region [1]. As explained in Section 3.3, the ground states of the Bose-Hubbard Hamiltonian exhibit another striking difference: In the SF regime, atom number fluctuations should be present and the on-site atom number should follow a Poissonian distribution. In the MI region in contrast these fluctuations are expected to be suppressed and only a well defined, constant atom number should be observed in an experiment. This atom number squeezing in the MI region can now be investigated using the non-destructive atom pair probe developed earlier in this chapter.

The experimental sequence and results can be found in Ref. [11] and will be only briefly outlined here. The main idea is to selectively detect different occupation numbers of atoms in the system for changing lattice depth and changing total atom number. We use resonant spin changing collisions as a probe for particle pairs. Here it becomes important that the interaction strength is occupation number dependent. Hence, if the AC-Zeeman effect tunes

atom pairs into resonance for the spin changing collisions, the atom triples are not resonant and the spin population conversion is strongly suppressed [11]. In the experiment, the system is prepared with a certain atom number in either a superfluid or a Mott-insulating state. In order to freeze out the actual atom number distribution (Poissonian in case of a SF or Fock states in case of a MI), the optical potential is quickly (within $\approx 50\,\mu$s) increased to a value where tunneling is strongly suppressed, see Fig. 4.17(a). In this situation, resonant spin changing collisions can be employed and yield a quantitative measure of the number of atom pairs in the originally prepared quantum state. For shallow lattices, the system is expected to be a superfluid. Atom number fluctuations of the Poissonian distribution in such a superfluid state are expected to lead to a non-zero amount of lattice sites with a filling of two, even when the overall filling is smaller than unity ($\bar{\nu} < 1$)[5]. This can be realized by preparing the system with a small total atom number. Indeed, in this case of small total atom number, the amplitude of the resonant spin changing collisions shows a finite value of doubly occupied sites, see Fig. 4.17(b). For larger mean filling $\bar{\nu}$, i.e. larger total atom number, the pair occupancy is expected to increase.

For deep lattice depth, such that the system is expected to be in the MI region, atom number fluctuations should be absent. In case of low total atom number $\bar{\nu} \leq 1$ there should be almost exclusively singly occupied lattice sites. Consequently, the signal of a spin-changing collision sequence should be close to zero. This can be seen in Fig. 4.17(c), where the signal of the spin changing collisions becomes non-zero only for total atom numbers starting from a value, where the shell with filling $n = 2$ is expected to form. For even larger total atom number a third shell is expected to appear; since the AC-Zeeman shift compensates the interaction detuning for one particular filling ($n = 2$ in our case), the triply occupied sites cannot show resonant population oscillations, and the signal of the pair probe Fig. 4.17(b) decreases.

4.6.2 Spatially resolving the Mott-insulator shells

The perfect MI is supposed to be a homogeneous array of equally populated lattice sites. In current experiments, however, a smoothly varying harmonic confinement on a large length scale makes the system inhomogeneous. The resulting distribution of occupation numbers has been calculated by e.g. a local chemical potential approach to take the form of a so-called wedding cake [76]. According to this distribution, in the center a region forms with constant filling, for example, $n = 2$. This region is surrounded by a superfluid shell. For larger distance from the center, another shell with constant, but small filling follows, here $n = 1$. Although a first consistent evidence has been obtained through the observation of number squeezing (see Fig. 4.17(b)), the predicted Mott-insulator shells with constant filling in each shell were not yet observed.

This could recently be achieved in our group [12] by combining a method to address the system with spatial resolution on the one hand with the occupation selective probe of spin changing collisions on the other hand. The spatial resolution was obtained by using

[5] The overall or mean filling $\bar{\nu}$ denotes the ratio of total atom number and number of occupied sites. In contrast, the onsite filling n is the number of atoms in a specific lattice well.

an analogue to nuclear magnetic resonance spectroscopy: Before the optical potential is applied, the BEC is held in a magnetic trap. Due to gravitation, however, it is not located at the magnetic field minimum, but at a position, where the magnetic gradient compensates the gravitational gradient. Thus, in the combined magnetic and optical potential, the system still experiences a (vertically oriented) magnetic gradient. This gradient exerts a spatially varying Zeeman shift onto the atomic sample. A narrow line-width microwave transition, tuned to a transition from $f = 1$ to $f = 2$, can now address only a small horizontal slice in the atomic system. The width of this slice can be approximately 3 to 5 lattice sites. In such a measurement, three quantities can be extracted as a function of vertical position, i.e. microwave frequency. First, the total atom number in such a slice is measured (see Fig. 4.18(a) to (c)). Furthermore, within this slice, resonant spin changing collisions can be induced, yielding the amount of particle pairs in each slice. Finally, the difference between the total number of atoms per slice and the number of pairs per slice can be calculated.

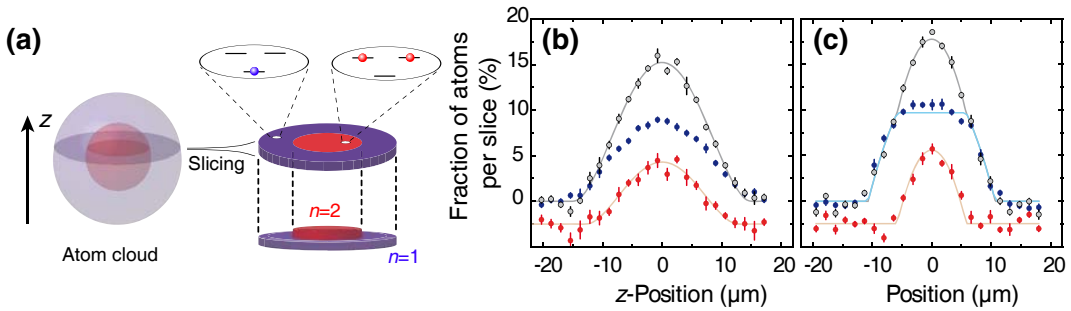

Figure 4.18: (a) By a technique similar to magnetic resonance tomography, only a thin slice of the trapped atom cloud is addressed, and the total atom number per slice is detected. Within this slice, atom pairs can undergo resonant spin changing collisions and change the Zeeman sublevel, while isolated atoms remain in their initial state. The final signal (cf. (b),(c)) yields the relative number of atom pairs (red, offset for clarity) and total number of atoms (gray) in each slice versus vertical position; the difference between the two curves (blue) corresponds to occupation numbers $n \neq 2$. Solid lines are fits to the expected model (see Ref. [12]). **(b)** Integrated density profile for a SF system. Doubly occupied sites are present even at the borders of the system and all occupation number show a similar density profile. **(c)** Integrated density profile for a MI with occupation numbers of $n = 1$ and $n = 2$. The $n = 2$ shell is concentrated to the center of the cloud, as expected from the predictions of a wedding cake structure in the inhomogeneous MI. The flat-top profile of the $n = 1$ shell is clearly visible. For details see Ref. [12]

An example for each of the two ground states shows the marked difference between the two regimes: The density profile in the SF regime (Fig. 4.18(b)) shows a Thomas-Fermi like distribution for all observed occupation numbers, in this case $n = 2$ on the one hand and $n \neq 2$ on the other hand. In particular, the $n = 2$ shell extends to the very border of the system, as expected in the SF ground state. This is in strong contrast to the profile observed in the MI region (Fig. 4.18(c)), where the profile of $n = 2$ has an inverted parabola profile,

as expected from an integrated sphere-like distribution with constant filling. Moreover, the $n = 2$ shell does not extend to the border of the system, but is indeed limited to the core of the atom cloud. Furthermore, the spatial distribution for $n \neq 2$, which corresponds to $n = 1$ in our case, exhibits a striking flat top profile, as expected from a shell embracing the inner core.

This measurement has been the first conclusive evidence for the formation of a shell structure in the inhomogeneous MI where the signal of resonant spin changing collisions allowed for a systematic investigation on how the $n = 2$ shell evolves with atom number. For details see Ref. [12]. It should be noted that occupation number dependent detection with spatial resolution in a 3D lattice system has also been realized in [134].

4.7 Conclusion

In this chapter, the coherent spin changing interaction between two atoms in an optical lattice has been discussed. The dynamics has been investigated in three different cases that can be realized in the present system. For most of the cases, the problem simplifies to a Rabi model which describes the observed dynamics quantitatively. The relevant parameters driving the spin changing collision could be related to fundamental scattering length differences that have been extracted from the measurements. These parameters determine the magnetic ground state of the system. For ^{87}Rb in the two hyperfine ground states $f = 1$ and $f = 2$ the magnetic ground state could be determined to be ferromagnetic and antiferromagnetic, respectively, in agreement with theoretical predictions.

Furthermore, a method to control the detuning of the spin population oscillations based on a selective levelshift has been introduced. This level shift could be realized by a detuned microwave field exerting an AC-Zeeman shift onto the various Zeeman sublevels. Using this novel technique, fully resonant population transfer between two-particle Zeeman states could be achieved.

This enabled a series of experiments, giving a more detailed insight into the SF to MI transition [11, 12]. The high degree of control and precision in the measurements combined with the intriguing properties of the states created by this interaction makes it a well suited tool for further quantum state engineering of correlated spin states. Some promising prospects will be outlined in Section 6.1.

5 Coherent interaction induced phase evolution

One of the most fascinating differences between the quantum world and every day "classical" life is the existence of states that exhibit non-trivial quantum correlations or entanglement. These quantum properties are an important prerequisite in many proposals for quantum information schemes or applications and experiments investigating quantum effects. The creation, analysis and application of such states is a focus of current research with ultracold atoms. This chapter describes one of the paths to the creation of correlated states by time evolution of an initially uncorrelated state in the presence of non-linear interactions [135, 136, 137, 138, 102, 139]. In general (for a review see [23]), a two-mode system is considered, where the two modes can be realized for example as two superconducting regions of a Josephson junction, the two sites of a double well potential, two internal spin states etc. Two additional conditions have to be fulfilled in order to observe the emergence of non-classical correlations is such systems. First, the two modes have to have a well defined relative phase. Second, the system has to be interacting. With these requirements, the relative phase between the two modes can exhibit a fascinating time evolution from an initially classical state via squeezed states to maximally entangled Schrödinger cat states.

In the following the case of effective spin 1/2 systems will be discussed, where the two spin states are "encoded" in the internal total angular momentum states of the ^{87}Rb atoms. In Section 5.1 the basic idea of interaction induced phase evolution will be introduced in a discussion of two spin-1/2 particles. This will be extended to the general case of N spin-1/2 particles in Section 5.2. Here the full phase evolution is calculated. It turns out that for these systems the speed of the non-trivial phase evolution depends on the relative strength of various scattering lengths in the problem. In a typical experimental realization this scattering length difference is very small. In order to speed up the phase evolution significantly, the relevant interaction strengths have to be enhanced, which can be achieved by the method of magnetic Feshbach resonances. This method allows to selectively tune particular scattering lengths and will be introduced in Section 5.3. The resonance which is eventually used in the experiments will be presented together with a novel, so far unknown hyperfine Feshbach resonance.

The situations of either two interacting particles or of an interacting many-body state can be experimentally realized in optical lattices, where in a 3D lattice atom pairs are trapped at many lattice sites and are isolated from their environment. The experimental realization of a two-particle entanglement oscillation in an array of such isolated atom pairs is presented in Section 5.4. Similarly, in a 2D optical lattice potential, an array of mesoscopic interacting quantum gases can be created, and the intriguing coherent time evolution of their relative phase mentioned above can be investigated. This will be demonstrated in Section 5.5.

Note added — Just recently, the data presented in Section 5.5 on spin dynamics in a many-body system have been re-interpreted. In the new model, the intrinsic fluctuations in relative phase between the two spin states arising from the deep 1D configuration could be modeled in a Luttinger liquid approach. This model could quantitatively reproduce the enhanced contrast drop close to the Feshbach resonance as well as the partial revivals observed in this work [1].

5.1 Interactions between two spin-1/2 systems

Arguably the simplest yet non-trivial model in quantum mechanics is the coupled two-level system, already considered in previous chapters. Here, this model will be considered in order to understand the basic effects that an interaction induced phase evolution can have on such a system. In the following we consider the two states $|\uparrow\rangle$ and $|\downarrow\rangle$, separated by an energy difference $\hbar\omega_0$. Two such two-level systems are allowed to interact. The effect of this interaction on the relative phase between the two spin states is investigated. As in chapter 2, we assume different interaction strengths for the intra-species and inter-species scattering, i. e. there are three relevant scattering lengths $a_{\uparrow\uparrow}$, $a_{\downarrow\downarrow}$ and $a_{\uparrow\downarrow} = a_{\downarrow\uparrow}$, where the last equality holds due to symmetry reasons.

5.1.1 State evolution of two interacting particles

In order to calculate the effect of the spin-dependent interaction, let us assume two particles trapped in a deep potential well. Tunneling is sufficiently small for the atoms to stay trapped on a time scale long compared to any interaction effect. Furthermore, any interaction energy is smaller than the energy needed to excite atoms into higher vibrational states. Consequently, we will consider the atomic spin wave function only, as the spatial wave function can be assumed stationary on the time scale of the spin evolution. We assume that both atoms are initially in a coherent superposition of the two internal states by applying a $\pi/2$-pulse to the spin polarized state in $|\downarrow\rangle$. The resulting two-body wave function can be written as

$$\begin{aligned} |\psi\rangle_i &= \frac{1}{\sqrt{2}}\left(|\downarrow\rangle - |\uparrow\rangle\right) \otimes \frac{1}{\sqrt{2}}\left(|\downarrow\rangle - |\uparrow\rangle\right) \\ &= \frac{1}{2}\left(|\downarrow\downarrow\rangle - |\downarrow\uparrow\rangle - |\uparrow\downarrow\rangle + |\uparrow\uparrow\rangle\right), \end{aligned} \tag{5.1}$$

where for simplicity we have contracted $|\psi_1\rangle \otimes |\psi_2\rangle = |\psi_1\ \psi_2\rangle$. The coherent superposition therefore can be considered as a combination of all possible relative spin orientations of the two spins involved as illustrated in Fig. 5.1.

[1] A. Widera et al. *Quantum spin dynamics of squeezed Luttinger liquids in two-component atomic gases*, to be published.

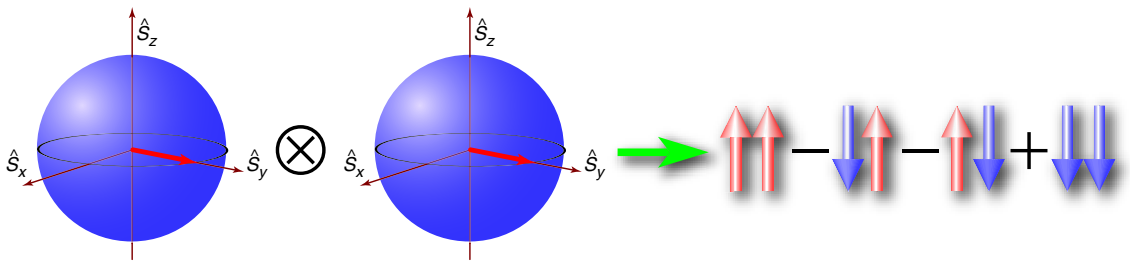

Figure 5.1: The two-particle state of two equal weight coherent superpositions can be seen as a combination of all possible relative spin orientations.

In the presence of interactions in the ultracold regime, each term acquires an interaction phase according to the interaction energy U_{ij} (cf. Eq. (2.11)) as

$$\phi_{ij} = \frac{U_{ij}}{\hbar} \times t. \tag{5.2}$$

Here, i (j) labels the state of the first (second) atom and can take the values $|\uparrow\rangle$ and $|\downarrow\rangle$. For the three scattering lengths, we find three interaction phases for a given interaction time, $\phi_{\uparrow\uparrow}$, $\phi_{\downarrow\downarrow}$ and $\phi_{\uparrow\downarrow} = \phi_{\downarrow\uparrow}$. Therefore after some interaction time t the state of the two interacting particles will read

$$|\psi(t)\rangle = \frac{1}{2}\left(e^{i\phi_{\downarrow\downarrow}}|\downarrow\downarrow\rangle - e^{i\phi_{\downarrow\uparrow}}\left(|\downarrow\uparrow\rangle + |\uparrow\downarrow\rangle\right) + e^{i\phi_{\uparrow\uparrow}}|\uparrow\uparrow\rangle\right). \tag{5.3}$$

The situation can be simplified by an approximation reflecting the experimental situation. As we will see in later sections, the scattering length $a_{\downarrow\downarrow} \approx a_{\uparrow\uparrow}$, so that we introduce the average interaction phase $\tilde{\phi} = (\phi_{\downarrow\downarrow} + \phi_{\uparrow\uparrow})/2$ and assume the two states $|\downarrow\downarrow\rangle$ and $|\uparrow\uparrow\rangle$ to both evolve with this average phase. In addition, we factor out the inter-species interaction phase $\phi_{\downarrow\uparrow}$. Thus we find

$$|\psi(t)\rangle = \frac{1}{2}e^{i\phi_{\downarrow\uparrow}}\left(e^{i(\tilde{\phi}-\phi_{\downarrow\uparrow})}|\downarrow\downarrow\rangle - \left(|\downarrow\uparrow\rangle + |\uparrow\downarrow\rangle\right) + e^{i(\tilde{\phi}-\phi_{\downarrow\uparrow})}|\uparrow\uparrow\rangle\right). \tag{5.4}$$

This can be further simplified by defining the effective interaction phase $\phi_\chi \equiv \tilde{\phi} - \phi_{\downarrow\uparrow}$. Omitting the overall phase factor $e^{i\phi_{\downarrow\uparrow}}$, the state after time t reads:

$$|\psi(t)\rangle = \frac{1}{2}\left(e^{i\phi_\chi}|\downarrow\downarrow\rangle - \left(|\downarrow\uparrow\rangle + |\uparrow\downarrow\rangle\right) + e^{i\phi_\chi}|\uparrow\uparrow\rangle\right). \tag{5.5}$$

The effective interaction phase ϕ_χ corresponds to an effective difference of interaction strengths which can be characterized by the energy

$$\hbar\chi = \frac{U_{\uparrow\uparrow} + U_{\downarrow\downarrow} - 2\,U_{\downarrow\uparrow}}{2}. \tag{5.6}$$

This effective spin dependent interaction energy, which is introduced here phenomenologically, will be defined more thoroughly in Eq. (5.26). In the single-mode approximation,

i.e. assuming that only one spatial mode is present for all spin states, this can be mapped onto a difference of scattering lengths

$$a_\chi \equiv \frac{a_{\uparrow\uparrow} + a_{\downarrow\downarrow} - 2\,a_{\downarrow\uparrow}}{2}. \tag{5.7}$$

The effective interaction phase ϕ_χ fully determines the intriguing time evolution of the two-particle state. In order to better study this evolution, a second $\pi/2$-pulse is applied to the state $|\psi(t)\rangle$ after the interaction in order to map the relative phase onto the populations of the internal states. The state then reads

$$|\psi\rangle_f = \frac{1}{2}\left\{\left(e^{i\phi_\chi} - 1\right)|\downarrow\downarrow\rangle + \left(e^{i\phi_\chi} + 1\right)|\uparrow\uparrow\rangle\right\}. \tag{5.8}$$

The properties of the final state now crucially depend on the effective interaction phase ϕ_χ. One can distinguish four important cases:

1. For vanishing interaction time, $\phi_\chi = 0$ and the final state becomes

   $$|\psi\rangle_f = |\uparrow\uparrow\rangle = |\uparrow\rangle \otimes |\uparrow\rangle \tag{5.9}$$

   just as expected from two subsequent $\pi/2$ pulses. In particular the state is separable.

2. For interaction times leading to $\phi_\chi = \pi/2$, the final state reads

   $$|\psi\rangle_f = \frac{1}{2}\left\{(i-1)|\downarrow\downarrow\rangle + (i+1)|\uparrow\uparrow\rangle\right\}. \tag{5.10}$$

   This state cannot be written as a product state any more. Up to the phase factors the state resembles the well known entangled Bell-state $|\mathrm{BELL}\rangle = (|\downarrow\downarrow\rangle + |\uparrow\uparrow\rangle)/2$. Here, the spins are perfectly correlated and therefore this state is of great importance in quantum mechanics [21].

3. For even longer interaction times, such that $\phi_\chi = \pi$, the final state is

   $$|\psi\rangle_f = -|\downarrow\downarrow\rangle = -|\downarrow\rangle \otimes |\downarrow\rangle, \tag{5.11}$$

   which is a separable state again.

4. For even larger effective interaction phases, the state entangles and disentangles again, until for $\phi_\chi = 2\pi$ the initial state is restored:

   $$|\psi\rangle_f = |\uparrow\uparrow\rangle = |\uparrow\rangle \otimes |\uparrow\rangle. \tag{5.12}$$

Due to the periodicity of the phase evolution, this entangling-disentangling dynamics is periodic with the effective interaction phase ϕ_χ. The time scale of the dynamics is given by the interaction energy $\hbar\chi$, or equivalently the scattering length difference a_χ.

This rather simple case of two particles already shows how interactions can lead to a non-trivial phase evolution and evolve an initially classical state into a non-classical, entangled state with fascinating properties.

5.1.2 Ramsey interferometry as a measure for entanglement

In order to detect the entanglement evolution of the two-particle state, outlined in eqs. (5.9-5.12), we make use of the fact that the sequence leading to the final state is essentially a Ramsey sequence. In a Ramsey interferometer as introduced in Section 3.4.4 the coherence properties of the system are probed by mapping the relative phase between the two spin states onto the population of these states. The fringe for one particular interaction time is obtained by scanning the phase α of the last $\pi/2$-pulse. This general final state for the interacting two-particle system is more complicated than the expressions (5.9-5.12). The probability of finding an atom in state $|\uparrow\rangle$ is given by

$$P_\uparrow = \frac{1}{2}(1 + \cos\phi_\chi \ \cos\alpha). \tag{5.13}$$

A detailed calculation of this probability can be found in Appendix B.1. Compared to the usual Ramsey fringe Eq. (3.43), the probability (5.13) is in addition modulated by the effective interaction phase ϕ_χ. Without interactions, the usual Ramsey fringe (3.43) is recovered. However, for the entangled state (5.10) the final signal of a Ramsey fringe would yield $P_\uparrow = 1/2$ irrespective of the particular value of α. Consequently the Ramsey fringe is collapsed.

This fact has already been observed in other context [58, 78, 140] for highly entangled two-particle and many-particle states. The collapse of the Ramsey fringe can be understood in a simple picture. If a single entangled entangled pair of the form $(|\uparrow\uparrow\rangle + |\downarrow\downarrow\rangle)/2$ is considered, a measurement will always yield a correlated result. Thus, either both atoms are detected in state $|\uparrow\rangle$ or none. Calculating the total Ramsey fringe signal, in particular Eq. (5.13), involves a quantum mechanical ensemble average. Although in an ensemble each individual system yields a correlated outcome, they are not correlated among each other. The individual results rather add up incoherently, so that in each realization on average half the atoms are in $|\uparrow\rangle$ and half are in $|\downarrow\rangle$. Consequently the total detected signal will always yield a probability of $P_\uparrow = 1/2$ independent of the phase α. In order to reveal the underlying quantum spin-correlations, higher order correlation functions would have to be considered.

A quantitative measure of the entanglement dynamics (5.9-5.12) can be defined through the visibility of the Ramsey fringe

$$\mathcal{V} \equiv \frac{\max_\alpha P_\uparrow - \min_\alpha P_\uparrow}{\max_\alpha P_\uparrow + \min_\alpha P_\uparrow}, \tag{5.14}$$

which for the two-particle system evolves as

$$\mathcal{V} = |\cos\phi_\chi|. \tag{5.15}$$

In particular, for a separable state ($\phi_\chi = n\pi, \ n = 0, 1, \ldots$) the visibility reaches unity, whereas it is zero for a maximally entangled state ($\phi_\chi = (2n+1)\pi/2, \ n = 0, 1, \ldots$). The time evolution of such an entanglement oscillation is displayed in Fig. 5.2(b).

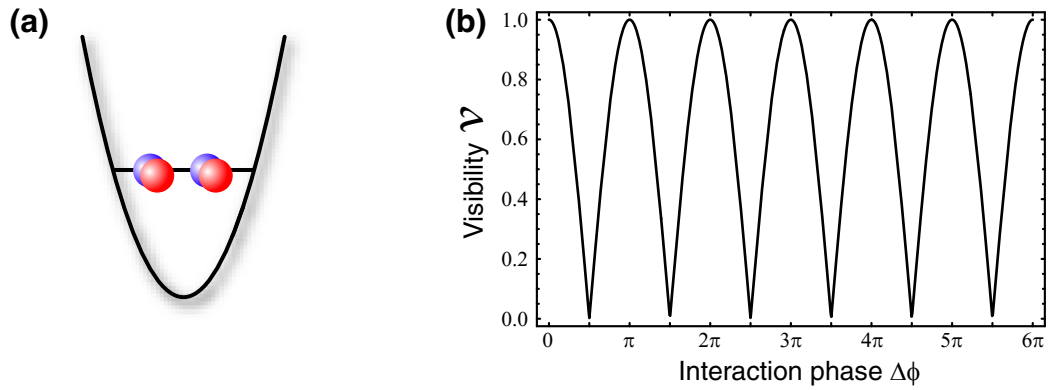

Figure 5.2: **(a)** The relative phase of two interacting spin-1/2 particles with internal spins $|\uparrow\rangle$ (red) and $|\downarrow\rangle$ (blue) can undergo an entanglement oscillation. **(b)** The resulting visibility of a Ramsey interferometer sequence exhibits oscillations, where the separable (classical) state is present for $\mathcal{V} = 1$ and the maximally entangled state for $\mathcal{V} = 0$.

The collapse of the Ramsey fringe is hence an indication for an entangled state. However, it is not a proof of entanglement, as decoherence also leads eventually to zero visibility. In the case of an incoherent state, however, there is no possibility that a time evolution could restore the coherence and the visibility could revive. The interaction induced collapse of the Ramsey fringe must therefore be distinguished from decoherence effects as in the final entangled state atom pairs are perfectly correlated. This can be seen by the phase dynamics (5.9-5.12) which shows that these correlations can be re-converted into coherence of the system. A full cycle of the dynamics as introduced above therefore shows the coherent entanglement evolution and rules out the ”trivial“ collapse due to decoherence.

5.2 Interactions in a many particle quasi spin-1/2 system

The two-particle example in the previous section already demonstrated how proper interatomic interactions can lead to a time evolution that evolves an initially classical state into a state with non-classical properties. A system where this method could lead to even more intriguing non-classical states is a many-particle spin-1/2 system. Here, the same type of interactions can lead to mesoscopic samples of e.g. spin-squeezed states or might even lead to highly entangled many-particle states, in particular mesoscopic material Schrödinger cat states. This section will investigate the effect of inter-particle interactions on a many-particle state analogous to the treatment of the two-particle case. For a more general review see Ref. [23].

5.2.1 Quasi spin-1/2 model

A many-particle state is much more difficult to describe than the two-particle state, as the number of terms in a state as given in Eq. (5.1) for an N particle state scales like 2^N. For larger atom numbers such an analysis can therefore not be done analogous to the two-particle case. Instead, the case of N spin-1/2 systems is mapped onto a pseudo spin-1/2 system with collective spin $\hat{S}$ of magnitude $N/2$. The cartesian components of this spin are defined as

$$\begin{aligned}\hat{S}_x &= \frac{\hat{c}_\downarrow^\dagger \hat{c}_\uparrow + \hat{c}_\uparrow^\dagger \hat{c}_\downarrow}{2} \\ \hat{S}_y &= \frac{\hat{c}_\downarrow^\dagger \hat{c}_\uparrow - \hat{c}_\uparrow^\dagger \hat{c}_\downarrow}{2i} \\ \hat{S}_z &= \frac{\hat{c}_\downarrow^\dagger \hat{c}_\downarrow - \hat{c}_\uparrow^\dagger \hat{c}_\uparrow}{2}.\end{aligned} \tag{5.16}$$

Here, $\hat{c}_\downarrow$ and $\hat{c}_\uparrow$ are the annihilation operators for the two states $|\downarrow\rangle$ and $|\uparrow\rangle$, respectively. The $\hat{S}_z$ component describes the population difference between the two spin states, whereas their relative phase is governed by the transverse components $\hat{S}_x$ and $\hat{S}_y$. The cartesian components of the collective spin $\hat{S}$ fulfill the usual angular momentum commutation relations

$$\left[\hat{S}_u, \hat{S}_v\right] = \varepsilon_{uvw}\, i\hbar\, \hat{S}_w, \tag{5.17}$$

with the Levi-Civita symbol ε_{uvw}.

In addition, raising and lowering operators can be defined as

$$\begin{aligned}\hat{S}_+ &= \hat{S}_x + i\hat{S}_y = \hat{c}_\downarrow^\dagger \hat{c}_\uparrow \\ \hat{S}_- &= \hat{S}_x - i\hat{S}_y = \hat{c}_\uparrow^\dagger \hat{c}_\downarrow.\end{aligned} \tag{5.18}$$

Ramsey interferometry

As for any spin 1/2 system, the quasi-spin 1/2 system introduced in eqs. (5.16) can be visualized by a macroscopic Bloch sphere of radius $N/2$. Similar to the two-particle example, a sample initially spin-polarized in $|\downarrow\rangle$, can be written as $|S_z = N/2\rangle$ and visualized as a vector on the Bloch sphere with length $N/2$ pointing to the lower pole. As before, a $\pi/2$-pulse prepares the N-particle system in a coherent superposition of the two internal states for each particle

$$|\psi\rangle = \left(\frac{|\uparrow\rangle + |\downarrow\rangle}{\sqrt{2}}\right)^{\otimes N}. \tag{5.19}$$

This state is an eigenstate of the $\hat{S}_y$ operator with eigenvalue $N/2$. It belongs to a class of many-particle states called *coherent spin states* (CSS) which can in general be written as

$$|\vartheta, \varphi\rangle \equiv \frac{1}{\sqrt{N!}}\left(\cos\left(\frac{\vartheta}{2}\right) e^{-i\varphi/2}\, \hat{c}_\uparrow^\dagger + \sin\left(\frac{\vartheta}{2}\right) e^{i\varphi/2}\, \hat{c}_\downarrow^\dagger\right)^N |\mathbf{0}\rangle. \tag{5.20}$$

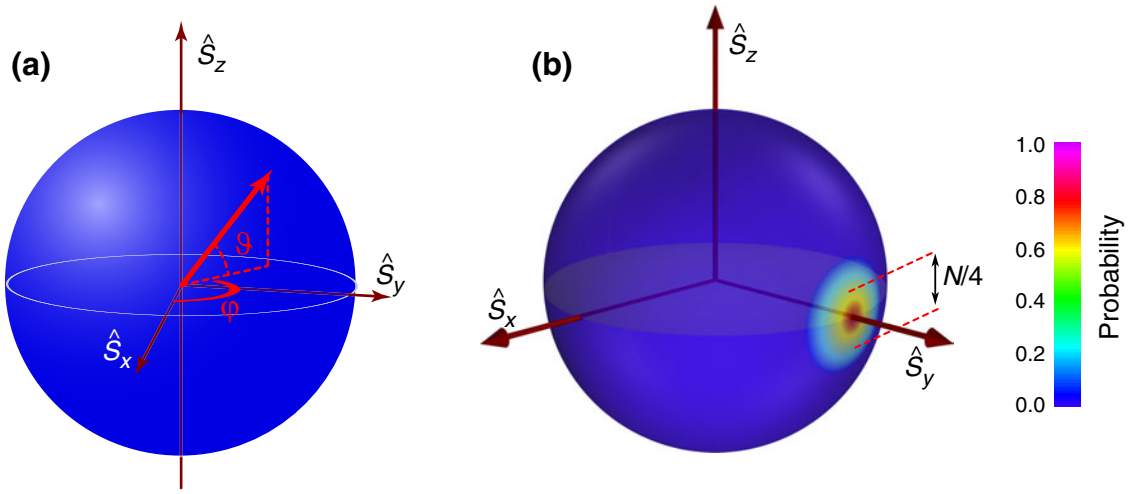

Figure 5.3: **(a)** Macroscopic Bloch sphere. **(b)** Quasi probability distribution (QPD) of a coherent spin state for $N = 100$ on the macroscopic Bloch sphere. The variance of the distribution is $N/4$ in any direction perpendicular to the spin vector. The color scale is the legend for the QPD.

Here, the angles ϑ and φ give the position of the state on the Bloch sphere in spherical coordinates, see Fig. 5.3(a). Different from the single-particle state, the many particle CSS has a Gaussian shaped uncertainty in any direction S_i perpendicular to the mean spin vector which is expressed as the variance

$$\Delta S_i^2 = \langle \hat{S}_i^2 \rangle - \langle \hat{S}_i \rangle^2 = \frac{S}{2} = \frac{N}{4}, \tag{5.21}$$

which is the standard quantum limit (SQL) for fluctuations due to the uncertainty principle for any value of ϑ and φ. This can be understood by expanding Eq. (5.19). All possible different spin configurations have to be summed, with the amplitude following a multinomial distribution. Consequently, terms arise with non-zero probability that have imbalanced spin-populations and lead to a distribution of spin populations along the $\hat{S}_z$ direction. Similarly fluctuations along the equator, i.e. fluctuations of the relative phase between the two spin-states arise. The total distribution of fluctuations leads to the initial Gaussian quasi-probability distribution (QPD) of the relative phase displayed in Fig. 5.3(b).

In order to extract information about the phase of the system, a phase operator is needed. This can be done for the *single particle phases* of a CSS $|\psi\rangle = |\pi/2, \varphi\rangle$. This state is often referred to as *phase state*, as it exhibits equal populations of $|\uparrow\rangle$ and $|\downarrow\rangle$, and well defined *single particle phases*, captured by the expectation value of the raising and lowering operators

$$\langle \pi/2, \varphi | \hat{S}_\pm | \pi/2, \varphi \rangle = \frac{N}{2} e^{\pm i\varphi}. \tag{5.22}$$

For the *many-body relative phase*, however, it is more difficult to define such a phase operator and is not a simple extension of the single particle phase. The discussion of

defining a many-body relative phase goes beyond the scope of this thesis; an approach can be found for example in Ref. [141]. Here, a macroscopic relative phase is assumed to be meaningful to the extend that the expectation values $\langle \hat{S}_\pm \rangle$ are non-zero. As a consequence, the relative phase $\phi \propto \langle \hat{S}_+ \rangle$ and atom number difference $n \equiv N_\downarrow - N_\uparrow \propto \langle \hat{S}_z \rangle$ fulfill a modified uncertainty relation

$$\Delta\phi \, \delta n \gtrsim 1. \tag{5.23}$$

In a Ramsey sequence, the first $\pi/2$-pulse preparing a CSS is followed by a second $\pi/2$-pulse with phase α compared to the first one. The final measurement of populations amounts to finding the expectations value $\langle \hat{S}_z \rangle$. According to Eq. (5.22), the phase expectation value before the final $\pi/2$-pulse will be rotated along $\hat{S}_z$ and thus

$$\langle \hat{S}_z \rangle = \frac{1}{2} \left(\langle \hat{S}_+ \rangle \, e^{i\alpha} + \text{h. c.} \right), \tag{5.24}$$

where $\langle \cdot \rangle$ denotes an average just before the final $\pi/2$-pulse. Taking into account that the relative phase in a Ramsey interferometer evolves as $\varphi = \delta t$ one finds the usual formula for the Ramsey fringe signal Eq. (3.43). It should be noted that as $\Delta \hat{S}_+^2 \neq 0$, also the final Ramsey fringe signal shows noise due to the fluctuations in the initial CSS. This noise is often referred to as "quantum projection noise". If such a measurement is performed on a single system, the outcome will consequently show scatter around the expectation value. The probability of the outcome in a measurement is is depending on the variance of the scatter in the corresponding observable. In an ensemble, as mentioned in the context of an array of particle pairs, all the individual results add up incoherently to the total signal.

5.2.2 Interaction Hamiltonian in a many-body system

So far, the discussion of the many-body spin 1/2 without interaction has been very similar to the one for a two-particle system. In case of interactions, however, the situation of the many-particle case becomes more intricate and shows an intriguing dynamics, markedly different from the entanglement oscillations discussed in Section 5.1.1.

Many-body interaction Hamiltonian

The Hamiltonian for an interacting ultracold two-component gas with states $|\uparrow\rangle$ and $|\downarrow\rangle$ can be written as [102]

$$\begin{aligned} \hat{H} \;=\; & \int d\mathbf{r} \; \hat{\Psi}_\uparrow^\dagger(\mathbf{r}) \left[-\frac{\hbar^2 \nabla_\mathbf{r}^2}{2M} + V_{\text{ext}}(\mathbf{r}) \right] \hat{\Psi}_\uparrow(\mathbf{r}) + \frac{g_{\uparrow\uparrow}}{2} \int d^3\mathbf{r} \; \left[\hat{\Psi}_\uparrow^\dagger(\mathbf{r}) \, \hat{\Psi}_\uparrow(\mathbf{r}) \right]^2 \\ & + \int d^3\mathbf{r} \; \hat{\Psi}_\downarrow^\dagger(\mathbf{r}) \left[-\frac{\hbar^2 \nabla_\mathbf{r}^2}{2M} + V_{\text{ext}}(\mathbf{r}) \right] \hat{\Psi}_\downarrow(\mathbf{r}) + \frac{g_{\downarrow\downarrow}}{2} \int d^3\mathbf{r} \; \left[\hat{\Psi}_\downarrow^\dagger(\mathbf{r}) \, \hat{\Psi}_\downarrow(\mathbf{r}) \right]^2 \\ & + g_{\uparrow\downarrow} \int d^3\mathbf{r} \; \hat{\Psi}_\uparrow^\dagger(\mathbf{r}) \, \hat{\Psi}_\downarrow^\dagger(\mathbf{r}) \, \hat{\Psi}_\uparrow(\mathbf{r}) \, \hat{\Psi}_\downarrow(\mathbf{r}). \end{aligned} \tag{5.25}$$

Here $\hat{\Psi}_i(\mathbf{r})$ is the bosonic field annihilation operator for an atom in state $|i\rangle$. In the first and second row in Eq. (5.25) the first and second term describe the kinetic and intra-species interaction for state $|\uparrow\rangle$ and $|\downarrow\rangle$, respectively. The term in the last row accounts for inter-species interaction. As usual, the coupling constants are defined as $g_{ij} = 4\pi\hbar^2 a_{ij}/M$, see Eq. (2.10).

The Hamiltonian (5.25) can be simplified by making the following assumptions. (i) All particles in a given spin state are assumed to occupy the same spatial ground state function $\phi_\uparrow$ or $\phi_\downarrow$. (ii) These wave functions are stationary and rigid, i.e. independent of time and changes in the respective atom number. And (iii) losses and dephasing do not occur. With these assumptions the field operators are substituted by $\hat{\Psi}_i(\mathbf{r}) \to \phi_i(\mathbf{r})\,\hat{c}_i$, with $\phi_i(\mathbf{r}) \to \phi_i$ the spatial wave function and $\hat{c}_i$ the annihilation operator of spin state $|i\rangle$. In fact, the assumptions (i) and (ii) imply that both condensate wave functions are equal (i.e. a single mode approximation can be used) if a CSS $|\pi/2, \varphi\rangle$ is considered that has been created from an initially spin polarized sample. In this case $\phi_\uparrow = \phi_\downarrow = \phi_0$, where ϕ_0 is the initial spatial wave function before the first $\pi/2$-pulse. With this Eq. (5.25) can be expressed in terms of the z-component of the macroscopic spin operator introduced in Section 5.2.1. Neglecting terms of higher order than quadratic in $\hat{S}_z$, the Hamiltonian reads [102]

$$\hat{H} = f(N) + N\hbar\eta\,\hat{S}_z + \hbar\chi\,\hat{S}_z^2, \tag{5.26}$$

where $f(N)$ is a function of the total atom number N, i.e. absorbing terms of the form $\hat{c}_\uparrow^\dagger\hat{c}_\uparrow + \hat{c}_\downarrow^\dagger\hat{c}_\downarrow$. This term sets a global energy scale of the system. The second term accounts for different interaction energies in the states $|\uparrow\rangle$ and $|\downarrow\rangle$, where

$$\hbar\eta \equiv \frac{a_{\downarrow\downarrow} - a_{\uparrow\uparrow}}{2}\,\tilde{U}, \tag{5.27}$$

with $\tilde{U} = 4\pi\hbar^2/M \times \int d^3\mathbf{r}\,|\phi_0|^4$, cf. Eq. (4.5). This term is the analogue to the precession of the Bloch vector due to the energy difference between the two states in the single-particle spin-1/2 Bloch sphere picture. The first two terms therefore lead to a dynamics of the many-particle phase that can be compensated for by a proper rotation of the Bloch sphere. Hence they will be neglected in the future discussion of the problem.

The third and non-linear term in Eq. (5.26) leads to a non-trivial phase dynamics of the many-body state that will be investigated in the following. Here, the energy scale is set by

$$\hbar\chi \equiv \frac{a_{\uparrow\uparrow} + a_{\downarrow\downarrow} - 2\,a_{\uparrow\downarrow}}{2}\,\tilde{U}. \tag{5.28}$$

This is the same effective interaction energy that has been introduced phenomenologically in Eq. (5.6); here, however, no further approximations have been made.

Time evolution under non-linear interactions

The form of the Hamiltonian (5.26) is in particular convenient to study the time evolution of a CSS (5.20). The Hamiltonian is expressed in terms of the operator $\hat{S}_z$ and a CSS

can be easily expanded in terms of eigenstates to this operator. The time evolution then reduces to a phase evolution of the various eigenstates. Assuming again a Ramsey like sequence, the initial phase state $|\vartheta = \pi/2, \varphi = 0\rangle$ can be written as (see Appendix B.2)

$$|\psi(t=0)\rangle \equiv |\vartheta = \pi/2, \varphi = 0\rangle = \sum_{m_z=-\frac{N}{2}}^{\frac{N}{2}} C_{m_z} |m_z\rangle. \tag{5.29}$$

Here $|m_z\rangle$ and m_z are eigenstates and eigenvalues of the $\hat{S}_z$-operator, respectively, and the coefficients C_{m_z} are the coefficients of the binomial distribution. The time evolution under the non-linear Hamiltonian

$$\hat{H}_{\mathrm{nl}} = \hbar\chi\, \hat{S}_z^2 \tag{5.30}$$

can therefore be calculated as

$$|\psi(t)\rangle = e^{-i\hat{H}t/\hbar}\, \psi(0) = \sum_{m_z=-\frac{N}{2}}^{\frac{N}{2}} C(m_z)\, e^{-i\chi m_z^2 t}\, |m_z\rangle. \tag{5.31}$$

A convenient visualization of the time evolution can be employed similar to the Q-function in quantum optics [19], i.e. finding the overlap with some arbitrary coherent state $|\theta, \phi\rangle$ in order to calculate the quasi-probability distribution

$$P(\theta, \phi, t) \equiv |\langle\theta, \phi|\psi(t)\rangle|^2. \tag{5.32}$$

This function can be displayed as a quasi-probability distribution on the Bloch sphere as shown in Fig. 5.4(a), or more conveniently as a projection onto a cylinder touching the equator of the Bloch sphere, see Fig. 5.4(b).

Non-linear interactions that can be described by a Hamiltonian of the form (5.30) can also be found in many other physical systems, where the situation is very similar to the one presented here. For example, non-linear interactions between single, highly excited Rydberg atoms coupled to a coherent electromagnetic field have been seen to induce a non-trivial time-evolution leading to entangled states of the light field [142, 143]. Also, an interacting BEC in a double well potential [144] can exhibit a similar dynamics [145], where the two potential wells are the analogue of the two internal states presented here. A general motivation of the form of (5.26) can be found in Ref. [23], where some of the systems realizing this Hamiltonian are presented.

5.2.3 Coherent phase evolution of the many-particle state

The time evolution of the initial CSS given by eqs. (5.31,5.32) splits into several parts. Some particular states resulting from this phase evolution are shown in Fig. 5.4.

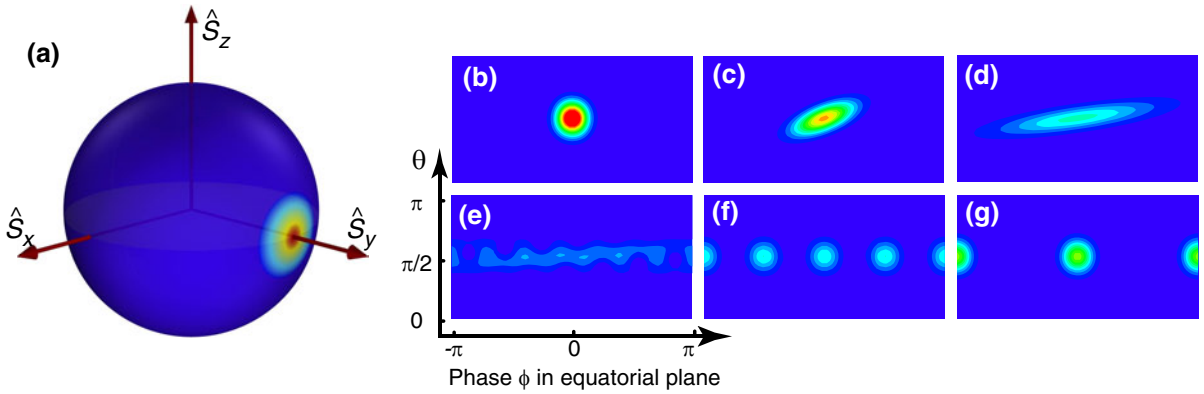

Figure 5.4: **(a)** Quasi probability distribution of a phase state (5.20) on the macroscopic Bloch sphere. **(b)** Projection of this QPD onto a plane touching the equator of the Bloch sphere. This initial state evolves under the non-linear Hamiltonian (5.30) to non-classical states. The acquired interaction phases shown are: **(c)** $\chi t = 0.08$; **(d)** $\chi t = 0.235$ and **(e)** $\chi t = 0.471$, spin squeezed states. **(f)** $\chi t = \pi/4$, partial revival. **(g)** $\chi t = \pi/2$, Schrödinger cat state.

Phase spreading For small interaction times $\chi t \ll 1$, the initially circular phase distribution becomes increasingly elongated and takes the form of an ellipse [102, 135, 136, 137, 138, 146], see Fig. 5.4(c) and (d). The long axis of this ellipse is tilted with respect to the equator where the tilt angle becomes smaller for larger interaction times. This stretching of the phase distribution is often referred to as "phase diffusion" in literature as the relative phase becomes more and more uncertain. This time evolution is, however, due to a unitary Hamiltonian. In particular, proper manipulation of this Hamiltonian, for example, would allow to reverse this evolution, in contrast to a real diffusive process. Therefore the term "phase dispersion" will be used for the interaction induced spreading of the relative phase.

Spin squeezing The short axis of the ellipse exhibits an uncertainty which becomes smaller than the SQL of $N/4$ [146]. Although the quantum fluctuations for conjugate variables still have to fulfill the Heisenberg uncertainty principle, the fluctuations in one observable can become smaller at the expense of the conjugate. These "spin squeezed states" are a class of well studied correlated many-body states [19]. In fact, it has been proposed to take advantage of the reduced fluctuations in order to improve the precision of experiments in metrology or interferometry [20, 147]. Squeezed states of the electromagnetic field have for example been realized in quantum optical experiments [148, 149, 150]; spin squeezed atomic states have been realized through the interaction with pre-squeezed light [151] or in experiments with back action on an atomic sample after quantum non-demolition measurements [152]. Although these methods can produce squeezed spin states in atomic samples, the advantage of the method presented here is that the initial state is a classical state that can be produced by default in experiments with ultracold atomic samples, involving a mesoscopic number of atoms. Moreover, a substantial amount of squeezing

can be achieved just by time evolution of this initial state. The minimal variance has been calculated to occur after an effective interaction phase $\chi t \approx 0.1$, see Appendix B.2. In fact, this method of creating spin squeezed states can be improved by choosing a slightly different interaction Hamiltonian, which does not only involve a rotation around a single axis ($\hat{S}_z$-axis here), but two perpendicular axes, for example $\hat{S}_+^2 + \hat{S}_-^2$ [146]. The advantages of the latter "two-axis squeezing" compared to the former "one-axis" squeezing are that a larger degree of squeezing can be achieved and the tilt of the ellipse is absent. For a different choice of the two axes, the time evolution can be faster [153]. This two-axes squeezing is not investigated in this thesis, but might be an interesting extension in future realizations.

Maximally entangled Schrödinger cat states For increasing interaction phases $\chi t > 0.15$, the phase distribution wraps around the whole Bloch sphere and shows a more complex sub-structure [102, 135, 136, 137, 138] (see Fig. 5.4(e)). For example, partial revivals can be seen as displayed in Fig. 5.4(f), when the phase distribution breaks up into a superposition of several CSS at different positions on the equator. After a well defined interaction phase $\chi t = \pi/2$, the distribution shows a superposition of two CSS on opposite sides of the Bloch sphere in Fig. 5.4(f) [136, 139]. This state is a mesoscopic, material Schrödinger cat state, the many-particle analogue to the Bell state introduced in Eq. (5.10). This state is in particular interesting as a macroscopic number of particles (the cat) is in an entangled many-body state

$$|\mathrm{CAT}\rangle = \frac{1}{\sqrt{2}}\left(|S_y = \tfrac{N}{2}\rangle + |S_y = -\tfrac{N}{2}\rangle\right) = \frac{1}{\sqrt{2}}\left(|\vartheta = \tfrac{\pi}{2}, \varphi = 0\rangle + |\vartheta = \tfrac{\pi}{2}, \varphi = \pi\rangle\right), \tag{5.33}$$

i.e. the sample is in a coherent superposition of having relative phase $\vartheta = 0$ or $\vartheta = \pi$. By application of a $\pi/2$-pulse, this can be mapped for example onto a Schrödinger cat state of the spin populations, i.e. $1/\sqrt{2}\,(|\uparrow\rangle^{\otimes N} + |\downarrow\rangle^{\otimes N})$. Although there is a strong demand for the experimental realization of macroscopic, maximally entangled states, large material Schrödinger cat states could so far not be produced. They are extremely fragile objects which are destroyed by a single decoherence event, which could be a spin flip or loss of an individual atom in the experiment. The probability for these events increases strongly with the number of particles involved. So far, only small "Schrödinger kitten", involving few entangled parties, could be realized in neutral atoms [110], ions [154] or photons [143, 155].

Revival of the initial state If the interaction phase becomes even larger $\chi t > \pi/2$, the phase distribution spreads again, until for $\chi t = 2\pi$ the initial state is restored up to a phase factor of -1 [136].

Interaction induced collapse of the Ramsey fringe contrast

In order to experimentally track the signature of the coherent phase evolution induced by the non-linear interactions, the method of observing the dynamics of the Ramsey fringe

visibility introduced in Section 5.1.2 can be employed. The final signal after the last $\pi/2$-pulse with phase α can be determined by calculating the expectation value of the spin raising operator $\hat{S}_+$ [23]. For this, the exact result given in Ref. [146] can be approximated as

$$\langle \hat{S}_+ \rangle = \frac{N}{2} \left(\cos(\chi t)\right)^{N-1} \approx \frac{N}{2} \exp\left\{-\frac{N\chi^2 t^2}{2}\right\}, \tag{5.34}$$

where the approximation is valid for small interaction times $\chi t \ll 1$. Substituting (5.34) into (5.24), one finds the expected Ramsey fringe signal as

$$P_\uparrow(t) = \frac{\mathcal{V}(t)}{2} \Big(1 + \cos(\delta t + \alpha)\Big), \tag{5.35}$$

where the visibility $\mathcal{V}(t)$ is defined in (5.14) and reflects the collapse of the Ramsey fringe for short times according to

$$\mathcal{V}(t) = \exp\left\{-\frac{N\chi^2 t^2}{2}\right\}. \tag{5.36}$$

From this a typical collapse time can be defined as

$$t_{\text{coll}} \equiv \frac{1}{\chi\sqrt{N}}. \tag{5.37}$$

The collapse of the Ramsey fringe is a consequence of the elongated phase distribution along the equator. This can be intuitively understood by considering the mapping of the phase distribution onto the Bloch sphere during the Ramsey sequence as shown in Fig. 5.5. In particular, after a certain interaction phase has been acquired, the increased fluctuations along the equator (neglecting the tilt of the ellipse) are rotated in the $\hat{S}_z$ direction by the last $\pi/2$-pulse and thereby translated into an uncertainty of the population measurement.

Comparing the typical collapse time (5.37) with the time scale on which squeezing of the phase distribution occurs (see Appendix B.2), one finds that the state with minimum variance in the squeezed axis is expected to occur already well before the Ramsey fringe signal has completely collapsed [146].

Importantly, the collapse of the Ramsey fringe signal as discussed before is valid only for short times. In fact, as the exact expression (5.34) is oscillatory, for interaction phases $\chi t_{\text{rev}} = 2\pi$, the initial CSS is expected to reform and the Ramsey fringe visibility would revive. Such a revival of coherence has been seen in a different context, where the phase evolution of a superposition of several lowest Fock states in a strongly interacting spinless system showed a collapse and subsequent revival of the coherent matter wave field [110]. For the case presented here, the relatively small spin dependent interactions result in a rather late revival. Compared to the typical collapse time (5.37) the revival is expected to occur at a time $t_{\text{rev}} = t_{\text{coll}} \times 2\pi\sqrt{N}$. Therefore the entanglement oscillations present in the two-particle case transform into rather sharp revivals of coherence. The time scale of the revival for typical mesoscopic atom numbers (≈ 100) can exceed the collapse time by roughly two orders of magnitude.

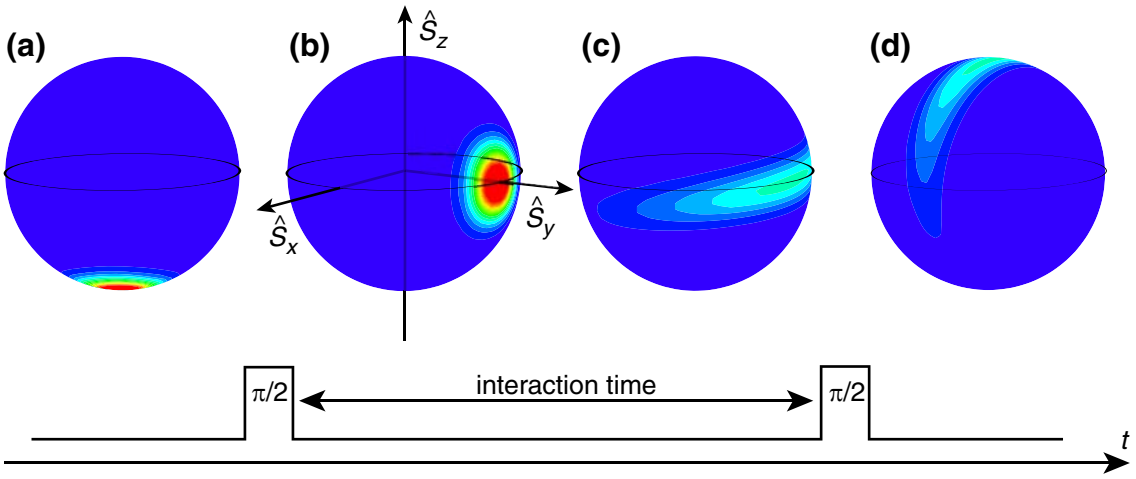

Figure 5.5: Illustration of the quantum phase distribution on the Bloch sphere during a Ramsey sequence. **(a)** Initial state $|S_z = -N/2\rangle$, **(b)** CSS $|S_y = N/2\rangle$ after the first $\pi/2$-pulse , **(c)** Elongated phase distribution due to phase dispersion according to (5.30). The final $\pi/2$-pulse rotates the increased fluctuations along the equator into the S_z-direction **(d)**.

The first part of Eq. (5.34) shows also another important issue. For the Schrödinger cat state $\chi t = \pi$, the expectation value of the annihilation operator is exactly zero, and a relative many-particle phase is not strictly defined.

5.3 Tuning elastic interactions

Observing the dynamics introduced in Section 5.1.1 for two spin 1/2-particles and in Section 5.2 for a many-body spin 1/2-system depends on the effective interaction energy $\hbar\chi$. In the single mode approximation it is essentially given by a difference of scattering lengths $a_\chi = (a_{\uparrow\uparrow} + a_{\downarrow\downarrow} - 2\,a_{\uparrow\downarrow})/2$, see (5.7). For example, when $\chi \approx 0$, the strength for various combinations of interacting spins are balanced, and the phase evolution introduced above takes place either on a very slow time scale, or it is completely absent for $\chi = 0$.

For the atomic species ^{87}Rb used in the experiments presented here, it turns out that the scattering lengths in the two hyperfine ground states are all approximately equal. In particular for the choice of $|\downarrow\rangle \equiv |f = 1, m = +1\rangle$ and $|\uparrow\rangle \equiv |f = 2, m = -1\rangle$, the predicted scattering lengths are $a_{\downarrow\downarrow} \approx 100.4\,a_B$, $a_{\uparrow\uparrow} \approx 95.7\,a_B$ and $a_{\downarrow\uparrow} \approx 98\,a_B$ [47], leading to an effective scattering length difference of $a_\chi \approx 0.1\,a_B$, where $a_B = 0.052918 \times 10^{-9}$ m is the Bohr radius. For typical experimental parameters (e.g. as given in Section 3.5) the spin independent interaction is typically $U/\hbar \approx 2\pi \times 3$ kHz, while the corresponding spin dependent interaction is on the order $\chi \approx 2\pi \times 3$ Hz. Consequently the time scale on which the interaction driven time evolution occurs changes from the order of milliseconds in the spin-independent to seconds in the spin dependent case. From an experimental point of view this makes it extremely difficult, if not impossible, to distinguish the phase evolution from

other effects occuring on much faster time scales. In addition, experimental constraints – summarized as decoherence processes – set a time limit on which a coherent evolution can be detected. Therefore it is crucial to enhance the role of spin-dependent interactions, i.e. increasing the effective interaction energy $\hbar\chi$. Unfortunately, the disadvantageous situation of $\chi \approx 0$ does not change significantly if other combinations of states within the two hyperfine ground state levels are chosen.

There are, however, two approaches to directly modify the effective interaction energy. First, the single mode approximation can be abandoned. Instead, an approximation with two spatial modes $\phi_\downarrow$ and $\phi_\uparrow$ can be introduced. If those two modes can be controlled independently, the corresponding interaction energies U_{ij} can be controlled via the wave function overlap $\int d^3 |\phi_i|^2 |\phi_j|^2$. In this case the effective spin-dependent interaction can be significantly larger than zero, and can even reach the strength of the spin-independent interaction [156, 157, 158]. This has been demonstrated recently by employing spin-dependent optical lattice potentials that can be controlled to a very high degree [159]. For proper conditions, the system has been predicted to show entanglement oscillations [160] leading in the ideal case to a maximally entangled "cluster state" [156, 160]. This class of states has intriguing properties making them a well suited candidate for quantum computation purposes [161]. The creation of entanglement by spin dependent lattices has been detected by collapse and revival of the contrast in a spatial interferometer as well as in a Ramsey interferometric sequence [140].

The second possibility of tuning the effective spin-dependent interaction strength is to directly affect the relevant scattering lengths. One tool offering this possibility is the magnetic Feshbach resonance (see for example Ref. [24]), which has received a lot of attention in recent years.

5.3.1 Magnetic Feshbach resonances

In chapter 2 the collision of two particles in a molecular potential has been considered. There, the relative wave function entered and left the molecular potential just above the dissociation threshold; this scattering channel will be called "open channel" from now on. Here the phase of the wave function was shifted due to the scattering potential. This phase shift, determining the s-wave scattering length, can be strongly affected, if the incoming wave is coupled via the hyperfine interaction (2.13) to a bound state in some other molecular potential, called "closed channel", see Fig. 5.6(a). This coupling mixes the two channels, so that part of the incoming wave acquires bound state character. The more bound state is admixed to the incoming wave, the more time both atoms will spend in close proximity. This will naturally lead to a larger phase shift of the asymptotic wave function and consequently to a larger value of the scattering length. The amount of bound state admixture in the open channel depends on the energy difference between the two channels. In general, the quantum states of the open and closed channels differ by angular momentum quantum numbers and have therefore different magnetic moments. Thus their energy difference will depend on the externally applied magnetic field. For a certain magnetic field the incoming wave couples resonantly to the bound state. If a non-zero energy

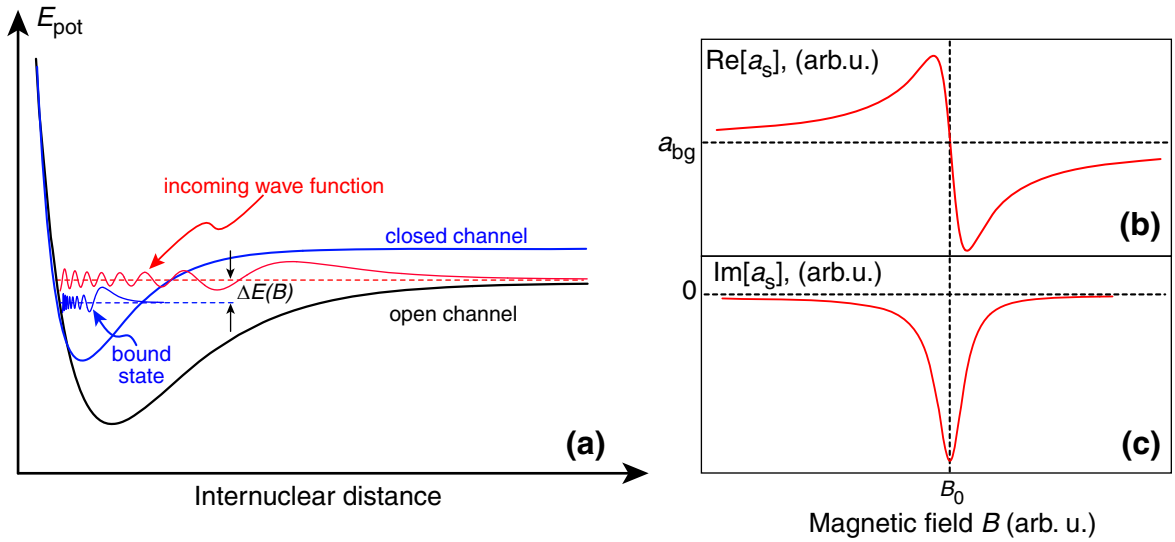

Figure 5.6: Principle of a Feshbach resonance. **(a)** The relative wave function (red) of two colliding particles in the scattering potential (open channel) has an energy just above dissociation threshold. If a bound state in some other molecular potential (closed channel, blue) is energetically close to the scattering energy, the scattering phase shift can be strongly affected provided that the channels are coupled via the hyperfine interaction. The energy difference between scattering wave function and bound state can be tuned in some cases by an external magnetic field. When the magnetic field is scanned across such a Feshbach resonance, the elastic **(b)** and inelastic **(c)** part of the scattering length show the typical dispersive profile (5.38).

difference between the two channels exist, the sign of this difference also determines the sign of the scattering length. For a strong coupling between the channels, there is a large admixture of the molecular state in the total wave function. In most cases this molecular state can decay to other ro-vibronic states such that a re-conversion to the open channel is not possible. This process is detected as loss of atoms from the trap, giving rise to an imaginary part of the scattering length.

As the detailed description of Feshbach resonances is extensive, only a phenomenological description will be given here. In particular, the change of s-wave scattering length with magnetic field B can be parametrized by the general expression [47, 32]

$$a_s(B) = a_{\mathrm{bg}} \left(1 - e^{2i\phi_R} \frac{\Delta_{\mathrm{el}}}{B - B_0 + \frac{1}{2} i \Delta_{\mathrm{inel}}} \right), \tag{5.38}$$

where B_0 is the position of the Feshbach resonance, a_{bg} is the background s-wave scattering length, i.e. far away from the resonance position, Δ_{el} and Δ_{inel} are the width of the elastic and inelastic part of the scattering length, respectively. The physical meaning of Δ_{el} is the coupling strength between the two channels, and Δ_{inel} depends on the energy width of the bound state, determined by loss channels from this state. The phase ϕ_R is an additional

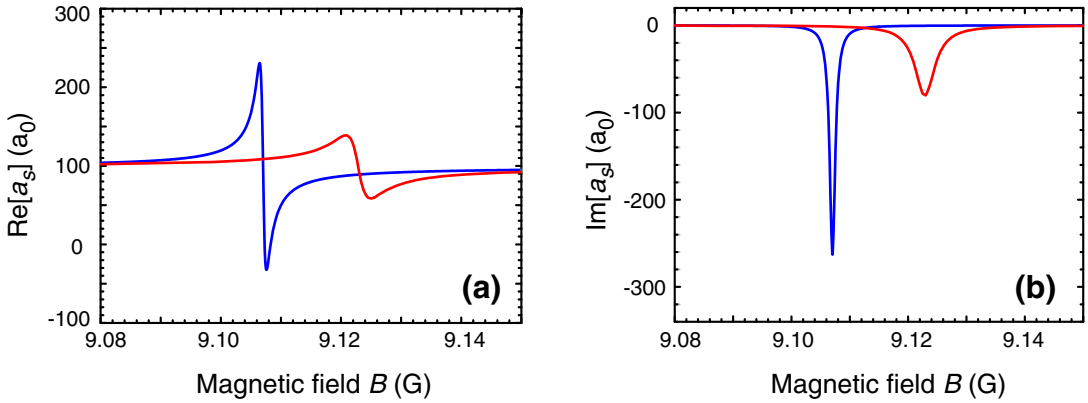

Figure 5.7: Elastic **(a)** and inelastic **(b)** part of the predicted hyperfine Feshbach resonance between $|f = 1, m = +1\rangle$ and $|f = 2, m = -1\rangle$ for ^{87}Rb. The curves have been calculated using different input parameters and models. In particular, the red line is the one presented in Ref. [47] and the blue includes in addition the data from Ref. [48]. Graphs are courtesy of Servaas Kokkelmans.

phase constant arising due to inelastic collisions [47] and resulting in an asymmetry of the elastic part of the scattering length around the resonance position.

The scattering length given in (5.38) is a complex function of magnetic field. As mentioned above, similar to e.g. the complex index of refraction, the real part $\mathrm{Re}(a)$ is the elastic scattering length, responsible for the coherent phase evolution. The imaginary part $\mathrm{Im}(a)$ describes inelastic interactions, leading to losses in the system. Fig. 5.6(b) and (c) show the typical course of the elastic and inelastic part of a Feshbach resonance. For ^{87}Rb, typical magnetic Feshbach resonances are at rather high magnetic fields between 400 G and 1000 G for two atoms in the state $|f = 1, m = +1\rangle$; typical widths are between 1% and up to 20% of the resonance magnetic field B_0 [48]. These resonances are suited to form a molecule from two colliding $|f = 1, m = +1\rangle$ atoms; moreover it would be possible to tune the scattering length $a_{\downarrow\downarrow}$ with respect to the other two scattering lengths, thereby changing χ. However, the relatively high magnetic fields are experimentally difficult to handle in the present experimental setup. Therefore another Feshbach resonance is used, where the open channel asymptotically connects to the mixed spin state $|\uparrow\downarrow\rangle$.

5.3.2 Mixed spin state Feshbach resonance in ^{87}Rb

Such a hyperfine Feshbach resonance has been predicted to exist between the two states $|f = 1, m = -1\rangle$ and $|f = 2, m = +1\rangle$, labelled as $|\downarrow\rangle$ and $|\uparrow\rangle$, respectively, for moderate magnetic fields around 9.1 G [47], see Fig. 5.7. Compared to other "usual" Feshbach resonances that are used in order to study ultracold molecules [48], the decay of the bound molecular state is relatively large. Therefore, this resonance is not suited to create an ultracold molecular sample. Moreover, the relatively large value of the inelastic width Δ_{inel} leads to a rather moderate change of $a_{\downarrow\uparrow}$ on the order of a few 10% of the background value.

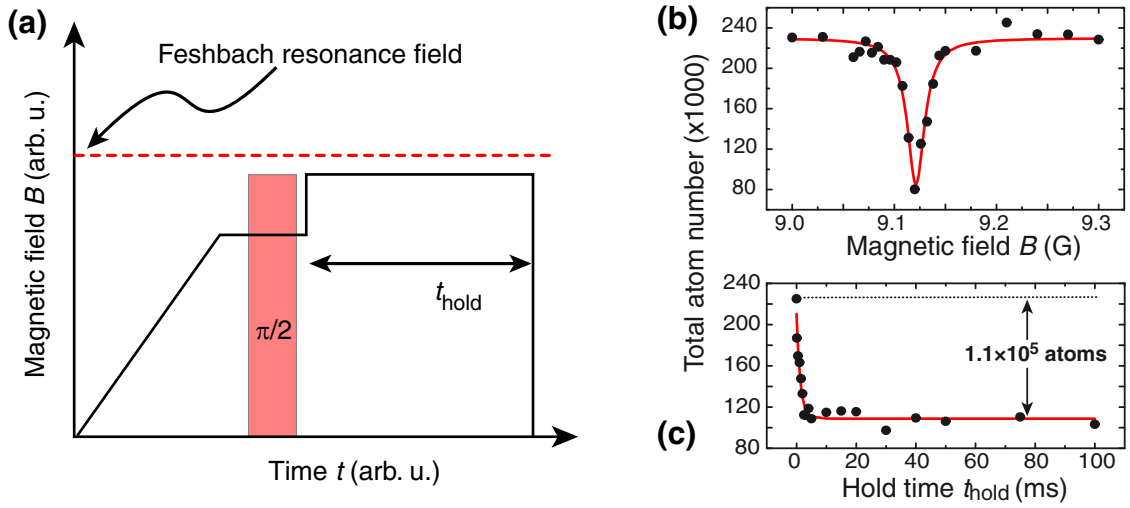

Figure 5.8: Loss channel of the hyperfine Feshbach resonance. **(a)** Experimental sequence locating the Feshbach resonance. **(b)** Remaining number of atoms after holding a coherent superposition of $|\uparrow\rangle$ and $|\downarrow\rangle$ at the respective field for 1 ms in a 2D optical lattice. **(c)** Time resolved loss of atoms right on the resonance field in a 3D optical lattice potential. Lattice sites occupied by more than one atom are depleted within 3 ms, while isolated atoms remain trapped for long times.

So far, the elastic part of the scattering length, responsible for the coherent phase evolution, has been at the focus of the discussion. As can be seen from Fig. 5.7(b), however, the Feshbach resonance not only enhances this elastic interaction, but also losses. Probable decay mechanisms are three-body recombination and two-body losses such as dipolar relaxation. In the first process two particles form a molecule, while a third particle absorbs the excess energy and momentum to ensure conservation of both quantities, thereby probably leaving the trap. Here all three particles are effectively lost, because the molecule cannot be detected by the imaging sequence, although it might stay trapped. The second process occurs between two particles, where without conservation of total angular momentum the spin of a particle can flip from $f = 2$ to $f = 1$, releasing the hyperfine energy of $h \times 6.8$ GHz. This energy is usually much larger than typical optical trap depths ($V_{\mathrm{lat}} = 40\,E_r$ corresponds to $\approx h \times 120$ kHz) and transformed into kinetic energy, causing the particle to leave the trap.

Experimentally locating the Feshbach resonance

In order to employ the hyperfine Feshbach resonance around 9.1 G its position has to be precisely known. Therefore the inelastic channel of the Feshbach resonance is located by detecting enhanced atomic loss in a superposition of the two relevant internal states close to the resonance position. The sequence starts from a BEC loaded into a pure 2D-optical lattice potential while a small homogeneous magnetic field along the x-axis of the

system is still present (see Section 3.5). This magnetic field is actively stabilized in the x-direction, while the magnetic fields along y and z are externally compensated without active regulation. The stabilization sequence takes roughly 120 ms before the atoms are transfered into the $|\downarrow\rangle = |f = 1, m = +1\rangle$ state by a Landau-Zener sweep. Subsequently the magnetic field is increased to ≈ 8.6 G (see Fig. 5.8(a)), and a resonant two photon transition involving a microwave photon around 6.8 GHz and an rf-photon around 6 MHz creates a coherent superposition of $|\downarrow\rangle$ and $|\uparrow\rangle = |f = 2, m = -1\rangle$. Then, the magnetic field is quickly ($\approx 10\,\mu$s) ramped to various magnetic fields around 9.12 G, the predicted position of the Feshbach resonance. The ramp speed is important, especially if the magnetic field crosses the position of the resonance; in this case the ramp has to be fast enough so that no effect of the increased interaction during the ramp already affects the state of the system. At the final magnetic field value, the system can interact for 1 ms with the corresponding scattering length. After this interaction time, all traps are switched off and the residual total atom number is detected after TOF. For a magnetic field around 9.12 G a strong atom loss is detected (see Fig. 5.8(b)), as is expected in the proximity of the Feshbach resonance. The measured position 9.121(9) G and width 20(5) mG agree with the theoretical prediction. The loss channel of this Feshbach resonance has also been detected independently by another group [162].

In addition, Fig. 5.8(c) shows a time resolved loss measurement right on resonance, where the sample has been prepared in a 3D-optical lattice. The system is expected to have sites filled with predominantly either one or two atoms per site. Sites with a filling of larger than two are expected to be depleted during the 150 ms wait time between the end of the lattice intensity ramp and the microwave pulse preparing the coherent superposition. After this pulse, only atom pairs can interact and consequently decay, while the isolated atoms are unaffected by the Feshbach resonance. Hence, after long time, all atom pairs will have decayed, while the isolated atoms remain trapped. The measured data therefore allows to extract the number of singly and doubly occupied lattice sites, and shows that roughly 10^5 atoms are trapped in doubly occupied sites. Further measurements, however, indicate that lost atoms can undergo secondary collisions and cause e.g. isolated atoms to also leave the trap. This effect can be on the order of 10% . Further, the time resolved loss curves taken in a 2D and a 3D optical lattice configuration do not show a drastic difference except for the offset due to isolated atoms trapped in the 3D lattice, as can be seen in Fig. 5.9(a). This points to the fact that two-body decay processes are dominant for the observed loss of atoms; in particular, as the losses are definitely enhanced by the vicinity of the Feshbach resonance, exactly one atom is lost from either spin state $|\uparrow\rangle$ and $|\downarrow\rangle$. This will be important in the later discussion of the role of losses during the many-body phase evolution.

Finally, a new, so far unknown hyperfine Feshbach resonance could be located in the loss channel. This resonance has been measured to exist between the states $|f = 1, m = +1\rangle$ and $|f = 2, m = 0\rangle$ at a magnetic field of ≈ 9.06 G. As can be seen from Fig. 5.9(b), the amplitude and width of the loss channel is comparable to the previously detected resonance. The position has subsequently been found in calculations [50].

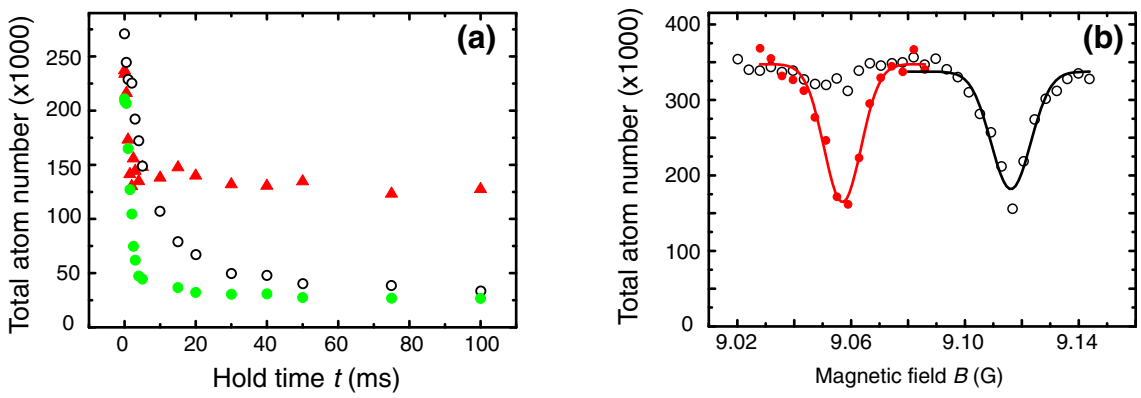

Figure 5.9: **(a)** Time resolved atom loss on resonance for systems optical lattices with varying spatial degree of freedom. 1D lattice (pan-cake shaped systems) (○), 2D lattice (cigar shaped systems) (●) and 3D lattice (isotropic lattice sites) (△). The increased loss rate from 1D to 2D is due to the enhanced density in the tubes. For a 3D lattice the atom number levels at a finite number, indicating the presence of isolated atom pairs. **(b)** Loss channels of the Feshbach resonances between $|f = 1, m = +1\rangle$ and $|f = 2, m = -1\rangle$ (○) and the so far unknown resonance between $|f = 1, m = +1\rangle$ and $|f = 2, m = 0\rangle$ (●). The fit for the new resonance yields $B_0 = 9.057(7)\,\mathrm{G}$ and $\Delta_{\mathrm{loss}} = 13(5)\,\mathrm{mG}$. For the previously known resonance the fitted position and width are $B_0 = 9.117(7)\,\mathrm{G}$ and $\Delta_{\mathrm{loss}} = 14(5)$.

5.4 Interaction induced binary entanglement in an optical lattice

The elastic channel of the Feshbach resonance found close to the predicted magnetic field opens the opportunity to study the phase evolution to binary entangled states, introduced in Section 5.1. In order to observe the expected entanglement oscillations, a Ramsey-type interferometer sequence is used to study the coherence properties of atom pairs trapped in a deep 3D optical lattice potential.

5.4.1 Observation of interaction induced entanglement oscillations

The experimental sequence is similar to the one used for locating the Feshbach resonance through enhanced atomic losses, see Section 5.3.2, and shown in Fig. 5.10. Instead of a single microwave pulse we perform a complete Ramsey sequence, where in the time between the pulses the interaction properties are changed by ramping the magnetic field to a certain magnetic field value in the proximity of the Feshbach resonance. Thereby the coherent superposition created by the first $\pi/2$-pulse (5.1) can evolve under the influence of an increased non-linear interaction energy $\hbar\chi$ to the various final states given in eqs. (5.9-5.12). The coherence properties of these states are probed by the last $\pi/2$-pulse. In order to apply this pulse, the magnetic field is ramped back to the value present during the first pulse. In addition, a single-particle spin echo π-pulse is included to compensate for time constant spatial inhomogeneities in the system. Finally, the relative number of atoms in

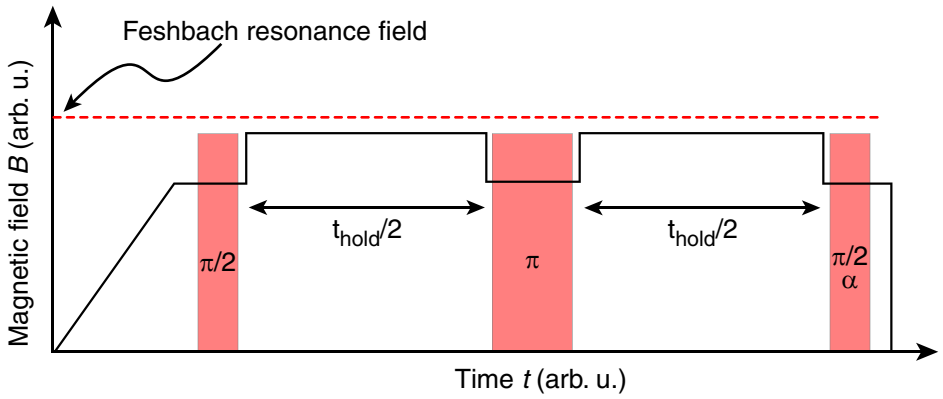

Figure 5.10: Experimental sequence for the Ramsey interferometer in order to observe the two-particle entanglement oscillations in a deep 3D optical lattice.

$|\uparrow\rangle$ is detected as a function of the phase of the last $\pi/2$-pulse.

The Ramsey fringes obtained by this sequence for a certain magnetic field show an interesting behaviour displayed in Fig. 5.11, which is expected from the discussion in Section 5.1.2. The contrast starts initially at a high value and follows an oscillatory collapse and revival evolution with time, as expected from the entanglement dynamics predicted in Eq. (5.15). However, it is important that the system is not described by the atom pair signal alone, but the isolated atoms have to be taken into account. Although these atoms do not take part in the interaction induced entanglement evolution, they do show a Ramsey fringe signal. The importance can be seen in particular for the effective interaction phase of $\phi_\chi = \pi/2$. The atom pairs are expected to not contribute to the total signal as suggested by Eq. (5.10). Isolated atoms, however, still show a Ramsey fringe. As their contribution can be up to 50% of the total signal, for this interaction phase, a total fringe signal is still expected. On the other hand, when the atom pairs have disentangled again, their Ramsey fringe is phase shifted by π compared to the fringe of isolated atoms, as can be seen by comparing the two final states (5.9) and (5.11). Thus if the isolated atoms are in state $|\uparrow\rangle$, the pairs will be in $|\downarrow\rangle$ and vice versa. Hence the detected total signal will exhibit a minimum modulation. The value of this residual modulation depends on the ratio of singly to doubly occupied sites. As approximately half the atoms are isolated and half are trapped in doubly occupied sites, the minimum visibility will be close to zero. However, loss of atom pairs during the interaction will increase the minimum observable visibility. Importantly, for an interaction phase of $\phi_\chi = 2\pi$ the final state is restored. Here, atom pairs and isolated atoms show in-phase Ramsey fringes. Consequently the contrast of the oscillations is maximal.

In summary, for the interpretation of the Ramsey fringe data obtained in a system with both isolated atoms and particle pairs, two effects have to be taken into account. First, the collapse and revival of the Ramsey fringe contrast of the atom pairs due to interaction. And second the phase between the Ramsey fringe contributions of atom pairs and isolated

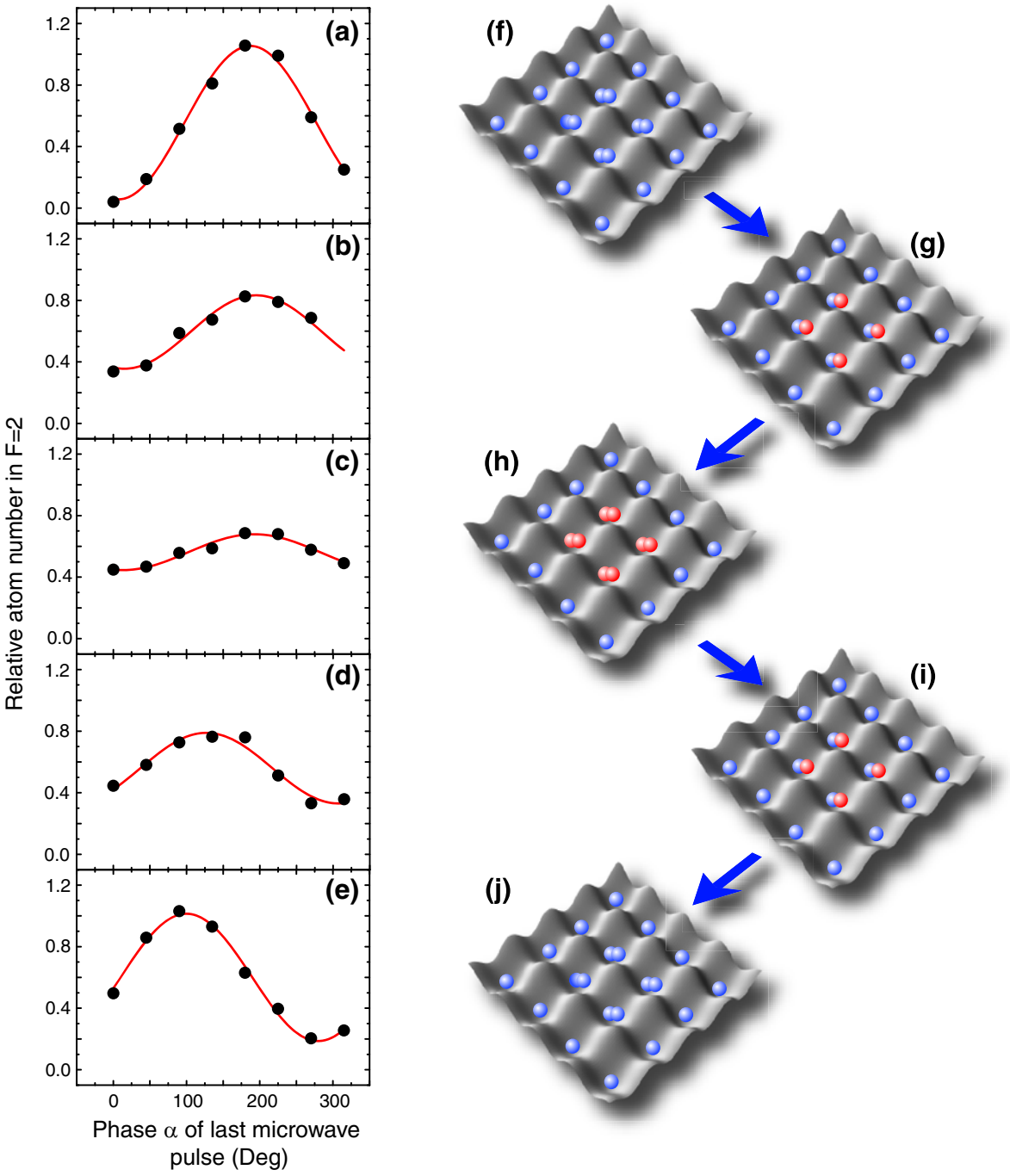

Figure 5.11: Ramsey fringes at a magnetic field of B = 9.081 G and interaction times of **(a)** 0.1 ms, **(b)** 2 ms, **(c)** 4 ms, **(d)** 7 ms, and **(e)** 10 ms. **(f) - (j)** On the right hand side a sketch illustrates for each respective interaction time the interplay between singly and doubly occupied lattice sites, where only the atom pairs undergo the entanglement oscillations: **(f)** in-phase Ramsey fringes, **(g)** entangled atom pairs, **(h)** fringes of isolated atoms and pairs are π out of phase, **(i)** entangled pairs, and **(j)** Ramsey fringes of all atoms are in phase again.

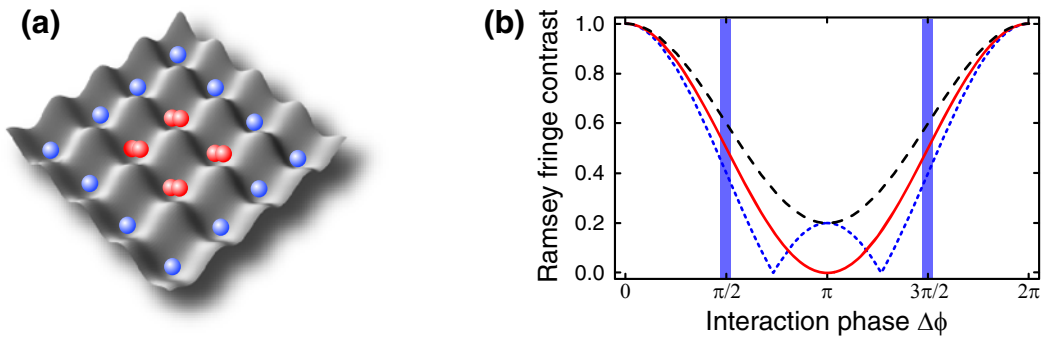

Figure 5.12: **(a)** In a mixture of isolated atoms and atoms pairs the contribution of both fractions add in the total signal of the Ramsey fringe measurement. **(b)** The form of the contrast versus interaction phase $\Delta\phi$ depends on the ratio n_1/n_2. For balanced populations (solid), the visibility reaches zero at exactly $\Delta\phi = \pi$, where both populations show a Ramsey fringe out of phase. For a ratio larger than unity ($n_1/n_2 = 3/2$ dashed line), the contrast never reaches zero, whereas for a ratio smaller than unity a small revival can be seen ($n_1/n_2 = 2/3$ dotted line). In all cases, the entangled pairs form for finite contrast at $\Delta\phi = \pi/2, 3\pi/2$ (blue shaded region). For $n_1/n_2 = 0$ the behavior shown in Fig. 5.2 is recovered.

atoms. This can be quantified by the expected Ramsey fringe signal which becomes

$$P_\uparrow = n_1 \cos(\alpha) + n_2 \cos(\alpha)\cos(\Delta\phi), \tag{5.39}$$

where n_1 is the fraction of isolated atoms and $n_2 = 1 - n_1$ is the relative number of atoms trapped at sites with double occupancy. The form of the resulting visibility oscillations depends very much on the ratio n_1/n_2, as can be seen in Fig. 5.12, and it can strongly deviate from the dynamics predicted by Eq. (5.15). In fact, the measured form of the visibility curve versus interaction time (see Fig. 5.13(a)) shows a rather harmonic oscillation, which in comparison with the theoretically calculated curve in Fig. 5.12(b) suggests a ratio of n_1/n_2 slightly larger than unity.

5.4.2 Precision measurements of elastic scattering properties

Another interesting feature of the interaction induced entanglement oscillations is the possibility to extract precise information about the altered interaction properties via the time scale of the phase evolution. In particular, for the revival of the Ramsey fringe contrast one finds

$$2\pi = \phi_\chi = \frac{1}{t_{\mathrm{rev}}}\,\tilde{U} \times a_\chi, \tag{5.40}$$

where t_{rev} is the interaction time after which the contrast has reached its maximum again. This can be precisely determined from the measured curves of visibility versus interaction time for a given magnetic field B as shown in Fig. 5.13(a).

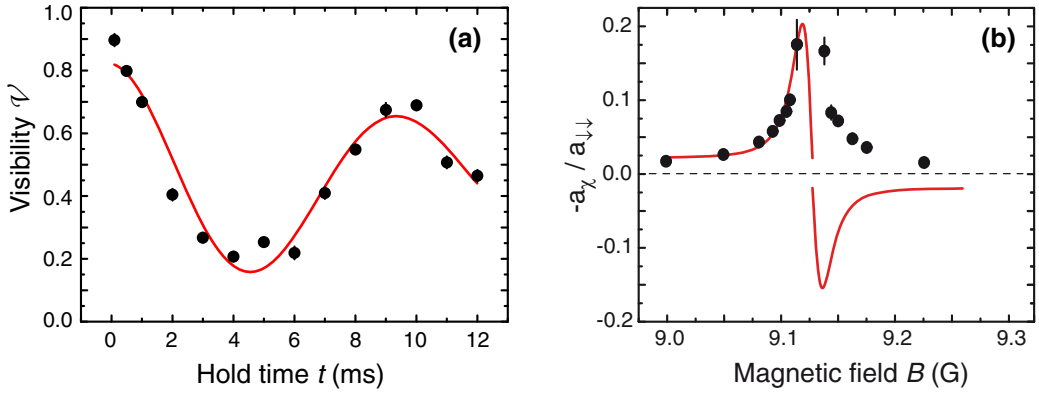

Figure 5.13: **(a)** Visibility $\mathcal{V}$ of Ramsey fringes versus interaction time t for a magnetic field of $B = 9.081\,\mathrm{G}$. The time t_{rev} when the visibility reaches a maximum again is determined by the change of elastic scattering length due to the Feshbach resonance. The value of the revival-visibility is limited by single-particle decoherence. Comparison with Fig. 5.12(b) suggests a ratio n_1/n_2 slightly larger than unity. **(b)** Extracted effective scattering length difference a_χ versus magnetic field in the proximity of the Feshbach resonance. The sign of the scattering length has been determined independently (see text).

The factor $\tilde{U}$ can be also independently determined by either calculations (see Section 3.3.2) or by calibrating the interaction strength via a collapse and revival of the coherent matter wave field [110]. The only unknown parameter is $a_\chi(B)$ which can be hence extracted from (5.40) by measuring t_{rev} as a function of the magnetic field value. This yields the basic form of the elastic channel for the predicted Feshbach resonance. This method, however, is not sensitive to the sign of the effective scattering length difference a_χ. In order to obtain also information about the sign of the effective scattering length difference, the size of the condensate prepared in a coherent superposition of $|\uparrow\rangle$ and $|\downarrow\rangle$ after TOF is measured, where during the first 3 ms of TOF the magnetic field is held at a certain value close to the Feshbach resonance [163]. The altered average scattering length is transformed into kinetic energy and can thereby change the expansion during TOF. The atom cloud changes size by $\approx 10\%$, indicating a larger average scattering length below the resonance and a smaller above. As the intra-species scattering lengths remain unchanged, this change can be attributed to the inter-species scattering, in agreement with the theoretical prediction. Including this information yields a complete measurement on the elastic channel of the Feshbach resonance; a fit to the expected dispersive profile returns a resonance position of $B_0 = 9.128(9)\,\mathrm{G}$ and a width of $\Delta = 15(4)\,\mathrm{mG}$, also in good agreement with theoretical predictions.

5.5 Reversible quantum phase dispersion in the many-particle system

Although the extension from the interacting two-particle case to N interacting particles appeared to be straightforward when turning from Section 5.1 to Section 5.2, the experimental realization turns out to be more involved. An important issue is the time scale on which the dynamics occurs compared to the coherence time of the system. Typical coherence times for the two states $|\uparrow\rangle$ and $|\downarrow\rangle$ are on the order of several ten milliseconds and limited by external, technical decoherence sources. The influence of decoherence can be seen e.g. in Fig. 5.13(a), where the decoherence limits the revival visibility to $\mathcal{V}(t_{\mathrm{rev}}) \lesssim 70\%$. Therefore the phase evolution must take place in a time short compared to this limit. In addition, in the many particle case several other physical mechanisms affecting the macroscopic relative phase have to be considered in order to gain a quantitative understanding of the experimentally obtained Ramsey fringe decay. Therefore the most important physical mechanisms will be discussed before the main results are presented.

5.5.1 Theoretical Model of Ramsey fringe collapse close to the Feshbach resonance

Single particle decoherence

Technical imperfections in the time period between the two $\pi/2$-pulses, such as magnetic field fluctuations or fluctuation of the lattice laser beam pointing or intensity, lead to a loss of coherence that typically suppresses the visibility of a Ramsey fringe exponentially with time

$$\mathcal{V}(t) \propto \exp\left(-\frac{1}{2}\frac{t}{t_{\mathrm{dec}}}\right). \tag{5.41}$$

Moreover, as the experimentally realized situation comprises many individual systems, spatial inhomogeneities cause a dephasing of the Ramsey fringes. This is also accounted for in the exponential decay (5.41). In practice, the time constant t_{dec} of this drop in the cases presented here is determined by an exponential fit to an experimentally obtained visibility decay far away from the Feshbach resonance, as shown in Fig. 5.14 with a typical decoherence time of $t_{\mathrm{dec}} = 27\,\mathrm{ms}$.

Phase dispersion

Preparing a 3D optical lattice system with a larger number of atoms might seem to be a simple way of increasing the number of interacting particles together with the non-linear interaction energy. Unfortunately, this approach is not feasible, as the resulting large densities at each lattice site combined with the relatively high loss rates in the $f = 2$ state would quickly deplete any lattice site with more than two atoms.

In order to keep losses low, instead of three pairs of standing waves only two are superimposed onto the BEC, creating a 2D optical lattice. In this case, atoms are trapped in an array of cigar shaped tubes (see Fig. 3.5(a)). In each of these tubes a quasi-1D Bose gas is realized [56, 67, 164]. Calculations (see Appendix B.3) show that for an atom number of 2.8×10^5 atoms, on the order of 8×10^3 tubes are filled with on average ~ 60 atoms. For

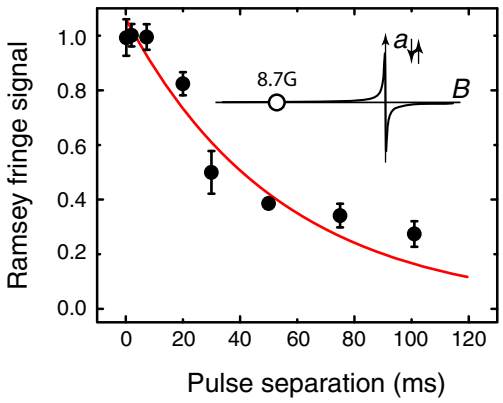

Figure 5.14: Time resolved decay of Ramsey fringe visibility far away from the Feshbach resonance at 8.7 G. The solid line is a fit to an exponential, yielding a decay to the $e^{-1/2}$ value in 27 ms.

typical final lattice depths of $40\,E_r$ along two axes, the radial confinement within each tube is strong, with trap frequencies $\omega_\perp \approx 2\pi \times 40\,\mathrm{kHz}$, while the axial confinement is relatively weak, $\omega_{\mathrm{ax}} \approx 2\pi \times 90\,\mathrm{Hz}$.

In order to calculate the non-linear interaction energy it is important to notice that the relevant quantity for the time evolution is the interaction energy rather than the chemical potential. The interaction energy is defined as

$$U_{\mathrm{tube}} = \left.\frac{\partial \mu}{\partial N}\right|_{N=N_{\mathrm{tube}}}, \tag{5.42}$$

where μ_{tube} and N_{tube} are the chemical potential and atom number in a single tube, respectively. As the chemical potential follows a power law (see Appendix B.3), the interaction energy can be calculated as [68]

$$U_{\mathrm{tube}} = \frac{2}{3}\,\frac{\mu_{\mathrm{tube}}}{N_{\mathrm{tube}}} \propto N_{\mathrm{tube}}^{-1/3}. \tag{5.43}$$

Hence, for constant chemical potential the interaction energy is effectively reduced with increasing number of particles. In order to estimate the value of the non-linear interaction parameter χ, the center of the Feshbach resonance is re-located in the 2D-lattice configuration ($B_0 = 9.120(4)\,\mathrm{G}$) and assumed to have the same width $\Delta_{\mathrm{el}} = 15(4)\,\mathrm{mG}$ and amplitude ≈20(4)% of the bare scattering length $a_{\downarrow\downarrow}$ as stated above. This yields scattering length differences a_χ on the order of a few 10% of the bare scattering length.

In order to calculate the interaction strength $\hbar\chi$, a single tube with N_{tube} atoms is considered that is axially in the Thomas-Fermi regime with known chemical potential μ [67]. The actual distribution of atom numbers N_{tube} in the array is calculated similar to the procedure in Ref. [16] by using the total atom number and actual trap parameters of our system. However, as argued in Appendix B.3, the total atom number affects the non-linear

interaction energy only very weakly. Therefore in the following a single tube is assumed and the average atom number and chemical potential in this system is calculated in order to find the relevant non-linear interaction energy. For the trapping parameters given above and an atom number of $N_{\mathrm{tube}} = 60$, the chemical potential can be calculated according to Ref. [67] as $\mu \approx h \times 2.5\,\mathrm{kHz}$. With this we find non-linear interaction parameters for $B = 9.131\,\mathrm{G}$ of $\chi \approx 2\pi \times 29\,\mathrm{Hz}$ and for $B = 9.106\,\mathrm{G}$ of $\chi \approx 2\pi \times -25\,\mathrm{Hz}$, respectively. The errors resulting from the uncertainty in the position and width are displayed in the calculated graphs below (Fig. 5.15 and 5.19) as shaded regions.

The role of losses

Atom losses can change the coherence of the system in various ways. If atoms are lost, usually internal energy is released as kinetic energy which can heat the system through secondary collisions and thereby diminish the coherence of the Ramsey interferometer prior to the last $\pi/2$-pulse. This effect becomes apparent as an exponential drop of the contrast of the Ramsey signal. In a fit, it is effectively described as single particle decoherence (5.41).

However, losses affect the phase distribution also in a more subtle way. As mentioned above, relative phase and atom number can be considered conjugate variables. Consequently, a random, uncorrelated loss from either spin state will lead to a phase kick of the expectation value $\langle \hat{S}_+ \rangle$. A series of such uncorrelated loss events will leave the expectation value of the phase unchanged. However, the distribution of the relative phase will spread irreversibly as has been shown in Ref. [165]. In this context it is important to note that the losses in the proximity of the Feshbach resonance are very likely to be correlated, as can be seen from the atom loss in a deep 3D optical lattice. There, the loss of atoms is strongly increased when approaching the resonance, even in a situation where three-body recombination is suppressed due to the lack of lattice sites with occupation number larger than two. This suggests that in particular the two-body loss rate is enhanced, which corresponds to a loss of exactly one atom from either spin state. From the formalism of Ref. [165] it can be shown that these correlated losses leave the phase distribution undisturbed. Therefore only the two-body and three-body loss rates far away from the resonance need to be considered. Applying the results of Ref. [165] to the case presented here, one finds a suppression of the Ramsey fringe contrast by a factor

$$\mathcal{V}(t) \propto \exp\left(-\frac{1}{2}\left(\frac{t}{t_{\mathrm{loss}}}\right)^3\right). \tag{5.44}$$

The characteristic decay time

$$t_{\mathrm{loss}} = \left(\frac{3}{\chi^2\, p^2 \lambda}\right)^{\frac{1}{3}} \tag{5.45}$$

depends on the specific loss process, where p particles are lost with an event rate λ per particle. With measured values of the three-body recombination rate for $f = 1$ of $K_3 \approx 5.8\times10^{-30}\,\mathrm{cm}^6/\mathrm{s}$ ([33]) and for $f = 2$ of $K_3 \approx 1.8\times10^{-29}\,\mathrm{cm}^6/\mathrm{s}$ ([43]) it can be estimated that

this contribution can be neglected for the experiments presented here. The corresponding decay time t_{loss} is on the order of a second. For the two-body loss the relevant process is the collision of two atoms in state $|\uparrow\rangle$ (i.e. $f = 2$), where losses have been seen to be significant [25]. Here the corresponding loss rate has been measured [25] as $K_2 \approx 8.8 \times 10^{-14}\,\text{cm}^3/\text{s}$. This contribution is more significant and yields for $B = 9.131\,\text{G}$ a value of $t_{\text{loss}} \approx 43\,\text{ms}$.

Effects on the spatial wave function

So far the discussion of interactions in a many-body system was greatly simplified by the single mode approximation, i.e. assuming a common, constant wave function for all spin states. Initially, all atoms occupy the same spatial wave function, as before the first $\pi/2$-pulse they are in the same spin state. The validity of this assumption after the preparation pulse depends strongly on the non-linear interaction parameter, in particular on its sign.

Below the Feshbach resonance $\chi < 0$ and the inter-species repulsion $a_{\uparrow\downarrow}$ is larger than the intra-species repulsion $a_{\downarrow\downarrow}$, $a_{\uparrow\uparrow}$. As the system tries to minimize the repulsive energy, the system tends to avoid the largest contribution due to inter-species interaction $a_{\uparrow\downarrow}$ and the initially well overlapped wave functions $\phi_\uparrow$ and $\phi_\downarrow$ will start to demix. Hence the system becomes dynamically unstable. The instability leads to the exponential creation of elementary excitations, resulting in a reduced wave function overlap and possibly heating prior to the final $\pi/2$-pulse. Therefore the Ramsey fringe contrast in this situation is reduced compared to the same absolute value of χ above the resonance. There, it is energetically favorable for the two spin states to mix as here the inter-species repulsion is smaller than the inter-species repulsion $a_{\uparrow\downarrow} < a_{\uparrow\uparrow}, a_{\downarrow\downarrow}$.

It should be noted that this kind of phase separation would also occur in a perfectly homogeneous system; it is therefore different from the one observed in Rubidium spinor BECs before [35], where $\chi \approx 0$ and the separation was driven by the inhomogeneity of the magnetic trap and a small difference between $a_{\uparrow\uparrow}$ and $a_{\downarrow\downarrow}$.

To quantify the effect of the phase separation on the final Ramsey fringe contrast, a Bogoliubov-type approach (cf. [54]) can be used to calculate the excitations in the system. From this one can estimate the visibility reduction of the Ramsey fringe due to the phase separation in the center of the tube as [166]

$$\mathcal{V}(t) \propto \exp\left(-\frac{1}{2}\,\frac{t}{t_\phi}\right), \tag{5.46}$$

with the time constant

$$t_\phi = c\,\frac{N\hbar^2\omega_z}{\mu^2} \times \frac{a_{\downarrow\downarrow}}{a_\chi}, \tag{5.47}$$

where ω_z is the axial trapping frequency along the tube, c is a proportionality constant and a_χ is assumed to be negative. In practice, the corresponding time constant is extracted from a fit to experimentally measured data.

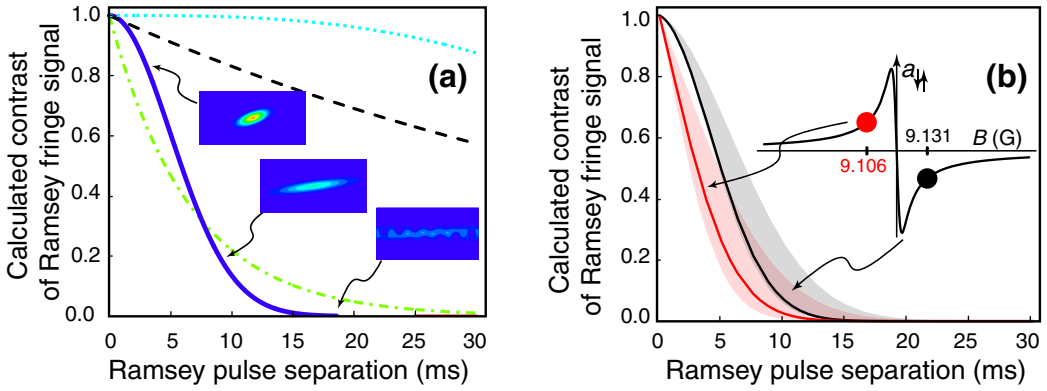

Figure 5.15: (a) Different contributions to the final Ramsey fringe collapse behavior. Included are the contributions of single particle decoherence (dashed line), phase dispersion (solid line), atom losses (dotted line), and phase separation below the Feshbach resonance (dashed-dotted line), calculated here for a typical experiment below the resonance at $B = 9.106\,\mathrm{G}$. At this magnetic field a non-linear interaction energy of $\chi = -25\,\mathrm{Hz}$ is expected. The single particle decoherence has been extracted from an independent measurement far away from the Feshbach resonance, see Fig. 5.14. **(b)** The total signal of Ramsey fringe collapse for magnetic fields above $B = 9.131\,\mathrm{G}$ (corresponding to $\chi \approx 29\,\mathrm{Hz}$), black, and below $B = 9.106\,\mathrm{G}$ the Feshbach resonance, red line. The latter is the signal obtained by incorporating all contributions shown in part (a). The shaded region reflects the possible values consistent with the uncertainties in position and width of the Feshbach resonance.

Total signal

The different effects presented above allow to estimate the total signal that is expected when the collapse of the Ramsey fringe is monitored in a time resolved measurement. Fig. 5.15(a) shows the contributions of the various mechanisms, according to phase dispersion (5.36), atom losses (5.44), and the phase separation below the Feshbach resonance (5.46). For the last contribution a proportionality constant c on the order of unity has been used; furthermore Eq. (5.46) has been assumed to be valid for the whole extension of the tube, instead of the tube center only. The resulting total signal for two magnetic fields above and below the Feshbach resonance are shown in Fig. 5.15(b).

5.5.2 Interaction induced collapse of the Ramsey fringe

The experimental sequence is very similar to the one used in the two-particle case, but the atoms are now confined in a quasi 1D geometry as explained above. A first $\pi/2$-pulse creates a CSS, which can evolve at a certain magnetic field B_1 for an interaction time t_{int}. Then a second $\pi/2$-pulse with variable phase α is again used to read out the relative phase between the two internal states. A Ramsey fringe is obtained by scanning α over 2π. The decay of contrast as defined in (5.14) is monitored over time at various magnetic fields.

Far away from the Feshbach resonance the effect of the non-linear term can be neglected.

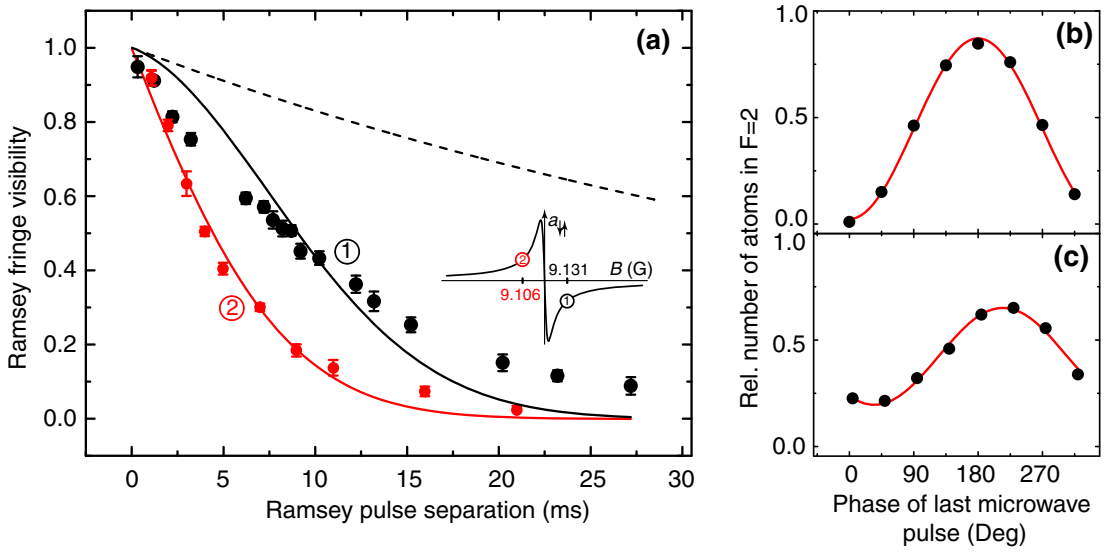

Figure 5.16: **(a)** Time resolved decay of Ramsey fringe visibility at two magnetic fields located almost symmetrically around the Feshbach resonance, $B = 9.106\,\mathrm{G}$ (red) and $B = 9.131\,\mathrm{G}$ (black). The solid lines are a constrained fit to (5.48). The dashed line reproduces the exponential decay far away from the resonance presented in Fig. 5.14. Each data point corresponds to a full Ramsey fringe, as shown here for 9.131 G and $t = 0.3\,\mathrm{ms}$ **(b)** and $t = 10.2\,\mathrm{ms}$ **(c)**.

An estimate using the scattering lengths quoted in Section 5.3 yields a typical time scale for the phase dispersion on the order of a second, far beyond the expected coherence time. In fact, a measurement of the Ramsey fringe visibility, including a single particle spin-echo pulse, shows an exponential decay to the $e^{-1/2}$ value within 27 ms as shown in Fig. 5.14. This decay is likely to be due to technical imperfections, such as technical noise on the currents creating the magnetic fields, background magnetic field fluctuations, or heating of the sample due to laser beam intensity or beam pointing fluctuations. We assume this decoherence to be approximately constant and use the measurement presented in Fig. 5.14 as a reference for the further discussion.

When the magnetic field is tuned close to the Feshbach resonance, the measured decay of Ramsey fringe visibility is much faster. In fact, this behavior is expected for an increased non-linear interaction. In Fig. 5.16 the time resolved decay of Ramsey fringe contrast is shown for two magnetic fields located almost symmetrically around the Feshbach resonance. As predicted by Eq. (5.36) the visibility drops faster than far away from the resonance. In fact, a single particle spin echo does not seem to have an effect on this behavior, supporting the assumption that the decay indeed is due to enhanced atomic interaction.

However, the observation differs from the prediction (5.36) in an important respect. Although both magnetic fields have the same separation from the center of the Feshbach resonance, implying an almost identical absolute value of the non-linear interaction energy $\hbar\chi$, the decay is much faster below the resonance. In contrast, Eq. (5.36) predicts a

symmetrical phase evolution if the change in interaction strength is symmetric. This can be attributed to the phase separation below the Feshbach resonance introduced in Section 5.5.1. In fact, a comparison between the measured data in Fig. 5.16 and the predictions of the model shown in Fig. 5.15 shows qualitative agreement between both figures. In order to extract quantitative information, a fit function is used, which includes the different contributions as introduced in Section 5.5.1

$$\mathcal{V}(t) = \exp\left\{-\frac{1}{2}\left(\frac{t}{t_{\mathrm{dec}}}\right)\right\} \times \exp\left\{-\frac{1}{2}\left(\frac{t}{t_{\mathrm{disp}}}\right)^2\right\} \times \exp\left\{-\frac{1}{2}\left(\frac{t}{t_{\mathrm{loss}}}\right)^3\right\} \times \exp\left\{-\frac{1}{2}\left(\frac{t}{t_{\phi}}\right)\right\}, \tag{5.48}$$

where the last term is relevant only below the Feshbach resonance.

For the data above the resonance at 9.131 G the independently determined value for $t_{\mathrm{dec}} = 27\,\mathrm{ms}$ (see Fig. 5.14) and the calculated value $t_{\mathrm{loss}} = 43\,\mathrm{ms}$ are fixed. The fit yields $t_{\mathrm{disp}} = 8.9(4)\,\mathrm{ms}$, on the same order as the calculated value of $4.5^{+2}_{-0.2}\,\mathrm{ms}$ for this magnetic field. For the measurement below the resonance $B = 9.106\,\mathrm{G}$, the contributions $t_{\mathrm{dec}} = 27\,\mathrm{ms}$ and $t_{\mathrm{loss}} = 47\,\mathrm{ms}$ are fixed. The remaining two parameters are fitted to be $t_{\mathrm{disp}} = 9(2)\,\mathrm{ms}$ and $t_{\phi} = 4.6(7)\,\mathrm{ms}$, also close to the calculated value $t_{\mathrm{disp}} = 5.0^{+2.5}_{-0.8}\,\mathrm{ms}$.

This enhanced Ramsey fringe collapse in the proximity of the Feshbach resonance is highly indicative of an interaction induced phase evolution. However, it is no proof for a coherent evolution of the relative phase, as other mechanisms such as decoherence can lead to a similar signature close to the Feshbach resonance. In particular, the systematic deviation of the fit from the measured data above the resonance in Fig. 5.16 suggests that the single particle decoherence has a larger effect on the total signal than far away from the resonance.

5.5.3 Time reversal

One possible way to prove that the quantum phase evolution is coherent, is to increase the interaction time, until the initial, disentangled state is restored. This could be detected by a revival of the coherence of the system as the initial CSS re-forms. From the discussion in Section 5.2.3 the revival time can be ≈ 50 times larger than the typical collapse time t_{disp}. For the cases shown above, this would correspond to a revival time $t_{\mathrm{rev}} \approx 400\,\mathrm{ms}$. Considering the fact that the other mechanisms tend to suppress the Ramsey fringe visibility on time scales already below 100 ms, it becomes apparent that this approach cannot be accomplished in the present setup. In fact, comparing the entanglement dynamics of two particles with the expected revival time of the many-body system (see Fig. 5.17) suggests that in the present situation the contrast of the many-body system is suppressed during the long waiting time until the revival occurs.

Instead, we follow a suggestion to time-reverse the evolution [167, 153], and thereby observe a revival of coherence in the system at much earlier times, well within the coherence time of our system. Such a time reversal sequence has been used in cavity quantum electrodynamics experiments [168] to probe the quantum dispersion of a coherent light field.

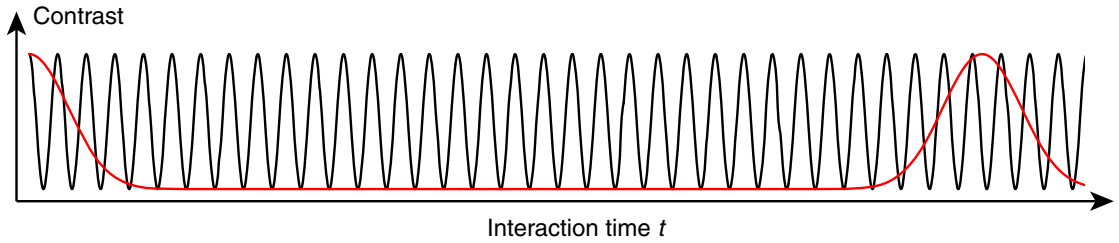

Figure 5.17: Calculated contrast versus interaction time for the two-particle case (black) and the many particle case (red). For illustration purposes, only every third oscillation in the two particle curve is shown. The parameters used are $U/\hbar = 2\pi \times 3\,\mathrm{kHz}$, $\mu_{\mathrm{tube}}/\hbar = 2\pi \times 2.5\,\mathrm{kHz}$, $N_{\mathrm{tube}} = 60$, $\chi = 0.1\, a_{\uparrow\uparrow}$.

Neglecting the effect of the spatial wave function, an initial contrast drop due to the non-linear interaction (5.30) can be restored by changing the sign of χ, which effectively reverses the time dynamics of the phase from $-i|\chi|\hat{S}^2 t$ to $+i|\chi|\hat{S}^2 t$. However, since the spatial wave function is also affected by a sign change of χ, an increase of Ramsey fringe contrast is not always a sufficient signal of coherent phase evolution, as the transition from a dynamically instable to a spin-mixing situation could increase the visibility similarly to the phase dynamics.

Experimental time reversal sequence

In order to be able to attribute the increased visibility to the coherent nature of the phase evolution, the following sequence is applied (see Fig. 5.18(a)).

After a first $\pi/2$-pulse, the system evolves for 6 ms under an effective interaction $\chi > 0$, i.e. at a magnetic field B_1 above the Feshbach resonance, until the Ramsey fringe contrast has dropped to approximately 60%. In this region the two spin components are miscible and the spatial wave functions are expected to be well overlapped. Subsequently, the sign of the effective interaction is rapidly changed from $\chi > 0$ to $\chi < 0$ by quickly ramping the magnetic field over the Feshbach resonance to a value B_2 a few 10 mG below the resonance. In this region demixing of the two spin components tends to decrease the Ramsey fringe contrast. Consequently, any increase in the visibility after changing the sign of χ can be attributed only to a reversed coherent phase evolution rather than to a change in the spatial wave function overlap.

Ramping through the resonance, however, is accompanied by drastically increased atom losses induced by the Feshbach resonance. If these losses cannot be omitted, they easily completely destroy the coherence of the system, leaving a small thermal atomic sample. In order to minimize the effect of losses on the system, shortly before the magnetic field ramp, the atomic density is reduced by lowering the trap depth of the optical potential to a value of the mean radial trap frequency of $\omega_\perp \approx 2\pi \times 27\,\mathrm{kHz}$. The ramp of the optical potential is done in $\approx 200\,\mu\mathrm{s}$, which is slow enough not to excite higher radial vibrational

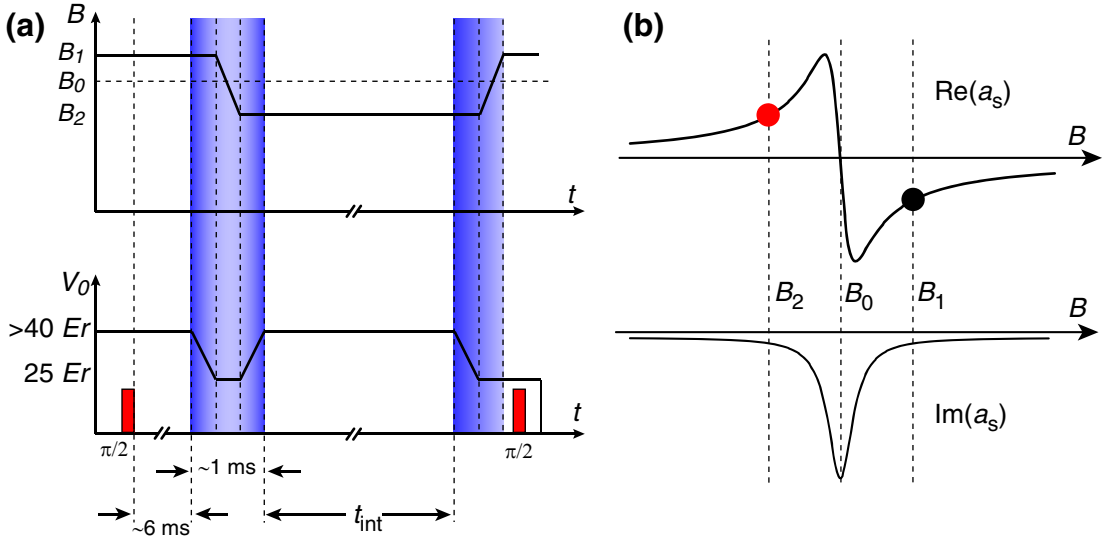

Figure 5.18: **(a)** Time reversal sequence for the magnetic field (upper graph) and optical potential (lower graph). Within the first 6 ms of interaction time, a π-pulse acts as a single-particle spin echo. This is, however, not possible in the second hold time at B_2, because this would imply two additional ramps through the resonance to reach the magnetic field B_1 while applying the π-pulse. Moreover, as stated above, an effect of the single-particle spin echo on the Ramsey fringe contrast decay could not be seen close to the Feshbach resonance. **(b)** Real and imaginary part of the scattering length around the Feshbach resonance. Ramping the magnetic field from B_1 to B_2 brings the system through a regime of extremely high losses. In order to avoid substantial heating, the optical potential is lowered in order to reduce the atomic density while the magnetic field is changed. Thereby the magnetic field ramp can be performed without measurable heating or losses.

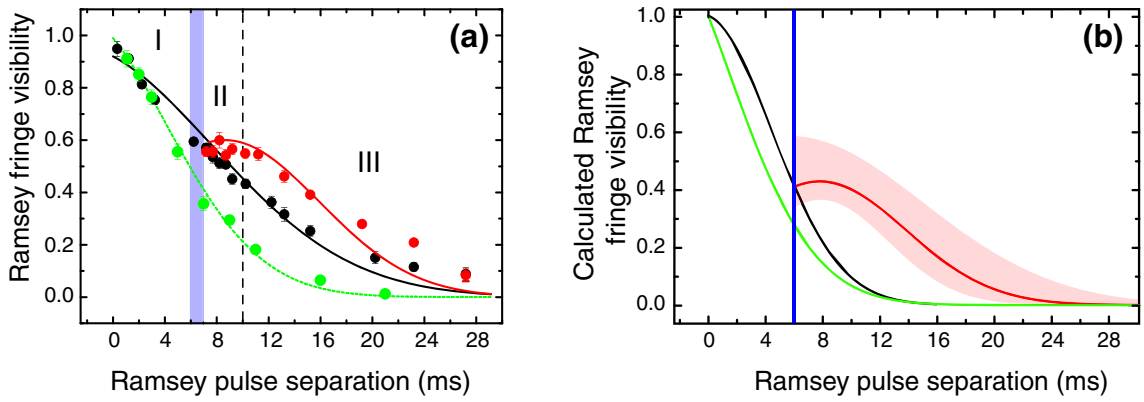

Figure 5.19: Result of a time reversal sequence on the quantum phase dispersion. **(a)** Measured data where the sample has been held exclusively at $B_1 = 9.131\,\mathrm{G}$ (black) or $B_2 = 9.101\,\mathrm{G}$ (green), and of the time reversal, where the system could interact for 6 ms at B_1. The magnetic field is subsequently changed to B_2 (red). **(b)** Predictions of the model with no free parameter for the same situation as predicted in (a). The red shaded region reflects the possible values consistent with the uncertainties in position and width of the Feshbach resonance. The time when the reversal is applied is indicated by a blue shaded region and blue line for (a) and (b), respectively.

modes in the system. The subsequent magnetic field ramp crosses the region of increased losses at the center of the resonance within a few $10\,\mu$s. Finally the magnetic field needs $\approx 200\,\mu$s to stabilize at the final value before the optical potential is ramped back up to its initial value. This sequence takes approximately 1 ms and enables us to cross the resonance without significant additional atom loss or heating.

Due to the changed sign of χ, the phase dynamics is effectively inverted and causes the phase distribution to evolve back towards the initially prepared Gaussian distribution, and beyond [136]. As a consequence, the measured contrast of a Ramsey fringe will increase with time until the initial distribution is restored; further time evolution will cause the Ramsey fringe contrast to drop again. It should be noted that the time reversal presented here relates to the evolution of the many-body wave function, while the more common single particle spin echo technique in magnetic resonance affects only the single particle evolution.

Fig. 5.19(a) displays the result of such a time-reversal sequence together with the prediction of the model introduced above (no free parameters) in Fig. 5.19(b). Although the model systematically predicts smaller visibilities, it qualitatively reproduces the observed behavior of the system: The visibility drops due to several mechanisms in Fig. 5.19(a), region I. After the time reversal has been applied, the quantum phase distribution evolves back towards the initial CSS, while other mechanisms continue to suppress the visibility, until a local maximum is reached when the CSS has revived (region II). For longer interaction time, the phase distribution starts to spread again, so that all contributions tend to decrease the visibility (region III).

Limitations on the restored coherence

Ideally one would expect the visibility to revive back to the initial value. However, due to several mechanisms a complete revival of the contrast cannot be observed. This can be seen in Eq. (5.48), where all physical effects but the phase dispersion tend to suppress the visibility irrespective of a time reversal sequence. In particular, the changed sign of the effective interaction below the resonance and the resulting strong consequences on the spatial wave function imply the by far strongest reduction of the Ramsey fringe contrast at the revival time. In order to partially compensate for this artificial decrease, we take the data including the time reversal by jumping to B_2 after a certain time on the one hand, and with just holding at the final B_2 from the start on the other hand. In both data sets the contrast decay due to decoherence, loss and especially due to the spatial wave function instability is expected to be approximately the same, because they evolve at the same magnetic field. The difference between both data sets, however, is exactly the behavior of the phase dispersion contribution. Therefore the calculated difference between both data sets is expected to exhibit a clear signature of the revival of the Ramsey fringe visibility. In fact, the experimentally determined difference displayed in Fig. 5.20 indeed reveals clearly the revival of coherence. The visibility maximum shifts to smaller times, when the final magnetic field is set closer to the Feshbach resonance. The shift of the maximum is due to the fact that closer to the Feshbach resonance the reversed time evolution takes place faster because of an increased value of the effective interaction χ.

5.6 Conclusion

The experiments presented in this chapter clearly show the coherent nature of the interaction induced evolution of the relative phase, leading to an entanglement evolution in the two particle case, and to a more intricate phase evolution in the many-body system.

The experimental demonstration of the two-particle entanglement evolution presented in Section 5.4 is a way to deterministically create a large array of maximally entangled atom pairs for $\phi_\chi = \pi/2$ that can be used for further experiments, e.g. a register or resource for quantum computing purposes. Moreover, the method presented also offers the possibility to non-destructively separate singly from doubly occupied sites. For an interaction phase $\phi_\chi = \pi$, the expectation value $\langle \hat{S}_z \rangle$ for singly and doubly occupied sites is maximally different, meaning that the Bloch vectors of these two different occupation numbers point to exactly opposite points on the Bloch sphere. Additional microwave or laser pulses can therefore manipulate the population of one specific occupation number, independent of the remaining population.

The demonstration of revival of coherence after time reversal of the many-body time evolution presented in Section 5.5 shows that the phase dispersion dynamics due to the non-linear interaction is indeed a coherent process. Importantly, many limitations discussed above are not fundamental but rather due to the specific experimental realization, i.e. an array of tubes.

The experiment presented is an example how interactions can transform coherence into

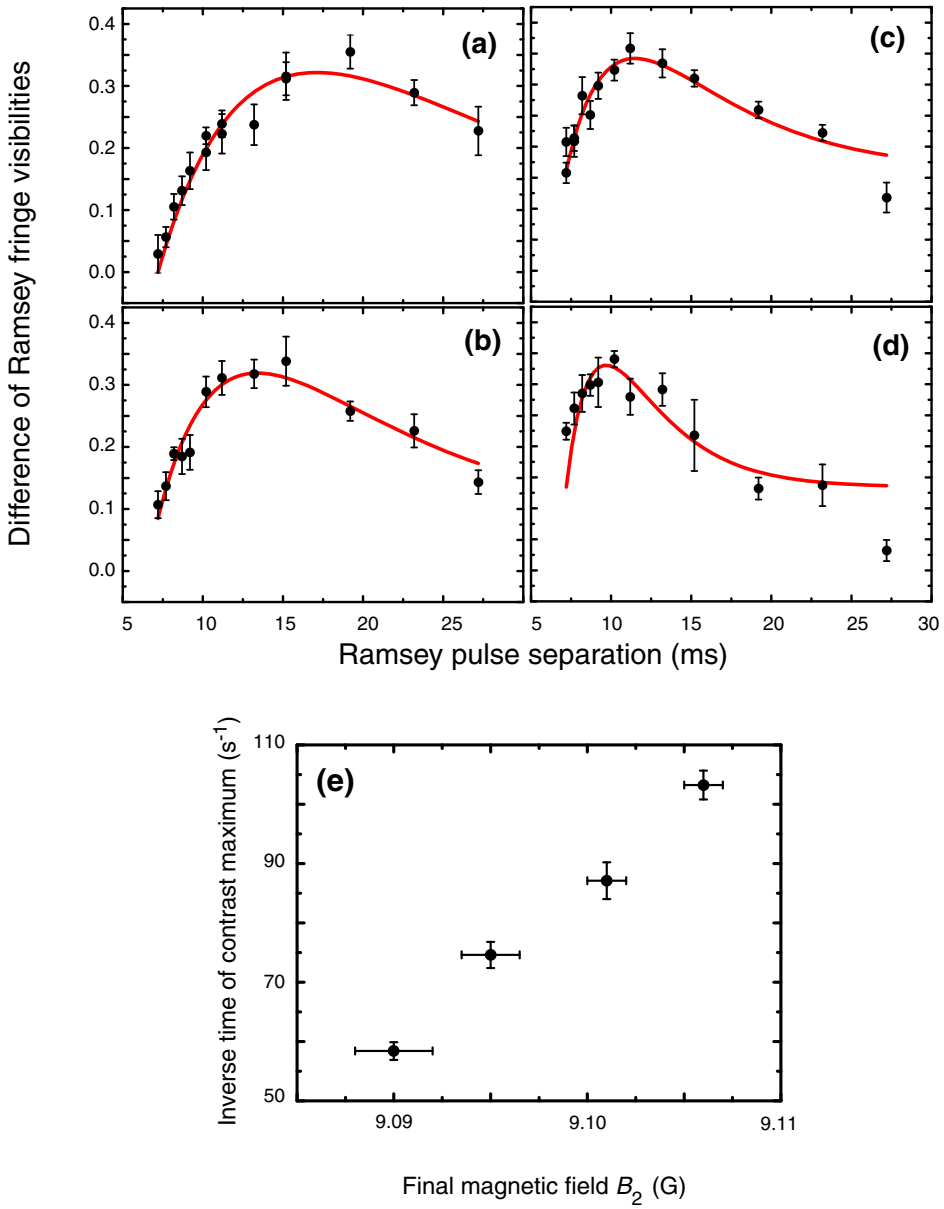

Figure 5.20: Revival of coherence after time reversal. Displayed is the Ramsey fringe contrast difference between signals obtained after a time reversal sequence, i.e. holding for 6 ms at a magnetic field B_1 above the resonance and subsequently jumping to B_2 below the resonance, and signals taken at B_2 from the start. Both signals are expected to show the same contribution of the altered spatial wave function overlap; this is to first order compensated in the difference. Solid lines are a guide to the eye. For all curves, $B_1 = 9.131$ G. **(a)** $B_2 = 9.090$ G, **(b)** $B_2 = 9.095$ G, **(c)** $B_2 = 9.101$ G, and **(d)** $B_2 = 9.105$ G. As the time of maximal contrast is related to the strength of the non-linear interaction, we plot the inverse time of maximal contrast versus B_2 in **(e)**, which shows an increase as expected for the left branch of the Feshbach resonance.

inter-particle correlations; if the information embedded in these correlations is not extracted, for example by higher order correlation measurements, the lack of this information becomes apparent as decoherence. This is the case in typical atom interferometer experiments, because they probe the first order coherence of the system only, whereas interatomic interactions tend to decrease the first order coherence in favor of higher order correlations. As demonstrated, the coherence is not irreversibly lost, but it can be restored by proper manipulation of the underlying interactions. At the same time the results underline the importance to develop more experimental tools to create and probe the fascinating properties of strongly correlated quantum states.

6 Outlook

The results of the experiments described in this thesis pave the way for the creation of several correlated spin states. In the following we will briefly summarize the main findings, and subsequently outline some future prospects and suggestions.

6.1 Spin changing collisions

In the course of this thesis, the coherent, interaction driven spin population oscillations due to spin changing collisions have been observed. The measured oscillations could be described by a Rabi-type model or a model of three coupled states, depending on the number of involved Zeeman states accessible as final scattering states. The extracted coupling parameters are directly related to atomic scattering length differences, which could be inferred with high precision. This allowed to determine the magnetic ground states for the ^{87}Rb hyperfine states to be ferromagnetic and antiferromagnetic for the $f = 1$ and $f = 2$ states, respectively.

We have been able to develop a method to control the spin changing population oscillations in terms of an AC-Zeeman effect. Thereby, fully resonant population transfer between different spin states could be achieved. The amplitude of such oscillations could be consequently employed as a quantitative probe for particle pairs in our lattice. This allowed to monitor the on-site number squeezing as the system is brought from the superfluid to the Mott-insulating regime on the one hand, and the spatial resolution of Mott-insulator shells on the other hand.

The potential of controlling spin changing collisions as described in chapter 4 goes well beyond the applications that have already been realized [11, 12]. Here two further promising applications will be outlined. First, a spin-spin interaction will be introduced that has been just briefly mentioned in the beginning of this thesis. Second, as shown in this thesis, atomic interactions can build up quantum correlations between particles in a system. The properties of a correlated spin state resulting from a coherent spin changing collision will be discussed.

Dipolar effects in spin dynamics A topic which has attracted lots of attention recently is the realization of dipole-dipole interactions in a degenerate gas of atoms, see e.g. [169, 170, 171, 172]. There are two main reasons for this attention. First, the dipole-dipole interaction is a long range interaction compared to the contact interaction that has been considered so far. And second, unlike the spherical symmetric s-wave interactions, the dipole-dipole interaction potential is not invariant under spatial rotations. This can be

seen by comparing the contact interaction for spin-1 atoms (cf. Eq. (4.23))

$$V_s = (c_0 + c_2\,\mathbf{f}_1 \cdot \mathbf{f}_2)\,\delta(\mathbf{r}) \tag{6.1}$$

with the dipole-dipole interaction potential

$$V_{\mathrm{dd}} = \frac{c_{dd}}{r^3}\,(\mathbf{f}_1 \cdot \mathbf{f}_2 - 3(\mathbf{f}_1 \cdot \hat{e}_r) \cdot (\mathbf{f}_2 \cdot \hat{e}_r))\,, \tag{6.2}$$

where c_0 and c_2 have been defined in Section 4.5 on page 76, $\mathbf{r} = \mathbf{r}_1 - \mathbf{r}_2$ is the relative coordinate between the two atoms, and

$$c_{\mathrm{dd}} \equiv \frac{\mu_0}{4\pi}\, g_F^2 \mu_B^2. \tag{6.3}$$

Here μ_0 is the permeability of the vacuum. For alkali atoms, the dipole-dipole interaction (and correspondingly c_{dd}) is several orders of magnitude smaller than the mean-field interaction (i.e. c_0). In order to relate the dipole-dipole interaction to the spin-independent interaction, the typical figure of merit is the dimensionless parameter

$$\varepsilon_{\mathrm{dd}} \equiv \frac{4}{3}\pi r^3 \times \frac{c_{\mathrm{dd}}/r^3}{c_0} = \frac{\mu_0 \mu_m^2 m}{12\pi a_s}, \tag{6.4}$$

where a "typical" volume $\frac{4}{3}\pi r^3$ is assumed in order to compare both strengths correctly, and μ_m is the permanent dipole moment. For alkali atoms, the relative dipole strength (6.4) can be calculated to be $\varepsilon_{\mathrm{dd}} = 6.4 \times 10^{-3}$ for ^{87}Rb and 3.5×10^{-3} for ^{23}Na. Therefore other species with larger permanent dipole moment are are usually considered more promising candidates in order to observe dipolar interactions. Recently, ^{52}Cr has been cooled to degeneracy [173]; this species has a magnetic moment of $6\,\mu_B$ and therefore exhibits dipole-dipole interactions that are larger by a factor 36 compared to alkali atoms; in fact the relative dipole-dipole interaction strength has been measured to be $\sim 160 \times 10^{-3}$ for ^{52}Cr [174] and the signature of dipole-dipole interactions in these gases has been observed [175].

In our case of a deep optical lattice, however, the spin dynamics is not driven by the mean field equivalent $\propto c_0$, but by the spin-changing interaction $\propto c_2$. Therefore it has been pointed out [80] that the dipole-dipole interaction should be rather compared to this quantity. In order to compare the different contributions, the interaction energies for our typical parameters (i. e. $40\,E_r$ deep lattice, $\lambda_{\mathrm{lat}} = 840\,\mathrm{nm}$) have been calculated [80] to be $c_0\,n_0/\hbar \approx 2\pi \times 6.6\,\mathrm{kHz}$ for the spin independent interaction, $c_2\,n/\hbar \approx 2\pi \times (-30)\,\mathrm{Hz}$ for the spin dependent interaction (the sign reflects ferromagnetic nature of the magnetic ground state), and $c_{\mathrm{dd}}\,n/\hbar \approx 2\pi \times 3\,\mathrm{Hz}$ for the dipole-dipole interaction in a spherical symmetric trap, with n_0 the density in the lowest vibrational state. Due to the spherical symmetry, the contribution of the dipole-dipole interaction will average to zero; still, the order of magnitude estimate shows that the contribution of a few Hz can in principle be detected, as the spin population oscillations have been seen to be sensitive enough. In the optical lattice, however, by choosing different lattice depths or laser wavelengths along different axes, the vibrational frequencies can be made different along the axes. The corresponding

asymmetry parameter $\lambda \equiv \omega_z/\omega_\perp$ can be adjusted to yield either oblate ($\lambda > 1$) or prolate ($\lambda < 1$) shaped lattice wells. This breaks the symmetry of the problem, so that the dipole-dipole interaction does not average to zero. It has been stated [80] that for $\lambda \geq 3$ the dipole-dipole interaction can exceed 10% of the spin dependent interaction, which should be detectable in the spin population oscillations. This approach is limited however, as the asymmetry is adjusted by reducing the lattice laser power along one axis while increasing it along other axes. The limitation to higher depths is imposed by available laser power. A typical maximum lattice depth here is around 70 to $80\,E_r$. Unfortunately, the trapping frequency scales with the square root of the lattice depth, so that compared to the measurements presented in this thesis at $40\,E_r$ the increase in λ is only a factor 1.4. For lower lattice depths the onset of tunneling limits the observation of spin population oscillations. For small anisotropy, the effect of the dipole-dipole interaction is small and the measurement time must be long in order to resolve this small change. Therefore, lattice depths smaller than $30\,E_r$ will probably allow for too much tunnel processes which will damp the spin changing oscillations. These problems can be overcome for example by using a different lattice laser wavelength along one of the axes. For example, with the same tunneling rate as in a $40\,E_r$ deep lattice at 840 nm, choosing on one axis a lattice with roughly the double periodicity would lead to an asymmetry parameter of $\lambda \approx 4$, which clearly enhances the contribution of dipole-dipole interaction. Therefore, it seems well possible that in optical lattice traps the effect of dipole-dipole interactions can be very precisely investigated.

A source for "decoherence free" qubits So far one important fact has been used implicitly in the discussion of the spin changing collision process. Initially the system has been prepared in state $|m_1 = 0; m_2 = 0\rangle$ and evolves for half an oscillation period of the spin oscillations. In the resulting state we have no information about which atom is in which Zeeman sublevel. This fact has been included in the discussion via the symmetrization operator $\mathcal{S}$ in Eq. (4.2). Explicitly writing the symmetrized wave function yields

$$|\psi_f\rangle = \frac{1}{\sqrt{2}}\left(|m_1 = -1, m_2 = +1\rangle + |m_1 = +1, m_2 = -1\rangle\right), \tag{6.5}$$

where again 1 and 2 label the atoms and we have omitted explicitly writing the total angular momentum f. The triplet state naturally emerges in the quantum mechanical description of the two-body spin problem and can be found for example in the electronic state of the Helium atom. It is, however, interesting as the embedded spin correlations can be transferred into entangled states.

The particular structure of the triplet state makes it very insusceptible to external perturbations due to e.g. magnetic field fluctuations. Those fluctuations affect the two Zeeman sublevels $m = +1$ and $m = -1$ differently because of their different magnetic moment. In many experiments the different Zeeman energies lead to an additional single particle phase evolution that is different for the two sublevels. In case of residual magnetic gradient fields, this will lead to a dephasing of the system. In the experimental signal this becomes visible

as decoherence. For the two-particle state given in Eq. (6.5), however, each term acquires the same phase, as we only consider the same combinations of Zeeman sublevels. This phase is therefore common to all terms and can be neglected as a global phase. For quantum information processing, it is therefore advantageous to encode the qubits in such "decoherence free subspaces" as this enables a larger number of operations within the typical coherence time. In recent experiments with trapped ions, this property of robustness has been already experimentally implemented in more sophisticated entangled quantum states to yield extremely long-lived Bell-states [176] and to improve the sensitivity of precision measurements [177].

Spin squeezing in a perfectly spin-correlated state An array of triplet states (6.5) has another intriguing property. If such an array, originally trapped in an optical lattice, is melted, i.e. the optical potential is adiabatically switched off, the final spin state becomes

$$|\Psi_T\rangle = \left(\left(\hat{c}_\uparrow^\dagger\right)^{\otimes N/2} + \left(\hat{c}_\downarrow^\dagger\right)^{\otimes N/2}\right)|0\rangle. \tag{6.6}$$

Compared to a "normal" coherent superposition of the two internal states

$$|\Psi_{\text{coh}}\rangle = \left(\frac{\hat{c}_\uparrow^\dagger + \hat{c}_\downarrow^\dagger}{\sqrt{2}}\right)^{\otimes N}|0\rangle, \tag{6.7}$$

the triplet state is not only a number squeezed state, i.e. fluctuations of the atom number in the spin states are reduced; it is moreover a perfectly correlated spin state, i.e. for every single atom in $|\uparrow\rangle$ there is exactly one in $|\downarrow\rangle$, in each single realization of the experiment. It might be interesting to closer investigate these correlations as it might give a deeper insight into other strongly spin-correlated systems and lead to a better understanding on how such correlations are affected by finite temperature, atom loss or other decoherence sources.

6.2 Coherent phase evolution

Interacting spin-1/2 systems can show an interesting time evolution of the relative phase between the two internal states. For two particles, the atom pair undergoes an interaction driven entanglement dynamics between a separable state and an entangled state. This dynamics could be observed by monitoring the coherence properties of an array of atom pairs in a Ramsey-type interferometer sequence. Here, the obtained Ramsey fringes showed an oscillatory collapse and revival demonstrating the predicted entanglement dynamics. For a many-body system, non-linear interactions is predicted to lead to a dispersion of the relative phase to a spin squeezed state and eventually to a Schrödinger cat state. The dynamics could be observed by the collapse of the Ramsey fringe contrast which is a consequence of increased phase fluctuation due to the phase dispersion. In a time-reversal sequence this dynamics could be reversed and a revival of coherence could be observed.

The ability to manipulate a quantum many-body state to see a coherent and reversible phase evolution is a promising starting point for further experiments. However, the various other mechanisms limiting the maximum revival contrast in the measurements seem to object to observe a further phase evolution. A close investigation reveals that most of these objections are not fundamental but rather due to the specific experimental realization.

Spin squeezing in a single tube First the coherence in the system can still be improved, e.g. by actively reducing magnetic field fluctuations over time. Further, investigating a single interacting many-body system instead of an array of quantum gases as created in the optical lattice leads to several advantages. Spatial inhomogeneities are expected to affect the coherence less than in the more extended array of tubes. Further, a measurement on a single system does not constitute an ensemble average as this was the case in the array of tubes. Thereby the variance of the quantum phase distribution could be directly accessed. The direct observation of the fluctuations would also allow to observe the phase dynamics on only one side of the Feshbach resonance, thereby avoiding the artificial decrease of Ramsey fringe contrast for negative values of the effective interaction energy χ due to the dynamical instability of the spatial wave function.

All these improvements might eventually bring the creation of a material Schrödinger cat into reach.

Simulation of quantum magnetism The dynamical instability at one side of the Feshbach resonance has so far been considered as an inconvenient complication in the observation of phase dynamics. The origin of a spin mixing region on the one side and a phase separating region on the other side of the Feshbach resonance, however, implies a very intriguing application.

Assuming a homogeneous system in a superposition of the two internal states (after a $\pi/2$-pulse) for $\chi = 0$, the spatial wave function in the two-mode approximation will be the same for both spin states. Tuning now $\chi < 0$, the difference in interaction energies will start to separate the two spin wave functions as explained already above. The ground state in this region is similar to a ferromagnet, where domains of equal spin form. Thereby a large repulsive interaction energy is present only at the borders to neighboring spin domains ("domain walls"), while the interaction energy in the bulk of the domain is reduced. Likewise, for $\chi > 0$ the spins mix. In the limit $a_{\uparrow\downarrow} = 0$ and for $T = 0$ the ground state of the system will exhibit antiferromagnetic order. In such a situation the interaction energy would be zero.

The Feshbach resonance therefore allows to tune magnetic interactions both qualitatively and quantitatively between ferro- and antiferromagnetic. In a single tube with a high resolution optical detection system [178, 179], this would offer the opportunity to study the quantum dynamics of domain formation, or to create an antiferromagnetic system.

The high degree of control over the spin interactions in this thesis pave the way for the creation of novel correlated spin states. However, for future experiments several points have

to be considered. First, for the realization of many novel quantum states, the temperature of the sample can become an issue [180]. Moreover, in order to verify the creation of correlated states and to exploit their properties, their correlations have to be directly detectable and accessible in experiments. In order to reveal the underlying structure of spin-correlated many body states, novel techniques have therefore to be developed. A promising candidate is the spin-sensitive extension of the noise-correlation measurements already used to see the particle correlations in a molecular BEC [14] or site correlations in a MI state [94]. Such a technique would enable the direct observation of e.g. a spin-antiferromagnet or spin pair correlations, as well as dynamical properties of such states.

A Calculating spin dependent interaction strengths

It is important to notice that for the collision of two spin-1 atoms only one scattering length difference is sufficient to describe the dynamics; for the case of two colliding spin-2 particles there are two relevant scattering length differences. For $f = 1$ this is the difference $a_2 - a_0$, and for $f = 2$ there are two differences $a_2 - a_0$ and $a_4 - a_2$. In most of the cases it is, however, more convenient to use derived quantities that directly describe the dynamics for the actual experimental situation. In this section the line of argumentation given in chapter 4 will be expanded. In particular, the relevant parameters for the spin dependent interaction in $f = 1$ will be explicitly calculated.

In order to keep notation simple, we employ second quantized notation and restrict the discussion to the case $f = 1$. The field annihilation operator for an atom in state $|1, m\rangle$ at position $\mathbf{r}$ is $\hat{\Psi}_m(\mathbf{r})$, and we assume a common, constant spatial wave function $\phi_0(r)$ for all spin states. In the following we might omit writing the spatial dependence explicitly. With this the Hamiltonian for the spin dependent interaction can be written as

$$\hat{H}_s = \frac{1}{2} \int d^3\mathbf{r} \sum_{ijkl} \hat{\Psi}_k^\dagger \hat{\Psi}_l^\dagger \sum_{F=0}^{2f} g_F \, \mathcal{P}_F \, \delta(\mathbf{r}) \, \hat{\Psi}_i \hat{\Psi}_j, \tag{A.1}$$

where the relative coordinate between the two particles is denoted as $\mathbf{r}$. The integration over the delta function can be evaluated by using the assumption of a common wave function to yield a factor $\int d^3\mathbf{r} |\phi_0|^4$. With this we define $\tilde{U} \equiv \frac{4\pi\hbar^2}{M} \times \int d^3r \, |\phi_0(r)|^4$. As the contribution of the spatial wave function can be considered as a constant factor, we use in the following "spin operators", where $\hat{\psi}_i$ is the annihilation operator of the spin state $|f, m = i\rangle$. Then the Hamiltonian can be written as

$$\hat{H}_s = \tilde{U} \times \frac{1}{2} \sum_{ijkl} \hat{\psi}_k^\dagger \hat{\psi}_l^\dagger \left(\sum_{F=0}^{2f} \sum_m \langle f, k; f, l | F, m \rangle \langle F, m | f, i; f, j \rangle \times a_F \right) \hat{\psi}_i \, \hat{\psi}_j, \tag{A.2}$$

where we have explicitly written the projection onto the intermediate, coupled state $|F, m\rangle$. As already mentioned, for bosons only even values of F are possible. Using the abbreviation

$$\Delta a_{ij}^{kl} \equiv \sum_{F=0}^{2f} \sum_m a_F \times \langle f, k; f, l | F, m \rangle \langle F, m | f, i; f, j \rangle \tag{A.3}$$

the re-sorted Hamiltonian (A.2) reads

$$\hat{H}_s \;=\; \frac{\tilde{U}}{2} \times \left(\sum_i \Delta a_{ii}^{ii} \, \hat{\psi}_i^{\dagger 2} \, \hat{\psi}_i^2 + \sum_{i,j} \Delta a_{ij}^{ij} \, \hat{\psi}_i^\dagger \, \hat{\psi}_j^\dagger \, \hat{\psi}_i \, \hat{\psi}_j \right. \tag{A.4}$$

$$+ \sum_{i+j=k+l} \Delta a_{ij}^{kl}\, \hat{\psi}_k^\dagger\, \hat{\psi}_l^\dagger\, \hat{\psi}_i\, \hat{\psi}_j \Bigg). \tag{A.5}$$

The terms in the first row (A.4) are the so-called "self-interaction energy"; the difference between each two of these terms gives rise to the interaction detuning δ_{int}. The second line (A.5) is responsible for the spin changing interaction; here, the conservation of magnetization has been indicated in the sum.

For the example of two interacting spin-1 atoms, the Hamiltonian reduces to three non-zero terms:

$$\hat{H}_s(f=1) = \frac{\tilde{U}}{2} \times \left(\Delta a_{00}^{00} \times \hat{\psi}_0^{\dagger 2}\, \hat{\psi}_0^2 + 4\, \Delta a_{+1-1}^{+1-1} \times \hat{\psi}_{+1}^\dagger\, \hat{\psi}_{-1}^\dagger\, \hat{\psi}_{+1}\, \hat{\psi}_{-1} + 2\, \Delta a_{00}^{+1-1} \times \hat{\psi}_{+1}^\dagger\, \hat{\psi}_{-1}^\dagger\, \hat{\psi}_0^2 \right). \tag{A.6}$$

Here, the first two terms are the self-interaction energies in the initial and final two-particle states, and the third term describes the spin-changing interaction. The interaction energy for changing an initial state $|i\rangle$ into a final state $|f\rangle$ can be calculated as $\langle f|\hat{H}_s|i\rangle$. The states in second quantized notation can be written as $|i\rangle = |m_1 = 0, m_2 = 0\rangle \rightarrow |2:0\rangle$ and $|f\rangle = |m_3 = -1, m_4 = +1\rangle \rightarrow |1:-1, 1:+1\rangle$. With this the spin changing interaction energy reads:

$$\begin{aligned} \langle f|\hat{H}_s|i\rangle &= \frac{\tilde{U}}{2}\, 2\, \Delta a_{00}^{+1-1} \times \langle 1:-1, 1:+1|\hat{\psi}_{+1}^\dagger\, \hat{\psi}_{-1}^\dagger\, \hat{\psi}_0^2|2:0\rangle \\ &= \sqrt{2}\, \tilde{U} \times \Delta a_{00}^{+1-1}. \end{aligned} \tag{A.7}$$

This yields a coupling strength according to $\frac{\hbar\Omega_{if}}{2} = \sqrt{2}\tilde{U} \times \Delta a_{00}^{+1-1}$. Similarly, the self interaction terms can be evaluated as

$$\begin{aligned} \langle i|\hat{H}_s|i\rangle &= \frac{\tilde{U}}{2} \times \Delta a_{00}^{00} \langle 2:0|\hat{\psi}_0^{\dagger 2}\, \hat{\psi}_0^2|2:0\rangle = \tilde{U} \times \Delta a_{00}^{00}, \\ \langle f|\hat{H}_s|f\rangle &= 4\, \frac{\tilde{U}}{2} \times \Delta a_{+1-1}^{+1-1} \langle 1:-1, 1:+1|\hat{\psi}_{+1}^\dagger\, \hat{\psi}_{-1}^\dagger\, \hat{\psi}_{+1}\, \hat{\psi}_{-1}|1:-1, 1:+1\rangle = 2\, \tilde{U} \times \Delta a_{+1-1}^{+1-1}. \end{aligned}$$

The interaction detuning is therefore determined by $\hbar\delta_{int} = \tilde{U} \times (\Delta a_{00}^{00} - 2\Delta a_{+1-1}^{+1-1})$.

The scattering length differences defined by Eq. (A.3) are easily evaluated by calculating the Clebsch-Gordan coefficients to give

$$\begin{aligned} \Delta a_{00}^{+1-1} &= \frac{a_2 - a_0}{3} \\ \Delta a_{00}^{00} &= \frac{a_0 + 2a_2}{3} \\ \Delta a_{+1-1}^{+1-1} &= \frac{2a_0 + a_2}{3}. \end{aligned} \tag{A.8}$$

With this we find

$$\hbar\delta_{\text{int}} = \tilde{U} \times \frac{a_2 - a_0}{3} \equiv \delta_1, \tag{A.9}$$

$$\hbar\Omega_{if} = 2\sqrt{2}\, \tilde{U} \times \frac{a_2 - a_0}{3}, \tag{A.10}$$

as stated in chapter 4.

Similarly the coupling parameters for the processes in $f = 2$ can be calculated. The results are summarized in Table A.1. It should be noted that there the scattering lengths a_0 and a_2 have different values depending on the hyperfine manifold, $f = 1$ or $f = 2$. As described in Section 4.3 we fit the measured oscillation frequency versus magnetic field with only one (two) free parameters for $f = 1$ ($f = 2$), independent of our uncertainty in optical potential depth. For this, we express all relevant quantities in terms of interaction detunings δ_{int} (see last column in Table A.1).

f	Process	Parameter	Corresponding Δa	
$f = 1$	$\|0,0\rangle \leftrightarrow \|+1,-1\rangle$	Ω_{if}	$(2\sqrt{2}/3)(a_2 - a_0)$	$2\sqrt{2}\delta_1$
		$\delta_{\text{int}} \equiv \delta_1$	$(a_2 - a_0)/3$	δ_1
$f = 2$	$\|0,0\rangle \leftrightarrow \|+1,-1\rangle$	Ω_{if}	$(2\sqrt{2}/35)[7(a_2 - a_0) + 12(a_4 - a_2)]$	$2\sqrt{2}(\delta_{2,1} + 2\delta_{2,2})$
		$\delta_{\text{int}} \equiv \delta_{2,1}$	$[7(a_2 - a_0) + 2(a_4 - a_2)]/35$	$\delta_{2,1}$
$f = 2$	$\|0,0\rangle \leftrightarrow \|+2,-2\rangle$	Ω_{if}	$(2\sqrt{2}/35)[-7(a_2 - a_0) + 3(a_4 - a_2)]$	$2\sqrt{2}(\delta_{2,2} - \delta_{2,1})$
		δ_{int}	$[7(a_2 - a_0) + 17(a_4 - a_2)]/35$	$(\delta_{2,1} + 3\delta_{2,2})$
$f = 2$	$\|+1,-1\rangle \leftrightarrow \|+2,-2\rangle$	Ω_{if}	$(4/35)[7(a_2 - a_0) + 2(a_4 - a_2)]$	$4\delta_{2,2}$
		δ_{int}	$3/7(a_4 - a_2)$	$3\delta_{2,2}$
$f = 2$	$\|-1,-1\rangle \leftrightarrow \|0,-2\rangle$	Ω_{if}	$(4\sqrt{3}/7)(a_4 - a_2)$	$4\sqrt{3}\delta_{2,2}$
		$\delta_{\text{int}} \equiv \delta_{2,2}$	$(a_4 - a_2)/7$	$\delta_{2,2}$

Table A.1: Summary of the collisional coupling strengths and detunings for the experimentally investigated cases as a function of the spin-dependent scattering lengths a_F. The last column gives expressions of the various parameters in terms of interaction detunings δ_i of the measured processes used in the fitting procedure presented in Section 4.3.3.

B Non-linear interactions in an array of quasi 1D-Bose gases

This appendix summarizes the calculations that allow to quantify the phase evolution of interacting systems. The first section considers the outcome of a Ramsey interferometer sequence for two interacting particles. Then, this is generalized to an array of strongly interacting quasi 1D quantum gases. First, the phase evolution under non-linear interactions is considered. Then the relevant interaction energy is calculated for a single tube. Finally the distribution of atoms throughout the lattice is considered.

B.1 Entanglement Interferometry

In this section the signal of a Ramsey interferometer will be calculated in the presence of interactions, leading to an entanglement evolution as introduced in Section 5.1.1. Again, we assume two interacting two-level systems with internal states $|\uparrow\rangle$ and $|\downarrow\rangle$. The spatial degree of freedom is assumed to be frozen so that only the spin will be considered. The two particles are initially in the internal state $|\downarrow\rangle$. A first $\pi/2$-pulse prepares them in a coherent superposition

$$|\psi\rangle_i = \frac{1}{2}\left(|\downarrow\downarrow\rangle - |\downarrow\uparrow\rangle - |\uparrow\downarrow\rangle + |\uparrow\uparrow\rangle\right). \tag{B.1}$$

After some interaction time t and the simplification made in section 5.1.1 we find the state in Eq. (5.5)

$$|\psi(t)\rangle = \frac{1}{2}\left(e^{i\phi_\chi}|\downarrow\downarrow\rangle - (|\downarrow\uparrow\rangle + |\uparrow\downarrow\rangle) + e^{i\phi_\chi}|\uparrow\uparrow\rangle\right). \tag{B.2}$$

In order to obtain a full Ramsey fringe we now apply a final $\pi/2$-pulse with variable phase α. This leads to the final state

$$\begin{aligned} |\psi\rangle_f \;=\; & \frac{1}{2}\Big\{e^{i\alpha}\left(e^{i\phi_\chi}\cos\alpha - 1\right)|\downarrow\downarrow\rangle \\ & + i\,e^{i\phi_\chi}\sin\alpha\,\left(|\downarrow\uparrow\rangle + |\uparrow\downarrow\rangle\right) \\ & + e^{-i\alpha}\left(e^{i\phi_\chi}\cos\alpha + 1\right)|\uparrow\uparrow\rangle\Big\}. \end{aligned} \tag{B.3}$$

In this form it is hard to recover the properties of the entangled or separable state. Therefore we calculate the probability to measure an atom in state $|\uparrow\rangle$ after the Ramsey sequence in order to find Eq. (5.13). The probability of finding the state $|i\rangle$ when performing a measurement on the final state $|\psi\rangle_f$ is $|\langle i|\psi\rangle_f|^2$.

For the state (B.3) there are three possibilities to detect atoms in $|\uparrow\rangle$: The final state could collapse onto $|\uparrow\downarrow\rangle$, $|\downarrow\uparrow\rangle$ or $|\uparrow\uparrow\rangle$. The total probability $P_\uparrow$ therefore can be calculated as

$$P_\uparrow = \frac{1}{2}(|\langle\uparrow\downarrow\,|\psi\rangle_f|^2 + |\langle\downarrow\uparrow\,|\psi\rangle_f|^2 + 2\,|\langle\uparrow\uparrow\,|\psi\rangle_f|^2), \tag{B.4}$$

where the pre-factor $1/2$ comes from the normalization of the probability to unity, and the factor 2 of the last term is due to the fact that in case $|\uparrow\uparrow\rangle$ is measured, two atoms are in $|\uparrow\rangle$.

From (B.3) we find

$$|\langle\uparrow\downarrow\,|\psi\rangle_f|^2 = |\langle\downarrow\uparrow\,|\psi\rangle_f|^2 = \frac{1}{4}\,\sin^2\alpha. \tag{B.5}$$

For the state $|\uparrow\uparrow\rangle$ we find

$$|\langle\uparrow\uparrow\,|\psi\rangle_f|^2 = \frac{1}{4}\,(\cos^2\alpha + 2\,\cos\alpha\,\cos\phi_\chi + 1). \tag{B.6}$$

Substituting eqs. (B.5) and (B.6) into Eq. (B.4) we find Eq. (5.13) as

$$P_\uparrow = \frac{1}{2}(1 + \cos\alpha\,\cos\phi_\chi). \tag{B.7}$$

B.2 Many-body phase evolution under non-linear interactions

Quasi-probability distribution

Here the problem of a many-body system of spin 1/2-particles is considered and the time evolution of the relative phase under the influence of non-linear interactions is calculated. The initial state is assumed to be created from a spin-polarized sample in $|\downarrow\rangle$ by a $\pi/2$-pulse. In order to find a convenient representation of the resulting CSS $|\pi/2, 0\rangle$, it can be expanded in terms of eigenstates of the $\hat{S}_z$ operator [146] as

$$|\vartheta,\varphi\rangle = \left(1 + \tan^2\frac{\vartheta}{2}\right)^{-S} \sum_{k=0}^{2S}\left(e^{i\varphi}\tan\frac{\vartheta}{2}\right)^k \binom{2S}{k}^{1/2} |S, S-k\rangle. \tag{B.8}$$

For the system under investigation one can identify $S = N/2$, $\vartheta = \pi/2$, $\phi = 0$, and $m_z = S - k$ the eigenvalue of the $\hat{S}_z$-operator for the eigenstate $|S, S-k\rangle$ in order to find (5.29).

$$\begin{aligned} |\vartheta = \pi/2, \varphi = 0\rangle &= \sum_{m_z=-\frac{N}{2}}^{\frac{N}{2}} \sqrt{\frac{N!}{\frac{N}{2}\left(\frac{N}{2}-m_z\right)!\left(\frac{N}{2}+m_z\right)!}}|m_z\rangle \\ &\equiv \sum_{m_z=-\frac{N}{2}}^{\frac{N}{2}} C(m_z)|m_z\rangle. \end{aligned} \tag{B.9}$$

The time evolution of this CSS under the non-linear Hamiltonian $\hat{H}_{\mathrm{nl}} = \hbar\chi\,\hat{S}_z^2$ then becomes

$$|\psi(t)\rangle = \sum_{m_z=-\frac{N}{2}}^{\frac{N}{2}} C(m_z)\, e^{i\chi\, m_z^2\, t}\, |m_z\rangle. \tag{B.10}$$

The quasi-probability distribution is calculated as the overlap of $|\psi(t)\rangle$ with an arbitrary coherent state $|\theta,\phi\rangle$:

$$\begin{aligned}\langle\theta,\phi|\psi(t)\rangle &= \sum_{m_z=-\frac{N}{2}}^{\frac{N}{2}} \left(e^{-i\phi/2}\,\sin\frac{\theta}{2}\right)^{\frac{N}{2}-m_z} \left(e^{i\phi/2}\,\cos\frac{\theta}{2}\right)^{\frac{N}{2}+m_z} C^2(m_z)\, e^{-i\chi m_z^2\, t}\,\langle m_z|m_z\rangle \\ &= \sum_{m_z=0}^{N} \frac{1}{2^{\frac{N}{2}}}\, e^{-i\chi m_z^2\, t} \left(e^{-i\phi/2}\,\sin\frac{\theta}{2}\right)^{\frac{N}{2}-m_z} \left(e^{i\phi/2}\,\cos\frac{\theta}{2}\right)^{\frac{N}{2}+m_z} \binom{N}{m_z}. \end{aligned} \tag{B.11}$$

With this the time evolution of the quasi probability distribution (QPD) $|\langle\theta,\phi|\psi(t)\rangle|^2$ can be numerically evaluated, see Fig. 5.4.

Spin squeezing in the interaction induced phase evolution

The spin squeezing of the phase distribution under the non-linear Hamiltonian (5.30) has been considered in Ref. [146].

There, from the phase distribution (B.11) the minimum variance V_{min} has been calculated as

$$V_{\mathrm{min}} = \frac{1}{2}\left(\frac{N}{6}\right)^{\frac{1}{3}} \approx 0.28\, N^{\frac{1}{3}}, \tag{B.12}$$

and it is reached after a time

$$t(V_{\mathrm{min}}) = t_{\mathrm{min}} = \frac{2^{\frac{5}{3}}}{24^{\frac{1}{6}}\,\chi}\, N^{-\frac{2}{3}} \approx \frac{1.35}{\chi}\, N^{-\frac{2}{3}}. \tag{B.13}$$

For a typical atom number of $N \approx 60$ atoms this corresponds to a squeezing below the standard quantum limit $N/4$ of $\xi \approx -0.75\,\mathrm{dB}$, reached after an interaction time $\chi\, t_{\mathrm{min}} \approx 0.088$. This has to be compared to the usual collapse time, where one finds $\chi\, t_{\mathrm{coll}} \approx 0.13$. Hence, the point of minimal variance is reached well before the Ramsey fringe has collapsed.

B.3 Degenerate gases in 1D

In the following the situation of an array of quasi-1D Bose gases in an optical lattice will be modeled. The analysis is based on the work of Ref. [67].

Chemical potential in a single tube

Within each tube atoms are in a quasi 1D-regime, where radially the situation can be described by a harmonic oscillator with oscillator length

$$l_r = \sqrt{\frac{\hbar}{m\,\omega_\perp}}, \tag{B.14}$$

where m is the mass of an atom, $\hbar$ is Planck's constant divided by $2\,\pi$, and $\omega_\perp$ is the radial trapping frequency.

For a harmonic confinement along the tube axis with trapping frequency ω_{ax}, interactions can be described by a 1D coupling constant given by

$$g = \frac{2\hbar^2}{m\,l_r^2} \times a, \tag{B.15}$$

from which one can obtain the dimensionless quantity

$$\alpha \equiv \frac{m g l_{\mathrm{ax}}}{\hbar^2}, \tag{B.16}$$

with $l_{ax} = \sqrt{\hbar/m\omega_{ax}}$ and a the s-wave scattering length.

For the central tube containing N_{00} atoms one finds a parabolic density profile

$$n_0(z) = n_{0,\max}\left(1 - \frac{z^2}{R_{\mathrm{TF,ax}}^2}\right), \tag{B.17}$$

where z is the coordinate along the tube, and $n_{0,\max}$ is the maximum density in the tube, given by

$$n_{0,\max} = \frac{\mu}{g}. \tag{B.18}$$

The Thomas-Fermi (TF) radius of the density distribution along the tube is given by

$$R_{\mathrm{TF,ax}} = \sqrt{\frac{2\mu}{m\,\omega_{\mathrm{ax}}^2}}, \tag{B.19}$$

and the chemical potential in the tube reads

$$\mu = \hbar\omega_{\mathrm{ax}}\left(\frac{3N_{00}\,\alpha}{4\,\sqrt{2}}\right)^{\frac{2}{3}}, \tag{B.20}$$

with N_{00} the number of particles in the central tube. Using equations (B.16) and (B.15), the expression for the chemical potential (B.20) can be rewritten to yield

$$\mu = \frac{\hbar\omega_{\mathrm{ax}}}{2}\left(3N_{00}\,\frac{a\,l_{\mathrm{ax}}}{l_r^2}\right)^{\frac{2}{3}}. \tag{B.21}$$

Interaction energy in a single tube

For a given tube (i, j), the interaction strength χ_{ij} depends on the total atom number N_{ij} in this tube. The definition of χ reads

$$\chi_{ij} \equiv \frac{a_{\uparrow\uparrow} + a_{\downarrow\downarrow} - 2a_{\downarrow\uparrow}}{2\bar{a}_s} \times \underbrace{\frac{4\pi\hbar^2}{m}\,\bar{a}_s \int |\phi_{ij}|^4 d^3r}_{=U_{ij}}. \tag{B.22}$$

The interaction parameter U_{ij} can either be calculated from the definition of the wave functions in the tube, or via the relation

$$\begin{aligned} U_{ij} &= \frac{\partial \mu_{ij}}{\partial N_{ij}} \\ &= \left.\frac{\partial \mu_{ij}}{\partial N}\right|_{N=N_{ij}}. \end{aligned} \tag{B.23}$$

We anticipate the discussion in the following section by introducing an overall harmonic confinement on large length scales with trapping frequency Ω_r. From equations (B.30),(B.29) we find the local chemical potential

$$\mu_{ij} = \mu - \frac{\lambda^2\, m\, \Omega_r^2}{8}\,(i^2 + j^2), \tag{B.24}$$

so that

$$\left.\frac{\partial \mu_{ij}}{\partial N}\right|_{N=N_{ij}} = \left.\frac{\partial \mu}{\partial N}\right|_{N=N_{ij}}. \tag{B.25}$$

From the form of the chemical potential (B.20) one finds

$$\begin{aligned} \left.\frac{\partial \mu}{\partial N}\right|_{N=N_{ij}} &= \frac{\hbar\omega_{ax}}{2}\left(\frac{3\bar{a}_s l_{ax}}{l_r^2}\right)^{2/3} \times N_{ij}^{-1/3} \\ &= \frac{\mu(N_{ij})}{N_{ij}}. \end{aligned} \tag{B.26}$$

Interestingly, the interaction strength scales with a negative power of the atom number, meaning that more atoms imply a smaller interaction parameter. This is, however, not the full story; usually one considers the complete interaction term of the Hamiltonian $U/2\sum_i \hat{n}_i(\hat{n}_i - 1)$, where the more familiar scaling with atom number is seen. In the case presented here the term $\hbar\chi\hat{S}_z^2$ is considered, where the parameter χ is fixed in a first approximation. If in contrast the time evolution of the QPD is considered for various initial atom numbers, the correct and intuitively expected behavior is found.

In fact, from eqs. (B.26) and (5.43) one finds the typical collapse time scales as $t_{\mathrm{disp}} \propto N^{-1/6}$, i.e. with a very small power of the atom number. Even by changing the atom number by a factor of 2 yields 90% of the initial collapse time. Therefore, in the calculations for the total Ramsey fringe contrast drop only a single tube is considered, as the distribution of atoms is expected to have only a minor effect. Still the distribution of atoms throughout the array is calculated below for completeness.

Extension to an array of tubes

Starting from a BEC, by ramping up a 2D optical lattice with laser wavelength λ, one ends with an array of 1D quantum gases, where the distribution of atoms over the tubes depends on the density distribution of the 3D gas in the moment where tunneling between tubes is suppressed. In the following an overall confinement which is the same for both directions perpendicular to the tube axis with trapping frequency of Ω_r is assumed. The tubes in the array are labeled by (i, j). The distance from a tube to the central tube is given by

$$d_{(i,j)} = \frac{\lambda^2}{4}\,(i^2 + j^2), \tag{B.27}$$

which can be related to the TF-radius of the overal system by

$$\frac{\lambda^2}{4}\,(i^2 + j^2) = \kappa\,(i^2 + j^2)\,\frac{R_{\mathrm{TF,r}}^2}{2}, \tag{B.28}$$

with $R_{\mathrm{TF,r}} = \sqrt{2\mu/m\Omega_r^2}$ the TF radius of the overall system, and

$$\kappa \equiv \frac{\lambda^2}{2} \times \frac{m\Omega_r^2}{2\mu}. \tag{B.29}$$

The local chemical potential of a tube (i, j) is approximated by the chemical potential of the central tube minus the potential due to the optical potential at the specific position, because the chemical potential tends to be flat over the whole system as long as tunneling is possible, see Fig. B.1. Therefore

$$\mu_{ij} = \mu_{00}(1 - \kappa(i^2 + j^2)/2). \tag{B.30}$$

Total number of particles in an array of 1D tubes

In the array of 1D gases the total number of atoms N_{tot} must be conserved. Hence the number of atoms in the tubes $N_{i,j}$ must obey

$$N_{\mathrm{tot}} = \sum_{i,j} N_{i,j}. \tag{B.31}$$

In principle this sum can be evaluated by solving (B.30) for N_{ij} and numerically solve (B.31). Here, the sum is approximated by the integral to get

$$N_{\mathrm{tot}} = \int dN_{ij}. \tag{B.32}$$

The local atom number can be calculated using the local chemical potential (B.30) as

$$N_{ij} = \left(\mu(1 - \frac{\kappa}{2}(i^2 + j^2))\right)^{\frac{3}{2}}\,\frac{N_{00}}{\mu^{3/2}}. \tag{B.33}$$

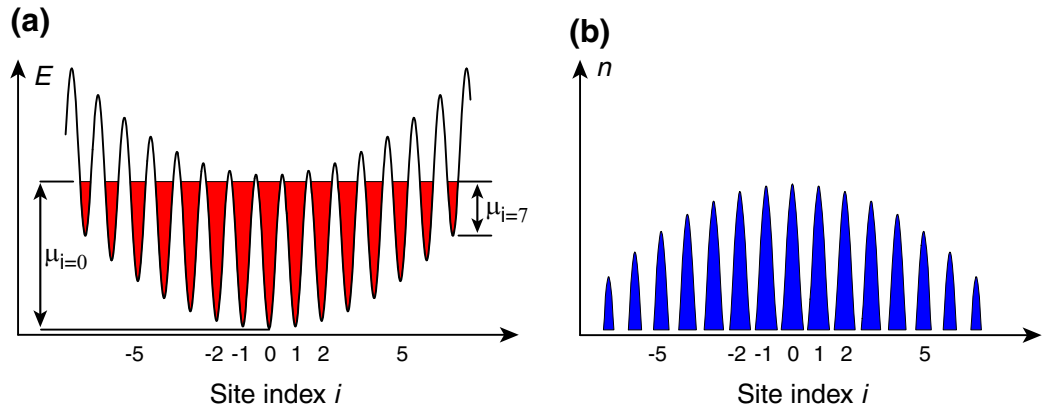

Figure B.1: (a) As long as tunneling is possible, the chemical potential tends to be flat over the whole system. In case tunneling is suppressed, at each site the local chemical potential is frozen, leading to the parabolic envelope of the density distribution in **(b)**.

Integration finally yields

$$\begin{aligned} N_{\text{tot}} &= \int_{\rho=0}^{\rho=\sqrt{2/\kappa}} \left(\mu(1-\kappa/2\rho^2)\right)^{3/2} \frac{N_{00}}{\mu^{3/2}}\, 2\pi\rho\, d\rho \\ &= \frac{4\pi N_{00}}{5\kappa}. \end{aligned} \tag{B.34}$$

If the total atom number is known, Eq. (B.34) allows to calculate the number of atoms in the central tube. From Eq. (B.33) the distribution N_{ij} throughout the array can be calculated. For the experimental parameters stated in section 5.5 the actual atom number distribution is shown in Fig. B.2.

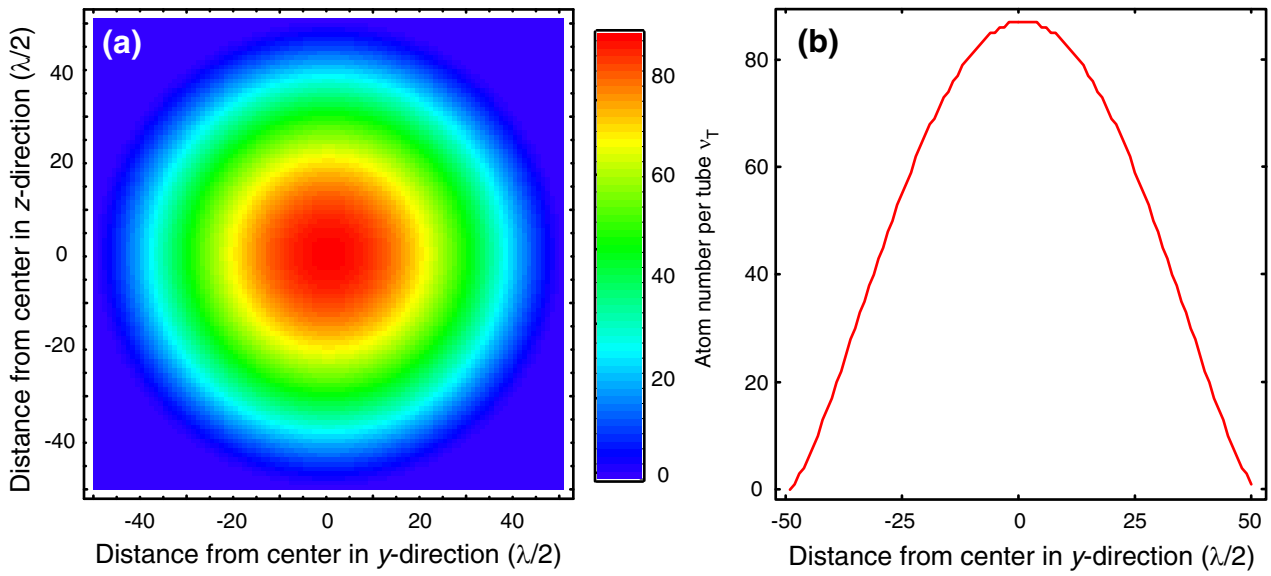

Figure B.2: **(a)** Spatial distribution of atoms throughout the 2D array of tubes for a lattice depth of $V_y = V_z = 20\,Er$, where tunneling is expected to be suppressed, and a total atom number of 2.8×10^5. **(b)** Profile through (a) at $z = 0$.

Bibliography

[1] M. Greiner, O. Mandel, T. Esslinger, T. W. Hänsch, and I. Bloch. Quantum phase transition from a superfluid to a Mott insulator in a gas of ultracold atoms. *Nature*, 415:39, 2002.

[2] T. Stöferle, H. Moritz, Ch. Schori, M. Köhl, and T. Esslinger. Transition from a Strongly Interacting 1D Superfluid to a Mott Insulator. *Phys. Rev. Lett.*, 92:130403, 2004.

[3] I.B. Spielman, W.D. Phillips, and J.V. Porto. Mott-Insulator Transition in a Two-Dimensional Atomic Bose Gas. *Phys. Rev. Lett.*, 98:080404, 2007.

[4] S. Jochim, M. Bartenstein, A. Altmeyer, G. Hendl, S. Riedl, C. Chin, J. Hecker Denschlag, and R. Grimm. Bose-Einstein Condensation of Molecules. *Science*, 302:2101, 2003.

[5] M. Greiner, C. A. Regal, and D. S. Jin. Emergence of a molecular Bose-Einstein condensate from a Fermi gas. *Nature*, 424:537, 2003.

[6] J. Cubizolles, T. Bourdel, S.J.J.M.F. Kokkelmans, G.V. Shlyapnikov, and C. Salomon. Production of Long-Lived Li_2 Molecules from a Fermi Gas. *Phys. Rev. Lett.*, 91:240401, 2003.

[7] M.W. Zwierlein, C.A. Stan, C. H. Schunck, S.M.F. Raupach, S. Gupta, Z. Hadzibabic, and W. Ketterle. Observation of Bose-Einstein Condensation of Molecules. *Phys. Rev. Lett.*, 91:250401, 2003.

[8] C.A. Regal, M. Greiner, and D.S. Jin. Observation of Resonance Condensation of Fermionic Atom Pairs. *Phys. Rev. Lett.*, 92:040403, 2004.

[9] C. Chin, M. Bartenstein, A. Altmeyer, S. Riedl, S. Jochim, J. Hecker Denschlag, and R. Grimm. Observation of the Pairing Gap in a Strongly Interacting Fermi Gas. *Science*, 305:1128, 2004.

[10] M.W. Zwierlein, C.A. Stan, C.H. Schunck, S.M.F. Raupach, A.J. Kerman, and W. Ketterle. Condensation of Pairs of Fermionic Atoms near a Feshbach Resonance. *Phys. Rev. Lett.*, 92:120403, 2004.

[11] F. Gerbier, S. Fölling, A. Widera, O. Mandel, and I. Bloch. Probing Number Squeezing of Ultracold Atoms across the Superfluid-Mott-Insulator Transition. *Phys. Rev. Lett.*, 96:090401, 2006.

[12] S. Fölling, A. Widera, T. Müller, F. Gerbier, and I. Bloch. Formation of Spatial Shell Structure in the Superfluid to Mott Insulator Transition. *Phys. Rev. Lett.*, 97:060403, 2006.

[13] M. Greiner, C.A. Regal, C. Ticknor, J.L. Bohn, and D.S. Jin. Detection of Spatial Correlations in an ultracold Gas of Fermions. *Phys. Rev. Lett.*, 92:150405, 2004.

[14] M. Greiner, C.A. Regal, J.T. Stewart, and D.S. Jin. Probing Pair-Correlated Fermionic Atoms through Correlations in Atom Shot Noise. *Phys. Rev. Lett.*, 94:110401, 2005.

[15] B. Paredes and J.I. Cirac. From Cooper Pairs to Luttinger Liquids with Bosonic Atoms in Optical Lattices. *Phys. Rev. Lett.*, 90:150402, 2003.

[16] B. Paredes, A. Widera, V. Murg, O. Mandel, S. Fölling, I. Cirac, G.V. Shlyapnikov, T.W. Hänsch, and I. Bloch. Tonks-Girardeau gas of ultracold atoms in an optical lattice. *Nature*, 429:277, 2004.

[17] T. Kinoshita, T. Wenger, and D.S. Weiss. Observation of a One-Dimensional Tonks-Girardeau Gas. *Science*, 305:1125, 2004.

[18] T. Kinoshita, T. Wenger, and D.S. Weiss. Local Pair Correlations in One-Dimensional Bose Gases. *Phys. Rev. Lett.*, 95:190406, 2005.

[19] L. Mandel and E. Wolf. *Optical Coherence and Quantum Optics*. Cambridge University Press, 1995.

[20] C.M. Caves. Quantum-mechanical noise in an interferometer. *Phys. Rev. D*, 23:1693, 1981.

[21] M.A. Nielsen and I.L. Chuang. *Quantum Computation and Quantum Information*. Cambridge University Press, 2000.

[22] T.-L. Ho. Spinor Bose Condensates in Optical Traps. *Phys. Rev. Lett.*, 81:742, 1998.

[23] A.J. Leggett. Bose-Einstein condensation in the alkali gases: Some fundamental concepts. *Rev. Mod. Phys.*, 73:307, 2001.

[24] E. Tiesinga, B.J. Verhaar, and H.T.C. Stoof. Threshold and resonance phenomena in ultracold ground-state collisions. *Phys. Rev. A*, 47:4114, 1992.

[25] A. Widera, F. Gerbier, S. Fölling, T. Gericke, O. Mandel, and I. Bloch. Coherent collisional spin dynamics in optical lattices. *Phys. Rev. Lett.*, 95:190405, 2005.

[26] A. Widera, F. Gerbier, S. Fölling, T. Gericke, O. Mandel, and I. Bloch. Precision measurement of spin-dependent interaction strengths for spin-1 and spin-2 ^{87}Rb atoms. *New J. Phys.*, 8:152, 2006.

[27] F. Gerbier, A. Widera, S. Fölling, O. Mandel, and I. Bloch. Resonant control of spin dynamics in ultracold quantum gases by microwave dressing. *Phys. Rev. A*, 73:041602(R), 2006.

[28] A. Widera, O. Mandel, M. Greiner, S. Kreim, T.W. Hänsch, and I. Bloch. Entanglement Interferometry for Precision Measurement of Atomic Scattering Properties. *Phys. Rev. Lett.*, 92:160406, 2004.

[29] A. Widera, S. Trotzky, P. Cheinet, S. Fölling, F. Gerbier, and I. Bloch. Reversible quantum phase dispersion in ultracold mesoscopic spinor gases. *To be published*, 2007.

[30] C. Cohen-Tannoudji, B. Diu, and F. Laloë. *Quantum Mechanics*. Wiley, 1977.

[31] Andreas Marte. *Feshbach-Resonanzen bei Stößen ultrakalter Rubidiumatome*. Dissertation, available online at http://tumb1.biblio.tu-muenchen.de/publ/diss/ph/2003/marte.html, Technische Universität München, 2003.

[32] E. van Kempen. *Feshbach Resonances in Cold Atomic Gases*. Dissertation, ISBN-13: 978-90-386-2541-6, Technische Universiteit Eindhoven, 2006.

[33] E.A. Burt, R.W. Ghrist, C.J. Myatt, M.J. Holland, E.A. Cornell, and C.E. Wieman. Coherence, Correlations and Collisions: What One Learns about Bose-Einstein Condensates from Their Decay. *Phys. Rev. Lett.*, 79:337, 1997.

[34] H.T.C. Stoof, J.M.V.A. Koelman, and B.J. Verhaar. Spin-exchange and dipole relaxation rates in atomic hydrogen: Rigorous and simplified calculations. *Phys. Rev. B*, 38:4688, 1988.

[35] D.S. Hall, M.R. Matthews, J.R. Ensher, C.E. Wieman, and E.A. Cornell. Dynamics of Component Separation in a Binary Mixture of Bose-Einstein Condensates. *Phys. Rev. Lett.*, 81:1539, 1998.

[36] D.S. Hall, M.R. Matthews, J.R. Ensher, C.E. Wieman, and E.A. Cornell. Measurements of Relative Phase in Two-Component Bose-Einstein Condensates. *Phys. Rev. Lett.*, 81:1543, 1998.

[37] P.S. Julienne, F.H. Mies, E. Tiesinga, and C.J. Williams. Collisional Stability of Double Bose Condensates. *Phys. Rev. Lett.*, 78:1880, 1997.

[38] Jr. J.P. Burke, J.L. Bohn, B.D.Esry, and C.H. Greene. Impact of the ^{87}Rb singlet scattering length on suppressing inelastic collisions. *Phys. Rev. A*, 55:R2511, 1997.

[39] B.D. Esry, C.H. Greene, Jr. J.P. Burke, and J.L. Bohn. Hartree-Fock Theory for Double Condensates. *Phys. Rev. Lett.*, 78:3594, 1998.

[40] A.J. Moerdijk, H.M.J.M. Boesten, and B.J. Verhaar. Decay of trapped ultracold alkali atoms by recombination. *Phys. Rev. A*, 53:916, 1995.

[41] P.O. Fedichev, M.W. Reynolds, and G.V. Shlyapnikov. Three-Body Recombination of Ultracold Atoms to a Weakly Bound *s* Level. *Phys. Rev. Lett.*, 77:2921, 1996.

[42] B.D. Esry, C.H. Greene, and Jr. J.P. Burke. Recombination of Three Atoms in the Ultracold Limit. *Phys. Rev. Lett.*, 83:1751, 1999.

[43] J. Söding, D. Guéry-Odelin, P. Desbiolles, F. Chevy, H. Inamori, and J. Dalibard. Three-body decay of a rubidium Bose-Einstein condensate. *Appl. Phys. B*, 69:257, 1999.

[44] H.M.J.M. Boesten, C.C. Tsai, B.J. Verhaar, and D.J. Heinzen. Observation of a Shape Resonance in Cold-Atom Scattering by Pulsed Photoassociation. *Phys. Rev. Lett.*, 77:5194, 1996.

[45] J.L. Roberts, N.R. Claussen, J.P.Jr. Burke, C.H. Green, E.A. Cornell, and C.E. Wieman. Resonant Magnetic Field Control of Elastic Scattering in Cold ^{85}Rb. *Physical Review Letters*, 81:5109, 1998.

[46] N.N. Klausen, J.L. Bohn, and Ch.H. Greene. Nature of spinor Bose-Einstein condensates in rubidium. *Phys. Rev. A*, 64:053602, 2001.

[47] E.G.M. van Kempen, S.J.J.M.F. Kokkelmans, D.J. Heinzen, and B.J. Verhaar. Interisotope Determination of Ultracold Rubidium Interactions from Three High-Precision Experiments. *Phys. Rev. Lett.*, 88:093201, 2002.

[48] A. Marte, T. Volz, J. Schuster, S. Dürr, G. Rempe, E.G.M. van Kempen, and B.J. Verhaar. Feshbach Resonances in Rubidium 87: Precision Measurement and Analysis. *Phys. Rev. Lett.*, 89(28):283202, Dec 2002.

[49] Servaas Kokkelmans. *Interacting Atoms in Clocks and Condensates.* Dissertation, available online at http://edoc.ub.uni-muenchen.de/archive/00003568/, Technische Universiteit, 2000.

[50] S. Kokkelmans. Private communication.

[51] M.H. Anderson, J.R. Ensher, M.R. Matthews, C.E. Wieman, and E.A. Cornell. Observation of Bose-Einstein condensation in a dilute atomic vapor. *Science*, 269:198, 1995.

[52] K.B. Davis, M.-O. Mewes, M.R. Andrews, N.J. van Druten, D.S. Durfee, D.M. Kurn, and W. Ketterle. Bose-Einstein condensation in a gas of sodium atoms. *Physical Review Letters*, 75:3969, 1995.

[53] F. Dalfovo, S. Giorgini, L.P. Pitaevskii, and S. Stringari. Theory of Bose-Einstein condensation in trapped gases. *Rev. Mod. Phys.*, 71:463, 1999.

[54] C.J. Pethick and H. Smith. *Bose-Einstein condensation in Dilute Gases*. Cambridge University Press, 2002.

[55] T. Esslinger, I. Bloch, and T.W. Hänsch. Bose-Einstein condensation in a quadrupole-Ioffe-configuration trap. *Phys. Rev. A*, 58:R2664, 1998.

[56] M. Greiner, I. Bloch, T.W. Hänsch, and T. Esslinger. Exploring Phase Coherence in a 2D Lattice of Bose-Einstein Condensates. *Phys. Rev. Lett.*, 87:160405, 2001.

[57] M. Greiner. *Ultracold quantum gases in three-dimensional optical lattice potentials*. Dissertation, available online at http://edoc.ub.uni-muenchen.de/archive/00000968/, Universität München, 2003.

[58] O. Mandel. *Entanglement with quantum gates in an optical lattice*. Dissertation, available online at http://edoc.ub.uni-muenchen.de/archive/00003568/, Universität München, 2005.

[59] A.L. Migdall, J.V. Prodan, W.D. Phillips, T.H. Bergeman, and H.J. Metcalf. First Observation of Magnetically Trapped Neutral Atoms. *Phys. Rev. Lett.*, 54:2596, 1985.

[60] W. Petrich, M.H. Anderson, J.R. Ensher, and E.A. Cornell. Stable, Tightly Confining Magnetic Trap for Evaporative Cooling of Neutral Atoms. *Phys. Rev. Lett.*, 74:3352, 1995.

[61] H.J. Metcalf and P. van der Straten. *Laser Cooling and Trapping*. Graduate Texts in Contemporary Physics. Springer, 1999.

[62] N. Masuhara, J.M. Doyle, J.C. Sandberg, D. Kleppner, and T.J. Greytak. Evaporative Cooling of Spin-Polarized Atomic Hydrogen. *Phys. Rev. Lett.*, 61:935, 1988.

[63] K.B. Davis, M.-O. Mewes, M.A. Joffe, M.R. Andrews, and W. Ketterle. Evaporative cooling of Sodium atoms. *Phys. Rev. Lett.*, 74:5202, 1995.

[64] A. Einstein. Zur Quantentheorie des idealen Gases. *Sitzungsberichte, Preussische Akademie der Wissenschaften*, Bericht 3:18, 1925.

[65] E. Timmermans, P. Tommasini, and K. Huang. Variational Thomas-Fermi theory af a nonuniform Bose condensate at zero temperature. *Phys. Rev. A*, 55:3645, 1997.

[66] K. Xu, Y. Liu, D.E. Miller, J.K. Chin, W. Setiawan, and W. Ketterle. Observation of Strong Quantum Depletion in a Gaseous Bose-Einstein Condensate. *Phys. Rev. Lett.*, 96:180405, 2006.

[67] D.S. Petrov, G.V. Shlyapnikov, and J.T.M. Walraven. Regimes of Quantum Degeneracy in Trapped 1D Gases. *Phys. Rev. Lett.*, 85:3745, 2000.

[68] D. van Oosten, P. van der Straten, and H.T.C. Stoof. Mott insulators in an optical lattice with high filling factors. *Phys. Rev. A*, 67:033606, 2003.

[69] I. Bouchoule, K.V. Kheruntsyan, and G.V. Shlyapnikov. Crossover to a quasi-condensate in a weakly interacting 1D Bose gas. *preprint*, arXiv:physics/0611237, 2006.

[70] H.J. Lewandowski, D.M. Harber, D.L. Whitaker, and E.A. Cornell. Observation of Anomalous Spin-State Segregation in a Trapped Ultracold Vapor. *Phys. Rev. Lett.*, 88:070403, 2002.

[71] J.M. McGuirk, H.J. Lewandowski, D.M. Harber, T. Nikuni, J.E. Williams, and E.A. Cornell. Spatial Resolution of Spin Waves in an Ultracold Gas. *Phys. Rev. Lett.*, 89:090402, 2002.

[72] J.M. McGuirk, D.M. Harber, H.J. Lewandowski, and E.A. Cornell. Normal-Superfluid Interaction Dynamics in a Spinor Bose Gas. *Phys. Rev. Lett.*, 91:150402, 2003.

[73] R. Grimm, M. Weidemüller, and Y.B. Ovchinnikov. Optical dipole traps for neutral atoms. *Adv. At. Mol. Opt. Phys.*, 42:95, 2000.

[74] I. Bloch. Ultracold quantum gases in optical lattices. *Nat. Phys.*, 1:23, 2005.

[75] M.P.A. Fisher, P.B. Weichman, G. Grinstein, and D.S. Fisher. Boson localization and the superfluid-insulator transition. *Phys. Rev. B*, 40(1):546–70, 1989.

[76] D. Jaksch, C. Bruder, J.I. Cirac, C.W. Gardiner, and P. Zoller. Cold Bosonic Atoms in Optical Lattices. *Phys. Rev. Lett.*, 81:3108, 1998.

[77] W. Zwerger. Mott-Hubbard transition of cold atoms in optical lattices. *J. Opt. B*, 5:S9, 2003.

[78] D. Jaksch. *Bose-Einstein condensation and applications.* Dissertation, available online at http://www2.arcs.ac.at/dissdb/rn034177, Universität Innsbruck, 1999.

[79] T. Busch, B.-G. Englert, K. Rzążewski, and M. Wilkens. Two Cold Atoms in a Harmonic Trap. *Found. Phys.*, 28:549, 1998.

[80] B. Sun, W.X. Zhang, S. Yi, M.S. Chapman, and L. You. Dipolar Effect in Coherent Spin Mixing of Two Atoms in a Single Optical Lattice Site. *Phys. Rev. Lett.*, 97:123201, 2006.

[81] J.H. Mentink. Interacting Atoms in Optical Lattices. Master's thesis, Eindhoven University of Technology, 2006.

[82] L.C. Allen and J.H. Eberly. *Optical Resonance and Two-Level Atoms*. Dover Publications Inc., 1987.

[83] L.D. Landau. *Phys. Z. Sowjetunion*, 2:46, 1932.

[84] C. Zener. Non-Adiabatic Crossing of Energy Levels. *Proceedings of the Royal Society London A*, 137:696, 1932.

[85] I.I. Rabi, S. Millman, P. Kusch, and J.R. Zacharias. The Molecular Beam Resonance Method for Measuring Nuclear Magnetic Moments. The Magnetic Moments of ${}_3Li^6$, ${}_3Li^7$ and ${}_9F^{19}$. *Phys. Rev.*, 55:526, 1939.

[86] P.E. Berman (Editor). *Atom Interferometry*. Academic Press Inc., U. S., 1996.

[87] N.F. Ramsey. A Molecular Beam Resonance Method with Separated Oscillating Fields. *Phys. Rev.*, 78:695, 1950.

[88] M. Greiner, I. Bloch, T.W. Hänsch, and T. Esslinger. Magnetic transport of trapped cold atoms over a large distance. *Phys. Rev. A*, 63:031401, 2001.

[89] S.R. Clark and D. Jaksch. Dynamics of the superfluid to Mott-insulator transition in one dimension. *Phys. Rev. A*, 70:043612, 2004.

[90] T. Gericke, F. Gerbier, A. Widera, S. Fölling, O. Mandel, and I. Bloch. Adiabatic loading of a Bose-Einstein condensate in a 3D optical lattice. *arXiv*, cond-mat:0603590, 2006.

[91] V.A. Kashurnikov, N.V. Prokof'ev, and B.V. Svistunov. Revealing the superfluid–Mott-insulator transition in an optical lattice. *Phys. Rev. A*, 66:031601, Sep 2002.

[92] G.G. Batrouni, V. Rousseau, R.T. Scalettar, M. Rigol, A. Muramatsu, P.J.H. Denteneer, and M. Troyer. Mott Domains of Bosons Confined in Optical Lattices. *Phys. Rev. Lett.*, 89:117203, 2002.

[93] B. DeMarco, C. Lannert, S. Vishveshwara, and T.-C. Wei. Structure and stability of Mott-insulator shells of bosons trapped in an optical lattice. *Phys. Rev. A*, 71(6):063601, 2005.

[94] S. Fölling, F. Gerbier, A. Widera, O. Mandel, T. Gericke, and I. Bloch. Spatial quantum noise interferometry in expanding ultracold atom clouds. *Nature*, 434:481, 2005.

[95] M. Walhout, U. Sterr, C. Orzel, M. Hoogerland, and S.L. Rolston. Optical Control of Ultracold Collisions in Metastable Xenon. *Phys. Rev. Lett.*, 74:506, 1995.

[96] W. Gerlach and O. Stern. Der experimentelle Nachweis der Richtungsquantelung im Magnetfeld. *Z. Phys.*, 9:349, 1922.

[97] N.F. Ramsey. *Molecular Beams*. Oxford University Press, 1956.

[98] J. Stenger, S. Inouye, D.M. Stamper-Kurn, H.J. Miesner, A.P. Chikkatur, and W. Ketterle. Spin domains in ground-state Bose-Einstein condensates. *Nature*, 396:345, 1998.

[99] H. Schmaljohann, M. Erhard, J. Kronjäger, M. Kottke, S. van Staa, L. Cacciapuoti, J.J. Arlt, K. Bongs, and K. Sengstock. Dynamics of $F = 2$ Spinor Bose-Einstein Condensates. *Phys. Rev. Lett.*, 92:040402, 2004.

[100] M.-S. Chang, C.D. Hamley, M.D. Barrett, J.A. Sauer, K.M. Fortier, W. Zhang, L. You, and M.S. Chapman. Observation of Spinor Dynamics in Optically Trapped ^{87}Rb Bose-Einstein Condensates. *Phys. Rev. Lett.*, 92:140403, 2004.

[101] T. Kuwamoto, T. Araki, T. Eno, and T. Hirano. Magnetic field dependence of the dynamics of ^{87}Rb spin-2 Bose-Einstein condensates. *Phys. Rev. A*, 69:063604, 2004.

[102] C.K. Law, H. Pu, and N.P. Bigelow. Quantum Spins Mixing in Spinor Bose-Einstein Condensates. *Phys. Rev. Lett.*, 81:5257, 1998.

[103] H. Pu, C.K. Law, S. Raghavan, J.H. Eberly, and N.P. Bigelow. Spin-mixing dynamics of a spinor Bose-Einstein condensate. *Phys. Rev. A*, 60:1463, 1999.

[104] Q. Gu, K. Bongs, and K. Sengstock. Spin waves in ferromagnetically coupled spinor Bose gases. *Phys. Rev. A*, 70:063609, 2004.

[105] T. Ohmi and K. Machida. Bose-Einstein condensation with internal degrees of freedom in alkali atom gases. *J. Phys. Soc. Jpn.*, 67:1822, 1998.

[106] C.V. Ciobanu, S.-K. Yip, and T.-L. Ho. Phase diagrams of $F = 2$ Bose-Einstein condensates. *Phys. Rev. A*, 61:033607, 2000.

[107] M. Koashi and M. Ueda. Exact Eigenstates and Magnetic Response of Spin-1 and Spin-2 Bose Einstein Condensates. *Phys. Rev. Lett.*, 84:1066, 2000.

[108] M.-S. Chang, Q. Qin, W. Zhang, L. You, and M.S. Chapman. Coherent spinor dynamics in a spin-1 Bose condensate. *Nature Physics*, 1:111, 2005.

[109] J. Kronjäger, C. Becker, M. Brinkmann, R. Walser, P. Navez, K. Bongs, and K. Sengstock. Evolution of a spinor condensate: Coherent dynamics, dephasing and revivals. *Phys. Rev. A*, 72:063619, 2005.

[110] M. Greiner, O. Mandel, T. W. Hänsch, and I. Bloch. Collapse and revival of the matter wave field of a Bose-Einstein condensate. *Nature*, 419:51, 2002.

[111] J.H. Mentink and S.J.J.M.F. Kokkelmans. Private communication.

[112] H.-J. Huang and G.-M. Zhang. Quantum beat phenomenon presence in coherent spin dynamics of spin-2 ^{87}Rb atoms in a deep optical lattice. *arXiv*, cond-mat:0601188, 2006.

[113] M.P. Fewell, B.W. Shore, and K. Bergmann. Coherent Population Transfer among Three States: Full Algebraic Solutions and the Relevance of Non Adiabatic Processes to Transfer by Delayed Pulses. *Aust. J. Phys.*, 50:281–308, 1997.

[114] D. Jaksch, V. Venturi, J.I. Cirac, C.J. Williams, and P. Zoller. Creation of a Molecular Condensate by Dynamically Melting a Mott Insulator. *Phys. Rev. Lett.*, 89:040402, 2002.

[115] F. Gerbier, A. Widera, S. Fölling, O. Mandel, T. Gericke, and I. Bloch. Phase Coherence of an Atomic Mott Insulator. *Phys. Rev. Lett.*, 95:050404, 2005.

[116] C.J. Myatt, E.A. Burt, R.W. Ghrist, E.A. Cornell, and C.E. Wieman. Production of Two Overlapping Bose-Einstein Condensates by Sympathetic Cooling. *Phys. Rev. Lett.*, 78:586, 1997.

[117] R. Jáuregui, N. Poli, G. Roati, and G. Modugno. Anharmonic parametric excitation in optical lattices. *Phys. Rev. A*, 64:033403, 2001.

[118] S. Kreim. Präzisionsmessung von Wechselwirkungseigenschaften in optischen Gittern. Master's thesis, Ludwigs-Maximilians-Universität München, 2004.

[119] T.-L. Ho and S.K. Yip. Fragmented and Single Condensate Ground States of Spin-1 Bose Gas. *Phys. Rev. Lett.*, 84:4031, 2000.

[120] H. Pu and P. Meystre. Creating Macroscopic Atomic Einstein-Podolski-Rosen States from Bose-Einstein Condensates. *Phys. Rev. Lett.*, 85:3987, 2000.

[121] L.-M. Duan, A. Sørensen, J.I. Cirac, and P. Zoller. Squeezing and Entanglement of Atomic Beams. *Phys. Rev. Lett.*, 85:3991, 2000.

[122] O. Müstecaplıoğlu, M. Zhang, and L. You. Spin squeezing and entanglement in spinor condensates. *Phys. Rev. A*, 66:033611, 2002.

[123] E. Demler and F. Zhou. Spinor Bosonic Atoms in Optical Lattices: Symmetry Breaking and Fractionalization. *Phys. Rev. Lett.*, 88:163001, 2002.

[124] S.K. Yip. Dimer State of Spin-1 Bosons in an Optical Lattice. *Phys. Rev. Lett.*, 90:250402, 2003.

[125] J.-M. Hou and M.-L. Ge. Quantum phase transition of spin-2 cold bosons in an optical lattice. *Phys. Rev. A*, 67:063607, 2003.

[126] A.A. Svidzinsky and S.T. Chui. Insulator-superfluid transition of spin-1 bosons in an optical lattice in magnetic field. *Phys. Rev. A*, 68:043612, 2003.

[127] A. Imambekov, M. Lukin, and E. Demler. Spin-exchange interaction of spin-one bosons in optical lattices: Singlet, nematic, and dimerized phases. *Phys. Rev. A*, 68:063602, 2003.

[128] M. Snoek and F. Zhou. Microscopic wave functions of spin-singlet and nematic Mott states of spin-one bosons in high-dimensional bipartite lattices. *Phys. Rev. A*, 69:094410, 2004.

[129] S. Jin, J.-M. Hou, B.-H. Xie, L.-J. Tian, and M.-L. Ge. Superfluid-Mott-insulator transition of spin-2 cold bosons in an optical lattice in a magnetic field. *Phys. Rev. A*, 70:023605, 2004.

[130] S. Tsuchiya, S. Kurihara, and T. Kimura. Superfluid-Mott insulator transition of spin-1 bosons in an optical lattice. *Phys. Rev. A*, 70:043628, 2004.

[131] J.J. García-Ripoll, M.A. Martin-Delgado, and J.I. Cirac. Implementation of Spin Hamiltonians in Optical Lattices. *Phys. Rev. Lett.*, 93:250405, 2004.

[132] H. Saito and M. Ueda. Diagnostics for the ground state phase of a spin-2 Bose-Einstein condensate. *Phys. Rev. A*, 72:053628, 2005.

[133] M. Ueda and M. Koashi. Theory of spin-2 Bose-Einstein condensates: Spin correlations, magnetic response, and excitation spectra. *Phys. Rev. A*, 65:063602, 2002.

[134] G.K. Campbell, J. Mun, M. Boyd, P. Medley, A.E. Leanhardt, L.G. Marcassa, D.E. Pritchard, and W. Ketterle. Imaging the Mott Insulator Shells by Using Atomic Clock Shifts. *Science*, 313:649, 2006.

[135] M. Lewenstein and L. You. Quantum Phase Diffusion of a Bose-Einstein Condensate. *Phys. Rev. Lett.*, 77:3489, 1996.

[136] E.M. Wright, D.F. Walls, and J.C. Garrison. Collapses and Revivals of Bose-Einstein condensates Formed in Small Atomic Samples. *Phys. Rev. Lett.*, 77:2158, 1996.

[137] Y. Castin and J. Dalibard. Relative phase of two Bose-Einstein condensates. *Phys. Rev. A*, 55:4330, 1997.

[138] J. Javanainen and M. Wilkens. Phase and Phase Diffusion of a Split Bose-Einstein Condensate. *Phys. Rev. Lett.*, 78:4675, 1997.

[139] A. Sørensen, L.-M. Duan, J.I. Cirac, and P. Zoller. Many-particle entanglement with Bose-Einstein condensates. *Nature*, 409:63, 2001.

[140] O. Mandel, M. Greiner, A. Widera, T. Rom, T.W. Hänsch, and I. Bloch. Controlled collisions for multi-particle entanglement of optically trapped atoms. *Nature*, 425:937, 2003.

[141] I. Goldhirsch. Phase operator and phase fluctuations of spins. *J. Phys. A*, 13:3479, 1980.

[142] J.M. Raimond, M. Brune, and S. Haroche. Reversible Decoherence of a Mesoscopic Superposition of Field States. *Phys. Rev. Lett.*, 79:1964, 1997.

[143] A. Auffeves, P. Maioli, T. Meunier, S. Gleyzes, G. Nogues, M. Brune, J.M. Raimond, and S. Haroche. Entanglement of a Mesoscopic Field with an Atom Induced by Photon Graininess in a Cavity. *Phys. Rev. Lett.*, 23:230405, 2003.

[144] G.-B. Jo, Y. Shin, S. Will, T.A. Pasquini, M. Saba, W. Ketterle, and D.E. Pritchard. Long Phase Coherence Time and Number Squeezing of two Bose-Einstein Condensates on an Atom Chip. *arXiv*, pages cond–mat/0608585, 2006.

[145] G.J. Milburn, J. Corney, and E.M. Wright. Quantum dynamics of an atomic Bose-Einstein condensate in a double-well potential. *Phys. Rev. A*, 55:4318, 1997.

[146] M. Kitagawa and M. Ueda. Squeezed spin states. *Phys. Rev. A*, 47:5138, 1993.

[147] D.J. Wineland, J.J. Bollinger, and W.M. Itano. Squeezed atomic states and projection noise in spectroscopy. *Phys. Rev. A*, 50:67, 1994.

[148] R.E. Slusher, L.W. Hollberg, B. Yurke, J.C. Mertz, and J.F. Valley. Observation of Squeezed States Generated by Four-Wave Mixing in an Optical Cavity. *Phys. Rev. Lett.*, 55:2409, 1985.

[149] L.-A. Wu, H.J. Kimble, J.L. Hall, and H. Wu. Generation of Squeezed States by Parametric Down Conversion. *Phys. Rev. Lett.*, 57:2520, 1986.

[150] G. Breitenbach, S. Schiller, and J. Mlynek. Measurement of the quantum states of squeezed light. *Nature*, 387:471, 1997.

[151] J. Hald, J.L. Sørensen, C. Schori, and E.S. Polzik. Spin Squeezed Atoms: A Macroscopic Entangled Ensemble Created by Light. *Phys. Rev. Lett.*, 83:1319, 1999.

[152] J.M. Geremia, J.K. Stockston, and H. Mabuchi. Control of Atomic Spin-Squeezing. *Science*, 304:270, 2004.

[153] A. Micheli, D. Jaksch, J.I. Cirac, and P. Zoller. Many-particle entanglement in two-component Bose-Einstein condensates. *Phys. Rev. A*, 67:013607, 2003.

[154] D. Leibfried, E. Knill, S. Seidelin, J. Britton, R.B. Blakestad, J. Chiaverini, D.B. Hume, W.M. Itano, J.D. Jost, C. Langer, R. Ozeri, R. Reichle, and D.J. Wineland. Creation of a six-atom 'Schrödinger cat' state. *Nature*, 438:639, 2005.

[155] Z. Zhao, Y.-A. Chen, A.-N. Zhang, T. Yang, H.J. Briegel, and J.-W. Pan. Experimental demonstration of five-photon entanglement and open-destination teleportation. *Nature*, 430:54, 2004.

[156] D. Jaksch, H.-J. Briegel, J.I. Cirac, C.W. Gardiner, and P. Zoller. Entanglement of Atoms via Cold Controlled Collisions. *Phys. Rev. Lett.*, 82:1975, 1999.

[157] G. Brennen, C.M. Caves, P.S. Jessen, and I.H. Deutsch. Quantum logic gates in optical lattices. *Phys. Rev. Lett.*, 82:1060, 1999.

[158] A. Sørensen and K. Mølmer. Spin-spin interaction and spin squeezing in optical lattices. *Phys. Rev. Lett.*, 83:2274, 1999.

[159] O. Mandel, M. Greiner, A. Widera, T. Rom, T.W. Hänsch, and I. Bloch. Coherent Transport of Neutral Atoms in Spin-Dependent Optical Lattice Potentials. *Phys. Rev. Lett.*, 91:010407, 2003.

[160] H.J. Briegel and R. Raussendorf. Persistent Entanglement in Arrays of Interacting Particles. *Phys. Rev. Lett.*, 86:910, 2000.

[161] R. Raussendorf and H.J. Briegel. A One-Way Quantum Computer. *Phys. Rev. Lett.*, 86:5188, 2001.

[162] M. Erhard, H. Schmaljohann, J. Kronjäger, K. Bongs, and K. Sengstock. Measurement of a mixed-spin-channel Feshbach resonance in ^{87}Rb. *Phys. Rev. A*, 69:032705, 2003.

[163] S. Inouyer, M.R. Andrews, J. Stenger, H.-J. Miesner, D.M. Stamper-Kurn, and W. Ketterle. Observation of Feshbach resonances in a Bose-Einstein condensate. *Nature*, 392:151, 1998.

[164] H. Moritz, T. Stöferle, M. Köhl, and T. Esslinger. Exciting Collective Oscillations in a Trapped 1D Gas. *Phys. Rev. Lett.*, 91:250402, 2003.

[165] A. Sinatra and Y. Castin. Binary mixtures of Bose-Einstein condensates: Phase dynamics and spatial dynamics. *Eur. Phys. J. D*, 8:319, 1999.

[166] F. Gerbier.

[167] G. Morigi, E. Solano, B.-E. Englert, and H. Walther. Measuring irreversible dynamics of a quantum harmonic oscillator. *Phys. Rev. A*, 65:040102, 2002.

[168] T. Meunier, S. Gleyzes, A. Auffeves, G. Nogues, M. Brune, J.M. Raimond, and S. Haroche. Rabi Oscillations Revival Induced by Time Reversal: A Test of Mesoscopic Quantum Coherence. *Phys. Rev. Lett.*, 94:010401, 2005.

[169] L. Santos, G.V. Shlyapnikov, P. Zoller, and M. Lewenstein. Bose-Einstein Condensation in Trapped Dipolar Gases. *Phys. Rev. Lett.*, 85:1791, 2000.

[170] H. Pu, W. Zhang, and P. Meystre. Ferromagnetism in a Lattice of Bose-Einstein Condensates. *Phys. Rev. Lett.*, 87:140405, 2001.

[171] W. Zhang, H. Pu, C. Search, and P. Meystre. Spin Waves in a Bose-Einstein-Condensed Atomic Spin Chain. *Phys. Rev. Lett.*, 88:060401, 2002.

[172] K. Góral, L. Santos, and M. Lewenstein. Quantum Phases of Dipolar Bosons in Optical Lattices. *Phys. Rev. Lett.*, 88:170406, 2002.

[173] A. Griesmaier, J. Werner, S. Hensler, J. Stuhler, and T. Pfau. Bose-Einstein Condensation of Chromium. *Phys. Rev. Lett.*, 94:160401, 2005.

[174] A. Griesmaier, J. Stuhler, T. Koch, M. Fattori, T. Pfau, and S. Giovanazzi. Comparing Contact and Dipolar Interactions in a Bose-Einstein Condensate. *Phys. Rev. Lett.*, 97:250402, 2006.

[175] J. Stuhler, A. Griesmaier, T. Koch, M. Fattori, T. Pfau, S. Giovanazzi, P. Pedri, and L. Santos. Observation of Dipole-Dipole Interaction in a Degenerate Quantum Gas. *Phys. Rev. Lett.*, 95:150406, 2005.

[176] C.F. Roos, G.P.T. Lancaster, M. Riebe, H. Häffner, W. Hänsel, S. Gulde, C. Becher, J. Eschner, F. Schmidt-Kaler, and R. Blatt. Bell States of Atoms with Ultralong Lifetimes and Their Tomographic State Analysis. *Phys. Rev. Lett.*, 92:220402, 2004.

[177] C.F. Roos, M. Chwalla, K. Kim, M. Riebe, and R. Blatt. 'Designer atoms' for quantum metrology. *Nature*, 443:316, 2006.

[178] J.M. Higbie, L.E. Sadler, S. Inouye, A.P. Chikkatur, S.R. Leslie, K.L. Moore, V. Savalli, and D.M. Stamper-Kurn. Direct Nondestructive Imaging of Magnetization in a Spin-1 Bose-Einstein Gas. *Phys. Rev. Lett.*, 95:050401, 2005.

[179] L.E. Sadler, J.M. Higbie, S.R. Leslie, M. Vengalattore, and D.M. Stamper-Kurn. Spontaneous symmetry breaking in a quenched ferromagnetic spinor Bose-Einstein condensate. *Nature*, 443:312, 2006.

[180] T.-L. Ho and Q. Zhou. Intrinsic Heating and Cooling in Adiabatic Processes for Bosons in Opitcal Lattices. *arXiv*, cond-mat:0703169, 2007.